EPFL

Thèse n° 7470

Propagation of fluid driven fractures in transversely isotropic material

Présentée le 31 janvier 2020

à la Faculté de l'environnement naturel, architectural et construit
Laboratoire de géo-énergie - Chaire Gaznat en géo-énergie
Programme doctoral en mécanique

pour l'obtention du grade de Docteur ès Sciences

par

Fatima-Ezzahra MOUKHTARI

Acceptée sur proposition du jury

Prof. C. Ancey, président du jury
Prof. B. T. A. Lecampion, directeur de thèse
Prof. E. Detournay , rapporteur
Prof. G. Mishuris, rapporteur
Prof. M. Violay, rapporteuse

École
polytechnique
fédérale
de Lausanne

2020

To my parents: Saida Motrib and Mustapha Moukhtari
To my sister and brother: Mariem Moukhtari and Badr Moukhtari
To my beloved husband: Jaafar Louadoudi

”Rabbi Ykhelikoum lia! ”

Acknowledgement of Support

Funding for this thesis came from an Assistant Professor Energy Grant of the Swiss National Science Fondation awarded to Brice Lecampion entitled “Hydraulic Stimulation of Anisotropic Rocks”, grant #160577. This support is greatly acknowledged.

Lausanne, January 17, 2020. F-E. Moukhtari

Acknowledgements

There were times that I thought that this moment will never come. So many ups and downs during this four years and also doubts and insecurities. Yet here we are and I can finally say: “Jaafar, we did it!”. Before everything, I must express my gratitude towards so many people that make this journey easier but challenging at the same time.

First, I would like to thank my thesis supervisor Prof. Brice Lecampion for letting me be the first child of the GEL laboratory. It was a steep slope during the first years but I learned too many things. Thanks for introducing me to the world of research and thank you for your guidance and your continuous help during this Phd.

A special thanks to my mentor Prof. Cristophe Ancey and the members of the committee, Prof. Marie Violay, Prof. Mishuris Gennady and Prof. Emmanuel Detournay for the time spent and effort evaluating my work. Thank you for your encouragements and your comments.

This work would never been accomplished without the help of Gary Perrenoud for the experimental study and Haseeb Zia for the numerical study. I am very grateful for all the help and the assistanat during these years.

During this thesis, I was really lucky to be surrounded by wonderful colleagues that become more than friends. I will start with my four years gossiping partner Federico Ciardo. Simply thank you for being there and thank you for being who you are (so Italian but so true). Gary Perrenoud, Dong lui and Dominique Gremaud, thank you for listening to me complaining many many times. Dmitry Loginov, seeing you always optimistic and smiling made me feel happy and hungry at the same time (sometimes I was about to kill you and take the credit for it). Thank you for your sweet thoughts and support. Carlo Perruzo, thank you for your patience and your help with the manuscript. Last but not least, thank you Alexis Saez and all the other members of GEL lab for sharing beautiful moments together.

I also met many master and bachelor students working with me and helping me along the four years. Thank you all!

Now I want to express my gratitude to my girls, especially the ones that were there for me (I apologize if I forget to mention all the names). I truly thank Lamyae Oummyhya, Nisrine Boujia and Houda Tadlaoui for everything. Also I want to thank Mouna Sitel and Hajar Lehbaoui for these amazing holidays together (although it was short!).

To my family from morocco, thank you for being that supportive despite the distance. To my uncles (especially Ismail Raqi) and my aunts (especially Tati Hamida). To my sister (and my best-friend) and brother. To Mamatii and Babatii. I love you.

It has been a long journey but fantastic because of you, Jaafar Louadoudi. You were my motor driver during this experience. My one and only, my husband, and the love of my life, thank you!

Lausanne, January 17, 2020 F-E.Moukhtari.

Abstract

The propagation of fluid driven fractures is used in a number of industrial applications (well stimulation of unconventional reservoirs, development of deep geothermal systems) but also occurs naturally (magmatic dyke intrusion). While the mechanics of hydraulic fractures (HF) in isotropic media is well established, the impact of the anisotropy of natural rocks on HF propagation is still far from being understood. Sedimentary rocks like shales and mudstones are ubiquitous in upper earth crust which are made of fine layers which result in transverse isotropy. In the framework of continuous mechanics, these rocks are commonly modelled as a transverse isotropic media (TI). In addition, a large number of fluids used in HF are non-Newtonian. They typically exhibit a shear-thinning behavior which can be reproduced by different rheological models with varying levels of accuracy (Carreau, power law, Ellis).

In this thesis, we focus on hydraulic fractures in impermeable TI media. We assume that the fracture propagates normal to the isotropy plane without any further assumption on its shape. This configuration is relevant for normal and strike-slip stress regimes where the minimum in-situ stress is horizontal.

We combine a boundary element and a finite volume method with an implicit level set scheme to model the growth of three dimensional planar HF. Both anisotropy of elasticity and fracture energy/toughness are accounted for. This algorithm couples a finite discretization of the fracture with the solution for a steadily moving hydraulic fracture in the tip region. We show that the near tip elastic operator has a similar expression than in the isotropy pending the use of a near-tip elastic modulus which now depends on the local propagation direction with respect to the isotropy plane. Using this numerical model we quantify the fracture elongation as a function of both the elastic and fracture toughness anisotropies. The elongation is maximal in the toughness dominated regime. The transition of the viscosity to the toughness regime occurs faster along the arrester direction, thus promoting fracture elongation.

In parallel, we report laboratory experiments of HF growth in cubic samples of slate Del Carmen under true-triaxial confinement. We were able to propagate a planar HF perpendicular to the bedding planes only when the initial stress normal to bedding was 20 times larger than the other two stresses. For both regimes, the fracture surfaces are very rough with a self-affine behavior in the direction of the bedding and a stationary state in the direction normal to bedding.

We also investigate the effect of a non-Newtonian rheology on HF growth. We solve the problem of steadily moving semi-infinite HF driven by a Carreau fluid. We use a Gauss-

Chebyshev method for elasticity combined with finite differences for lubrication flow and solve the resulting non-linear system with the Newton Raphson method. The solution exhibits four asymptotic regions: a linear elastic fracture mechanics (lefm) asymptote near the tip, high-shear rate Newtonian and power law asymptotes in an intermediate region and a low-shear Newtonian asymptote in the far field. For the same dimensionless toughness, the fluid lag is smaller than for a Newtonian fluid of low shear rate viscosity. We show that simpler rheological models (Ellis and power law) cannot capture the complete solution, which accounts for the full rheological behavior.

Keywords: Hydraulic fracture mechanics, transverse isotropy, shear-thinning rheology, asymptotic solutions, fluid-solid coupling, experiments, numerical modeling, boundary element method, tensile fractures.

Résumé

La propagation des fractures hydrauliques (FH) est utilisée dans un certain nombre d'applications industrielles (stimulation des réservoirs non conventionnels, développement de systèmes géothermiques profonds) mais se produit aussi naturellement (intrusion de dykes magmatique). Alors que la mécanique des fractures hydrauliques dans les milieux isotropes est bien établie, l'impact de l'anisotropie des roches naturelles sur la propagation des FH est encore loin d'être comprise. Les roches sédimentaires comme les schistes et les mudstones sont omniprésentes dans la croûte terrestre supérieure. Elles sont faites de couches fines qui se traduit par une isotropie transverse. Dans le cadre de la mécanique des mileux continus, ces roches sont généralement modélisées comme un milieu isotrope transverse (IT). En outre, un grand nombre de fluides utilisées dans la fracturation hydraulique sont non-Newtoniennes. Elles présentent généralement un comportement rhéo-fluidifiant qui peut être reproduit par différents modèles rhéologiques avec un différent niveau de précision (Carreau, loi en puissance, Ellis).

Dans cette thèse, nous nous concentrons sur les fractures hydrauliques dans les milieux IT imperméables. Nous supposons que la fracture propage normale au plan d'isotropie sans aucune autre hypothèse sur sa forme. Cette configuration est pertinente pour les cas des régime de contraintes normale et décrochante pour lesquels la contrainte in-situ minimale est horizontale. Nous combinons une méthode d'éléments frontière avec des volumes finis et la méthode des surfaces de niveau implicites pour modéliser la croissance d'une FH planaire tridimensionnel. L'anisotropie est prise en compte à la fois dans l'élasticité et dans l'énergie de fracture / ténacité. Cet algorithme lie la discrétisation finie de la fracture avec la solution d'une fracture hydraulique propageant avec une vitesse constante dans la région près du pointe. Nous montrons que l'opérateur élastique près du pointe de la fracture a une expression semblable à celle de la solution isotrope sauf que maintenant le module élastique dépend de la direction de la propagation locale par rapport au plan d'isotropie. A l'aide de ce modèle numérique, nous quantifions l'élongation de la fracture en fonction de l'anisotropie de la ténacité et de l'élasticité. L'élongation est maximale dans le régime dominé par la ténacité. La transition du régime dominé par la viscosité au régime de ténacité se produit plus rapidement le long de la direction perpendiculaire au plan d'isotropie, favorisant ainsi l' élongation de la fracture.

En parallèle, nous rapportons des expériences de laboratoire de la croissance de la FH sur des échantillons cubiques de l'ardoise Del Carmen sous confinement triaxial. Nous avons

été en mesure de propager une FH planaire perpendiculaire aux plans de lamination que lorsque le confinement initial normal au lamination était 20 fois plus grand que les deux autres contraintes. Pour les deux régimes, la surface de la fracture est très rugueuse avec un comportement de type auto-affine dans la direction de lamination et comportement stationnaire dans la direction normale au lamination.
Nous étudions également l'effet d'une rhéologie non-Newtonienne sur la croissance de la FH. Nous résolvons le problème d'une fracture hydraulique semi-infinie conduite par le fluide de Carreau. Nous utilisons une méthode de Gauss-Chebyshev pour l'élasticité combinée avec la différence finie pour la loi de Poiseuille et nous résolvons le système non linéaire résultant avec la méthode Newton Raphson. La solution présente quatre régions asymptotiques : l'asymptote de la mécanique linéaire de fracture élastique (lefm) près de la pointe de fissure, l'asymptote Newtonienne relative à la valeur maximale de la viscosité et de la loi en puissance dans une région intermédiaire et l'asymptote Newtonienne relative à la valeur minimale de la viscosité dans le champ lointain. Pour la même ténacité adimensionnelle, la distance entre la pointe de la fracture et le front du fluide est plus petite que pour un fluide Newtonien avec la valeur de viscosité la plus faible. Nous montrons que les modèles rhéologiques plus simples (Ellis et la loi en puissance) ne peuvent pas englober la solution complète en tenant compte du comportement rhéologique complet.

Mots-clés : Mécanique des fractures hydrauliques, isotropie transversale, fluides rhéo-fluidifiants, solutions asymptotiques, couplage fluide-solide, expériences, modélisation numérique, méthode des éléments frontière, fractures en tension.

Contents

Acknowledgement of Support **iii**

Acknowledgements **v**

Abstract (English/Français) **vii**

List of Figures **xv**

List of Tables **xxv**

1 Introduction **1**
- 1.1 Motivations and Background . . . 1
  - 1.1.1 Hydraulic fracturing . . . 1
  - 1.1.2 Unconventional reservoir . . . 3
- 1.2 Hydraulic fracture growth - a brief review . . . 5
- 1.3 Research questions addressed in this thesis . . . 7
- 1.4 Outline of the different chapters . . . 8

2 Fracture mechanics of transversely isotropic media **11**
- 2.1 Elasticity . . . 11
  - 2.1.1 Voigt notation . . . 11
  - 2.1.2 Stress-strain relation in the material basis . . . 12
  - 2.1.3 Thomsen's parameters . . . 13
  - 2.1.4 Stress-strain relation in a rotated basis . . . 14
- 2.2 Boundary element method for a planar fracture in TI . . . 15
  - 2.2.1 Boundary Value Problem . . . 15
  - 2.2.2 Reciprocity identity . . . 16
  - 2.2.3 Fundamental point force solution - Green function . . . 16
  - 2.2.4 Boundary Integral representation . . . 17
  - 2.2.5 Displacement discontinuity method . . . 22
- 2.3 Near-tip elastic operator . . . 24
  - 2.3.1 Near-tip elastic operator via a change of reference . . . 25
  - 2.3.2 Near-tip elastic operator via the edge dislocation solution . . . 28
  - 2.3.3 Evolution of the near-tip elastic modulus along the crack front . . . 31
- 2.4 Fracture propagation criterion . . . 34

2.4.1 Energy release rate 34
2.4.2 Irwin relation in transverse isotropy 34
2.4.3 Stress Intensity Factor (SIF) 34
2.4.4 Irwin relation in transverse isotropy 35
2.5 Elastic solutions of fracture problem in TI material 36
2.5.1 Existing solutions 36
2.5.2 Elliptical fracture in a transversely isotropic media 37
2.6 Conclusions 41

3 A semi-infinite hydraulic fracture driven by a shear thinning fluid 43
3.1 Abstract 44
3.2 Introduction 44
3.3 Problem formulation 47
3.4 Scaling 49
3.5 Asymptotes 51
3.6 Numerical scheme 53
3.7 Results for a finite fluid lag 55
3.7.1 Effect of dimensionless toughness κ 55
3.7.2 Effect of the dimensionless transition shear stress α 56
3.7.3 Effect of the fluid shear thinning index n 59
3.7.4 Effect of the viscosity ratio μ_∞/μ_o 61
3.7.5 Comparison between the Carreau, power-law & Ellis Models 61
3.8 Case of a vanishing fluid lag / large dimensionless toughness ($\Lambda \approx 0$ / $\kappa \gg 1$) . . 63
3.8.1 Scaling 63
3.8.2 Evolution of the different asymptotic regions 68
3.8.3 Comparison between the Carreau, power-law & Ellis Models 69
3.9 Conclusions 73
3.10 Supplemental material 75
3.10.1 Poiseuille flow for a Carreau fluid 75
3.10.2 Power-law model 76
3.10.3 Ellis model 77
3.10.4 Scaling for the zero lag / large κ case 78

4 Planar hydraulic fracture growth in transversely isotropic materials perpendicular to the isotropy plane 81
4.1 Abstract 82
4.2 Introduction 82
4.3 Problem formulation 84
4.3.1 Elastic deformation 84
4.3.2 Fluid flow inside the fracture 86
4.3.3 Boundary conditions 86
4.3.4 Fracture Propagation condition 87
4.4 Near-tip HF asymptotes for a TI material 87

4.5 Numerical solution 88
4.6 Scaling and structure of the solution 90
4.7 Viscosity dominated regime 92
4.8 Toughness dominated regime 97
  4.8.1 Elliptical hydraulic fracture 97
  4.8.2 Isotropic toughness 98
  4.8.3 Isotropic fracture energy 100
  4.8.4 Self-similar fracture shape: planar 3D numerical versus approximated elliptical solution 104
4.9 Transition from viscosity to toughness dominated growth 105
  4.9.1 Elliptical toughness 108
  4.9.2 Isotropic toughness 109
  4.9.3 Isotropic fracture energy 109
4.10 Conclusions 110
4.11 Supplemental material 112
  4.11.1 Elliptical hydraulic fracture - toughness dominated solution 112

5 Laboratory experiments: Materials and Hydraulic Fracture Tests 115
5.1 Experimental hydraulic fracturing setup 115
  5.1.1 Hydraulic fracturing frame 115
  5.1.2 Experimental design 117
5.2 Material characterization 119
  5.2.1 Mineralogy 119
  5.2.2 Static measurements 121
  5.2.3 Ultrasonic measurements 125
  5.2.4 Fracture toughness tests 131
5.3 Hydraulic fracturing tests: Preliminary results 136
  5.3.1 Toughness tests 136
  5.3.2 Viscosity test: SLATE_M_1 142
5.4 Conclusions 146

6 Conclusions 149
6.1 Main contributions 149
6.2 Recommendations for future work 150

Appendices 153

A1 Relation between the different set of elastic constants in TI 155
A1.1 Compliance tensor S_{ij} 155
A1.2 Elastic constants E_i, ν_{ij} and G_{13} 156
A1.3 Stiffness tensor C_{ij} 157

B1 A polyaxial frame for hydraulic stimulation experiments with acoustic monitoring 161
  B1.1 Abstract 162
  B1.2 Polyaxial frame & injection system 162
    B1.2.1 Description of the frame 162
    B1.2.2 Stiffness qualification tests 164
    B1.2.3 Numerical model of the applied stresses 169
    B1.2.4 Sample preparation and injection system 171
  B1.3 Measurement system 174
    B1.3.1 General experimental control system 174
    B1.3.2 Pressure and volume control and recording 175
    B1.3.3 Active elastic wave monitoring 175
    B1.3.4 Data recording and storage 176
  B1.4 Signal processing and analysis sequence 176
    B1.4.1 Transmitted waves: fluid thickness estimation 176
    B1.4.2 Diffracted waves 177

Bibliography 179

Curriculum Vitae 191

List of Figures

1.1 Typical setup of a hydraulic fracturing job at the surface. Picture taken from Montgomery and Smith (2010). 2

1.2 Mineral composition of gas-bearing shales. Picture taken from Rutter et al. (2017). 4

1.3 Natural gas flaring in underground rock layers of Rhinestreet shale, Chestnut Ridge Park, New York, USA. Picture taken from: www.oilprice.com 4

1.4 World map of shale gas basins. Taken from: EIA study based on Advanced Resources International Inc data, BP. 5

2.1 Left: Transversely isotropic material frame where $\boldsymbol{e_3}$ is the axis of symmetry and $(\boldsymbol{e_1}, \boldsymbol{e_2})$ is the plane of isotropy. Right: Configuration of the rotated basis $(\boldsymbol{e'_1}, \boldsymbol{e'_2}, \boldsymbol{e'_3})$ with respect to the material basis $(\boldsymbol{e_1}, \boldsymbol{e_2}, \boldsymbol{e_3})$. 13

2.2 Schematic of crack in media Ω. 16

2.3 Finite rectangular dislocation in an infinite TI media. 24

2.4 Far-field verification: Displacement due to a unit rectangle tensile dislocation function of the relative distance using the analytical solution (Fabrikant, 1989) and the numerical solution of Pan et al. (2014). 25

2.5 Schematic of a planar three dimensional hydraulic fracture growing perpendicular to the isotropy plane. The different configurations of the near-tip region along the fracture front are also depicted: case A is a semi-infinite fracture propagating along the plane of isotropy or the so-called "divider direction", case B is a semi-infinite fracture propagating within the plane $(\boldsymbol{e_1}, \boldsymbol{e_3})$ and case C is a semi-infinite fracture propagating in the direction perpendicular to the layering defined as the "arrester direction" 26

2.6 Near-tip elastic modulus as a function of α using the exact solution obtained analytically (solid line) and its approximation (Laubie and Ulm, 2014) (dashed line). The reference set of values of the dimensionless parameters: $\beta = 1.5$, $C_{13}/C_{11} = 0.5$, $\epsilon = 0.3$ and $\delta = 0.2$ is displayed in dark grey with the variations of each elastic scalar: (a) effect of $\beta = \{1.2, 1.5, 2\}$, (b) effect of $C_{13}/C_{11} = \{0.4, 0.5, 0.7\}$, (c) effect of $\epsilon = \{0.2, 0.3, 0.5\}$, and (d) effect of $\delta = \{0.1, 0.2, 0.3\}$. 33

2.7 Co-linear extension of the fracture in the local basis. 35

2.8 The point (x_1, x_3) inside the elliptical fracture and its closest projection (x_1^f, x_3^f). 39

2.9 Left: Schematic of elliptical planar fracture normal to the bedding and subject to uniform pressure p, and right: Fracture plane discretised into rectangular elements. 40

2.10 Opening profile $[\![u(x_1,x_3)]\!]_2$ along $\boldsymbol{e_1}$ and $\boldsymbol{e_3}$ of elliptical fracture of $\gamma_e = 0.5$ embedded in slate Del Carmen under a uniform pressure $p = 1$ MPa. Comparison of the analytical solution in black solid line with the numerical elastic kernel in red dots (Pan et al., 2014). 40

3.1 Viscosity as function of shear rate for two fracturing fluids: Hydroxypropylguar (HPG - data taken from Guillot and Dunand (1985)) and in inset a viscoelastic surfactant (VES - data taken from Kefi et al. (2004)). These experimental data do not cover the large shear rate region where the viscosity typically tends toward the solvent viscosity (water in those case) - see e.g. Pipe et al. (2008) for experimental data on Xanthan gum covering the complete range of shear rates. A number of rheological models can be used to reproduce these data over parts or all of the range of shear rates. We display here the best fit for the power-law (dashed brown line), Carreau (continuous black line) and Ellis (dot-dashed red line) rheological models. The corresponding best-fit parameters are listed in table 3.1 for these two fluids and the different models. 45

3.2 Fluid velocity profiles for a lubrication flow between parallel plates (as it occurs within a fracture) at a given mean velocity $< u >= V = 1$ m/s for a Carreau, power-law, Ellis and Newtonian fluids. The corresponding fluid pressure gradient is also displayed for each model. The rheological parameters correspond to a HPG fluid (see table 3.1 for the different models, figure 3.1 for the rheogram). For the Newtonian velocity profile (dotted green line), the low shear rate viscosity of the HPG is used. Note that the solution for a Carreau fluid is semi-analytical while the solution for the other models can be obtained analytically (see sections 3.10.1, 3.10.2 and 3.10.3 for details). 47

3.3 Sketch of a semi-infinite hydraulic fracture propagating at a constant velocity V in an impermeable elastic material under a pre-existing normal compressive stress σ_o. A fluid lag zone of a-priori unknown length λ adjacent to the fracture tip may be present. 48

3.4 Dimensionless fracture opening $w/\epsilon L_{\mu_o}$ along the fracture for $\kappa = 0, 0.002, 0.008, 0.043, 0.33, 0.74$ (with corresponding lag size $\Lambda = 0.049, 0.048, 0.047, 0.041, 0.008, 8.3 \times 10^{-8}$) in log-log scale for $\alpha = 10^2$, $\mu_\infty/\mu_o = 10^{-3}$, and $n = 0.5$. The dashed lines correspond to the asymptotic solution in the toughness dominated regime (κ-asymptote), power-law viscosity regime (m_n-asymptote) and low shear-rate Newtonian viscosity regime (m_o-asymptote). 56

3.5 Dimensionless apparent viscosity Γ along the fracture starting from the fluid front $\xi = \Lambda$ for $\kappa = 0$ ($\Lambda = 0.049$) and $\kappa = 0.74$ ($\Lambda = 8.3 \times 10^{-8}$) in log-log scale for $\alpha = 10^2$, $\mu_\infty/\mu_o = 10^{-3}$, and $n = 0.5$. 57

3.6 Dimensionless fluid pressure p/σ_o along the fracture for $\kappa = 0$, 0.002, 0.008, 0.043, 0.33, 0.74 in semi-log scale for $\alpha = 10^2$, $\mu_\infty/\mu_o = 10^{-3}$, and $n = 0.5$. The dashed lines correspond to the asymptotic solution of pressure in power-law viscosity regime (m_n-asymptote) and in Newtonian viscosity regime (m_o-asymptote). 57

3.7 Extent of the regions where the numerical solution can be approximated by the different asymptotes (κ-asymptote, m_n-asymptote, and m_o-asymptote) with accuracy of 10^{-2} as function of dimensionless toughness with $\alpha = 10^2$, $\mu_\infty/\mu_o = 10^{-3}$, $n = 0.5$. The position of the fluid lag is also displayed for comparisons. . . 58

3.8 Dimensionless lag length λ/L_{μ_o} versus the dimensionless toughness κ for a Carreau rheology for different value of α ($\mu_\infty/\mu_o = 10^{-3}$, $n = 0.5$). The corresponding results for a power-law rheology are also displayed for $\alpha = 10^5$ and $\alpha = 10^3$ for comparisons. 59

3.9 a) Dimensionless fracture opening $w/\epsilon L_{\mu_o}$ along the fracture for $\kappa = 0$, 0.013, 0.045, 0.085, 0.11 (with corresponding lag size $\Lambda = 0.0004$, 0.00025, 5.8×10^{-5}, 2.5×10^{-6}, 8.3×10^{-8}) in log-log scale for $\alpha = 10^7$, $\mu_\infty/\mu_o = 10^{-3}$, and $n = 0.5$ (the dashed lines correspond to the asymptotic solution of opening in the toughness dominated regime (κ-asymptote), high shear rate Newtonian viscosity regime (m_∞-asymptote) and the power-law viscosity regime (m_n-asymptote)). b) Corresponding dimensionless apparent viscosity Γ starting from the fluid front $\xi = \Lambda$ for $\kappa = 0$, 0.11. 60

3.10 Dimensionless lag length λ/L_{μ_o} versus the dimensionless toughness κ for different values of n, ($\mu_\infty/\mu_o = 10^{-3}$, $\alpha = 10^2$). 61

3.11 Dimensionless lag length λ/L_{μ_o} versus the dimensionless toughness κ for a Carreau rheology with respect to μ_∞/μ_o ($\alpha = 10^3$, $n = 0.5$). The results for a power-law rheology are also displayed for $\mu_\infty/\mu_o = 10^{-3}$. 62

3.12 Dimensionless fracture opening $w/\epsilon L_{\mu_o}$ along the fracture in log-log scale for Carreau (with $\mu_\infty/\mu_o = 10^{-3}$), Ellis, power-law rheology: left- $\alpha = 7\times10^3$ ($\alpha_e = 4975$, Ellis Model), $n = 0.46$ and $\kappa = 0.01$, right- $\alpha = 10^6$ ($\alpha_e = 7.2\times10^5$, Ellis Model), $n = 0.46$ and $\kappa = 0.002$. 63

3.13 Occurrence of the different viscous asymptotes as function of $\bar{\alpha}$ and μ_∞/μ_o for $n = 0.46$. Three distinct regions separate the parametric space: region (A) defined as $\bar{\alpha} < \bar{\alpha}_{l_n}(\mu_\infty/\mu_o, n)$ where the solution transition from k directly to m_o, region (B) defined as $\bar{\alpha}_{l_n}(\mu_\infty/\mu_o, n) < \bar{\alpha} < \bar{\alpha}_{l_\infty}(\mu_\infty/\mu_o, n)$ where three asymptotes k, m_n and m_o can be observed, and region (C) defined for $\bar{\alpha} > \bar{\alpha}_{l_\infty}(\mu_\infty/\mu_o, n)$ where up to four asymptotes k, m_∞, m_n and m_o may be observed. The dot-dashed orange lines refer to the coordinates of the numerical simulations performed in figure 3.14. 67

3.14 Numerical bounds and transition lengthscales (black solid lines) between the different asymptotic regions:(a) variations of $\bar{\alpha}$ for $n = 0.46$, $\mu_\infty/\mu_o = 10^{-3}$, (b) variations of $\bar{\alpha}$ for $n = 0.46$, $\mu_\infty/\mu_o = 10^{-1}$, (c) variations of μ_∞/μ_o for $n = 0.46$, $\bar{\alpha} = 10^2$, and (d) μ_∞/μ_o for $n = 0.46$, $\bar{\alpha} = 10^5$. The regions where the numerical results fall within 1% of accuracy of an asymptote are also displayed. For the power-law region, limits where the numerical results are within 1% accuracy of the m_n asymptote are displayed in red, and in orange when within 5% of accuracy. 70

3.15 Zero lag case. Dimensionless fracture opening $w/w_{m_o k}$ as function of the dimensionless distance from the tip $x/\ell_{m_o k}$ for the three rheologies (see table 3.2 for the expressions of the characteristic scales $w_{m_o k}$ and $\ell_{m_o k}$). The rheological parameters of the fluid are the one of a HPG. Influence of $\bar{\alpha}$ with $\mu_\infty/\mu_o = 10^{-3}$: (a) $\bar{\alpha} = 74 \times 10^{-8}$ (Ellis $\bar{\alpha}_e = 53.4 \times 10^{-8}$), (b) $\bar{\alpha} = 74$ (Ellis $\bar{\alpha}_e = 53.4$; (c) $\bar{\alpha} = 10^3$ (Ellis $\bar{\alpha}_e = 2088.7$), (d) $\bar{\alpha} = 46.2 \times 10^3$ (Ellis $\bar{\alpha}_e = 33.4 \times 10^3$) with also the solution for different μ_∞/μ_o for the Carreau model. The Ellis model starts to depart from the Carreau in the intermediate region for $\alpha \geq 10^3$ even for a large shear thinning magnitude ($\mu_\infty/\mu_o = 10^{-3}$). 72

3.16 Exact and interpolated values of the dimensionless tangent viscosity in log-log scale with respect to the wall shear stress for different values of α and: $n = 0.46$, $\mu_\infty/\mu_o = 10^{-3}$. 76

4.1 Schematic of a planar three dimensional hydraulic fracture growing perpendicular to the isotropy plane. Different configurations of the near-tip region along the fracture front are also depicted: A) a semi- infinite fracture propagating along the plane of isotropy (divider direction), B) a semi-infinite fracture propagating within the plane $(\boldsymbol{e_1}, \boldsymbol{e_3})$ at angle α from $\boldsymbol{e_1}$ and C) a semi-infinite fracture propagating along the direction perpendicular to the isotropy plane (arrester direction). 85

4.2 Near-tip elastic modulus as function of α using the exact solution obtained analytically (solid line) and its approximation (Laubie and Ulm, 2014) (dashed line). Reference values: $\beta = 1.5$, $C_{13}/C_{11} = 0.5$, $\epsilon = 0.3$ and $\delta = 0.2$ displayed in dark grey. (a) Effect of $\beta = (1.2, 1.5, 2)$, (b) effect of $C_{13}/C_{11} = (0.4, 0.5, 0.7)$, (c) effect of $\epsilon = (0.2, 0.3, 0.5)$, and (d) effect of $\delta = (0.1, 0.2, 0.3)$. 89

4.3 Viscosity dominated propagation: Time evolution of the dimensionless major $a(t)/L_m(t_m)$ and minor $b(t)/L_m(t_m)$ semi axis in (a), and of the dimensionless width at the injection point $w(0,0)/W_m(t_m)$ in (b). The numerical simulations are performed for different values of $\beta = (1.2, 1.5, 2)$ with: $\epsilon = 0.3$, $\delta = 0.2$, and $C_{13}/C_{11} = 0.5$. 93

4.4 Viscosity dominated propagation: Self similar fracture footprint γ_m for the reference values: $\beta = 1.5$, $C_{13}/C_{11} = 0.5$, $\epsilon = 0.3$, and $\delta = 0.2$. The effect of the dimensionless elastic parameters is also depicted: (a) variations of $\beta = (1.2, 1.5, 2)$, (b) variations of $C_{13}/C_{11} = (0.4, 0.5, 0.7)$, (c) variations of $\epsilon = (0.2, 0.3, 0.5)$, and (d) variations of $\delta = (0.1, 0.2, 0.3)$. The inset figure in (a) show the evolution of the fracture aspect ratio b/a function of β. 94

4.5 Viscosity dominated regime: Self similar width profiles $\Omega_m = w/W_m(t)$ along the major axis $\boldsymbol{e_1}$ for the reference values: $\beta = 1.5$, $C_{13}/C_{11} = 0.5$, $\epsilon = 0.3$, and $\delta = 0.2$. The effect of the dimensionless elastic parameters is also depicted: (a) variations of $\beta = (1.2, 1.5, 2)$, (b) variations of $C_{13}/C_{11} = (0.4, 0.5, 0.7)$, (c) variations of $\epsilon = (0.2, 0.3, 0.5)$, and (d) variations of $\delta = (0.1, 0.2, 0.3)$. 95

4.6 Viscosity dominated regime: Self similar pressure profiles $\Pi_m = p/P_m(t)$ along the major axis $\boldsymbol{e_1}$ for the reference values: $\beta = 1.5$, $C_{13}/C_{11} = 0.5$, $\epsilon = 0.3$, and $\delta = 0.2$. The effect of the dimensionless elastic parameters is also depicted: (a) variations of $\beta = (1.2, 1.5, 2)$, (b) variations of $C_{13}/C_{11} = (0.4, 0.5, 0.7)$, (c) variations of $\epsilon = (0.2, 0.3, 0.5)$, and (d) variations of $\delta = (0.1, 0.2, 0.3)$. 96

4.7 Toughness dominated regime - Elliptical toughness anisotropy: (a,b) dimensionless self-similar width profile Ω_k along $\boldsymbol{e_1}$ and $\boldsymbol{e_3}$ respectively, (c) exhibit the dimensionless length of the major $a(t)/L_k(t_k)$ and minor $b(t)/L_k(t_k)$ semi-axis in semi-log scale as well as the relative error with respect to the analytical solution (section 4.11.1) in (d), and (e,f) exhibit the dimensionless width $w(0,0)/W_k(t_k)$ and pressure $p(0,0)/P_k(t_k)$ respectively at the injection versus the dimensionless time t/t_k for: $\kappa^{-1} = 1.2$, $\beta = 1.2$, $\epsilon = 0.3$, $\delta = 0.2$, and $C_{13}/C_{11} = 0.5$. 99

4.8 Toughness dominated propagation - Isotropic toughness case: self similar footprint γ_k obtained using the exact expression for E'_α (solid line) and the approximation function E'_{app} (dashed line) as the near-tip elastic modulus. Reference parameters: $\beta = 1.5$, $C_{13}/C_{11} = 0.5$, $\epsilon = 0.3$, and $\delta = 0.2$. (a) variations of $\beta = (1.2, 1.5, 2)$, (b) variations of $C_{13}/C_{11} = (0.4, 0.5, 0.7)$, (c) variations of $\epsilon = (0.2, 0.3, 0.5)$, and (d) variations of $\delta = (0.1, 0.2, 0.3)$. The insets display the corresponding evolution of the fracture aspect ratio b/a. 101

4.9 Toughness dominated propagation - Isotropic toughness case: self similar width profiles Ω_k along $\boldsymbol{e_1}$ and $\boldsymbol{e_3}$. Reference parameters: $\beta = 1.5$, $C_{13}/C_{11} = 0.5$, $\epsilon = 0.3$, and $\delta = 0.2$. (a, b) variations of $\beta = (1.2, 1.5, 2)$, (c, d) variations of $C_{13}/C_{11} = (0.4, 0.5, 0.7)$, (e, f) variations of $\epsilon = (0.2, 0.3, 0.5)$, and (g, h) variations of $\delta = (0.1, 0.2, 0.3)$. 102

4.10 Toughness dominated propagation - Isotropic toughness case: Dimensionless pressure evolution at the injection point $p(0,0)/P_k(t_k)$ with time t/t_k. Reference parameters: $\beta = 1.5$, $C_{13}/C_{11} = 0.5$, $\epsilon = 0.3$, and $\delta = 0.2$. (a) variations of $\beta = (1.2, 1.5, 2)$, (b) variations of $C_{13}/C_{11} = (0.4, 0.5, 0.7)$, (c) variations of $\epsilon = (0.2, 0.3, 0.5)$, and (d) variations of $\delta = (0.1, 0.2, 0.3)$. 103

4.11 Toughness dominated propagation - Isotropic fracture energy case: (a) Self similar footprint γ_k, and (b) dimensionless major $a(t)/L_k(t_k)$ and minor $b(t)/L_k(t_k)$ semi axis with time t/t_k for different values of $\beta = (1.2, 1.5, 2)$ with $\epsilon = 0.3$, $\delta = 0.2$, and $C_{13}/C_{11} = 0.5$. The inset figure in (a) shows the evolution of the fracture aspect ratio b/a function of β. 104

4.12 Toughness dominated regime - Isotropic toughness: Comparison of the fracture aspect ratios b/a obtained from the SIF minimization using E'_{α} (black square) or the approximation E'_{app} (black diamond) for the near-tip elastic modulus and results of the numerical solution using E'_{α} (black dot) or E'_{app} (black triangles). $\epsilon = 0.3$, $\delta = 0.2$, and $C_{13}/C_{11} = 0.5$ for all cases. 105

4.13 Toughness dominated regime - Isotropic toughness: Residual of the variation of the scaled stress intensity factor $K_I/K_{I,1}$ after minimization as function of $\theta = \arctan\left(\frac{b}{a}\alpha\right)$ with $\epsilon = 0.3$, $\delta = 0.2$, and $C_{13}/C_{11} = 0.5$ for all cases. 106

4.14 Toughness dominated regime - Isotropic fracture energy: Comparison of the fracture aspect ratios b/a obtained from the numerical solution (black dot), the fracture energy minimization criterion using E'_{α} (black square) or the approximation E'_{app} (black diamond) for the near-tip elastic modulus as function of β^{-1}. $\epsilon = 0.3$, $\delta = 0.2$, and $C_{13}/C_{11} = 0.5$ for all cases. 106

4.15 Toughness dominated regime - Isotropic fracture energy: Residual of the variation of the scaled fracture energy G/G_1 after minimization as function of $\theta = \arctan\left(\frac{b}{a}\alpha\right)$ with $\epsilon = 0.3$, $\delta = 0.2$, and $C_{13}/C_{11} = 0.5$ for all cases. 107

4.16 Elliptical toughness - Viscosity to toughness regime: Dimensionless major $a(t)/L_{mk,1}$ and minor $b(t)/L_{mk,1}$ semi axis in log-log scale function of the dimensionless time $t/t_{mk,1}$ for toughness ratio $\kappa^{-1} = 1.2$ with $\beta = 1.5$, $\epsilon = 0.3$, $\delta = 0.2$, and $C_{13}/C_{11} = 0.5$. Comparison with the approximated solution of Dontsov (2019) in green-dashed lines. 108

4.17 Isotropic toughness ($\kappa = 1$) - viscosity to toughness transition: time evolution of the dimensionless major $a(t)/L_{mk,1}$ and minor $b(t)/L_{mk,1}$ semi axis for $\beta = 1.5$, $\epsilon = 0.3$, $\delta = 0.2$, and $C_{13}/C_{11} = 0.5$. The approximated M+K solution of Dontsov (2019) is displayed in green-dashed lines. 109

4.18 Isotropic fracture energy viscosity to toughness transition: time evolution of the dimensionless major $a(t)/L_{mk,1}$ and minor $b(t)/L_{mk,1}$ semi axis for $\beta = 1.5$, $\epsilon = 0.3$, $\delta = 0.2$, and $C_{13}/C_{11} = 0.5$. The approximated M+K solution of Dontsov (2019) is displayed in green-dashed lines. 110

5.1 A cubic block of Del Carmen slate in place in the polyaxial cell (without connection of the wellbore). 116

5.2 3D drawing of the reaction frame with top of the cell open. The platens for the acoustic transducers are also displayed in the frame. 117

5.3 Schematic evolution of the initiation and propagation of radial fracture in isotropic impermeable media (taken from Lecampion et al. (2017)). 119

5.4 Mineralogical composition of Del Carmen slate in intensity using XRD method. We thank Professor Thierry Adatte for the mineralogical analysis that was done in the institute of Earth Sciences in University of Lausanne. 121
5.5 Schematic slate block showing the configuration of the three cores and the mechanical properties measured from each orientation. 122
5.6 Elastic equations governing the uniaxial compression test for a TI media (Cho et al., 2012). 122
5.7 Uniaxial loading function of the vertical strain during a cycle of loading-unloading on a cylindrical core of slate. The axial compression is applied parallel to the bedding. 123
5.8 Uniaxial loading function of the vertical strain during a cycle of loading-unloading on a cylindrical core of slate. The axial compression is applied normal to bedding. 124
5.9 Uniaxial loading function of the vertical strain during a cycle of loading-unloading on cylindrical core of slate. The axial compression is inclined at 45° with respect to the bedding. 124
5.10 Uniaxial loading function of the radial strain during a cycle of loading-unloading on a cylindrical core of slate. The axial compression is applied parallel to the bedding in the left figure, whereas it is normal to the bedding in the right figure. 125
5.11 Confining stress (in MPa) function of time (in s) for a cycle of loading-unloading of the cubic block. 126
5.12 Velocities of the P-waves propagating in the arrester direction of the horizontal (top-figure) and vertical (bottom-figure) confining stress for the loading-unloading cycle defined in figure 5.11. 127
5.13 Velocities of the P-waves propagating in the divider direction of the horizontal (top-figure) and vertical (bottom-figure) confining stress for the loading-unloading cycle defined in figure 5.11. 128
5.14 The dynamic stiffness coefficients C_{ij} in GPa for six slate Del Carmen samples. 129
5.15 Stiffness ratios C_{11}/C_{33}, C_{13}/C_{12} and C_{66}/C_{44} for six Del Carmen slate ultrasonic measurements. 130
5.16 A notched semi-circular specimen in bending (SCB specimen): front view (left-figure) and side view (right-figure). 131
5.17 Principal crack orientations with respect to the bedding planes, left to right: Arrester, short-transverse, divider and 45° inclined configurations. The angle α characterizes the fracture propagation direction with respect to the divider. . . 132
5.18 Example of load in kN versus vertical displacement in mm for the arrester configuration (figure 5.17). The critical load is $F_{max} = 11.92$ kN. 133
5.19 Example of load in kN versus vertical displacement in mm for the short-transverse configuration (figure 5.17). The critical load is $F_{max} = 2.38$ kN. 133
5.20 Example of load in kN versus vertical displacement in mm for the divider configuration (figure 5.17). The critical load is $F_{max} = 8.5$ kN. 134
5.21 Example of load in kN versus vertical displacement in mm for the 45° inclined configuration (figure 5.17). The critical load is $F_{max} = 7.04$ kN. 134

5.22 Mean value and standard deviation of K_{Ic} as function of α. 135

5.23 SLATE_K_3 test: A planar hydraulic fracture crossing all sides of the block. The black arrow indicates the orientation of the bedding plane. 136

5.24 SLATE_K_3 test: Experimental data for the pressure at the well upstream and downstream of the valve in (a), and the flux entering the fracture in (b). 137

5.25 SLATE_K_4 test: Left- Loading configuration of SLATE_K_4 test with the exact block size. Right- Schematic of the fracture patterns (black lines) for the upper-left quarter of the block (red dashed quadrant in left figure). 139

5.26 SLATE_K_4 test: Experimental data for the pressure at the well upstream and downstream of the valve in (a), with a zoom at the propagation in log-log scale in (b). 139

5.27 SLATE_K_4 test: (a) Experimental data for the flux entering the fracture with time and (b) Experimental data for the flat-jack volumes with time. 139

5.28 SLATE_K_4 test: Snapshots of the width profiles along the vertical axis $\boldsymbol{e_3}$ of the main horizontal fracture obtained from ultrasonic measurements. 140

5.29 SLATE_K_4 test: Record time function of the experiment time for compressional-diffraction data for a set of source-receiver presented in purple-dashed line in figure 5.25-left. The corresponding interval of the downstream pressure (in MPa) is plotted in the black solid line. 140

5.30 SLATE_K_3: Image corresponding to the upper (left-figure) and lower (right-figure) quarter part of the surface of the fracture resulting from the toughness dominated regime test. The red arrows refer to the wellbore location. 141

5.31 SLATE_K_3: Topographic image corresponding to the upper quarter part of the surface of the fracture. The 3D scan corresponds to the sample in figure 5.30. . 142

5.32 SLATE_K_3: (a,c): Height profile along $\boldsymbol{e_1}$ and along $\boldsymbol{e_3}$ respectively. (b,d): Δh and σ representation in log-log scale averaged over profiles at different x_3 as function of $\delta = \Delta x_1$ in (b) and at different x_1 as function of $\delta = \Delta x_3$ in (d). . . . 143

5.33 SLATE_M_1 test: Loading configuration of SLATE_M_1 test with the exact block size. The purple dots represent the positions of the acoustic sensors for the diffracted signal. 144

5.34 SLATE_M_1 test: Experimental data for the pressure at the well upstream and downstream of the valve in (a), with a zoom at the propagation in log-log scale in (b). 144

5.35 SLATE_M_1 test: Experimental data for flux into the fracture as a function of time. 145

5.36 SLATE_M_1 test: Snapshots of the width profiles along the vertical axis $\boldsymbol{e_3}$ of the main horizontal fracture obtained from ultrasonic measurements. 145

5.37 SLATE_M_1 test: Record time function of the experiment time for compressional-diffraction data for a set of source-receiver presented in purple-dashed line in figure 5.33. The corresponding interval of the downstream pressure (in MPa) is plotted in the black solid line. 146

5.38 SLATE_M_1: (a,c): Height profile along $\boldsymbol{e_1}$ and along $\boldsymbol{e_3}$ respectively. (b,d): Δh and σ representation in log-log scale averaged over profiles at different x_3 as a function of $\delta = \Delta x_1$ in (b) and at different x_1 as a function of $\delta = \Delta x_3$ in (d). . . 147

B1.1 3D drawing of the reaction frame with top of the cell open. The four steel rods used to tighten the top and bottom covers are clearly apparent, threads are not shown here. 163

B1.2 Top view of the reaction frame, loaded with sample, platen and flat-jacks on the side, and top platen. 163

B1.3 Polyaxial frame from the side view with the configuration of the frame axis. . . 164

B1.4 Schematic of the reaction frame. 165

B1.5 Photo of the setup with main features highlighted. Green: ISCO pump, Blue: LVDTs, Red: LVDT power supply and acquisition board, Purple: high-pressure lines and valves connecting the flat jacks. 165

B1.6 Close up of LVDT positioned in the center of the middle rib, along the $\boldsymbol{x}-$axis, with mounting bracket. 166

B1.7 Top view of the cell with aluminum block, steel spacer plates and flat-jacks sandwiched between steel plates on each side of the aluminum block. 166

B1.8 Results for the bottom rib along the $\boldsymbol{x}-$axis. The total displacement is plotted in blue and the flat-jack pressure in red. The measured displacement follows increases and decreases in pressure. 167

B1.9 Results for the top rib along the $\boldsymbol{y}-$axis. The total displacement is plotted in blue and the flat-jack pressure in red. The measured displacement follows increases and decreases in pressure. 167

B1.10 Photo of the LVDT setup for loading along the $\boldsymbol{z}-$axis. 168

B1.11 Results for the $\boldsymbol{z}-$axis at the center of the top and bottom plates. The total displacement is plotted in blue and the flat-jack pressure in red. Due to a leaky flat-jack, we had to refill the pump which caused a drop in pressure at $T = 36$ min. During that time, the pump sensor records the refill (room) pressure, and not the flat-jack (confining) pressure. At the end ($T = 110$ min, we let the pressure decrease from the leak only, and again we see that the displacement matches the pressure drop. 168

B1.12 Results for the pore pressure test. Ramping up the pressure requires a lot of fluid volume, thus we have to refill the pump at $T = 25$ min. As for the previous measurement, during that time the measured pressure is not the pore pressure. 169

B1.13 The assembly of the quarter of cubic block with the aluminium platens. The axis $\boldsymbol{z}$ is along the vertical top-bottom direction. 170

B1.14 Hydrostatic loading: σ_{33} in MPa for the eighth of the block (at the mid-height of the frame-figure B1.13). Each color represents a surface of iso-stress in linear scale of 0.5 MPa gradient. Here negative values of stress refer to compression tensor. 171

B1.15 Hydrostatic loading: σ_{13} in MPa for the eighth of the block (at the mid-height of the frame-figure B1.13). The linear scale varies from -1 MPa to 1 MPa. Here negative values of stress refer to compression tensor. 172

B1.16 Deviatoric loading: σ_{33} in MPa for the eighth of the block (at the mid-height of the frame-figure B1.13). Each color represents a surface of iso-stress in linear scale of 0.5 MPa gradient. Here negative values of stress refer to compression tensor. 173

B1.17 Estimation of the fracture opening using the technique described in Groenenboom and Fokkema (1998). 177

B1.18 Schematic of elastic propagation modes inside a cubic sample with transducers on the sides. D: wave diffracted at the fracture tip, T: transmitted wave, R: direct wave. 178

List of Tables

2.1 Correspondence between the Voigt notation and the classical notation for the stiffness tensor. 12

2.2 Example of elastic coefficients C_{ij} for TI rocks (in GPa). 13

2.3 Comparison of 3rd component of the fundamental displacement U_3^2 (in GPa^{-1}) at point $\boldsymbol{y} = (0, 10, 5)$ meters due to a unit force along $\boldsymbol{e_2}$ applied at the center $\boldsymbol{x} = (0, 0, 0)$ using the analytical solutions of Pan and Chou (1976); Lin and Keer (1989); Távara et al. (2008) with respect to the reference solution of Fabrikant (1989). The rocks are defined in table 2.2. 22

2.4 Comparison of fundamental stress Σ_{22}^3 (in m^{-1}) at point $\boldsymbol{y} = (0, 10, 5)$ meters due to a unit force along $\boldsymbol{e_3}$ applied at the center $\boldsymbol{x} = (0, 0, 0)$ using the analytical solutions of Pan and Chou (1976); Távara et al. (2012) with respect to the reference solution of Fabrikant (1989). The rocks are defined in table 2.2. 23

2.5 Example of the dimensionless parameters values for the anisotropic rocks given in table 2.2. 32

2.6 Opening magnitude (in mm) for an elasto-static elliptical fracture of $\gamma_e = 0.5$ subject to uniform pressure $p = 1$ MPa. Comparison of the analytical solution is with numerical simulations in Abaqus and with the analytical solutions of Fabrikant (2011); Kanaun (2007). The rocks are defined in table 2.2. 39

3.1 Rheological parameters of a HPG and VES fluids (for a given temperature) for the power-law, Carreau and Ellis models corresponding to the experimental data of figure 3.1. Note that the majority of fracturing fluids have a power-law index n between 0.1 and 0.5. 46

3.2 Characteristic scales for the zero lag case for the three different rheology. The low shear rate viscosity Newtonian scaling is used for both the Ellis and Carreau model. 64

3.3 Transition lengthscales between the different asymptotic regions expressed as function of the asymptotes characteristic scales (equation (3.13)) and directly as function of the problem parameters. 66

3.4 Values of the dimensionless parameters for example hydraulic fracturing fluids and materials for propagating velocity V. PMMA data from Bunger and Detournay (2008) and Bebertal sandstone data from Stoeckhert et al. (2015). . 75

4.1 Characteristic scales and dimensionless parameters in the viscosity (M), toughness (K) and the transition from viscosity to toughness (M-K). Note that $\mathscr{M} = \mathscr{K}^{-18/5}$. 91

5.1 Transition time scales between limiting propagation regimes (Lecampion et al., 2017). 120
5.2 Sample configuration for laboratory tests in toughness and viscosity dominated regime. 120
5.3 Sample configuration and test parameters for the three successful lab experiments. The elastic properties and fracture toughness are taken from the results of static tests (section 5.2.2) and SCB tests (section 5.2.4). 120
5.4 Experimental HF propagation time, transition time scales and dimensionless parameters of the three successful lab experiments. 120
5.5 C_{ij} coefficients from six ultrasonic measurements: mean value and standard deviation in GPa. 130
5.6 Mean value of K_{Ic} for the four configurations: arrester, short-transverse, divider and 45° inclined. 135

A1.1 Example of elastic moduli $\{E_1, E_3, G_{13}\}$ and Poisson ratios ν_{ij} for TI rocks. 159

B1.1 Maximum pressure and maximum displacement for stiffness test along $\boldsymbol{x}-$axis. 166
B1.2 Maximum pressure and maximum displacement for stiffness test along $\boldsymbol{y}-$axis. 167

1 Introduction

1.1 Motivations and Background

1.1.1 Hydraulic fracturing

Hydraulic fractures (HF) are a class of tensile fractures that propagate in rock under a pre-existing compressive state of stress due to the flow of a pressurized fluid. They occur naturally as magmatic intrusions in the upper earth crust in the forms of dykes (Lister, 1990; Rivalta et al., 2015), but also at glacier beds due to surface lake meltwater release (Tsai and Rice, 2010). Hydraulic fractures are also routinely engineered in order to increase the productivity of oil and gas wells - in particular in low to very low permeability reservoirs (Montgomery and Smith, 2010). The process involves the injection of a fluid at a given pump rate into a wellbore in order to initiate and propagate a (or possibly several) hydraulic fracture. In a second stage, proppant (solid particles) are added to the injected fluid in order to keep the fracture open in the long term, thus creating a high permeability channel connecting the reservoir to the well.

Services associated with hydraulic fracturing amount to a market size in excess of 25 Billions USD in 2019 in the United States alone (see also the press release at: ibisworld.com/industry-statistics/market-size/hydraulic-fracturing-services-united-states). A typical hydraulic fracture job requires several pump trucks for high-pressure injection, fluid and acid tanks, proppant conveyer, a blender for fluid mixing, as well as other auxiliary equipment (figure 1.1). High-pressure pumps up to100 MPa maximum pressure can be used[1], and the injection rates vary from 0.5 m^3/min up to 6 m^3/min for a single fracture treatment (Wan, 2011). Such injection rates are typically multiplied by the number of fractures in cases where several hydraulic fracture are propagated simultaneously (Lecampion and Desroches, 2015).

Upon injection into a fracture, the pumped fluid volume is balanced between the fracture volume and the volume lost due to leak-off into the rock mass.The ratio between the fracture volume and the injected volume is coined the "fracturing efficiency". A good design for

---

[1] The pressure downhole at the hydraulic fracture entrance is equal to the sum of the surface pump pressure plus the hydrostatic pressure minus the pressure drop due to fluid flow inside the wellbore (friction pressure drop).

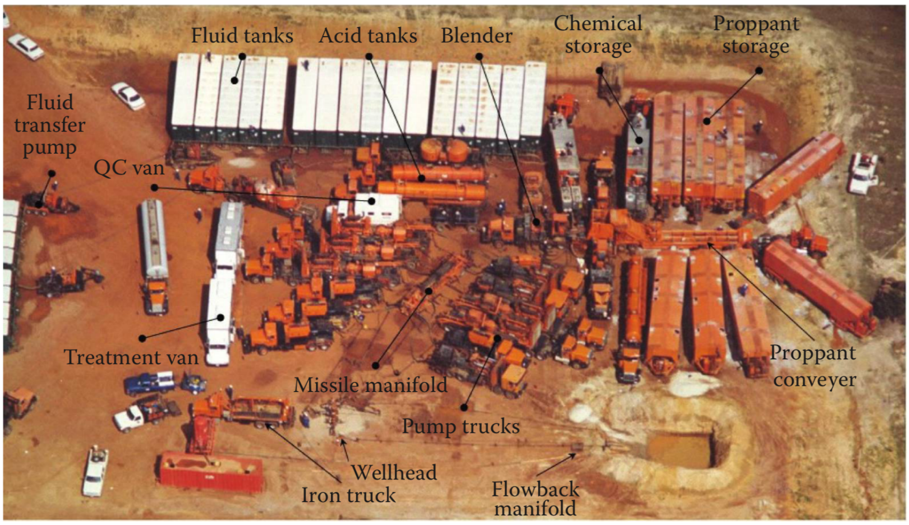

Figure 1.1 – Typical setup of a hydraulic fracturing job at the surface. Picture taken from Montgomery and Smith (2010).

hydraulic fracturing (HF) aims to create a desired fracture geometry with a good proppant coverage. It promotes maximizing the fracture efficiency and the ability to place sand particles in the fracture for the long term improvement of well productivity. Thus the critical parameters for the efficiency of the HF technique are the final propped fracture dimensions (surface area and width) which directly depend on the rock mass properties (stiffness, toughness, permeability), as well as the pumped fluid rheology and injection schedule (rate, proppant loading).

For a given geological formation, the design of a treatment involves the selection of appropriate fracturing fluids and proppants. Each fluid rheology will result in a specific fracture geometry and fracture opening. Fluids are also selected according to their ability to carry fluid particles efficiently. Shear-thinning fluids like Guar, Xanthan gum or VES (Viscoelastic Surfactant) are commonly used in the oil and gas industries for their property of fluid loss control and good proppant carrier capability (Montgomery and Smith, 2010).

Other applications of the hydraulic fracturing technique

Besides oil and gas well stimulation in conventional and unconventional reservoirs, other applications of hydraulic fracturing exist in fields such as mining, geothermal energy, rock mechanics and civil engineering. Hydraulic fracturing is used to improve water production in rock aquifers by pumping water at low pressure into existing fractures to connect them together within the water table. It is also used in the technique referred to as "compensation grouting" in civil engineering, which is used to re-level buildings (Lancellotta et al., 2017).

In mining, hydraulic fracturing is carried out to pre-condition the rock in block-cave mining operations. This is achieved by drilling multiple boreholes into the ore, placing multiple fractures to ensure continuous caving of the rock mass (Detournay, 2016). It is also used in Coal Mine Methane (CMM) to reduce the methane content of coal seams in both horizontal and vertical configurations but also in Coalbed Methane (CBM) reservoirs to increase gas recovery.

A more recent development of hydraulic fracturing is in geothermal energy. In 2013, a large scale stimulation was performed for producing heat or hot water in a subterranean area adjacent to the Newbury volcano in Oregon (Adams and Rowe, 2013). Geothermal power plants provide a tiny percentage of the world's energy electricity (about 0.5%) but may have a large growth potential (Bertani, 2016).

Another important hydraulic fracturing application relates to the measurement of in-situ stress (Haimson and Cornet, 2003). A micro-hydraulic fracturing test consists of pumping fluid into a small section of a borehole isolated by inflatable packers under a constant injection rate in order to initiate and propagate a fracture away from the wellbore concentrations. Upon shut-in, the pressure in the interval decays to ultimately reach the in-situ pore-pressure. In between, the pressure at which the fracture closes is a direct measure of the in-situ confining stress normal to the fracture plane. It can be seen as a kink in specialized pressure decay plots (Economides and Nolte, 2000). Multiple injection and shut-in cycles are typically performed to ensure proper measurement of the minimum in-situ stress.

A new area of application of hydraulic fracturing remaining under development is the storage of carbon in coal basins as well as saline aquifers where it is most likely that well injectivity will need to be enhanced.

1.1.2 Unconventional reservoir

The term "unconventional reservoir" refers usually to very low permeability rocks such as tight sandstone, coal, mudstones and shale in which hydrocarbons can not be produced without hydraulic fracturing. Unconventional gas includes shale gas and tight gas which is extracted from respectively tight sandstone, and mudstones (figure 1.3). Shale gas rocks include clays, carbonate, quartz feldspar and micas as well as organic matter - and are thus the "source" rock of conventional reservoirs. Their exact natures vary widely (figure 1.2). These sedimentary rocks are typically anisotropic due to i) their lamination resulting from the deposition process and ii) the intrinsic anisotropy of their constituents (e.g. clay). They represent the largest distribution of hydrocarbon reservoirs on earth. Shale rocks are abundant with more than 200 trillion cubic meters of reserves (figure 1.4). The propagation of hydraulic fractures in these rocks is likely affected by their anisotropy. However, conventional stimulation designs do not consider material anisotropy. How such anisotropy impacts hydraulic fracture growth is still an open question and is the primary driver of this thesis.

Hydraulic fractures propagates at depth normal to the principal minimum in-situ stress direction as first demonstrated in the experiments of Hubbert and Willis (1957). In normal

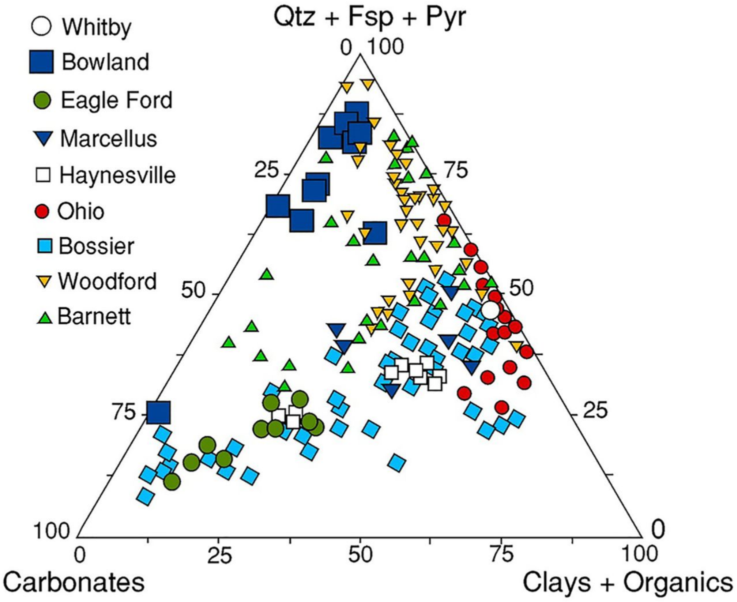

Figure 1.2 – Mineral composition of gas-bearing shales. Picture taken from Rutter et al. (2017).

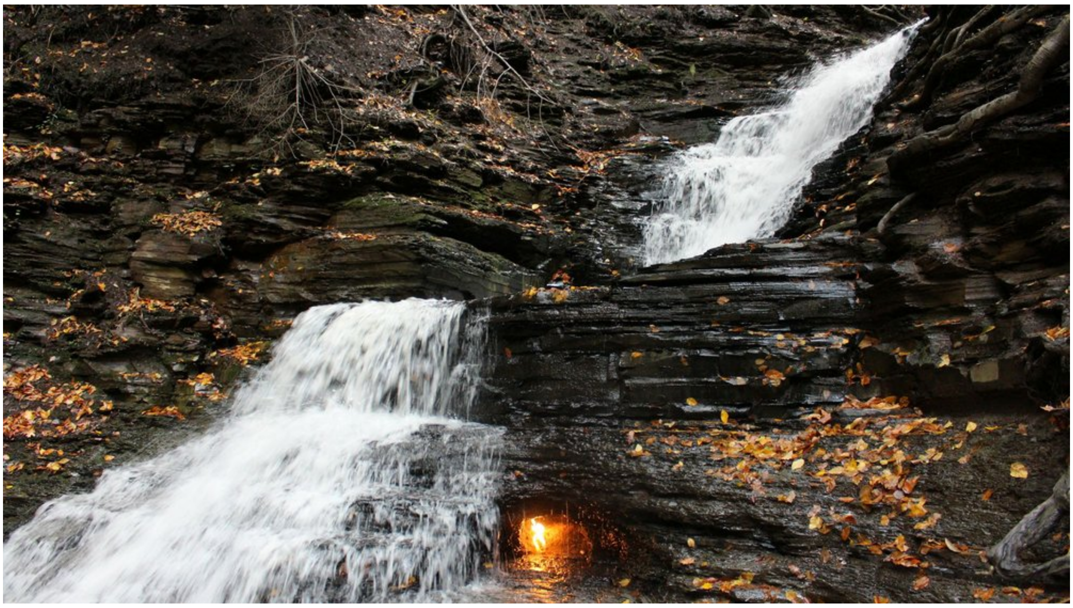

Figure 1.3 – Natural gas flaring in underground rock layers of Rhinestreet shale, Chestnut Ridge Park, New York, USA. Picture taken from: www.oilprice.com

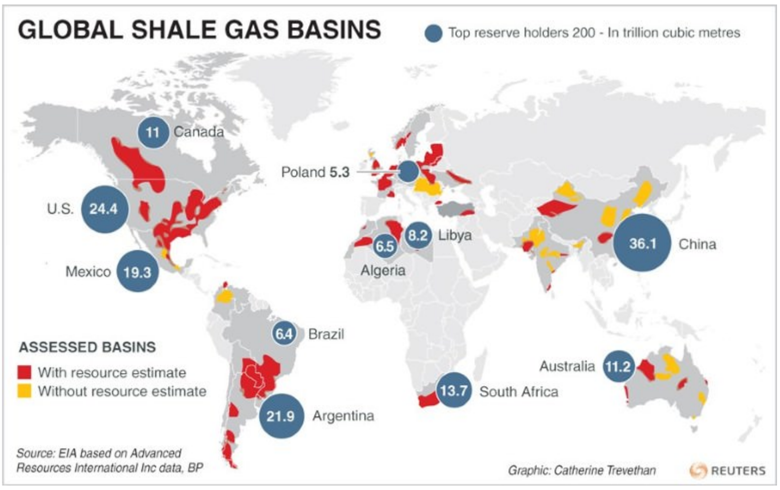
GLOBAL SHALE GAS BASINS
Top reserve holders 200 - In trillion cubic metres
11 Canada
U.S. 24.4
Mexico 19.3
Poland 5.3
8.2 Libya
6.5 Algeria
36.1 China
6.4 Brazil
ASSESSED BASINS
With resource estimate
Without resource estimate
Australia 11.2
13.7 South Africa
21.9 Argentina
Source: EIA based on Advanced Resources International Inc data, BP
Graphic: Catherine Trevethan
REUTERS

Figure 1.4 – World map of shale gas basins. Taken from: EIA study based on Advanced Resources International Inc data, BP.

and strike-slip stress regimes, which prevail in most unconventional reservoirs, the minimum in-situ stress is horizontal. The vertical stress is generally equal to the weight of the overburden, whereas the horizontal stress arises from a combination of the compaction of the overburden in the horizontal direction and tectonic forces (Montgomery and Smith, 2010).

In the case of weak interfaces or the vertical stress not being sufficiently large, the HF may deviate from the vertical plane to form a “T”-shaped fracture or to create jogs at the boundaries. Furthermore, for tight reservoirs, the permeability of the rock normal to bedding can be assumed negligible, whereas at the beddings it may not.

1.2 Hydraulic fracture growth - a brief review

The importance of the coupling between fluid flow and elastic deformation was recognized early by Khristianovic and Zheltov (1955); Barenblatt (1962). A number of solutions were constructed in the 1960s/1970s under a series of different simplifying assumptions: the PKN model (Perkins and Kern, 1961) assumes that the fracture height is constant and that each vertical cross section is deforming under a state of plane strain, whereas the KGD model (Geertsma and De Klerk, 1969) assumes a cusp-shaped fracture with a plane strain condition in the horizontal plane. PKN and KGD both consider a one-dimensional fluid flow problem. Besides the PKN and KGD models, a radial fracture solution was developed for the case of great toughness in impermeable media (Abe et al., 1976). An extension of the PKN was proposed by Simonson et al. (1978) as a pseudo-3D model dividing the fracture into cells along the lateral plane, so that the width and the height are calculated functions of the local fluid pressure (see Adachi et al. (2010) for discussion). Detournay et al. (1990) introduced an explicit finite difference scheme with a moving mesh for a PKN problem, followed by Adachi et al. (2001) for KGD fracture driven in elastic media with zero fracture toughness.

Spence and Sharp (1985); Lister (1990); Barenblatt (1962), were the first to discuss the fact that in many cases the resistance of the solid to fracture (i.e. the fracture toughness) plays a very small role in comparison to the viscous flow in the fracture. It was observed that the limit of negligible fracture toughness leads to a peculiar behavior near the crack tip which was further clarified by Desroches et al. (1994). The complete solution accounting for finite toughness as well as fluid leak-off can be found in Garagash et al. (2011) under the assumption of a vanishing fluid lag. The importance of properly resolving the different lengthscales associated with the near-tip behavior has prompted the development of specific numerical algorithms.

The implicit level set scheme, introduced first by Peirce and Detournay (2008), was applied to the solution of the problem of planar three-dimensional hydraulic fracture growth in isotropic media (Dontsov and Peirce, 2017). This scheme is fully implicit based on the tip asymptotic solution of a steadily moving fracture combined with a fast marching method for the front reconstruction. The scheme has been extended to the case where the fracture toughness is anisotropic by Zia et al. (2018). A new approach to three-dimensional full coupling numerical code was developed by Itasca (XSite) based on the Lattice method. The solver simulates propagation of hydraulic fracture in reservoirs naturally fractured. A review of recent developments in the numerical solution of this class of problem can be found in Lecampion et al. (2018).

One approach that enables us to quantify the competition between the elastic deformation of the rock and the viscous flow is to zoom into the tip of a finite fracture where a plane-strain configuration occurs. This technique allows us to derive analytically asymptotic solutions and to better characterize the effect of the different physical processes on HF growth. The impact of a power law fluid rheology was investigated in the zero toughness and zero lag case (Desroches et al., 1994). Desroches et al. (1994) derived the analytical asymptotic solution for fracture width and pressure using Goursat-Muskhelishkvili complex potential functions for the rheological parameters of the power law fluid, elastic properties of the medium and fracture velocity. The near-tip region of a fluid-driven fracture, with a lag, was studied by Garagash and Detournay (2000, 1998) for the case of an impermeable elastic medium. They developed a solution for a material of arbitrary toughness assuming a lag of a priory unknown length between the fluid front and the crack tip. The fluid pressure in the tip cavity (lag) was considered to be unknown and not uniform. Flow of pore fluid within the cavity, as well as circulation of pore fluid between the rock and the tip cavity, was also assumed to take place (Detournay and Garagash, 2003). The condition at which cavitation takes place was also examined.

Another important line of research aims at clarifying, via scaling and dimensional analysis, the structure of the HF growth solution. One of the key features of scaling is to grasp the different dominant physical processes at play during hydraulic fracture evolution. One can thus separate the different physical phenomena (fracture energy, viscosity, leak-off) and the corresponding propagation regimes via a finite set of dimensionless numbers. Asymptotic solutions for specific regimes are valid when one or more dimensionless groups of parameters goes to zero (Bunger et al., 2005; Madyarova and Detournay, 2003). Furthermore, the extent of each propagation regime can be easily grasped via characteristic time and lenghtscales (Garagash, 2009; Madyarova and Detournay, 2003; Savitski and Detournay, 2002; Lecampion et al., 2017). This allows us to chiefly capture the evolution of a hydraulic fracture without resorting to any complex numerical simulations. It is also particularly useful in properly designing laboratory experiments targeting for example a given growth regime.

Proper measurement of hydraulic fracture growth in the laboratory is particularly challenging. We must measure fracture opening on the order of micrometers and track precisely the growing fracture front that may not be strictly planar. In 1957, Hubbert and Willis presented experimental work performed in gelatin where they indicated that the fractures grow perpendicular to the minimum in-situ stress: i.e. vertically in most sedimentary basins contradictory to the thinking at the time, which had thought that fractures grew horizontally. Daneshy (1978) performed a HF test on limestone and sandstone by injecting fluid normal to the bedding. Facing such a bedding boundary, the fluid pressure increases to remove the obstacle. His results showed that depending on the strength of the interface and the in-situ stress, the fracture may grow through them or not.

The first acoustic measurements of HF growth were carried out by Medlin and Masse (1984) showing the possibility of measuring the fracture length by the transmission of compressional P-waves. The first strong diffractions scattered from the perimeter of the fracture were detected on a cement block (Savic, 1995). Both Savic (1995); Medlin and Masse (1984) have measured two distinct fronts, corresponding to a dry fracture front and fluid front - confirming the existence of a fluid lag in some cases.

A photometry technique was developed for a fluid driven fracture experiment in transparent material (Bunger and Detournay, 2008). These experiments verified the predicted multi-scale nature of the near-tip region of a HF. They also confirm the steady-state propagation solution with scaling in different propagation regimes. The fracture curving effect, the near surface effect and the stress shadowing due to multiple fracture stimulation were investigated in Bunger and Detournay (2008); Bunger (2005). Experiments with in-situ stress variations were performed to validate the results obtained with a numerical planar 3D HF simulator (Wu et al., 2008). Comparisons between numerical predictions and laboratory experiments for the initiation and propagation of radial-driven fracture were reported in Lecampion et al. (2017). These laboratory experiments have shown the importance of the fluid compressibility effect at early stages of injection which induce a transient regime that may govern laboratory scale experiments if not properly controlled.

1.3 Research questions addressed in this thesis

For an anisotropic rock mass, the orientation of the hydraulic fracture is only dependent on the in-situ stress configuration. In an infinite isotropic medium with uniform properties and in-situ stresses, the hydraulic fracture propagates in a radial shape with its center located at the point of injection. However, for laminated transversely anisotropic rocks, the hydraulic fracture, initially propagating normal to the horizontal bedding plane may deviate to open bedding planes forming a “T’”-shaped fracture due to the low resistance of bedding in sedimentary rocks. In this thesis, we focus on the limiting case of very large vertical stress or/and very strong bedding plane interfaces. As a result, we assume that the HF grows in a vertical plane (normal to the minimum stress which as previously discussed is horizontal for most unconventional reservoirs) perpendicular to the plane of material isotropy which is assumed to be horizontal. Such a configuration is the most commonly encountered in oil and gas unconventional reservoirs for which the minimum stress is typically horizontal as previously discussed.

When considering transversely isotropic media, the elastic properties as well as the fracture energy are no longer isotropic. The fracture will grow from a point source and may elongate with different increments of length depending on the local orientation of the fracture front with respect to the plane of material isotropy. We will investigate here how such a TI anisotropy impacts the fracture shape and quantify the main problem parameters affecting the solution. We will also present preliminary experimental results aiming at verifying these theoretical predictions.

In industrial applications, non-linear fluids such as HPG, for which the viscosity decays with the shear rate with two cutoffs at high and low share rates values, are extensively used. The rheology of these fluids can be represented by different constitutive models, i.e: Carreau, power law or Ellis. We focus here on the near-tip region and derive the solution of a semi-infinite hydraulic fracture driven by a shear-thinning fluid. How the Carreau model differ from simpler alternative rheological models (Ellis, power law and Newtonian) and how the extent of the fluid lag reduces as compared to a Newtonian fluid is also studied.

1.4 Outline of the different chapters

This thesis is structured in six chapters which we briefly present below.

Chapter 2- Fracture mechanics of transversely isotropic media

This chapter recalls important results of fracture mechanics with a focus on transversely isotropic medium. We notably discuss the boundary integral equation method for the solution of crack problem. We also clarify the near-tip linear elastic fracture mechanics asymptote for a fracture growing perpendicular to the material isotropy plane, and obtain an exact expression of the near-tip plane-strain elastic modulus as a function of the direction of propagation. We additionally re-derive the solution of a static elliptical fracture subject to uniform fluid pressure in a TI material. We use it to validate a displacement discontinuity solver for planar tensile crack in TI media.

Chapter 3- A semi-infinite hydraulic fracture driven by a shear thinning fluid

We investigate the near-tip region of a steadily moving semi-infinite hydraulic fracture driven by a shear-thinning fluid propagating in an impermeable isotropic medium. A solution that can be directly applied to the TI case depends on the use of the proper near-tip elastic modulus as a function of propagation direction. We use the Carreau rheological model which reproduces properly the experimental data of shear-thinning fluid on the whole range of shear rate. We account for the presence of a fluid lag of a priori unknown length at the tip of the fracture. Simpler rheological models (power-law, Ellis) are also used and compared to the Carreau model with respect to HF growth.

Chapter 4- Planar hydraulic fracture growth in transversely isotropic materials perpendicular to the isotropy plane

This chapter presents a three dimensional simulator for a planar hydraulic fracture propagating normal to the isotropy plane in transversely isotropic media. The elastic media exhibits both an anisotropy of elasticity and fracture toughness. A solution for the limiting case where the fracture is exactly elliptical (for a peculiar form of anisotropy) is derived in the toughness dominated regime and allows us to validate the numerical solver.

Chapter 5- Laboratory experiments: Materials and Hydraulic Fracture Tests

This chapter reports the characterisation of the Del Carmen slate: notably measurements of its mineralogy, elastic constants (static and ultrasonic) and fracture toughness in different directions. The results of hydraulic fracture experiments are discussed with a focus on three specific tests covering toughness and viscosity dominated growth. The roughness of the created fracture surfaces are measured and analysed.

Chapter 6- Conclusions

This chapter summarizes the main outcomes of this research and discusses perspectives for further development of this work.

Appendix A- A polyaxial frame for hydraulic stimulation experiments with acoustic monitoring

The experimental set-up is detailed in the appendix both in terms of mechanical hardware and measurement systems.

2 Fracture mechanics of transversely isotropic media

The most general definition of anisotropy is “the directional variation in the value of a vector measurement of a property” (Tsvankin, 2012). It is important to note that this definition is scale dependent. Sedimentary rocks - in particular- are composed of beds of metric to sub-metric scales. The effect of such rock configuration on a propagation of a fracture is still an open question. One of the goals of this chapter is to study the elastic deformation due to the discontinuity in displacement in transversely isotropic (TI) homogeneous media. This issues from the existence of a fracture that is assumed planar and perpendicular to the bedding planes. Additionally, the elastic field near the fracture tip is direction dependent. The case of an elliptical static fracture subject to uniform pressure is also addressed in this chapter.

2.1 Elasticity

2.1.1 Voigt notation

The theory of linear elasticity postulates that strains and stresses at each material point are proportional (Ting, 1996):

$$\sigma_{ij} = c_{ijkl}\epsilon_{kl} \tag{2.1}$$

where c_{ijkl} is the 4-th order symmetric stiffness tensor and σ_{ij} and ϵ_{kl} are 2×2 tensors.

Since the stresses and strains are symmetric, the stiffness matrix must satisfy the minor symmetries $c_{ijkl} = c_{jikl} = c_{ijlk}$. In addition, the strain energy density $\psi = \frac{1}{2}\epsilon_{ij}c_{ijkl}\epsilon_{kl}$ should not change when interchanging ij and kl, thus, the tensor c_{ijkl} satisfies also the major symmetries $c_{ijkl} = c_{klij}$. Using these symmetries, we can reduce the number of the subscripts of the stiffness constants by regrouping into one subscript the first two and the last two subscripts ($c_{ij\to\alpha,kl\to\beta}$) according to table 2.1. This is called the Voigt notation.

In the following, we will use the notation C_{ij} to refer to the stiffness tensor in Voigt notation, and write:

$$\sigma_i = C_{ij}\epsilon_j \tag{2.2}$$

Classical notation ij/kl	11	22	33	23	32	13	31	12	21
Voigt notation α/β	1	2	3	4	4	5	5	6	6

Table 2.1 – Correspondence between the Voigt notation and the classical notation for the stiffness tensor.

where $\sigma_i = (\sigma_{11}\ \sigma_{22}\ \sigma_{33}\ \sigma_{23}\ \sigma_{13}\ \sigma_{12})^t$ and $\epsilon_i = (\epsilon_{11}\ \epsilon_{22}\ \epsilon_{33}\ \epsilon_{23}\ \epsilon_{13}\ \epsilon_{12})^t$ are the 6×1 vector representations of stress and strain tensors.

2.1.2 Stress-strain relation in the material basis

We introduce in figure 2.1 the basis $(\boldsymbol{e_1}, \boldsymbol{e_2}, \boldsymbol{e_3})$ where $\boldsymbol{e_3}$ is the axis of rotational symmetry. The plane $(\boldsymbol{e_1}, \boldsymbol{e_2})$ is a plane of material isotropy. In the case of a transversely isotropic (TI) material, the elastic properties have an axis of symmetry. The stiffness tensor C_{ij} is completely defined by five independent parameters: $C_{11}, C_{12}, C_{13}, C_{33}, C_{44}$. In the material frame, we express the tensor c_{ijkl} function of C_{ij}'s as:

$$\begin{aligned} c_{ijkl} =& (C_{11} - 2C_{66})\delta_{ij}\delta_{kl} + C_{66}(\delta_{ik}\delta_{jl} + \delta_{il}\delta_{jk}) \\ &+ (C_{11} + C_{33} - 2C_{13} - 4C_{44})\delta_{i3}\delta_{j3}\delta_{k3}\delta_{3l} \\ &+ (C_{13} - C_{11} + 2C_{66})(\delta_{i3}\delta_{j3}\delta_{kl} + \delta_{k3}\delta_{l3}\delta_{ij}) \\ &+ (C_{44} - C_{66})(\delta_{j3}\delta_{k3}\delta_{il} + \delta_{i3}\delta_{l3}\delta_{jk} + \delta_{j3}\delta_{l3}\delta_{ik} \\ &+ \delta_{i3}\delta_{k3}\delta_{jl}) \end{aligned}$$

where $C_{66} = \frac{1}{2}(C_{11} - C_{12})$ and δ_{ij} is the Kronecker delta.

The stress strain relation (2.1) in Voigt notation reads:

$$\begin{pmatrix} \sigma_{11} \\ \sigma_{22} \\ \sigma_{33} \\ \sigma_{23} \\ \sigma_{13} \\ \sigma_{12} \end{pmatrix} = \begin{pmatrix} C_{11} & C_{12} & C_{13} & 0 & 0 & 0 \\ C_{12} & C_{11} & C_{13} & 0 & 0 & 0 \\ C_{13} & C_{13} & C_{33} & 0 & 0 & 0 \\ 0 & 0 & 0 & C_{44} & 0 & 0 \\ 0 & 0 & 0 & 0 & C_{44} & 0 \\ 0 & 0 & 0 & 0 & 0 & \frac{1}{2}(C_{11} - C_{12}) \end{pmatrix} \begin{pmatrix} \epsilon_{11} \\ \epsilon_{22} \\ \epsilon_{33} \\ 2\epsilon_{23} \\ 2\epsilon_{13} \\ 2\epsilon_{12} \end{pmatrix} \tag{2.3}$$

The elastic constitutive relation can be also expressed in terms of compliance matrix $S_{ij} = C_{ij}^{-1}$ or the set of engineering elastic constants $\{E_1, E_3, \nu_{12}, \nu_{13}, G_{13}\}$. The relationships between three sets of constants are given in appendix A1.

We introduce in table 2.2 the C_{ij} constants for TI rocks. The anisotropy for the direct compression along $\boldsymbol{e_1}$ and $\boldsymbol{e_3}$ is computed using the ratio C_{11}/C_{33} which varies from 1 for an isotropic

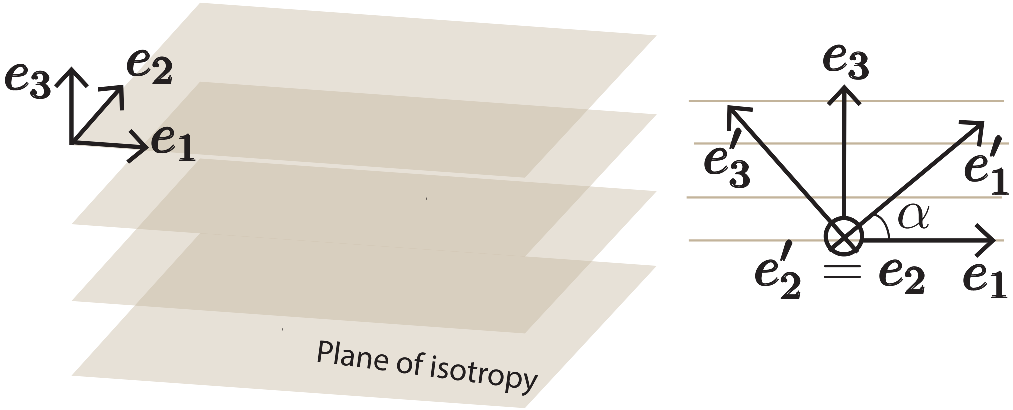

Figure 2.1 – Left: Transversely isotropic material frame where $\boldsymbol{e_3}$ is the axis of symmetry and $(\boldsymbol{e_1}, \boldsymbol{e_2})$ is the plane of isotropy. Right: Configuration of the rotated basis $(\boldsymbol{e'_1}, \boldsymbol{e'_2}, \boldsymbol{e'_3})$ with respect to the material basis $(\boldsymbol{e_1}, \boldsymbol{e_2}, \boldsymbol{e_3})$.

Material	C_{11}	C_{33}	C_{12}	C_{13}	C_{44}	C_{11}/C_{33}
Stripa granite (Alm et al., 1985) (isotropic)	73.17	73.17	19.45	19.45	26.9	1
Olkiluoto mica gneiss (Hakala et al., 2007)	89.74	65.87	22.22	23.51	24	1.36
Gas-saturated Shaly Coal (Wang, 2002)	22.08	10.91	8.36	1.25	3.71	2.02
Woodford53 shale (Laubie, 2013)	28	17.3	7.5	8.3	5.6	1.62
Opalinius Clay (Thöny, 2014)	57.65	28.8	54.61	38.7	0.9	2
Yeocheon schist (Cho et al., 2012)	91.44	27.61	33.76	20.03	13.7	3.31
Calcareous mudstone (Chertov, 2012)	90.4	35.13	51.57	39.85	6.49	2.57
Callovo-Oxfordian argilite (David et al., 2007)	20.5	13.11	8.16	4.87	5.22	1.56
Jurassic shale (Hornby, 1998)	39.42	27.09	15.65	16.52	6.9	1.45
Slate Del Carmen (this study)	35.4	26.4	0.41	1.03	21.2	1.34

Table 2.2 – Example of elastic coefficients C_{ij} for TI rocks (in GPa).

media (e.g: Stripa-granite) to 3.31 for highly anisotropic medium (e.g: Yeocheon schist).

2.1.3 Thomsen's parameters

The Thomsen parameters necessarily arise to describe the effective parameters that principally govern the wavefields. The anisotropy of a P-wave is described by Thomsen's parameters ϵ and δ, whereas γ quantifies the fractional difference of S-waves propagating in $\boldsymbol{e_1}$ and $\boldsymbol{e_3}$ (Tsvankin, 2012). The idea of Thomsen notation is also based in separating the effect of anisotropy from isotropy since these dimensionless parameters are Null for isotropic media.

$$\begin{aligned}\epsilon &= \frac{C_{11}-C_{33}}{2C_{33}}\\ \delta &= \frac{(C_{13}+C_{44})^2-(C_{33}-C_{44})^2}{2C_{33}(C_{33}-C_{44})}\\ \gamma &= \frac{C_{11}-C_{12}-2C_{44}}{4C_{44}}\end{aligned} \tag{2.4}$$

Measurements made for TI formations at seismic frequencies indicate that typically $\epsilon > \delta$ even in cases where the intrinsic anisotropy of shales dominates the contribution of fine layering (Tsvankin, 2012) (see table 2.5). The anisotropy is called elliptical when $\epsilon = \delta$, which refers to elliptical P wavefronts emanating from a point source (Thomsen, 1986).

The comparison of P-wave velocities for TI formations usually yields moderate positive δ values (typically on the order of 0.1–0.2), whereas interbedding of different thin isotropic layers typically produces small negative δ (Berryman, 1979). The values of ϵ in sedimentary sequences, on the other hand, ranges from 0.1 – 0.3 for moderately anisotropic rocks to 0.3 – 0.5 for compacted shale formations (Thomsen, 1986). As for γ, it should be positive (Tsvankin, 2012) as we can see from table 2.5.

2.1.4 Stress-strain relation in a rotated basis

Consider the orthonormal basis $(\boldsymbol{e'_1}, \boldsymbol{e'_2}, \boldsymbol{e'_3})$ of figure 2.1-right where $\boldsymbol{e'_2}$ is parallel to $\boldsymbol{e_2}$. We denote the angle α as the rotation angle between the two axis $\boldsymbol{e_1}$ and $\boldsymbol{e'_1}$. We will refer to the material basis $(\boldsymbol{e_1}, \boldsymbol{e_2}, \boldsymbol{e_3})$ using the subscripts (i, j) and to the rotated basis $(\boldsymbol{e'_1}, \boldsymbol{e'_2}, \boldsymbol{e'_3})$ using the subscripts (i', j'). The relation between the two basis is such that:

$$\boldsymbol{e'_{i'}} = P_{i'i}\boldsymbol{e_i}$$

where:

$$P_{i'i} = \begin{pmatrix} \cos(\alpha) & 0 & \sin(\alpha) \\ 0 & 1 & 0 \\ -\sin(\alpha) & 0 & \cos(\alpha) \end{pmatrix} \tag{2.5}$$

The stiffness tensor c'_{ijkl} in the basis $(\boldsymbol{e'_1}, \boldsymbol{e'_2}, \boldsymbol{e'_3})$ can be deduced from the one in the material basis using the formula:

$$c'_{ijkl} = P_{i'i}P_{j'j}P_{k'k}P_{l'l}c_{ijkl} \tag{2.6}$$

In the Voigt notation we obtain:

$$C'_{ij}(\alpha) = \begin{pmatrix} C'_{11}(\alpha) & C'_{12}(\alpha) & C'_{13}(\alpha) & 0 & C'_{15}(\alpha) & 0 \\ C'_{12}(\alpha) & C_{11} & C'_{23}(\alpha) & 0 & C'_{25}(\alpha) & 0 \\ C'_{13}(\alpha) & C'_{23}(\alpha) & C'_{33}(\alpha) & 0 & C'_{35}(\alpha) & 0 \\ 0 & 0 & 0 & C'_{44}(\alpha) & 0 & C'_{46}(\alpha) \\ C'_{15}(\alpha) & C'_{25}(\alpha) & C'_{35}(\alpha) & 0 & C'_{55}(\alpha) & 0 \\ 0 & 0 & 0 & C'_{46}(\alpha) & 0 & C'_{66}(\alpha) \end{pmatrix}$$

The three dimensional Hooke's law in the rotated basis becomes:

$$\sigma_{i'} = C'_{ij}(\alpha)\epsilon_{j'}$$

where: $\sigma_{i'} = (\sigma_{1'1'}\ \sigma_{2'2'}\ \sigma_{3'3'}\ \sigma_{2'3'}\ \sigma_{1'3'}\ \sigma_{1'2'})^T$ and $\epsilon_{j'} = (\epsilon_{1'1'}\ \epsilon_{2'2'}\ \epsilon_{3'3'}\ 2\epsilon_{2'3'}\ 2\epsilon_{1'3'}\ 2\epsilon_{1'2'})^T$.

2.2 Boundary element method for a planar fracture in TI

The boundary value problem for elastic media describes the problem in a region Ω which is subject to constraints on the boundary (see figure 2.2). Relating the field problem to the enclosed boundary leads to a small algebraic system of equations. Boundary element methods are used to solve not only elasto-static problems, linear viscoelasticity or dynamic elasticity, but also heat flow. The literature on boundary element methods in elasticity is divided between direct and indirect approaches. Indirect methods were introduced by Crouch and Starfield (1983); Massonnet (1965) and consist of expressing the elastic field using a combination of surface potentials sought as density functions and regularizing the equations to avoid the integral singularities. In the general case, the physical meaning of the unknown density is unclear. However for crack problems, the unknown involved in the representations takes the meaning of a jump in displacement (Mogilevskaya, 2014). The direct approach explained by Cruse (1996); Green (1828) and introduced in the following, involved the so called Green representation of potential theory based on the Maxwell-Betti reciprocal formula. This method enables us to solve for the unknown boundary displacements or stresses in terms of the specified boundary conditions. In the case of equilibrated cracks, the two approaches are equivalent.

2.2.1 Boundary Value Problem

Let's consider an infinite medium Ω loaded with a far field stress $\boldsymbol{\sigma}^{\infty}$ (see figure 2.2). The finite crack is treated as a cut over a surface Γ, creating a discontinuity of displacement $[\![\boldsymbol{u}]\!] = \boldsymbol{u}^{+} - \boldsymbol{u}^{-}$ (see figure 2.2) while the vector traction remains continuous. In the case of a loaded crack, the

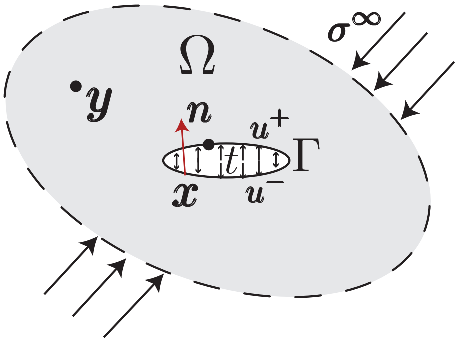

Figure 2.2 – Schematic of crack in media Ω.

equilibrium field equation of elastostatic problems with no body forces reads:

$$\sigma_{ij,j}(\boldsymbol{y}) = 0, \quad y \in \Omega \tag{2.7}$$

$$\sigma_{ij} n_j = -t n_j, \quad y \in \Gamma \tag{2.8}$$

$$\sigma_{ij}(\boldsymbol{y} \to \infty) = \sigma_{ij}^{\infty} \tag{2.9}$$

where: n_j is the unit outward normal vector and t is the internal normal loading. For hydraulically loaded fracture, a shear stress is also induced which we neglect in this present work (more details on the effect introduced by hydraulically induced tangential traction is in Wrobel et al. (2017)). We adopt the rock mechanics sign convention: the traction components are considered positive if they are oriented in the directions opposite to the outward unit normal vector.

2.2.2 Reciprocity identity

We consider two different states of the same elastic media Ω defined by stresses and strains $\boldsymbol{\sigma}^{(1)}, \boldsymbol{\epsilon}^{(1)}$ and $\boldsymbol{\sigma}^{(2)}, \boldsymbol{\epsilon}^{(2)}$. Maxwell-Betti's reciprocal theorem states that the work of stresses of the first state on the strains of the second state is equal to the work of stresses of the second state on the strains of the first state:

$$\sigma_{ij}^{(1)} \epsilon_{ij}^{(2)} = \sigma_{ij}^{(2)} \epsilon_{ij}^{(1)} \tag{2.10}$$

After integration of equation (2.10) and making use of the divergence theorem, we obtain:

$$\int_{\Gamma} \sigma_{ij}^{(1)} u_j^{(2)} n_i \mathrm{d}S - \int_{\Omega} \sigma_{ij,j}^{(1)} u_i^{(2)} \mathrm{d}V = \int_{\Gamma} \sigma_{ij}^{(2)} u_j^{(1)} n_i \mathrm{d}S - \int_{\Omega} \sigma_{ij,j}^{(2)} u_i^{(1)} \mathrm{d}V \tag{2.11}$$

2.2.3 Fundamental point force solution - Green function

The fundamental solution for a unit point force $\delta(\boldsymbol{y} - \boldsymbol{x})$ applied at the point source $\boldsymbol{x} \in \Omega$ is referred as Green's function. We write $U_k^m(\boldsymbol{x}, \boldsymbol{y})$ as the k-th component of displacement at point $\boldsymbol{y} \in \Omega$ due to the point force in the direction m located at $\boldsymbol{x} \in \Omega$. The fundamental solution is formulated as the following:

$$c_{ijkl} U^{m}_{k,lj}(\boldsymbol{x},\boldsymbol{y}) + \delta_{im}\delta(\boldsymbol{y}-\boldsymbol{x}) = 0$$

where the notation $f_{,j}$ above is the convention for the partial derivative of a function f with respect to the j-th component of the field point $\boldsymbol{y}$, and δ_{im} is the Kronecker delta. The fundamental stress is given by the formula:

$$\Sigma^{k}_{ij}(\boldsymbol{x},\boldsymbol{y}) = c_{ijmn} U^{k}_{m,n}(\boldsymbol{x},\boldsymbol{y})$$

The fundamental point force solution is singular at $y_i = x_i$.

General properties of the point force solution

We can use the Maxwell-Betti theroem (2.10) for two elastic states corresponding to: 1) a point force at $\boldsymbol{x}$ in the direction m and 2) a point force at $\boldsymbol{y}$ in the direction k. Thus, we obtain the following symmetry of the Green's function:

$$U^{m}_{k}(\boldsymbol{x},\boldsymbol{y}) = U^{k}_{m}(\boldsymbol{y},\boldsymbol{x})$$

Introducing small perturbations δx_i and δy_i of the points $\boldsymbol{x}$, and $\boldsymbol{y}$ respectively, the equality

$$U^{m}_{k}(\boldsymbol{x}+\delta\boldsymbol{x},\boldsymbol{y}+\delta\boldsymbol{y}) = U^{k}_{m}(\boldsymbol{y}+\delta\boldsymbol{y},\boldsymbol{x}+\delta\boldsymbol{x})$$

holds true for any $\delta\boldsymbol{x}$ and $\delta\boldsymbol{y}$. Matching the first and second order terms in $\delta\boldsymbol{x}$, $\delta\boldsymbol{y}$ on both sides of the equality, we obtain:

$$U^{m}_{k,j}(\boldsymbol{x},\boldsymbol{y}) = U^{k}_{m,\bar{j}}(\boldsymbol{y},\boldsymbol{x}) \tag{2.12}$$

$$U^{m}_{k,\bar{i}j}(\boldsymbol{x},\boldsymbol{y}) = U^{k}_{m,i\bar{j}}(\boldsymbol{y},\boldsymbol{x})$$

where $f_{,\bar{l}}$ refers to the partial derivative with respect to the l-th component of the source $\boldsymbol{x}$. For a free surface we can interchange $\boldsymbol{x}$ and $\boldsymbol{y}$ of the formula (2.12):

$$U^{m}_{k,\bar{j}}(\boldsymbol{x},\boldsymbol{y}) = -U^{k}_{m,j}(\boldsymbol{x},\boldsymbol{y})$$

2.2.4 Boundary Integral representation

The displacement of any point in the domain $\boldsymbol{y} \in \Omega$ not located on Γ is given in terms of the elastic variables on the boundary Γ via the integral representation formula of displacements also known as Somigliana's identity. If we consider the boundary as the fracture's surface, the displacement $\boldsymbol{u}$ and the stress σ_{ij} interior to Ω are obtained in terms of the body force distribution and the values of the displacement discontinuity $[\![\boldsymbol{u}]\!]$ and the surface traction $\boldsymbol{t}$ found on the boundary. In the case of a self equilibrated fracture with no body force,

Somigliana's identity becomes:

$$u_k(\boldsymbol{y}) = \int_\Gamma \Sigma^k_{ij}(\boldsymbol{x},\boldsymbol{y})\, n_j(\boldsymbol{x})\, [\![u(\boldsymbol{x})]\!]_i \,\mathrm{d}S_{\boldsymbol{x}} \tag{2.13}$$

where $\Sigma^k_{ij}(\boldsymbol{x},\boldsymbol{y}) = c_{ijmn} U^m_{k,n}(\boldsymbol{x},\boldsymbol{y})$. The equation (2.13) is derived from Maxwell-Betti's identity (2.10) using the point force solution as one of the two states.

Applying the stress-strain relation and making use of the symmetry properties of the stiffness, we obtain the integral representation of the stress tensor for an infinite medium as:

$$\begin{aligned}\sigma_{mn}(\boldsymbol{y}) &= c_{mnkl} u_{k,l}(\boldsymbol{y}) \\ &= -c_{mnkl} \int_\Gamma \Sigma^k_{ij,\bar{l}}(\boldsymbol{x},\boldsymbol{y})\, n_j(\boldsymbol{x})\, [\![u(\boldsymbol{x})]\!]_i \,\mathrm{d}S_{\boldsymbol{x}}\end{aligned}$$

We introduce a tangent differential operator (Bonnet, 1999) $D_{ij}(f) = n_i(f)_{,j} - n_j(f)_{,i}$ and since we have $\Sigma^k_{ij,\bar{j}}(\boldsymbol{x},\boldsymbol{y}) = 0$ on Γ when $\boldsymbol{y} \notin \Gamma$, the previous equation gives:

$$\begin{aligned}\sigma_{mn}(\boldsymbol{y}) &= -c_{mnkl} \int_\Gamma D_{jl} \Sigma^k_{ij}(\boldsymbol{x},\boldsymbol{y})\, [\![u(\boldsymbol{x})]\!]_i \,\mathrm{d}S_{\boldsymbol{x}} - c_{mnkl} \int_\Gamma \Sigma^k_{ij,\bar{j}}(\boldsymbol{x},\boldsymbol{y})\, n_j(\boldsymbol{x})\, [\![u(\boldsymbol{x})]\!]_i \,\mathrm{d}S_{\boldsymbol{x}} && (2.14) \\ &= -c_{mnkl} \int_\Gamma D_{jl} \Sigma^k_{ij}(\boldsymbol{x},\boldsymbol{y})\, [\![u(\boldsymbol{x})]\!]_i \,\mathrm{d}S_{\boldsymbol{x}} && (2.15)\end{aligned}$$

Making use of integration by parts, we obtain:

$$\sigma_{mn}(\boldsymbol{y}) = -c_{mnkl} \int_\Gamma \Sigma^k_{ij}(\boldsymbol{x},\boldsymbol{y}) D_{lj}\, [\![u(\boldsymbol{x})]\!]_i \,\mathrm{d}S_{\boldsymbol{x}} \tag{2.16}$$

For a traction vector applied at the surface, we have:

$$t_m(\boldsymbol{y}) = \sigma_{mn}(\boldsymbol{y}) n_n(\boldsymbol{y})$$

$$t_m(\boldsymbol{y}) = -c_{mnkl} \int_\Gamma \Sigma^k_{ij}(\boldsymbol{x},\boldsymbol{y}) D_{lj}\, [\![u(\boldsymbol{x})]\!]_i \, n_n(\boldsymbol{y}) \mathrm{d}S_{\boldsymbol{x}} \tag{2.17}$$

Planar fracture in a pure opening mode

We assume that the fracture surface lies in the $(\boldsymbol{e_1},\boldsymbol{e_3})$ plane subject to a normal traction along $\boldsymbol{e_2}$ (figure 2.5). For any $\boldsymbol{x}$ and $\boldsymbol{y}$ on the fracture plane, we have:

$$n_n(\boldsymbol{y}) = n_n(\boldsymbol{x}) = \boldsymbol{e_2},$$

$$x_2 = y_2 = 0,$$

$$[\![u(\boldsymbol{x})]\!]_i = [\![u(x_1,x_3)]\!]_2\, \boldsymbol{e_2},$$

$$D_{lj}\, [\![u(\boldsymbol{x})]\!]_2 = \delta_{l2}\, [\![u(\boldsymbol{x})]\!]_{2,j} - \delta_{j2}\, [\![u(\boldsymbol{x})]\!]_{2,l}\,.$$

The elastic traction and the strains integral representation become:

$$t_m(\boldsymbol{y}) = -c_{m2kl}\int_\Gamma \Sigma^k_{2j}(\boldsymbol{x},\boldsymbol{y})D_{lj}\,[\![u(\boldsymbol{x})]\!]_2\,\mathrm{d}S_{\boldsymbol{x}} \tag{2.18}$$

$$\epsilon_{kl}(\boldsymbol{y}) = -\int_\Gamma \Sigma^k_{2j}(\boldsymbol{x},\boldsymbol{y})D_{lj}\,[\![u(\boldsymbol{x})]\!]_2\,\mathrm{d}S_{\boldsymbol{x}} \tag{2.19}$$

Existing Green's function

The Green's function was derived for the case of transversely isotropic media by Pan and Chou (1976) using displacement complex potentials. This solution presents some errors corrected in Loloi (2000) for the displacement field and extended to transformed TI materials by Pouya (2007), although its first derivative is still not correct for some components. Lin and Keer (1989) obtained the same Green's functions in compact form for the full space and also for the multilayered media using a Hankel approach. Távara et al. (2008, 2012) also give the Green's functions with the first and second derivatives using a Cauchy residue theory. The first derivative of the point force solution is also described in Fabrikant (1989, 2004) for the non degenerate case in which: $\sqrt{C_{11}C_{33}} - C_{13} - 2C_{44} \neq 0$. An alternative form of the Green function, extended to the degenerate case, was given by Fabrikant (2004) but the analytical expressions suffer from some misprints.

Green function solution - Fabrikant (2004, 1989)

Our study is based on the analytical solution of Fabrikant (1989, 2004) of the Green's functions and their first derivatives. The analytical expression for the elastic field uses the effective harmonic complex potential functions, while the displacement is given by their first derivatives. Two basic sets of material constants are introduced:

$$\begin{aligned} m_{1,2} = &-1 + \frac{1}{2C_{44}(C_{13}+C_{44})} \\ &\times\left(C_{11}C_{33} - C_{13}^2 \pm \sqrt{C_{11}C_{33}-C_{13}^2}\sqrt{C_{11}C_{33}-(C_{13}+2C_{44})^2}\right) \end{aligned}$$

and

$$\gamma_i = \sqrt{\frac{C_{44}+m_i(C_{13}+C_{44})}{C_{11}}} = \sqrt{\frac{m_iC_{33}}{m_iC_{44}+(C_{13}+C_{44})}}, \quad i = \{1,2\}$$

$$\gamma_3 = \sqrt{\frac{C_{44}}{C_{66}}}$$

where

$$\begin{cases} m_1m_2 = & 1 \\ m_1 - m_2 = & C_{11}\left(\gamma_1^2-\gamma_2^2\right)/(C_{13}+C_{44}) \end{cases}$$

This solution is only valid for the non degenerate case: $\sqrt{C_{11}C_{33}} - C_{13} - 2C_{44} \neq 0 : \gamma_1 \neq \gamma_2$ (i.e. $m_1 \neq m_2$). We point out that for the isotropic case: $m_1 = m_2 = 1$, the stiffness matrix should be defined slightly different:

$$\begin{cases} C_{44} = & (1+\epsilon_e)\mu \\ C_{66} = & (1+3\epsilon_e)\mu \\ C_{13} = & (1+5\epsilon_e)\lambda \\ C_{11} = & (1+7\epsilon_e)(\lambda+2\mu) \\ C_{33} = & (1+9\epsilon_e)(\lambda+2\mu) \end{cases} \tag{2.20}$$

where λ and μ are Lame constants for isotropic media, and ϵ_e is a small perturbation (for example: $\epsilon_e = 10^{-4}$). The second term in the C_{ij} coefficients is defined slightly different in order to avoid a proportional factor C_{ij}/C_{kl} of 1.

Let a concentrated force be applied at the origin $\boldsymbol{x} = (0,0,0)$, where P is the component along $\boldsymbol{e_3}$ and $T = T_1 + iT_2$ ($i^2 = -1$) is the corresponding tangential force along $\boldsymbol{e_1}$ and $\boldsymbol{e_2}$. The general solution for the elastic field at the point $\boldsymbol{y}$ is solved in terms of the elastic parameters and the applied force for the complex tangential displacement $U = U_1 + iU_2$ and the normal displacement U_3 such that:

$$\begin{cases} U_1^k = & \mathrm{Re}\left(U\left(P=0; T=T_k=1\right)\right), \quad k=1,2 \\ U_1^3 = & \mathrm{Re}\left(U\left(P=1; T=0\right)\right) \\ U_2^k = & \mathrm{Im}\left(U\left(P=0; T=T_k=1\right)\right), \quad k=1,2 \\ U_2^3 = & \mathrm{Im}\left(U\left(P=1; T=0\right)\right) \\ U_3^k = & U_3\left(P=0; T=T_k=1\right), \quad k=1,2 \\ U_3^3 = & U_3\left(P=1; T=0\right) \end{cases}$$

We denote $\bar{T}$ as the conjugate of T: $\bar{T} = T_1 - iT_2$ and we introduce the following variables:

$$q = y_1 + iy_2$$

$$z_k = \frac{y_3}{\gamma_k}, \quad k = 1,2,3$$

$$R_k^2 = y_1^2 + y_2^2 + z_k^2, \quad k = 1,2,3$$

The displacement is given as the following:

$$U = \frac{1}{4\pi C_{44}(m_1 - m_2)}\left[\frac{\gamma_1}{2m_1}\left(\frac{q^2\bar{T}}{R_1\left(R_1+z_1\right)^2} - \frac{T}{R_1}\right) - \frac{\gamma_2}{2m_2}\left(\frac{q^2\bar{T}}{R_2\left(R_2+z_2\right)^2} - \frac{T}{R_2}\right) - \frac{P}{\bar{q}}\left(\frac{z_1}{R_1} - \frac{z_2}{R_2}\right)\right] + \frac{\gamma_3}{8\pi C_{44}}\left(\frac{q^2\bar{T}}{R_3\left(R_3+z_3\right)^2} + \frac{T}{R_3}\right), \tag{2.21}$$

$$U_3 = \frac{1}{4\pi C_{44}(m_1 - m_2)}\left[\frac{1}{2}\left(\frac{T}{q} + \frac{\bar{T}}{\bar{q}}\right)\left(\frac{z_2}{R_2} - \frac{z_1}{R_1}\right) + P\left(\frac{m_1}{\gamma_1 R_1} - \frac{m_2}{\gamma_2 R_2}\right)\right]. \tag{2.22}$$

We compare in table 2.3 the 3rd component of the Green's functions U_3^2 at the field point $\boldsymbol{y} = (0,10,5)$ (in meters) due to a unit point force applied at $\boldsymbol{x} = (0,0,0)$ using the solutions of Pan and Chou (1976); Fabrikant (1989); Lin and Keer (1989); Távara et al. (2008) for different elastic coefficients. We set our reference solution to the Fabrikant (1989) solution (equation 2.22) and we calculate the relative difference of the solutions of Pan and Chou (1976); Lin and Keer (1989); Távara et al. (2008). As we can see from table 2.3, the analytical solutions match exactly except for the isotropic case where the solution of Fabrikant (1989) is 0.005% off from the others possibly due to the small perturbation $\epsilon_e = 10^{-4}$ in the definition of the isotropic C_{ij} (2.20). Thus, we can use either the solution of Fabrikant (1989), Pan and Chou (1976), Lin and Keer (1989) or Távara et al. (2008) to express the fundamental solution of the displacement $U(\boldsymbol{x},\boldsymbol{y})$.

Similarly, using the complex variables to express the fundamental stress:

$$\Sigma_1 = \Sigma_{11} + \Sigma_{22}, \quad \Sigma_2 = \Sigma_{11} - \Sigma_{22} + 2i\Sigma_{12}, \quad \tau_3 = \Sigma_{31} + i\Sigma_{32},$$

in such a way that:

$$\begin{cases}
\Sigma_{11}^k = & \mathrm{Re}\left(\left(\Sigma_1\left(P=0; T=T_k=1\right) + \Sigma_2\left(P=0; T=T_k=1\right)\right)/2\right), \quad k=1,2 \\
\Sigma_{11}^3 = & \mathrm{Re}\left(\left(\Sigma_1\left(P=1; T=0\right) + \Sigma_2\left(P=1; T=0\right)\right)/2\right) \\
\Sigma_{22}^k = & \mathrm{Re}\left(\left(\Sigma_1\left(P=0; T=T_k=1\right) - \Sigma_2\left(P=0; T=T_k=1\right)\right)/2\right), \quad k=1,2 \\
\Sigma_{22}^3 = & \mathrm{Re}\left(\left(\Sigma_1\left(P=1; T=0\right) - \Sigma_2\left(P=1; T=0\right)\right)/2\right) \\
\Sigma_{12}^k = & \mathrm{Im}\left(\Sigma_2\left(P=0; T=T_k=1\right)\right), \quad k=1,2 \\
\Sigma_{12}^3 = & \mathrm{Im}\left(\Sigma_2\left(P=1; T=0\right)\right) \\
\Sigma_{33}^k = & \Sigma_{33}\left(P=0; T=T_k=1\right), \quad k=1,2 \\
\Sigma_{33}^3 = & \Sigma_{33}\left(P=1; T=0\right) \\
\Sigma_{31}^k = & \mathrm{Re}\left(\tau_3\left(P=0; T=T_k=1\right)\right), \quad k=1,2 \\
\Sigma_{31}^3 = & \mathrm{Re}\left(\tau_3\left(P=1; T=0\right)\right) \\
\Sigma_{32}^k = & \mathrm{Im}\left(\tau_3\left(P=0; T=T_k=1\right)\right), \quad k=1,2 \\
\Sigma_{32}^3 = & \mathrm{Im}\left(\tau_3\left(P=1; T=0\right)\right)
\end{cases}$$

, the fundamental solution for stress is expressed as:

$$\begin{aligned}\Sigma_1 =& \frac{1}{4\pi\gamma_3^2(m_1 - m_2)}\left[-\left(1 - \frac{(1+m_1)\gamma_3^2}{\gamma_1^2}\right)\left(\frac{\gamma_1}{m_1}\frac{T\bar{q} + \bar{T}q}{R_1^3} + \frac{2Pz_1}{R_1^3}\right)\right. \\ &\left. + \left(1 - \frac{(1+m_2)\gamma_3^2}{\gamma_2^2}\right)\left(\frac{\gamma_2}{m_2}\frac{T\bar{q} + \bar{T}q}{R_2^3} + \frac{2Pz_2}{R_2^3}\right)\right],\end{aligned} \tag{2.23}$$

	Fabrikant	Pan and Chou	Lin and Keer	Tavara
	U_3^2 (1/GPa)	relative difference		
Degenerate case-Stripa granite	0.047	0.005%	0.005%	0.005%
Woodford53 shale	1.48×10^{-4}	0	0	0
Opalinius Clay	1.45×10^{-3}	0	0	0
Yeocheon schist	7.05×10^{-5}	0	0	0

Table 2.3 – Comparison of 3rd component of the fundamental displacement U_3^2 (in GPa^{-1}) at point $\boldsymbol{y} = (0, 10, 5)$ meters due to a unit force along $\boldsymbol{e_2}$ applied at the center $\boldsymbol{x} = (0, 0, 0)$ using the analytical solutions of Pan and Chou (1976); Lin and Keer (1989); Távara et al. (2008) with respect to the reference solution of Fabrikant (1989). The rocks are defined in table 2.2.

$$\begin{aligned}\Sigma_2 =& \frac{C_{66}}{4\pi C_{44}(m_1 - m_2)}\left[\frac{\gamma_1}{m_1}\left(\frac{Tq}{R_1^3} - \bar{T}\frac{q^3\left(3R_1 + z_1\right)}{R_1^3\left(R_1 + z_1\right)^3}\right) - \frac{\gamma_2}{m_2}\left(\frac{Tq}{R_2^3} - \bar{T}\frac{q^3\left(3R_2 + z_2\right)}{R_2^3\left(R_2 + z_2\right)^3}\right)\right. \\ & \left. - \frac{2Pq^2\left(2R_1 + z_1\right)}{R_1^3\left(R_1 + z_1\right)^3} + \frac{2Pq^2\left(2R_2 + z_2\right)}{R_2^3\left(R_2 + z_2\right)^3}\right] - \frac{1}{4\pi\gamma_3}\left(\frac{Tq}{R_3^3} + \bar{T}\frac{q^3\left(3R_3 + z_3\right)}{R_3^3\left(R_3 + z_3\right)^3}\right),\end{aligned} \tag{2.24}$$

$$\Sigma_{33} = -\frac{1}{4\pi}\left[\frac{1}{2}\left(T\bar{q} + \bar{T}q\right)\left(\frac{\gamma_1}{\left(m_1 - 1\right)R_1^3} + \frac{\gamma_2}{\left(m_2 - 1\right)R_2^3}\right) + P\left(\frac{m_1 z_1}{\left(m_1 - 1\right)R_1^3} + \frac{m_2 z_2}{\left(m_2 - 1\right)R_2^3}\right)\right], \tag{2.25}$$

$$\begin{aligned}\tau_3 =& \frac{T}{8\pi}\left(\frac{z_1}{\left(m_1 - 1\right)R_1^3} + \frac{z_2}{\left(m_2 - 1\right)R_2^3} - \frac{z_3}{R_3^3}\right) - \frac{\bar{T}q^2}{8\pi}\left[\frac{2R_1 + z_1}{\left(m_1 - 1\right)R_1^3\left(R_1 + z_1\right)^2}\right. \\ & \left. + \frac{2R_2 + z_2}{\left(m_2 - 1\right)R_2^3\left(R_2 + z_2\right)^2} + \frac{2R_3 + z_3}{R_3^3\left(R_3 + z_3\right)^2}\right] - \frac{Pq}{4\pi}\left(\frac{m_1}{\gamma_1\left(m_1 - 1\right)R_1^3} + \frac{m_2}{\gamma_2\left(m_2 - 1\right)R_2^3}\right).\end{aligned} \tag{2.26}$$

Table 2.4 exhibits the expressions of the stress Σ_{22}^3 at the field point $\boldsymbol{y} = (0, 10, 5)$ (in meters) due to unit point force applied at $\boldsymbol{x} = (0, 0, 0)$ using Pan and Chou (1976); Távara et al. (2012) and Fabrikant (1989) (equation 2.25) in the example of TI rocks. We also validate Fabrikant (1989), taken as the reference solution, using numerical calculations (see section 2.2.5). The analytical solution of Pan and Chou (1976) converges for this example (table 2.4) which is not the case for all components due to some misprints (see (Loloi, 2000; Pouya, 2007) for more details), whereas the solution of Távara et al. (2012) differs very much from the reference solution (Fabrikant, 1989).

2.2.5 Displacement discontinuity method

An easy approach is to discretise the fracture plane over $n_e \times m_e$ rectangular elements and assume piece-wise constant displacement over element Γ_e. For $\boldsymbol{y} \in \Gamma_e$, evaluated at the centers

	Fabrikant	Pan and Chou	Tavara
	Σ^3_{22} (1/m)	relative difference	
Degenerate case-Stripa granite	-3×10^{-4}	0.01%	63%
Woodford53 shale	-5×10^{-4}	0	187%
Opalinius Clay	-9×10^{-4}	0	4116%
Yeocheon schist	-6×10^{-4}	0	361%

Table 2.4 – Comparison of fundamental stress Σ^3_{22} (in m^{-1}) at point $\boldsymbol{y} = (0,10,5)$ meters due to a unit force along $\boldsymbol{e_3}$ applied at the center $\boldsymbol{x} = (0,0,0)$ using the analytical solutions of Pan and Chou (1976); Távara et al. (2012) with respect to the reference solution of Fabrikant (1989). The rocks are defined in table 2.2.

of the elements, the elasticity equation (2.18) can be written in the following matrix form:

$$t_i = K_{ij}\,[\![u]\!]_i \tag{2.27}$$

where K_{ij} depends on the coordinates of the point source x_i and the observation point y_j (besides the elastic constants) and is known as the "global influence matrix" for stresses .

The matrix K_{ij} was derived by Pan et al. (2014) using the point-force Green's solution of Fabrikant (1989). This area integral is transformed to a line integral along a closed dislocation loop using Stokes' theorem (Yuan et al., 2013). This integrated element also allowed propagation of a a fracture inclined with respect to the bedding plane. Furthermore, it accounts also for the half space by superposing two solutions: i- dislocation solution in TI full space, ii- the image source due to the free surface of the half-space. In our study, we carry out our calculations while assuming a planar fracture normal to the bedding in full space with constant displacement jumps over uniform rectangular elements. For a uniform rectangular mesh, the global influence matrix verifies the Pseudo-Toeplitz property which reduces the assembly by storing only a 1D array. But first, we start by benchmarking the elastic matrix with some verified solutions.

Verification of the rectangular displacement discontinuity-Far field

Here we examine the case of rectangular dislocation of a unit surface embedded in a transversely isotropic medium. When the observation point $\boldsymbol{y}$ is far from the dislocation loop, the fundamental stress solution $\Sigma^k_{ij}(\boldsymbol{x},\boldsymbol{y})$ at any point $\boldsymbol{x}$ in the loop can be simplified to the center $\boldsymbol{x_0}$ of the rectangle.

$$\Sigma^k_{ij}(\boldsymbol{x},\boldsymbol{y}) \approx \Sigma^k_{ij}(\boldsymbol{x_0},\boldsymbol{y})$$

Thus, the displacement due to a unit dislocation in direction i is given by equation (2.13):

$$u_k(\boldsymbol{y}) = \Sigma^k_{ij}(\boldsymbol{x_0},\boldsymbol{y})\,n_j\,[\![u(\boldsymbol{x_0})]\!]_i$$

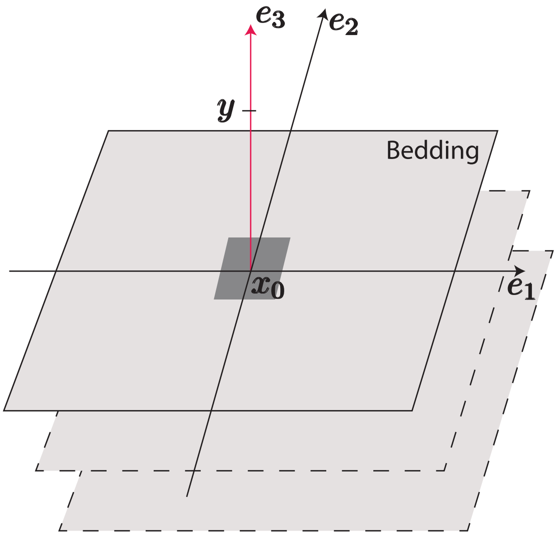

Figure 2.3 – Finite rectangular dislocation in an infinite TI media.

We use the fundamental stress derived by Fabrikant (1989) for the non degenerate case, with C_{ij} corresponding to Olkiluoto mica gneiss (table 2.2). The displacement discontinuity along the vector $\boldsymbol{e_3}$ is set to: $[\![u(\boldsymbol{x_0})]\!]_i = [\![u(\boldsymbol{x_0})]\!]_3 = 1$. The observation point $\boldsymbol{y}$ is taken as the projection of the point $\boldsymbol{x_0}$ in the third axis such that (figure 2.3):

$$y_1 = x_{0_1}, \quad y_2 = x_{0_2}, \quad ||x_{0_i} - y_i|| = y_3$$

We compare in figure 2.4 the displacement in the $\boldsymbol{e_3}$ direction obtained numerically using the elastic kernel of Pan et al. (2014) (red dots) and the analytical solution (solid line) (Fabrikant, 1989) where we span the $\boldsymbol{e_3}$ axis as shown in figure 2.3. The displacement decays with $||x_{0_3} - y_3||^{-2}$ and the two solutions match precisely.

We will perform an another verification of the colocation method for the case of elliptical static fracture (section 2.5.2). But first, we need to derive the near-tip elastic operator for mode I propagation.

2.3 Near-tip elastic operator

Here we zoom into the region near the tip, where point along the edge (parameterised by angle α) behaves locally as the tip of a semi-infinite fracture propagating quasi-statically. The two-dimensional equivalent fracture belongs to the plane $(\boldsymbol{e'_1}, \boldsymbol{e'_2})$ and the problem is identical to that of a plane strain fracture where the infinite direction lies along $\boldsymbol{e'_3}$ (figure 2.5).

We recall the local system of coordinates $(\boldsymbol{e'_1}, \boldsymbol{e'_2})$ defined in figure 2.1, where $\boldsymbol{e'_1}$ is the axis of propagation of the semi-infinite fracture and $\boldsymbol{e'_2} = \boldsymbol{e_2}$ is the normal axis to the surface.

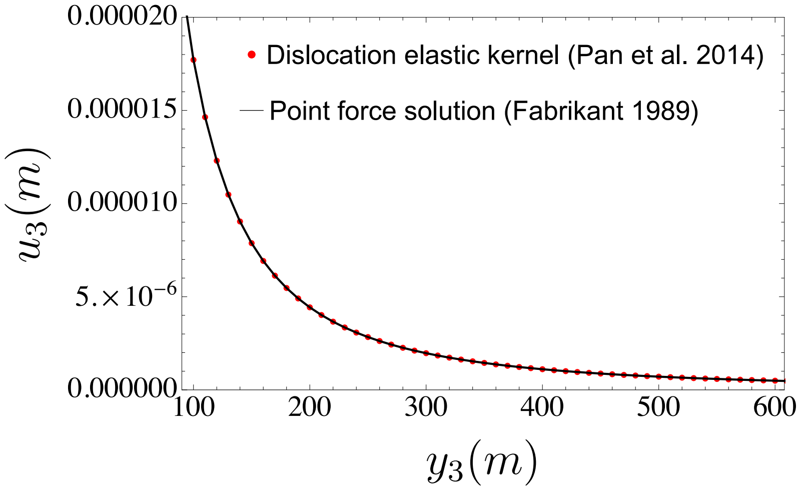

Figure 2.4 – Far-field verification: Displacement due to a unit rectangle tensile dislocation function of the relative distance using the analytical solution (Fabrikant, 1989) and the numerical solution of Pan et al. (2014).

2.3.1 Near-tip elastic operator via a change of reference

For each point along the fracture front, the orientation of the semi-infinite fracture changes, and does the plane of propagation, as we can observe from figure 2.5. For the first case where the edge is on the bedding plane (case A in figure 2.5, $\alpha = 0$), the equivalent fracture propagates on the plane of isotropy of the body $(\boldsymbol{e_1}, \boldsymbol{e_2})$ and is infinite along the axis of symmetry $\boldsymbol{e_3}$. The fracture propagates along $\boldsymbol{e_1}$ and $[\![u(x_1)]\!]_2$ is the fracture opening, which depends only on the coordinate x_1. Whereas, in case C ($\alpha = \pi/2$), the semi-infinite fracture propagates perpendicular to the bedding ($\boldsymbol{e'_1} = \boldsymbol{e_3}$) and $\boldsymbol{e_1}$ is the axis of plane strain ($\epsilon_{1i} = 0$, $i = 1,2,3$). For the general case when the axis of propagation forms an angle α with the horizontal (case B), the semi-infinite fracture propagates along $\boldsymbol{e'_1}$ and is contained in the plane $(\boldsymbol{e_1}, \boldsymbol{e_3})$ while the normal is aligned with $\boldsymbol{e_2}$.

We will refer to the coordinate in the local basis by using x'_i while in the material basis we will use x_i. Consider two points x'_i and y'_i with the corresponding coordinates in the local system $(\boldsymbol{e'_1}, \boldsymbol{e'_2}, \boldsymbol{e'_3})$:

$$\boldsymbol{x'} = (x'_1, 0, x'_3), \quad \boldsymbol{y'} = (y'_1, 0, 0)$$

$$[\![u(\boldsymbol{x'})]\!]_i = [\![u(x'_1)]\!]_2 \boldsymbol{e_2}$$

$$D_{l'j'}\left([\![u(x'_1)]\!]\right) = \delta_{l'2}\delta_{1'j'}[\![u(x'_1)]\!]_{2,1'} - \delta_{j'2}\delta_{l'1'}[\![u(x'_1)]\!]_{2,1'} \tag{2.28}$$

It results from combining equation (2.28) and the equation of strains (2.19), that $\epsilon_{1'3'} = \epsilon_{2'3'} =$

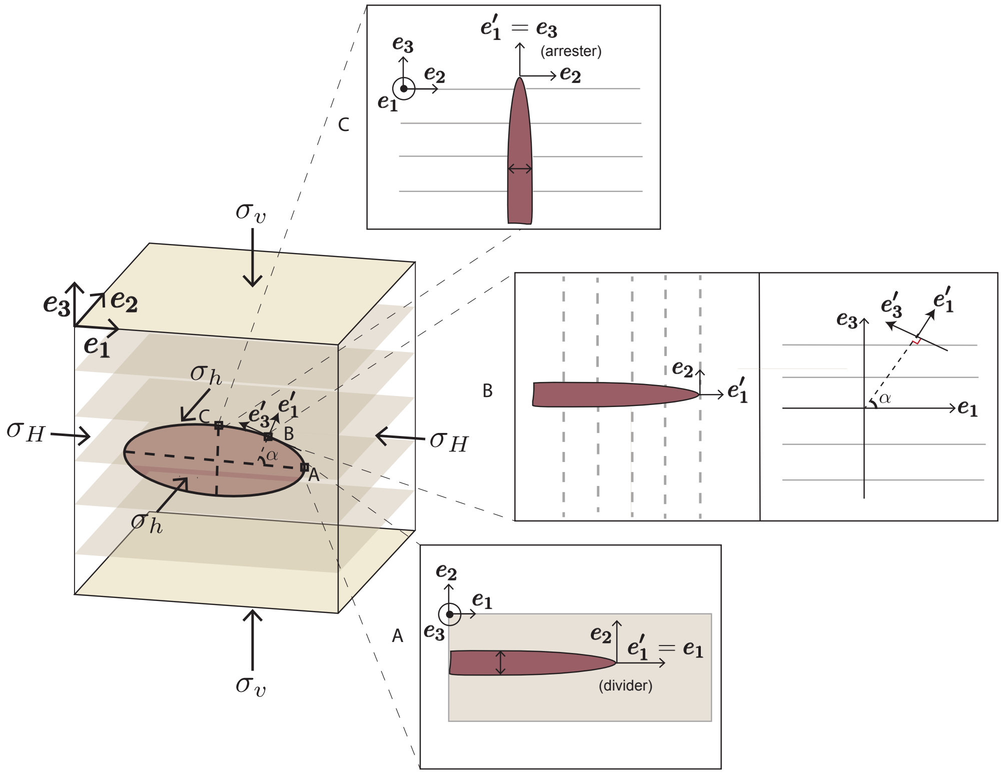
$e'_1 = e_3$
(arrester)
e_3
e_2
e_1
C
σ_v
e_3
e_2
e_1
σ_h
σ_H
e'_3
e'_1
B
α
A
e_2
e'_1
e_3
e'_3
e'_1
α
e_1
e_2
e_1
e_3
e_2
$e'_1 = e_1$
(divider)
A
σ_v

Figure 2.5 – Schematic of a planar three dimensional hydraulic fracture growing perpendicular to the isotropy plane. The different configurations of the near-tip region along the fracture front are also depicted: case A is a semi-infinite fracture propagating along the plane of isotropy or the so-called "divider direction", case B is a semi-infinite fracture propagating within the plane $(\boldsymbol{e_1}, \boldsymbol{e_3})$ and case C is a semi-infinite fracture propagating in the direction perpendicular to the layering defined as the "arrester direction"

$\epsilon_{3'3'} = 0$ and the remaining non zero components are:

$$\epsilon(\boldsymbol{y'}) = \begin{pmatrix} \epsilon_{1'1'} & \epsilon_{1'2'} & 0 \\ \epsilon_{1'2'} & \epsilon_{2'2'} & 0 \\ 0 & 0 & 0 \end{pmatrix} \tag{2.29}$$

Thus, the normal component of the traction is described by:

$$t_2(\boldsymbol{y'}) = -c'_{22k2} \int_\Gamma \Sigma^{k'}_{21'}\left(\boldsymbol{x'},\boldsymbol{x'}\right) \left[\!\left[u(x'_1) \right]\!\right]_{2,1'} \mathrm{d}S_{\boldsymbol{x'}} + c'_{22k1} \int_\Gamma \Sigma^{k'}_{22}\left(\boldsymbol{x'},\boldsymbol{y'}\right) \left[\!\left[u(x'_1) \right]\!\right]_{2,1'} \mathrm{d}S_{\boldsymbol{x'}}$$

Semi-infinite fracture propagating along the divider $\boldsymbol{e_1}$

Since the local basis for this case corresponds to the material basis $(\boldsymbol{e'_1},\boldsymbol{e'_2},\boldsymbol{e'_3}) = (\boldsymbol{e_1},\boldsymbol{e_2},\boldsymbol{e_3})$, we have $c_{2221} = c_{2212} = c_{2232} = c_{2231} = 0$ and $c_{2211} = C_{12}$, $c_{2222} = C_{11}$. This configuration corresponds to case A in figure 2.5. The traction depends on two fundamental stresses $\Sigma^2_{21}(\boldsymbol{x},\boldsymbol{y})$ and $\Sigma^1_{22}(\boldsymbol{x},\boldsymbol{y})$, which in plane strain condition gives:

$$t_2(\boldsymbol{y}) = -C_{11} \int_0^\infty [\![u(x_1)]\!]_{2,1} \left(\int_{-\infty}^\infty \Sigma^2_{21}(\boldsymbol{x},\boldsymbol{y}) dx_3 \right) dx_1 + C_{12} \int_0^\infty [\![u(x_1)]\!]_{2,1} \left(\int_{-\infty}^\infty \Sigma^1_{22}(\boldsymbol{x},\boldsymbol{y}) dx_3 \right) dx_1 \tag{2.30}$$

Using the expressions of the fundamental stress derived by Fabrikant (1989) and integrating them with respect to x_3, we get:

$$t_2(y_1) = \frac{(C_{11}-C_{12})(C_{11}+C_{12})}{4\pi C_{11}} \int_0^\infty \frac{1}{y_1 - x_1} [\![u(x_1)]\!]_{2,1} \, \mathrm{d}x_1 \tag{2.31}$$

Semi-infinite fracture propagating along the arrester $\boldsymbol{e_3}$

In this case (corresponding to sketch C in figure 2.5), the local basis is a rotation of the material basis with respect to the normal $\boldsymbol{e_2}$: $(\boldsymbol{e'_1},\boldsymbol{e'_2},\boldsymbol{e'_3}) = (\boldsymbol{e_3},\boldsymbol{e_2},-\boldsymbol{e_1})$ (see figure 2.5). We can still express the traction vector function of the elastic parameters in the material basis ($\Sigma^{k'}_{21'}\left(\boldsymbol{x'},\boldsymbol{y'}\right) = \Sigma^{k}_{23}\left(\boldsymbol{x},\boldsymbol{y}\right)$, $\Sigma^{k'}_{23'}\left(\boldsymbol{x'},\boldsymbol{y'}\right) = \Sigma^{k}_{21}\left(\boldsymbol{x},\boldsymbol{y}\right)$). Since the stiffness matrix in the global space is characterized by $c_{2223} = c_{2213} = c_{2212} = c_{2232} = 0$ and $c_{2233} = C_{13}$, $c_{2222} = C_{11}$, the remaining components of the traction are the fundamental stresses $\Sigma^2_{23}(\boldsymbol{x},\boldsymbol{y})$ and $\Sigma^3_{22}(\boldsymbol{x},\boldsymbol{y})$, which in the plane strain condition give:

$$t_2(\boldsymbol{y}) = -C_{11} \int_0^\infty [\![u(x_3)]\!]_{2,3} \left(\int_{-\infty}^\infty \Sigma^2_{23}(\boldsymbol{x},\boldsymbol{y}) \mathrm{d}x_1 \right) \mathrm{d}x_3 + C_{13} \int_0^\infty [\![u(x_3)]\!]_{2,3} \left(\int_{-\infty}^\infty \Sigma^3_{22}(\boldsymbol{x},\boldsymbol{y}) \mathrm{d}x_1 \right) \mathrm{d}x_3$$

Integrating the expression of the stress tensor Σ^k_{ij} (Fabrikant, 1989) for x_1, we find that the plane strain elastic expression for this case is:

$$t_2(\boldsymbol{x}) = \frac{\sqrt{C_{33}/C_{11}}(-C_{13}^2 + C_{11}C_{33})}{2\pi C_{33}\sqrt{\dfrac{-C_{13}^2 - 2C_{13}C_{44} + C_{11}(C_{33} + 2\sqrt{C_{33}/C_{11}}C_{44})}{C_{11}C_{44}}}} \int_0^{\infty} \frac{1}{y_3 - x_3} [\![u(x_3)]\!]_{2,3}\,\mathrm{d}x_3 \quad (2.32)$$

Semi-infinite fracture propagating in the rotated plane

For this case (corresponding to sketch B in figure 2.5), we first need to describe the stress density tensor Σ^k_{ij} in the rotated plane $\Sigma^{k'}_{i'j'}$ using the rotation matrix $P_{i'i}$ (equation (2.5)):

$$\Sigma^{k'}_{i'j'}(\boldsymbol{x}') = P_{i'i}P_{j'j}P_{k'k}\Sigma_{ijk}(\boldsymbol{x})$$

We obtain the traction function of the stiffness matrix c'_{ijkl} (2.6) as:

$$\begin{aligned} t_2(\boldsymbol{x}') =& c'_{2222}\int_0^{\infty} [\![u(x'_1)]\!]_{2,1'}\left(\int_{-\infty}^{\infty}\Sigma^2_{21'}(\boldsymbol{x}',\boldsymbol{y}')\mathrm{d}x'_3\right)\mathrm{d}x'_1 - c'_{2211}\int_0^{\infty} [\![u(x'_1)]\!]_{2,1'}\left(\int_{-\infty}^{\infty}\Sigma^{1'}_{22}(\boldsymbol{x}',\boldsymbol{y}')\mathrm{d}x'_1\right)\mathrm{d}x'_1 \\ & -c'_{2231}\int_0^{\infty} [\![u(x'_1)]\!]_{2,1'}\left(\int_{-\infty}^{\infty}\Sigma_{223'}(\boldsymbol{x}',\boldsymbol{y}')\mathrm{d}x'_3\right)\mathrm{d}x'_1 \end{aligned} \quad (2.33)$$

where

$$c'_{2222} = C_{11},\ c'_{2211} = C_{12}\cos^2(\alpha) + C_{13}\sin^2(\alpha),\ c'_{2231} = \frac{\sin(2\alpha)}{2}(-C_{12} + C_{13})$$

The equation (2.33) has no known simpler analytical expression. Therefore, we will now use the edge dislocation solution for anisotropic media to re-derive the explicit expression for the elastic operator (equation (2.33)).

2.3.2 Near-tip elastic operator via the edge dislocation solution

We consider a general case of a semi-infinite fracture propagating in the local axis $\boldsymbol{e}'_1$, where $\boldsymbol{e}_2$ is the fracture opening direction (Case B in figure 2.5). The corresponding strains in the basis $(\boldsymbol{e}'_1, \boldsymbol{e}_2, \boldsymbol{e}'_3)$ where $\boldsymbol{e}'_3$ is a axis such that $(\boldsymbol{e}'_1, \boldsymbol{e}_2, \boldsymbol{e}'_3)$ is a direct orthonormal basis, are (see equation (2.19)):

$$\epsilon_{k'l'}(\boldsymbol{y}') = -\int_{\Gamma}\Sigma^{k'}_{2j'}(\boldsymbol{x}',\boldsymbol{y}')D_{l'j'}\,[\![u(x'_1)]\!]_2\,\mathrm{d}S_{\boldsymbol{x}'}$$

with the surface gradient:

$$D_{l'j'}\left([\![u(x'_1)]\!]\right) = \delta_{l'2}\delta_{1'j'}\,[\![u(x'_1)]\!]_{2,1'} - \delta_{j'2}\delta_{l'1'}\,[\![u(x'_1)]\!]_{2,1'}$$

As shown in equation (2.29), we have:

$$\epsilon_{1'3'}(\boldsymbol{y'}) = \epsilon_{2'3'}(\boldsymbol{y'}) = \epsilon_{3'3'}(\boldsymbol{y'}) = 0$$

Form the above equation we have the plane strain conditions. The following study will be conducted in 2D where the out of plane stresses $\sigma_{i'3'}, \{i, 1', 3'\}$ are substituted from the remaining non zero strains via Hooke's law (2.3). The stress-strain relation in plane strain conditions on the local basis $(\boldsymbol{e'_1}, \boldsymbol{e_2}, \boldsymbol{e'_3})$ becomes:

$$\begin{pmatrix} \sigma_{1'1'} \\ \sigma_{22} \\ \sigma_{1'2} \end{pmatrix} = \begin{pmatrix} C'_{11}(\alpha) & C'_{12}(\alpha) & 0 \\ C'_{12}(\alpha) & C'_{22}(\alpha) & 0 \\ 0 & 0 & C'_{66}(\alpha) \end{pmatrix} \begin{pmatrix} \epsilon_{1'1'} \\ \epsilon_{22} \\ 2\epsilon_{1'2} \end{pmatrix}$$

The given problem is equivalent to a pure edge dislocation in anisotropic media for which the edge component $\llbracket u(x'_1) \rrbracket$ gives rise only to displacement $u_{1'}$ and u_2. The classical anisotropic elasticity theory of dislocations was developed by Eshelby et al. (1953) and extended by Foreman (1955). Hirth and Lothe (1982) followed the method of Eshelby et al. (1953); Stroh (1958) to explicitly establish the stress and displacement elastic tensors for pure edge and pure screw dislocations.

The Stroh formalism (Stroh, 1958) for a pure edge dislocation consists in the solution of a fourth order polynomial equation (second order polynomial equation for screw dislocation) function of the anisotropic parameters C_{ij}. The roots give the magnitude of the displacement field. The stress components for a single normal dislocation density $b_2 = \delta \llbracket u(x'_1) \rrbracket_{2,1'}$ are (see Hirth and Lothe (1982) for details):

$$\delta\sigma_{1'1'}(\boldsymbol{y'}) = -\frac{MC'_{66}(\alpha)}{2\pi} \frac{1}{y'_1 - x'_1} b_2 \tag{2.34}$$

$$\delta\sigma_{22}(\boldsymbol{y'}) = \frac{MC'_{22}(\alpha)C'_{66}(\alpha)}{2\pi\bar{C}'_{11}(\alpha)} \frac{1}{y'_1 - x'_1} b_2 \tag{2.35}$$

$$\delta\sigma_{12}(\boldsymbol{y'}) = 0 \tag{2.36}$$

with:

$$M = \left(\sqrt{C'_{22}(\alpha)C'_{11}(\alpha)} + C'_{12}(\alpha)\right) \left(\frac{\sqrt{C'_{22}(\alpha)C'_{11}(\alpha)} - C'_{12}(\alpha)}{C'_{22}(\alpha)C'_{66}(\alpha)\left(\sqrt{C'_{22}(\alpha)C'_{11}(\alpha)} + C'_{12}(\alpha) + 2C'_{66}(\alpha)\right)} \right)^{1/2}$$

Integrating the normal stress due to a single dislocation (2.35) over the line of the fracture gives:

$$\sigma_{22}(\boldsymbol{y'}) = \frac{MC'_{22}(\alpha)C'_{66}(\alpha)}{2\pi\bar{C}'_{11}(\alpha)} \int_0^{\infty} \frac{1}{y'_1 - x'_1} \llbracket u(x'_1) \rrbracket_{2,1'} \mathrm{d}x'_1$$

We retrieve the well known elasticity integral equation for isotropic media depending on an equivalent near-tip elastic modulus E'_α.

$$t_2(\boldsymbol{y'}) = \frac{E'_\alpha}{4\pi}\int_0^\infty \frac{1}{y'_1 - x'_1} \llbracket u(x'_1) \rrbracket_{2,1'} \, \mathrm{d}x'_1 \tag{2.37}$$

$$E'_\alpha = \frac{2MC'_{22}(\alpha)C'_{66}(\alpha)}{\bar{C}'_{11}(\alpha)} \tag{2.38}$$

For isotropy, this elastic modulus reduces to the plane strain Young's modulus:

$$E'_{iso} = \frac{(C_{11} + C_{12})\,(C_{11} - C_{12})}{C_{11}} \tag{2.39}$$

Semi-infinite fracture propagating along the divider $\boldsymbol{e_1}$

For the case of a semi-infinite fracture propagating in the material axis $\boldsymbol{e_1}$ and perpendicular to $\boldsymbol{e_2}$ (case A in figure 2.5), we get the same elastic modulus, called E'_1 as in equation (2.31):

$$\bar{C}'_{11}(\alpha = 0) = C_{11}$$

$$M(\alpha = 0) = \frac{C_{11} + C_{12}}{C_{11}}$$

$$E'_1 = \frac{(C_{11} + C_{12})\,(C_{11} - C_{12})}{C_{11}}$$

The fracture lies in the isotropic plane and the elastic modulus depends on two stiffness constants, as in the isotropic case (equation (2.39)).

Semi-infinite fracture propagating along the arrester direction $\boldsymbol{e_3}$

The semi-infinite fracture propagates in the material symmetry axis $\boldsymbol{e_3}$, which corresponds to case C of figure 2.5

$$\bar{C}'_{11}(\alpha = \frac{\pi}{2}) = \sqrt{C_{33}C_{11}}$$

$$M(\alpha = \frac{\pi}{2}) = \left(\sqrt{C_{33}C_{11}} + C_{13}\right)\left(\frac{\sqrt{C_{33}C_{11}} - C_{13}}{C_{11}C_{44}\left(\sqrt{C_{33}C_{11}} + C_{13} + 2C_{44}\right)}\right)^{1/2}$$

After some simplifications, we obtain the same anisotropic modulus as was shown in equation (2.32):

$$E'_3 = \frac{2\sqrt{C_{33}/C_{11}}(-C_{13}^2 + C_{11}C_{33})}{C_{33}\sqrt{\frac{-C_{13}^2 - 2C_{13}C_{44} + C_{11}(C_{33} + 2\sqrt{C_{33}/C_{11}}C_{44})}{C_{11}C_{44}}}}$$

The elastic modulus depends on four elastic parameters and is also given in Chertov (2012); Laubie and Ulm (2014).

2.3.3 Evolution of the near-tip elastic modulus along the crack front

We can rewrite E'_α as the product of an equivalent elastic modulus and a dimensionless function $\mathscr{F}$ depending on four elastic C_{ij}: $E'_\alpha = E_* \mathscr{F}(C_{ij})$. The characteristic elastic modulus E_* can be either E'_1, E'_3, or any combination of C_{ij}. Here, however, we choose the mean value:

$$\langle E' \rangle = \frac{E'_1 + E'_3}{2}$$

The anisotropy of the TI medium is quantified via the ratio of $E'_1 = E'_\alpha\,(\alpha = 0)$ and $E'_3 = E'_\alpha\left(\alpha = \frac{\pi}{2}\right)$ (see table 2.5) that we call β

$$\beta = E'_1 / E'_3$$

The dimensionless function $\mathscr{F}\left(\beta, \epsilon, \delta, C_{13}/C_{11}\right)$, however, is a rearranged function of relevant dimensionless parameters such as the anisotropy ratio $\beta = E'_1/E'_3$, the ratio C_{13}/C_{11}, and the Thomsen parameters $\{\epsilon, \delta\}$ (Thomsen, 1986), as were in equations (2.4). The anisotropic near-tip modulus is redefined as:

$$E'_\alpha = < E' > \times \mathscr{F}(\beta, \epsilon, \delta, C_{13}/C_{11})$$

The near-tip elastic modulus function of the scaling elastic parameters in the divider and arrester directions simply become:

$$E'_1 = \frac{2\beta \langle E' \rangle}{1+\beta}, \quad E'_3 = \frac{2\langle E' \rangle}{1+\beta}.$$

For most rocks, the Thomsen parameters range from 0 for weak anisotropy to 1 for strong anisotropy, where $\epsilon > \delta$ for fine layering anisotropic media (Berryman, 1979). The anisotropy ratio β varies between 1 and 2 for typical orders of magnitude of the stiffness parameters, while C_{13}/C_{11} is usually smaller than 1 (see table 2.5). We plot in figure 2.6 the scaled anisotropic modulus $E'_\alpha / \langle E' \rangle$ function of the angle α where we study the effect of the dimensionless parameters $\{\beta, \epsilon, \delta, C_{13}/C_{11}\}$. We compare the analytical expression $E'_\alpha / \langle E' \rangle$ (equation (2.38)) (solid line) to the approximation function $E'_{app} / \langle E' \rangle$ derived in Laubie and Ulm (2014) (dashed line).

$$\frac{1}{E'_{app}} = \frac{\cos^2(\alpha)}{E'_1} + \frac{\sin^2(\alpha)}{E'_3}$$

We first set our dimensionless parameters to the given reference values: $\beta = 1.5$, $\epsilon = 0.3$, $\delta = 0.2$, and $C_{13}/C_{11} = 0.5$, and then vary each dimensionless parameter while maintaining other

Material	β	C_{13}/C_{11}	ϵ	δ	γ
Isotropy-Stripa granite (Alm et al., 1985)	1	0.26	0	0	0
Olkiluoto mica gneiss (Hakala et al., 2007)	1.159	0.262	0.181	0.0912	0.203
Gas-saturated Shaly Coal (Wang, 2002)	1.259	0.057	0.511	-0.173	0.424
Woodford53 shale (Laubie, 2013)	1.311	0.296	0.309	0.139	0.415
Opalinius Clay (Thöny, 2014)	1.327	0.671	0.5	0.491	0.344
Yeocheon schist (Cho et al., 2012)	1.434	0.219	1.156	1.229	0.552
Calcareous mudstone (Chertov, 2012)	1.903	0.441	0.786	0.659	0.995
Callovo-Oxfordian argilite (David et al., 2007)	1.066	0.238	0.281	0.191	0.091
Jurassic shale (Hornby, 1998)	1.32	0.419	0.227	0.128	0.361
Slate Del Carmen (this study)	1.03	0.029	0.17	1.7	0

Table 2.5 – Example of the dimensionless parameters values for the anisotropic rocks given in table 2.2.

parameters at the default values. We should note that the approximation function does not depend on $\{\epsilon, \delta, C_{13}/C_{11}\}$. For the case of a given constant β, $E'_{app}/\langle E' \rangle$ has only one plot (see figure 2.6.b, c and d).

The anisotropic elastic modulus is monotonically varying with respect to α (see figure 2.6) and satisfies:

$$E'_{\alpha}(\alpha) = E'_{\alpha}(\pi - \alpha) = E'_{\alpha}(\pi + \alpha) = E'_{\alpha}(-\alpha).$$

As we can see from figure 2.6, the magnitude of the elastic modulus depends on the ratio β, whereas the slope is a function of all the elastic parameters $\{\beta, \delta\, \epsilon, C_{13}/C_{11}\}$. The transition from E'_1 to E'_3 happens more slowly when increasing $\{\beta, \delta\}$ and more quickly when increasing $\{\epsilon, C_{13}/C_{11}\}$. For the case of $\beta = 1.2$ in figure 2.6.a, where the anisotropy ratio is low, a similar evolution is observed for the analytical and the approximation solution. As the anisotropy ratio increases, the E'_{app} differs drastically from the analytical solution except at the two fixed boundaries $E'_{\alpha}(\alpha = 0) = E'_{app}(\alpha = 0)$ and $E'_{\alpha}(\alpha = \pi/2) = E'_{app}(\alpha = \pi/2)$. The approximation solution also significantly diverges from the analytical solutions with a variation of δ (see figure 2.6.d). Whereas, $E'_{app}/\langle E' \rangle$ corresponds more to the case of high $C_{13}/C_{11} = 0.7$ (steep transition slope) or high $\epsilon = 0.5$ (see figure 2.6.b and c) for the case when varying C_{13}/C_{11} or ϵ respectively. The approximation solution, thus underestimates in most of the cases the anisotropic plane strain modulus and decreases more quickly when compared to E'_{α} with respect to the angle.

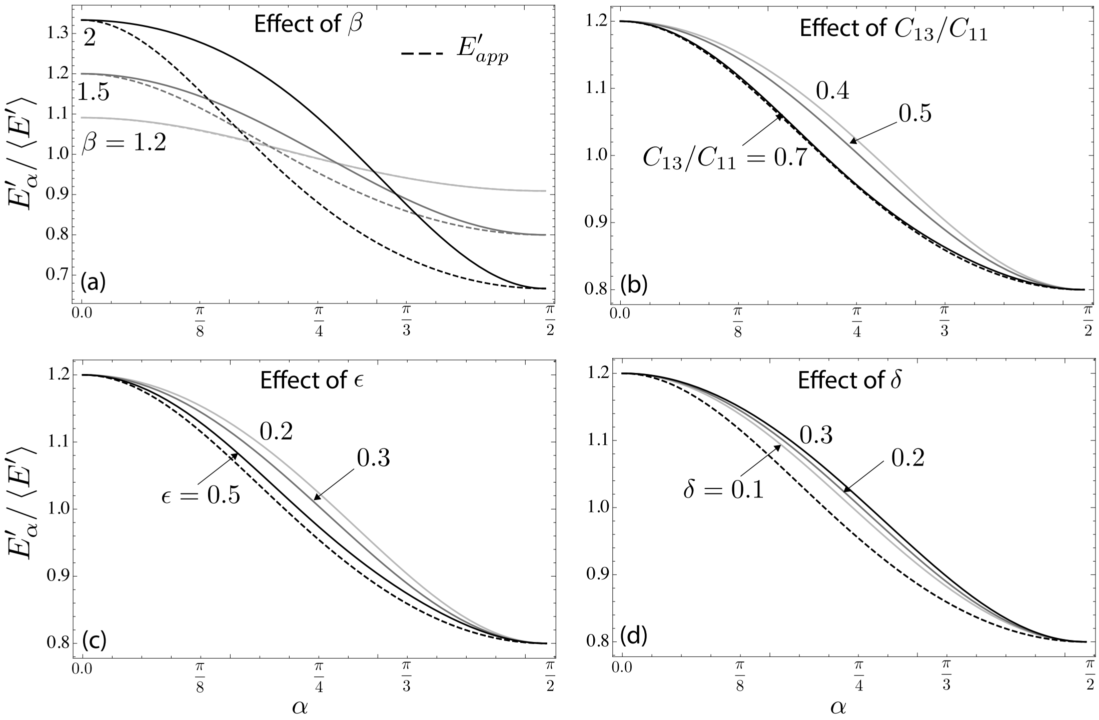

Figure 2.6 – Near-tip elastic modulus as a function of α using the exact solution obtained analytically (solid line) and its approximation (Laubie and Ulm, 2014) (dashed line). The reference set of values of the dimensionless parameters: $\beta = 1.5$, $C_{13}/C_{11} = 0.5$, $\epsilon = 0.3$ and $\delta = 0.2$ is displayed in dark grey with the variations of each elastic scalar: (a) effect of $\beta = \{1.2, 1.5, 2\}$, (b) effect of $C_{13}/C_{11} = \{0.4, 0.5, 0.7\}$, (c) effect of $\epsilon = \{0.2, 0.3, 0.5\}$, and (d) effect of $\delta = \{0.1, 0.2, 0.3\}$.

2.4 Fracture propagation criterion

2.4.1 Energy release rate

We define the "energy release rate" as the energy that flows to the fracture tip of new area S when a crack is created:

$$\mathscr{G} = -\frac{\partial \mathscr{P}}{\partial S}$$

where: $\mathscr{P}$ is the elastic potential energy of the media

$$\mathscr{P} = \frac{1}{2}\int_S \sigma_{ij}\epsilon_{ij}\mathrm{d}S$$

The Griffith theory postulates that a crack will grow when the energy released by the body per unit area is equal to $2\gamma_s$ where γ_s is the surface energy and the factor2 refers to the upper and lower fracture surfaces.

Griffith also introduced a local energy release rate known as fracture energy G. For an increment of fracture length l (figure 2.7), the elastic potential is given as a function of G as (Irwin, 1962):

$$\mathrm{d}\mathscr{P} = \int_0^l G\mathrm{d}x_1'$$

The propagation criterion in terms of the local energy release rate G is summarised as follows:

$$\begin{cases} G \leq G_c \\ (G - G_c)\,V = 0 \\ V > 0 \end{cases}$$

where V is the crack velocity and G_c is the critical local energy release rate which is also called the "fracture energy". For anisotropy, the fracture energy is direction dependent: $G_c\,(\alpha)$.

2.4.2 Irwin relation in transverse isotropy

2.4.3 Stress Intensity Factor (SIF)

In linear elastic fracture mechanics, the stress is singular at the crack tip. The singularity term is a square root of the normal distance to the tip $\sigma \sim x_1'^{-1/2}$ (Williams, 1961). We introduce, following the configuration of figure 2.7, the stress intensity factors (SIF) K_I, K_{II} and K_{III} as the amplitude of the stress singularity for opening, shear and out-of plane shear modes as (Sih et al., 1965):

$$[\![u_i(x_1')]\!] = \sqrt{\frac{32}{\pi}}\Lambda_{ij}K_j(\alpha)\sqrt{x_1'}, \quad x_1' \ll 1 \tag{2.40}$$

where $K_i = (K_I, K_{II}, K_{III})^t$ and Λ_{ij} is the 3×3 Irwin's matrix (Ting, 1996).

Similarly to fracture energy, there is a critical SIF denoted, as fracture toughness $K_{Ic}\,(\alpha)$ cannot

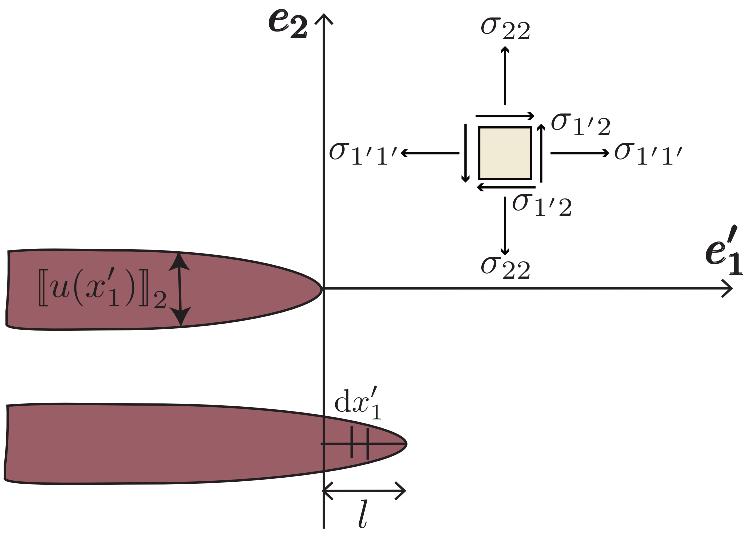

Figure 2.7 – Co-linear extension of the fracture in the local basis.

be exceeded and below which the fracture can not propagate. The propagation criterion is formulated as the following:

$$\begin{cases} K_I \leq K_{Ic} \\ (K_I - K_{Ic})\, V = 0 \\ V > 0 \end{cases}$$

2.4.4 Irwin relation in transverse isotropy

For a coplanar crack extension and at the limit of l ($l \rightarrow 0$), the stress intensity factor and the fracture energy are connected via Irwin's formula (Stroh, 1958; Barnett and Asaro, 1972) . In the case of three dimensional problems, it can be written (Barnett and Asaro, 1972):

$$G = K_i^t \Lambda_{ij} K_j$$

For an isotropic material, Λ_{ij} is a diagonal matrix with: $\Lambda_{11} = \Lambda_{22} = 1/E'_{iso}$, and $\Lambda_{33} = (1 + \nu)/E_{iso}$. However, the Irwin matrix Λ_{ij} for an anisotropic solid is not necessarily diagonal. It depends on the local direction of propagation and a matrix related to the pre-factor of the solution of an edge dislocation (Stroh, 1958; Barnett and Asaro, 1972) - which is related to the point force Green's function. For general anisotropy and arbitrary orientation planar fracture, its expression can be obtained numerically (Barnett and Swasger, 1971; Barnett and Asaro, 1972), or semi-explicitly in the material frame (Malén and Lothe, 1970).

Irwin relation for a planar fracture in TI

In the configuration investigated here where the planar fracture is perpendicular to the isotropy plane of a transversely isotropic material (figure 2.5), as already mentioned, the fracture mode decouples (shear dislocation does not induce normal traction on the fracture plane and vice versa). As a result the Irwin matrix is diagonal. However, the expressions for Λ_{ii} remain functions of the local propagation direction. For such a planar fracture, they are entirely captured by the angle α between the normal to the local tangent to the fracture front and the material axis $\boldsymbol{e_1}$ (the divider direction).

For a fracture subjected to pure opening mode $\boldsymbol{e_2}$ (see figure 2.7), we can relate the fracture energy to the stress intensity factor through the expression:

$$G(\alpha) = \frac{K_I^2(\alpha)}{E'_\alpha} \tag{2.41}$$

where:

$$\Lambda_{11}^{-1} = E'_\alpha.$$

The displacement discontinuity is reduced to the normal non zero component:

$$[\![u_2(x'_1)]\!] = \sqrt{\frac{32}{\pi}} \frac{K_{Ic}(\alpha)}{E'_\alpha} \sqrt{x'_1}, \quad x'_1 \ll 1. \tag{2.42}$$

As a result of equation (2.37), all the linear elastic tip asymptote (lefm) obtained for the isotropic case can be used in anisotropy depending on the proper use of the anisotropic modulus. In the following, we use $w(x'_1)$ to refer to the normal component of the displacement jump $w(x'_1) = [\![u(x'_1)]\!]_2$.

2.5 Elastic solutions of fracture problem in TI material

2.5.1 Existing solutions

When considering anisotropy, extensive studies have been made on fractures of elliptical shape. One classic paper dealing with cracks is Eshelby et al. (1953) which deals with inhomogeneities in anisotropic bodies using stress-free strains. Ting (1996) derived in implicit form the problem of an elliptic rigid body subject to an external moment. He also investigated the Green's functions in half-space for an ellipse rotated with respect to the plane of anisotropy. A general expression for the stress concentration was presented in Hwu and Ting (1989) using the Stroh formalism. Willis (1968) also addressed the problem of the stress field around an elliptical crack in a linear anisotropic media but is not applicable to the degenerate case of TI medias. Irwin (1962) on the other hand established the analytical expression for the displacement and stress intensity factor for a flat crack in isotropic media that was extended to TI by Hoenig (1978). More recently, Fabrikant (2011); Kanaun (2007) have also worked on elliptical cracks subject to uniform pressure in TI media but their analytical solutions contain some errors as we will prove in the next section. In the light of the work of Hoenig (1978), we will re-derive below an analytical solution of static elliptical fracture in TI media.

2.5.2 Elliptical fracture in a transversely isotropic media

For an elliptical fracture of semi-major axis a and semi-minor axis b subject to a uniform pressure p in an infinite medium, following Eshelby et al. (1953) the corresponding fracture opening takes the following form:

$$w = B_o p \sqrt{ab} \sqrt{1 - \frac{x_1^2}{a^2} - \frac{x_3^2}{b^2}} \tag{2.43}$$

where B_o is a pre-factor that needs to be determined. We will follow here the approach described by Hoenig (1978) to obtain B_o.

First we define a point (x_1, x_3) inside the fracture and its projection on the ellipse front (x_1^f, x_3^f) (see figure 2.8). The distance between these two points is $|x_1'|$, where α is the angle between the major axis $\boldsymbol{e_1}$ and the local axis $\boldsymbol{e_1'}$ as described in figure 2.8. With the use of the geometrical properties of the ellipse:

$$\tan\alpha = \frac{a^2}{b^2} \frac{x_3^f}{x_1^f}$$

Introducing the angle characterizing the ellipse:

$$\begin{cases} x_1^f = & a\cos\theta \\ x_3^f = & b\sin\theta \end{cases}$$

we have:

$$\tan\alpha = \frac{a}{b}\tan\theta \tag{2.44}$$

The series expansion of the equation of the opening (2.43) to first order is:

$$1 - \frac{x_1^2}{a^2} - \frac{x_3^2}{b^2} = 2\left|x_1'\right| \left(\frac{x_1^f \cos\alpha}{a^2} + \frac{x_3^f \sin\alpha}{b^2} \right) + O\left({x_1'}^2\right) \tag{2.45}$$

Using the definition of angle θ, the equation (2.45) becomes:

$$1 - \frac{x_1^2}{a^2} - \frac{x_3^2}{b^2} = 2\left|x_1'\right| \left(\frac{\cos^2\theta}{a^2} + \frac{\sin^2\theta}{b^2} \right)^{1/2} + O\left({x_1'}^2\right)$$

We thus obtain near-tip the first order term of the fracture opening as (Hills et al., 2013):

$$w = B_o p\sqrt{a}\sqrt{2\left|x_1'\right|}\left(\sin^2\theta + \gamma_e^2\cos^2\theta\right)^{1/4} \tag{2.46}$$

where $\gamma_e = b/a < 1$ is the fracture aspect ratio.

We substitute the expression of the stress intensity factor by equalizing the tip asymptote (2.42) and taking the limit of equation (2.46) for small $\left|x_1'\right|$

$$K_I = \frac{B_o}{4}\sqrt{\pi a}E_\alpha' p\left(\sin^2\theta + \gamma_e^2\cos^2\theta\right)^{1/4} \tag{2.47}$$

On the other hand, the global energy release rate $\mathscr{G}$ is obtained from the work W applied by the uniform pressure as:

$$\mathscr{G} = \frac{1}{2\pi\gamma_e a}\frac{\partial W}{\partial a} = \frac{1}{2\pi\gamma a}\frac{\partial}{\partial a}\left(\frac{1}{2}pV_{frac}\right) = \frac{1}{2}p^2\gamma_e^{1/2}aw_0. \tag{2.48}$$

The global energy is also equal to the integral of the local energy release rate along the fracture front:

$$\mathscr{G} = \frac{1}{2\pi}\int_0^{2\pi} G\mathrm{d}\theta, \tag{2.49}$$

where G is given by the local stress intensity factor and the near-tip anisotropic modulus via equation (2.41).

Equalizing the two expression of the global energy release rate (2.48) and (2.49), we obain B_o:

$$B_o = 16\gamma_e^{1/2}\frac{1}{\int_0^{2\pi} E_\alpha'\left(\gamma_e^2\cos[\theta]^2 + \sin[\theta]^2\right)^{1/2}\mathrm{d}\theta}. \tag{2.50}$$

For the isotropic elastic case, B_o can be obtained analytically as a function of the complete elliptical integral of the second kind $\mathbb{E}\left(\sqrt{1-\gamma_e^2}\right)$ (Irwin, 1962).

$$B_{o,iso} = \frac{4}{\langle E'\rangle\,\mathbb{E}\left(\sqrt{1-\gamma_e^2}\right)}\gamma^{1/2} \tag{2.51}$$

We should point out that Lin and Keer (1989) gives an approximation of B_o for the case of a penny shaped crack $a = b$ as: $B_{o,app}^{-1} = \dfrac{\pi E_1}{8\left(1-\nu_{13}^2\right)}$, where E_1 is the elastic Young's modulus in the divider direction and ν_{13} is the Poisson's ratio in the $\boldsymbol{e_1}$ direction due to a loading in $\boldsymbol{e_3}$ direction. The approximation coincides with the exact solution only in the isotropic case.

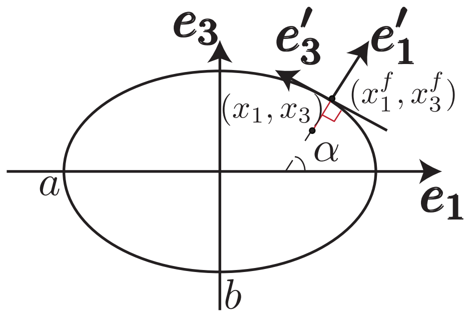

Figure 2.8 – The point (x_1, x_3) inside the elliptical fracture and its closest projection (x_1^f, x_3^f).

	Analytic	TI Kernel	Abaqus	Fabrikant	Kanaun
	$B_o p\sqrt{ab}$ (mm)	relative error			
Isotropy-Stripa granite	0.096	0.05%	0.95%	29%	5.7%
Olkiluoto mica gneiss	0.086	0.11%	0.42%	30.4%	28.4%
Gas-saturated Shaly Coal	0.4	1.45%	0.83%	52%	62.6%
Slate Del Carmen (this study)	0.092	0.04%	0.26%	38.6%	55%

Table 2.6 – Opening magnitude (in mm) for an elasto-static elliptical fracture of $\gamma_e = 0.5$ subject to uniform pressure $p = 1$ MPa. Comparison of the analytical solution is with numerical simulations in Abaqus and with the analytical solutions of Fabrikant (2011); Kanaun (2007). The rocks are defined in table 2.2.

Verification against Finite Element Method

We aim to validate our analytical solution using finite element Abaqus calculations and also by modeling an ellipse in rectangular media described by the TI kernel of Pan et al. (2014) (see equation(2.27)) (see figure 2.10). We consider an ellipse of major axis $a = 2$ m and minor axis $b = 1$ m embedded in a TI medium (table 2.2) and subject to net pressure $p = 1$ MPa. We compare the resulting maximum width with the solutions of Fabrikant (2011); Kanaun (2007) in table 2.6. As we can see from table 2.6, the numerical solutions are aligned with the analytic one with a maximum of 1.45% of error, whereas the solutions given by Fabrikant (2011); Kanaun (2007) are incorrect and their relative errors range up to 62.6%.

Verification against Displacement Discontinuity Method solver

Here we consider the fracture plane of dimension $[-3, -2, 3, 2]$ meters, divided into 80*80 cells (figure 2.9-right). We use the elastic parameters corresponding to slate Del Carmen (table 2.2). We set the pressure at $p = 1$ MPa and the ellipse aspect ratio to $\gamma_e = 0.5$ ($a = 2$m and $b = 1$m) . We compare in figure 2.10 the opening profile in the $\boldsymbol{e_1}$ and $\boldsymbol{e_3}$ directions using the analytical expression 2.43 (black line) and the numerical model using the TI kernel of Pan et al. (2014) (red dots) (see equation(2.27)). The numerical solution accurately follows the analytical solution along both axes $\boldsymbol{e_1}$ and $\boldsymbol{e_3}$.

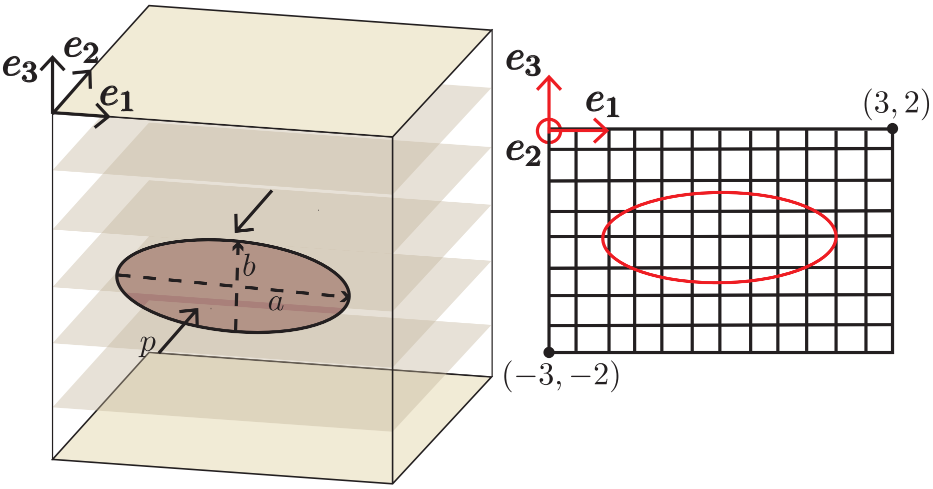

Figure 2.9 – Left: Schematic of elliptical planar fracture normal to the bedding and subject to uniform pressure p, and right: Fracture plane discretised into rectangular elements.

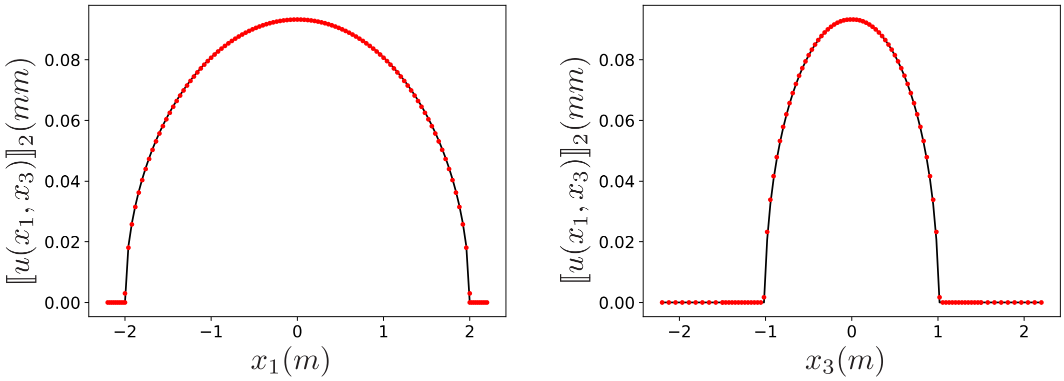

Figure 2.10 – Opening profile $[\![u(x_1,x_3)]\!]_2$ along $\boldsymbol{e_1}$ and $\boldsymbol{e_3}$ of elliptical fracture of $\gamma_e = 0.5$ embedded in slate Del Carmen under a uniform pressure $p = 1$ MPa. Comparison of the analytical solution in black solid line with the numerical elastic kernel in red dots (Pan et al., 2014).

2.6 Conclusions

The main conclusions of this chapter are the following:

- We have reviewed the elasticity principles and the fundamental solutions of a point force in a transverse isotropic media. A displacement discontinuity method (DDM) was developed to discretise the boundary elastic representation over a cartesian rectangular mesh assuming a piece-wise constant displacement. We benchmarked the DDM solver against some existing solutions.
- Zooming into the near-tip region, we showed that for planar fracture normal to the isotropy plane, the fracture mode decouples and the fracture propagates in pure opening mode.
- Solving the steady-state growth near the tip allows us to derive the asymptotic elastic integral operator – which has a similar expression to that in the isotropic space – with the use of an elastic modulus accounting for the anisotropic local propagation direction. Therefore, all the known mode I solutions for fracture problems in isotropic media can be easily used in the TI case.
- We re-derived an exact solution for elliptical fracture in TI media that we validated against a finite element method and a DDM solver. This solution will be further used for the case of a self-similar elliptical fracture propagating in the toughness dominated regime (chapter 4).

3 A semi-infinite hydraulic fracture driven by a shear thinning fluid

This chapter is a modified version of an article published in the Journal of Fluid Mechanics:

Moukhtari and Lecampion (2018): "A semi-infinite hydraulic fracture driven by a shear-thinning fluid." Journal of Fluid Mechanics 838:573-605.

Contributions:

F-E. Moukhtari has formulated the problem, performed the scaling analysis and write the numerical solver. B. Lecampion has participated in the methodology. F-E. Moukhtari and B. Lecampion have written the manuscript. B. Lecampion have guided the discussion of the numerical results.

3.1 Abstract

In this chapter, we focus our study on the near tip solution of a hydraulic fracture driven by a Non-Newtonian fluid in isotropic impermeable media. We use the Carreau rheological model which properly account for the shear-thinning behavior between the low and high shear rates Newtonian limits. We allow for the occurrence of a region without fluid of a-priori unknown length at the fracture tip. We show that the solution depends on four dimensionless parameters: a dimensionless toughness (function of the fracture velocity, confining stress, material and fluid parameters), a dimensionless transition shear stress (related to both fluid and material behaviour), the fluid shear thinning index and the ratio between the high and low shear rate viscosities. We solve this problem numerically combining a Gauss-Chebyshev method for the discretization of the elasticity equation, the quasi-static fracture propagation condition and a finite difference scheme for the width-averaged lubrication flow. The solution exhibits a complex structure with up to four distinct asymptotic regions as we move away from the fracture tip: a region governed by the classical linear elastic fracture mechanics behaviour near the tip, a high shear rate viscosity asymptotic and power-law asymptotic region in the intermediate field and a low shear rate viscosity asymptotic far away from the fracture tip. The occurrence and order of magnitude of the extent of these different viscous asymptotic regions are obtained analytically. Our results also quantify how shear thinning drastically reduces the size of the fluid lag compared to a Newtonian fluid.

We also investigate the response obtained with simpler rheological models (power- law, Ellis). In most cases, the power-law model does not accurately match the predictions obtained with a Carreau rheology. In the zero lag limit, the Ellis model properly reproduces the results of a Carreau rheology, albeit only for a dimensionless transition shear stress below a critical dimensionless transition shear stress whose expression is given analytically as function of the shear thinning index and magnitude.

3.2 Introduction

In the stimulation of oil and gas wells by hydraulic fracturing, the rheology of the fluid is the only thing that can be engineered (beside the value of the rate at which the fluid is injected). Large research efforts have thus led to the development of various fluid types over the years, essentially trying to maximize fracture opening and minimize particles settling (Barbati et al., 2016; Economides and Nolte, 2000). Although other complex rheologies are sometimes encountered in practice (viscoelasticity, yield stress etc.), most of these engineered fluids exhibit a shear thinning behaviour: their viscosity decreases as a function of the applied shear rate (see figure 3.1 for examples of the rheology of typical fracturing fluids). All these fluids exhibit a Newtonian plateau at low shear rate where their viscosity is maximum and starts to shear thin for value of shear rate larger than a critical value $\dot{\gamma}_c$. At very large shear rate, the viscosity tends to the Newtonian viscosity of the base solvent used (typically water). How such a complex rheological behaviour of the fluid impacts the actual propagation of a

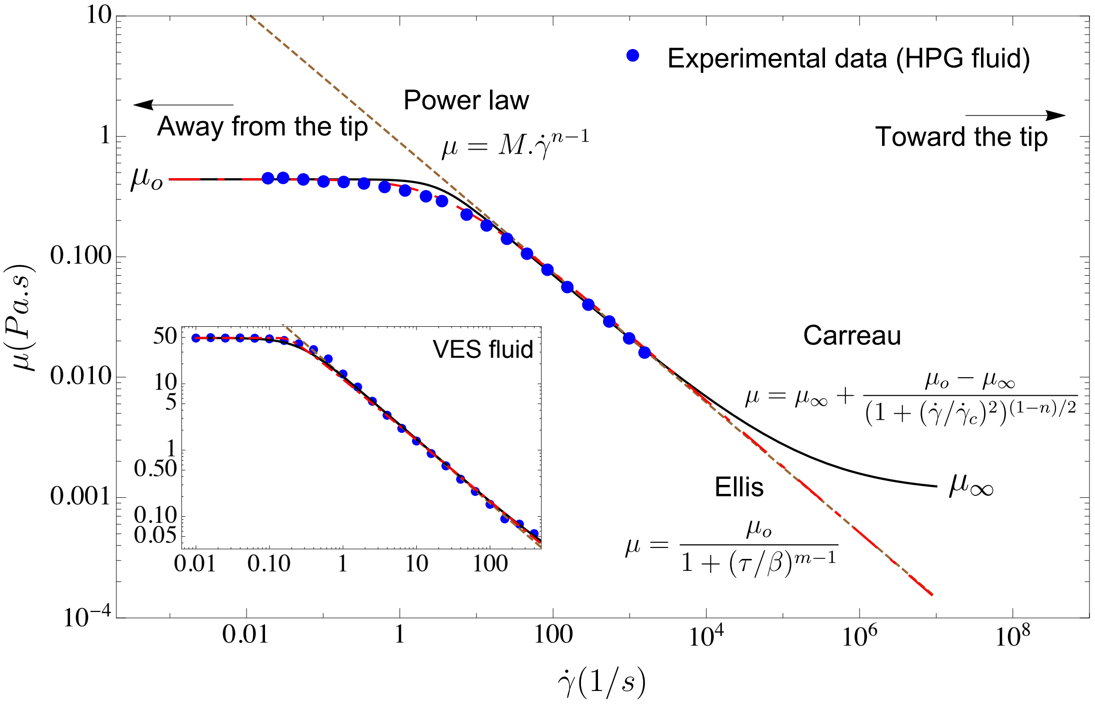

Figure 3.1 – Viscosity as function of shear rate for two fracturing fluids: Hydroxypropylguar (HPG - data taken from Guillot and Dunand (1985)) and in inset a viscoelastic surfactant (VES - data taken from Kefi et al. (2004)). These experimental data do not cover the large shear rate region where the viscosity typically tends toward the solvent viscosity (water in those case) - see e.g. Pipe et al. (2008) for experimental data on Xanthan gum covering the complete range of shear rates. A number of rheological models can be used to reproduce these data over parts or all of the range of shear rates. We display here the best fit for the power-law (dashed brown line), Carreau (continuous black line) and Ellis (dot-dashed red line) rheological models. The corresponding best-fit parameters are listed in table 3.1 for these two fluids and the different models.

hydraulic fracture has been mostly investigated using a simple power-law model (e.g. Sousa et al., 1993; Desroches et al., 1994; Adachi and Detournay, 2002). The impact of the low and large shear rate plateau as well as the amplitude of shear thinning remains poorly understood. Similarly the effect of shear thinning on the extent of the fluid-less cavity at the fracture tip (fluid lag) observed for a Newtonian fluid (Garagash and Detournay, 2000) remains unknown.

The rheology of a shear thinning fluid over the whole range of shear rates can be well reproduced by either the Carreau (1972) or Cross (1965) constitutive models. We focus here on the Carreau rheology, but similar results would be obtained using the Cross model. Two others rheological models are often used for shear thinning fluids: i) the power-law model which captures only the shear thinning part of rheological data (over-estimating viscosity at low shear rate, under-predicting at large shear rate) and ii) the Ellis model (Brodkey, 1969) which reproduces the low shear rate Newtonian plateau as well as the power-law shear thinning

Fluid	Power-law		Carreau				Ellis		
	n	$M\ (Pa.s^n)$	n	$\mu_o\ (Pa.s)$	$\mu_\infty\ (Pa.s)$	$\dot{\gamma}_c\ \left(s^{-1}\right)$	m	$\mu_o\ (Pa.s)$	$\beta\ (Pa)$
HPG (15°C)	0.46	0.75	0.46	0.44	0.001	3.3	2.22	0.44	2.01
VES (77°C)	0.1	13	0.1	49	0.0003	0.254	13	49	8.836

Table 3.1 – Rheological parameters of a HPG and VES fluids (for a given temperature) for the power-law, Carreau and Ellis models corresponding to the experimental data of figure 3.1. Note that the majority of fracturing fluids have a power-law index n between 0.1 and 0.5.

region but does not reproduce the large shear rate Newtonian limit. The differences between these models can be clearly seen in figure 3.1 while the corresponding rheological parameters are listed in table 3.1. In order to best fit the experimental data, the power-law index may be adjusted independently from the Carreau index (see examples in Sochi (2015); Myers (2005)). However, in the interest of comparison and simplification, we will consider that the power-law index is equal to the Carreau shear thinning index. The power-law consistency M (dimensions $Pa.s^n$) can thus be expressed directly from the rheological parameters of the Carreau model:

$$M = \frac{\mu_o + \mu_\infty}{2\dot{\gamma}_c{}^{n-1}\left(\sqrt{2^{-2/(n-1)}-1}\right)^{n-1}} \tag{3.1}$$

where μ_o, μ_∞ are the viscosity at low and high shear rates respectively and $\dot{\gamma}_c$ is the critical shear rate at which the fluid starts to shear thin in the Carreau model.

Within a fracture, fluid flow occurs under lubrication condition between parallel plates. For the same average velocity (and the rheological parameters of the HPG fluid listed in table 3.1), the different rheologies exhibit a different velocity profile across the cross section of the fracture and the corresponding pressure gradient differs significantly between models as can be seen in figure 3.2. For that particular example, the power-law fluid has a profile close to a plug flow around the centerline and yield the largest pressure gradient. The Carreau and Ellis models exhibit similar velocity profiles except close to the centerline (but with different pressure gradients). We shall see in the following that these differences between models will impact the solution of the hydraulic fracturing problem.

In order to study the impact of the fluid shear thinning behaviour on hydraulic fracturing, we focus our analysis on the case of a semi-infinite hydraulic fracture propagating at a constant velocity in a linear elastic and impermeable material. Such a configuration corresponds to a zoom into the tip region of a finite hydraulic fracture (Garagash, 2009; Detournay, 2016) where a state of plane-strain locally prevails. Such a semi-infinite fracture problem has been extensively studied for the case of a Newtonian fluid (Spence and Sharp, 1985; Desroches et al., 1994; Garagash and Detournay, 2000; Garagash et al., 2011). It has notably enabled to properly quantify the competition between the dissipative processes associated with fracture surface creation and viscous flow. Such a competition is intrinsically linked to the transition between the classical linear elastic fracture mechanics asymptotic region near the fracture tip to a viscosity dominated asymptotic region far from the tip. The extent of the transition being

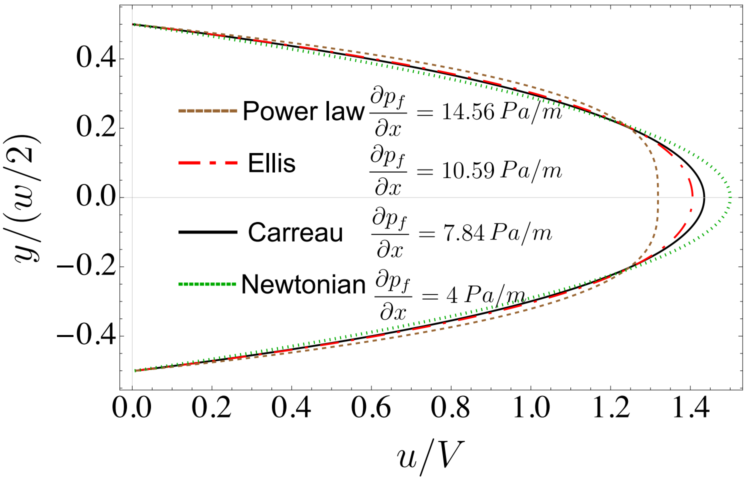

Figure 3.2 – Fluid velocity profiles for a lubrication flow between parallel plates (as it occurs within a fracture) at a given mean velocity $< u >= V = 1$ m/s for a Carreau, power-law, Ellis and Newtonian fluids. The corresponding fluid pressure gradient is also displayed for each model. The rheological parameters correspond to a HPG fluid (see table 3.1 for the different models, figure 3.1 for the rheogram). For the Newtonian velocity profile (dotted green line), the low shear rate viscosity of the HPG is used. Note that the solution for a Carreau fluid is semi-analytical while the solution for the other models can be obtained analytically (see sections 3.10.1, 3.10.2 and 3.10.3 for details).

governed by a combination of the fluid viscosity, material fracture toughness, elasticity and fracture velocity.

Our goal is to perform a similar analysis for a shear thinning fluid. We will use the Carreau rheology to model the complete shear thinning behaviour of the fluid. We also allow for the possible presence of a fluid-less cavity of a priori unknown length at the fracture tip. Using scaling analysis and a numerical solution of the problem, we aim at understanding the structure of the solution and in particular the extent of the different asymptotic regions (associated with different dissipative mechanisms) as function of the different problem parameters. We will also investigate how an approximation of the shear thinning behaviour by either the power-law or the Ellis rheological model compare with the more precise Carreau rheology. In other words, how precise we need to be on the fluid rheology in hydraulic fracturing modeling.

3.3 Problem formulation

We consider a semi-infinite fluid-driven fracture under plane-strain condition propagating at a constant velocity V in an impermeable linear elastic medium (see figure 3.3). The fracture is propagating normal to the minimum in-situ compressive stress σ_o and is internally loaded by the spatially non-uniform fluid pressure p_f. We also allow for the presence of zone of a-priori unknown size λ without fluid at the fracture tip (fluid lag). The fracture is assumed to

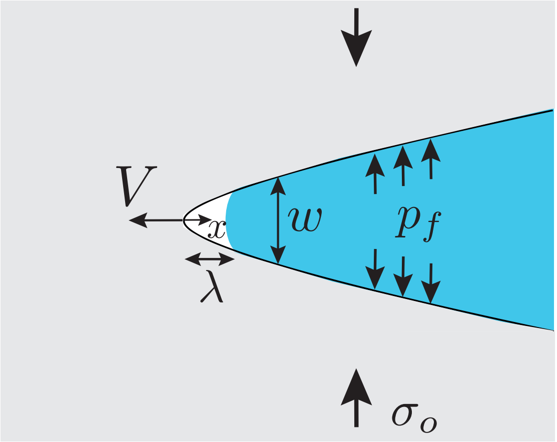

Figure 3.3 – Sketch of a semi-infinite hydraulic fracture propagating at a constant velocity V in an impermeable elastic material under a pre-existing normal compressive stress σ_o. A fluid lag zone of a-priori unknown length λ adjacent to the fracture tip may be present.

propagate at a constant velocity V in quasi-static equilibrium under a pure opening mode loading. The fracture propagation condition is written as the equality of the mode I stress intensity factor K_I to the material fracture toughness K_{Ic} (Rice, 1968):

$$K_I = K_{Ic} \tag{3.2}$$

The linear elastic fracture near-tip asymptote for the fracture opening w is related to the mode I stress intensity factor K_I and can be written in view of the propagation condition (3.2) as (Rice, 1968):

$$w(x) = \sqrt{\frac{32}{\pi}} \frac{K_{Ic}}{E'} x^{1/2} \qquad x \ll 1. \tag{3.3}$$

In the plane-strain pure tensile configuration of figure 3.3, the elastic deformation of the material reduces to the following normal traction boundary integral equation between the net pressure loading $p(x) = p_f(x) - \sigma_o$ and the fracture opening $w(x)$ (see e.g. Garagash and Detournay (2000)):

$$p(x) = p_f(x) - \sigma_o = \frac{E'}{4\pi} \int_0^\infty \frac{\partial w(s)}{\partial s} \frac{\mathrm{d}s}{x - s} \tag{3.4}$$

where $E' = E/(1 - \nu^2)$ is the material plane-strain elastic modulus, related to the Young's modulus E and Poisson's ratio ν. We account explicitly for the possible presence of a region of length λ without fluid near the tip of the fracture due to the possible occurrence of cavitation. This fluid lag zone is filled with fluid vapor and is under a constant pressure equal to the fluid cavitation pressure. Such a cavitation pressure is typically smaller than the confining stress σ_o such that we write the net loading in this lag zone simply as:

$$p(x) = p_{cav} - \sigma_o \approx -\sigma_o \qquad x \in [0, \lambda] \tag{3.5}$$

The semi-infinite hydraulic fracture propagates under a constant velocity V, such that for an impermeable medium, in the moving coordinates centered on the fracture tip, the fluid continuity equation reduces to (Desroches et al., 1994):

$$V_f = V.$$

The width-averaged fluid velocity V_f is equal to the fracture velocity V at any distance from the tip. Under the lubrication approximation, this width-averaged fluid velocity can be related at any x to the fracture opening and pressure gradient via the solution of pressure-driven flow between parallel plates. For a Carreau rheology, no analytical formula exists but the solution can be expressed in a similar form that the well-known Poiseuille solution for a Newtonian fluid:

$$V = \frac{1}{12\mu_o \Gamma\left(\tau_w, n, \mu_\infty/\mu_o, \dot{\gamma}_c\right)} w^2 \frac{\partial p_f}{\partial x}, \; x \in]\lambda, \infty[\tag{3.6}$$

where the dimensionless apparent width-averaged viscosity for parallel plates flow $\Gamma\left(\tau_w, n, \mu_\infty/\mu_o, \dot{\gamma}_c\right)$ depends non-linearly on the shear stress at the fracture wall $\tau_w = \frac{w}{2}\left|\frac{\partial p}{\partial x}\right|$ as well as the rheological parameters of the Carreau model. This dimensionless apparent viscosity requires the solution of the rheological equation at the fracture wall in order to obtain the wall shear rate $\dot{\gamma}_w = \tau_w/\mu(\dot{\gamma}_w)$ for a given value of wall shear stress (Sochi, 2014, 2015) (see section 3.10.1 for details). It is interesting to note that an analytical solution exists for the lubrication of a power-law rheology as well as for the Ellis rheological model (Myers, 2005). Also the lubrication flow for a simplified Carreau modelled as truncated power law fluid is explicitly given in Lavrov (2015).

The aim is to solve for both the fracture opening $w(x)$ and net pressure $p(x)$ profiles as well as the extent of the lag λ as function of the fracture velocity V, solid material properties (elastic modulus E', fracture toughness K_{Ic}) and fluid rheological properties.

3.4 Scaling

We follow the scaling first introduced by Garagash and Detournay (2000) for the case of a semi-infinite hydraulic fracture driven by a Newtonian fluid. A characteristic viscous lengthscale L_{μ_o} scales all distances, while the fracture width is scaled by ϵL_{μ_o} (with ϵ a small number) and the characteristic pressure is taken as the in-situ compressive stress σ_o. We thus define the normalized moving coordinate $\xi = x/L_{\mu_o}$ and the normalized fracture opening $\Omega(\xi)$, net pressure $\Pi(\xi)$ and fluid lag Λ size as

$$w = \epsilon L_{\mu_o}\Omega(\xi) \qquad p = \sigma_o \Pi(\xi) \qquad \lambda = L_{\mu_o}\Lambda$$

The scaling parameters (L_{μ_o},ϵ) can be obtained from the elasticity equation (3.4) and the lubrication relation (3.6): L_{μ_o} is a fracture characteristic lengthscale related to the viscosity propagation regime and its expression depends on the fluid rheological model. The small dimensionless parameter ϵ is independent of the fluid rheology and is defined as the ratio between confining stress and the solid material plane-strain Young's modulus. For a Carreau rheology, choosing the low-shear rate viscosity μ_o as a representative value of viscosity, we write similarly to Garagash and Detournay (2000)

$$L_{\mu_o} = \frac{12\mu_o V E'^2}{\sigma_o^3} \qquad \epsilon = \frac{\sigma_o}{E'}.$$

These scales for the slightly different cases of a power-law and Ellis rheology are discussed in sections 3.10.2 and 3.10.3.

The corresponding dimensionless governing equations in that scaling simplify to the following:

- Elasticity equation relating net pressure to fracture opening

$$\Pi(\xi) = \frac{1}{4\pi}\int_0^{\infty} \frac{\partial \Omega(\xi')}{\partial \xi'} \frac{\mathrm{d}\xi'}{\xi - \xi'} \tag{3.7}$$

- The fracture propagation expressed as a near tip width asymptotic

$$\Omega(\xi) = \kappa\sqrt{\xi} \text{ for } \xi \to 0 \tag{3.8}$$

  where κ is a dimensionless toughness defined in such a scaling as

$$\kappa = \sqrt{\frac{8}{3\pi}}\left(\frac{\sigma_o}{V\mu_o}\right)^{1/2} \frac{K_{Ic}}{E'} \tag{3.9}$$

- The net pressure in the lag region

$$\Pi = -1 \text{ for } \xi \in [0, \Lambda] \tag{3.10}$$

- The lubrication flow equation

$$\frac{1}{\Gamma\left(\frac{\Omega}{2}\left|\frac{\partial \Pi}{\partial \xi}\right|, \alpha, n, \mu_\infty/\mu_o\right)} \Omega^2 \frac{\partial \Pi}{\partial \xi} = 1 \text{ for } \xi \in]\Lambda, \infty[\tag{3.11}$$

The dimensionless apparent viscosity $\Gamma\left(\frac{1}{2}\Omega\left|\frac{\partial \Pi}{\partial \xi}\right|, \alpha, n, \mu_\infty/\mu_o\right)$ can be written as a function of the dimensionless fluid shear stress at the wall $\frac{\Omega}{2}\left|\frac{\partial \Pi}{\partial \xi}\right|$, the fluid shear thinning index n, the viscosity ratio μ_∞/μ_o and a parameter α which is defined as the ratio between the characteristic shear stress at the wall $\epsilon\sigma_o$ and the critical fluid shear stress $\tau^c = \mu_o\dot{\gamma}_c$ corresponding to the critical shear rate $\dot{\gamma}_c$ at which the fluid starts to shear-thin (see figure 3.1):

$$\alpha = \frac{\epsilon \sigma_o}{\mu_o \dot{\gamma}_c} = \frac{\sigma_o^2}{\mu_o \dot{\gamma}_c E'}. \tag{3.12}$$

For typical order of magnitude of the far field stress σ_o (MPa) and elastic modulus E' (GPa), such a dimensionless transition shear stress α ranges from 10 for a fluid with a large low shear-rate Newtonian plateau (large value of $\dot{\gamma}_c$) to 10^5 for a fluid with a shorter transition to a shear thinning behaviour (small $\dot{\gamma}_c$). The fluid index n varies for most of hydraulic fracturing fluids between 0.1 and 0.5. For a fluid with large shear thinning magnitude, the viscosity ratio is about 10^{-3} versus 0.1 for a fluid with a small shear thinning magnitude.

The dimensionless solution of the problem thus depends on four dimensionless parameters: the dimensionless toughness κ defined in (3.9), dimensionless transition shear stress α (3.12), fluid index n and the overall extent of the shear thinning behaviour of the fluid captured by the ratio between the large and low shear rate viscosity μ_∞/μ_o.

3.5 Asymptotes

The knowledge of the solution for the case of a Newtonian fluid (Garagash and Detournay, 2000) as well as the limiting solution for zero-lag / zero toughness for a power-law rheology (Desroches et al., 1994) will provide some guideline to understand how the solution for a Carreau rheology is structured as we move away from the fracture tip. The different tip asymptotes can be expressed in terms of the following characteristic lengthscales:

$$\ell_k = \frac{32}{\pi}\left(\frac{K_{Ic}}{E'}\right)^2, \qquad \ell_{m_o} = \frac{12\mu_o}{E'}V, \qquad \ell_{m_n} = \left(\frac{M'}{E'}\right)^{1/n} V, \qquad \ell_{m_\infty} = \frac{12\mu_\infty}{E'}V, \tag{3.13}$$

where $M' = \dfrac{2^{n+1}(2n+1)^n}{n^n}M$, and M is the power-law consistency which is defined from the Carreau parameters as per equation (3.1).

Near field asymptote

The near tip asymptote of the fracture opening is governed by linear elastic fracture mechanics (lefm). In this region, the fracture width evolves with the square-root of distance to the tip and the toughness characteristic lengthscale ℓ_k (see equation 3.13):

$$\kappa - asymptote: w_k = \ell_k^{1/2} x^{1/2} + O(x^{3/2}), \qquad p_k = -\sigma_o$$

which takes the following form in the scaling previously defined:

$$\Omega_k = \kappa \xi^{1/2} + O(\xi^{3/2}), \qquad \Pi_k = -1 \tag{3.14}$$

For the strictly zero toughness case ($\kappa = 0$), the width evolves as $\xi^{3/2}$ which corresponds to the higher order term in the linear elastic fracture mechanics asymptotic development (see e.g. Rice (1968); Garagash (2009)). In the complete problem, the extent of this lefm region depends on the viscous lengthscale L_{μ_o} as well as the value of the dimensionless toughness (i.e. the corresponding lag size).

Far field asymptotes

In the case where both the fluid lag and toughness are negligible ($\kappa \ll 1$, $\Lambda \ll 1$), the behaviour of the solution is governed by the coupling between lubrication flow and elasticity which yields a different power-law dependence of the opening with distance from the tip. The solution for a power-law rheology (for zero-lag and zero toughness) have been obtained in Desroches et al. (1994). Such a solution corresponds to a far-field asymptote valid at a distance from the tip where the effect of dimensionless toughness and the presence of the lag vanishes (see e.g. Garagash and Detournay (2000); Garagash (2009); Garagash et al. (2011) for discussion). For a Carreau rheology, as the average shear rate V/w decreases as we move away from the fracture tip, we can expect to see two or more viscosity dominated asymptotes. Far away from the fracture tip, i.e. for very low shear-rate, we should recover the viscosity asymptote for a Newtonian with the low shear-rate viscosity (see figure 3.1), i.e:

$$m_o\text{-asymptote } (\kappa = \Lambda = 0): \; w_{m_o} = \beta_o \ell_{m_o}^{1/3} x^{2/3}, \qquad p_{m_o} = -\frac{\beta_o}{6\sqrt{3}} E' \ell_{m_o}^{1/3} x^{-1/3},$$

where

$$\beta_o = 2^{1/3} \times 3^{5/6}.$$

This m_o-asymptote in the scaling previously defined in section 3.4 has the following form:

$$\Omega_{m_o} = \beta_o \xi^{2/3}, \qquad \Pi_{m_o} = -\frac{\beta_o}{6\sqrt{3}} \xi^{-1/3}. \tag{3.15}$$

As we move closer to the fracture tip, the fluid will exhibit shear thinning. The fracture opening should thus eventually follow the viscosity asymptote for a power-law fluid. We will refer to this power-law asymptote -first derived by Desroches et al. (1994)- as m_n:

$$w_{m_n} = \beta_n \ell_{m_n}^{n/(2+n)} x^{2/(n+2)},$$

$$p_{m_n} = -\frac{\beta_n}{2(n+2)} \cot\left(\frac{-2\pi}{n+2}\right) E' \ell_n^{n/(2+n)} x^{-n/(n+2)}$$

where

$$\beta_n = \left(2\frac{(n+2)^2}{n} \tan\left(\frac{-2\pi}{n+2}\right)\right)^{1/(n+2)}.$$

We can re-express this asymptote using the expression of the power-law consistency M as function of the Carreau rheological parameters (see equation (3.1)). Moreover, using the low shear rate scaling defined in the section 3.4, such m_n asymptote ($\kappa = \Lambda = 0$) reads:

$$\Omega_{m_n} = \alpha^{\frac{n-1}{n+2}} \beta_\mu \beta_n \xi^{2/(n+2)}, \; \Pi_{m_n} = -\frac{\alpha^{\frac{n-1}{n+2}} \beta_\mu \beta_n}{2(n+2)} \cot\left(\frac{-2\pi}{n+2}\right) \xi^{-n/(n+2)}$$

where

$$\beta_\mu = \left(\left(\frac{2n+1}{6n}\right)^n \frac{1+\mu_\infty/\mu_o}{\left(\sqrt{2^{-2/(n-1)}-1}\right)^{n-1}} \right)^{1/(n+2)}.$$

Finally, as we move closer to the fracture tip, for larger average shear rate, it may well be that another Newtonian viscous asymptote linked to the Newtonian behaviour at large shear-rate μ_∞ could be observed (see equation 3.16). In the low-shear rate scaling, this large shear rate asymptote is given by :

$$m_\infty\text{-asymptote } (\kappa = \Lambda = 0): \; w_{m_\infty} = \beta_o \ell_{m_\infty}^{1/3} x^{2/3}, \qquad p_{m_\infty} = -\frac{\beta_o}{6\sqrt{3}} E' \ell_{m_\infty}^{1/3} x^{-1/3} \tag{3.16}$$

or alternatively in dimensionless form in the lag scaling:

$$\Omega_{m_\infty} = \beta_o \left(\mu_\infty/\mu_o\right)^{1/3} \xi^{2/3}, \qquad \Pi_{m_\infty} = -\frac{\beta_o}{6\sqrt{3}} \left(\mu_\infty/\mu_o\right)^{1/3} \xi^{-1/3}. \tag{3.17}$$

The evolution of the complete solution between these different asymptotes as well as the extent of the regions where these asymptotes may be valid will depend on the values of the different dimensionless parameters governing the problem, namely κ, α, n and μ_∞/μ_o.

3.6 Numerical scheme

We develop a numerical scheme for the solution of the complete problem for a given set of dimensionless parameters (κ, α, n and μ_∞/μ_o). In our simulation, following Garagash and Detournay (2000), we actually prescribe the dimensionless lag size Λ such that the domain where the lubrication equation is enforced is known a-priori. We thus solve for the corresponding value of dimensionless toughness κ, as well as dimensionless pressure and opening.

We use a Gauss-Chebyshev quadrature for the discretization of the elasticity equation. We embed the linear fracture mechanics asymptote directly in the discretization of the dislocation density:

$$\frac{d\Omega}{d\xi} = \frac{\kappa}{\sqrt{\xi}} + \sqrt{\xi}\phi(\xi),$$

We also perform the following changes of coordinates to map the semi-infinite interval $\xi \in [0,\infty[$ to $\upsilon \in [-1,1]$ so as the Gauss-Chebyshev quadrature to become applicable to the numerical solution (Ioakimidis and Theocaris, 1980; Viesca and Garagash, 2015)

$$\xi = \frac{1+v}{1-v}$$

in order to discretize the elasticity equation using a Gauss-Chebyshev quadrature of the third kind at N collocation points:

$$\frac{\Pi[\xi(v_j)]}{1-v_j} = \frac{1}{4\pi}\sum_{i=1}^{N}\frac{A_i}{1-u_i}\frac{\phi[s(u_i)]}{v_j-u_i} \tag{3.18}$$

where $u_i = \cos\left(\frac{\pi(i-0.5)}{N}\right)$ and $A_i = \frac{\pi}{N}(1+u_i)$. The net pressure is evaluated at points $v_j = \cos\left(\frac{\pi j}{N}\right)$ for $j = 1, 2, ..., N$, whereas the dislocation density $\phi[s(u_i)]$ is evaluated at points u_i for $i = 1, 2, ..., N$.

The lubrication equation is discretized at the mid distance $\xi_{i+1/2}$ between net pressure collocation points, and the pressure gradient is approximated by centered finite difference. The discretization of equation (3.11) is thus:

$$\Omega^2(\xi_{i+1/2})\frac{\Pi(\xi_{i+1})-\Pi(\xi_i)}{\xi_{i+1}-\xi_i} = \Gamma\left(\frac{\Omega(\xi_{i+1/2})}{2}\frac{\Pi(\xi_{i+1})-\Pi(\xi_i)}{\xi_{i+1}-\xi_i}, \alpha, n, \mu_\infty/\mu_o\right) \tag{3.19}$$

The opening $\Omega(\xi_{i+1/2})$ at $\xi_{i+1/2}$ is evaluated from a linear interpolation of the opening evaluated at ξ_i and ξ_{i+1}. The non-linear tangent viscosity Γ function of the wall shear stress is estimated from the interpolated function built for the given values of α, n and μ_∞/μ_o over the whole range of dimensionless wall shear stress (see section 3.10.1). The net pressure Π is directly set in the lag zone for the collocation points $i \in [1, N_\Lambda]$ where N_Λ is the number of points in the lag region:

$$\Pi(\xi_i) = -1, \tag{3.20}$$

while at infinity the net pressure is set to zero, i.e. we set the following constraint at the last collocation point

$$\Pi(\xi_N) = 0. \tag{3.21}$$

It follows that the solution for the fracture opening Ω is positive while the net pressure Π is everywhere negative. This is a direct consequence of the semi-infinite nature of this problem where pressure is determined up to a constant (see e.g. Garagash and Detournay (2000) for discussion).

The resulting non-linear system of equations is solved via a quasi-Newton root-finding scheme using the dimensionless net pressure at the collocation points and κ as the primary unknown variables. The algorithm has been implemented in Mathematica with computational accuracy in mind (but not efficiency). The numerical results reported in the remaining of this paper have been obtained with a total number of collocation points between 1600 and 3000. Convergence of the lubrication equation (3.19) has been obtained with an accuracy of 10^{-8} on the norm of the residuals. A simulation typically takes from few minutes up to three hours on a modern personal computer (Macbook Pro, Early 2015, 2.9 GHz Intel core i5) depending on the prescribed size of the lag, the amplitude of shear thinning and the number of collocation points.

3.7 Results for a finite fluid lag

3.7.1 Effect of dimensionless toughness κ

We first investigate the effect of dimensionless toughness κ for a given set of rheological dimensionless parameters representative of a Carreau fluid: $\mu_\infty/\mu_o = 10^{-3}$, $n = 0.5$, and $\alpha = 10^2$. The profile of dimensionless fracture opening with distance from the tip for different values of dimensionless lag size/ dimensionless toughness is displayed on figure 3.4, while the corresponding dimensionless net pressure profiles (in semi-log) and the apparent viscosity Γ are displayed on figures 3.5 and 3.6. We can directly observe the extent of the lag on the net-pressure profiles which depart from the value $\Pi = -1$ at the fluid front $\xi = \Lambda$. The relation between the dimensionless toughness and the dimensionless lag size for these simulations are better grasped on figure 3.7. The dimensionless lag size Λ is decreasing function of dimensionless toughness κ. This is similar to the Newtonian case (see Garagash and Detournay (2000)) with the difference that for a given value of dimensionless toughness, due to shear thinning, the dimensionless lag is always smaller compared to the Newtonian case (see figure 3.10 for more simulations with different shear thinning index n, and figure 3.8 for different transition shear-stress α).

The dimensionless opening profiles (figure 3.4) also evolve in a similar way to that in the Newtonian case with a region dominated by the lefm toughness κ-asymptote (3.14) near the fracture tip (for $x \ll L_{\mu_o}$) and a region in the far-field (for $x \gg L_{\mu_o}$) dominated by the low shear-rate viscosity asymptote m_o (equation (3.15)). However, here due to the shear thinning nature of the Carreau rheology, an intermediate region following the power-law dominated asymptote m_n can be observed for intermediate distances between the lefm near-tip region and the far-field low shear rate viscosity region. It is worth noting the particularity of the zero toughness case ($\kappa = 0$) for which the dimensionless lag is maximum and the opening in the near-tip lefm region evolves as $\xi^{3/2}$ (see figure 3.4).

The same evolution can be seen on the net pressure profiles (figure 3.6). The different viscosity regimes as function of distance from the tip are also visible in figure 3.5 where the dimensionless apparent viscosity Γ is plotted along the fracture for the two cases $\kappa = 0$ ($\Lambda = 0.049$) and $\kappa = 0.74$ ($\Lambda = 8.3 \times 10^{-8}$). The largest shear rate and therefore the lowest tangent apparent viscosity is always located at the fluid front. For the largest lag case, a smaller shear thinning region can be observed (see figure 3.5). On the other hand, for a very small lag ($\kappa = 0.74$), the fluid strongly shear thin, although the value of the tangent viscosity at the fluid-front

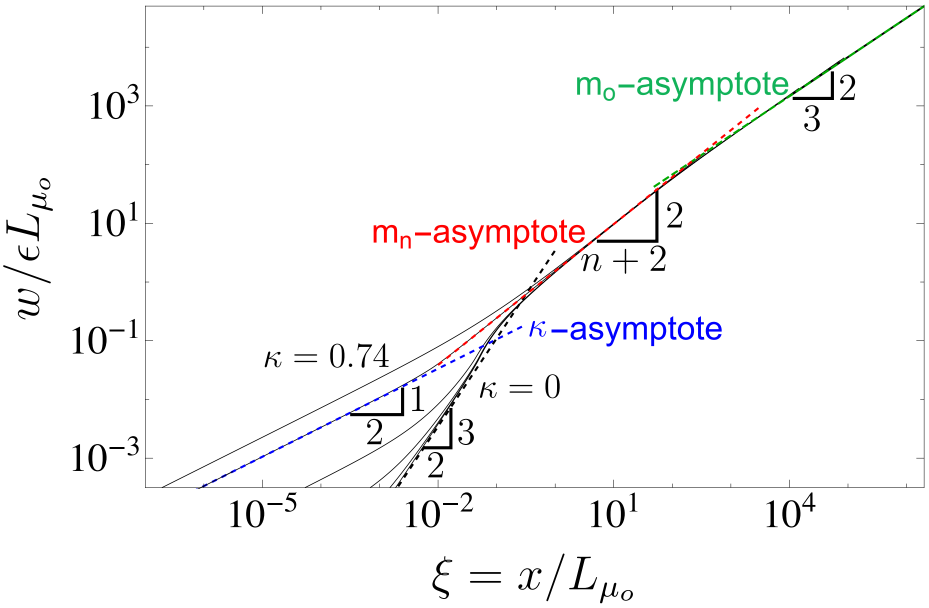

Figure 3.4 – Dimensionless fracture opening $w/\epsilon L_{\mu_o}$ along the fracture for $\kappa = 0$, 0.002, 0.008, 0.043, 0.33, 0.74 (with corresponding lag size $\Lambda = 0.049,\ 0.048,\ 0.047,\ 0.041$, 0.008, 8.3×10^{-8}) in log-log scale for $\alpha = 10^2$, $\mu_\infty/\mu_o = 10^{-3}$, and $n = 0.5$. The dashed lines correspond to the asymptotic solution in the toughness dominated regime (κ-asymptote), power-law viscosity regime (m_n-asymptote) and low shear-rate Newtonian viscosity regime (m_o-asymptote).

($\xi = \Lambda$) remains larger than the large shear rate value μ_∞/μ_o. It is important to note that the large shear rate asymptote is absent for all the simulations performed with this given set of rheological parameters ($n = 0.5$, $\alpha = 10^2$, and $\mu_\infty/\mu_o = 10^{-3}$).

The relative extent of these different asymptotic regions depends on the values of the dimensionless problem parameters. In order to picture the variation of the size of these asymptotic regions as function of dimensionless toughness κ, we determine from our numerical results the spatial locations (ξ_κ, ξ_n and ξ_o) where our numerical results for the fracture opening are within 1% of these different asymptotes. The results are displayed on figure 3.7 for that same set of parameters ($\alpha = 10^2$, $\mu_\infty/\mu_o = 10^{-3}$, and $n = 0.5$) where we see that the extent of the power-law and low shear-rate viscosity regions do not significantly change with dimensionless toughness while the lefm near-tip region shrinks when the dimensionless toughness decreases (and the lag size increases) as expected. We also see that the fluid lag region is always localized in the toughness asymptotic region (for large κ) - or in the transition between the toughness and power-law region (small κ).

3.7.2 Effect of the dimensionless transition shear stress α

The value of the dimensionless transition shear stress ratio α reflects the extent of the low shear rate plateau: α is inversely proportional to the critical shear rate $\dot{\gamma}_c$ (see equation (3.12)).

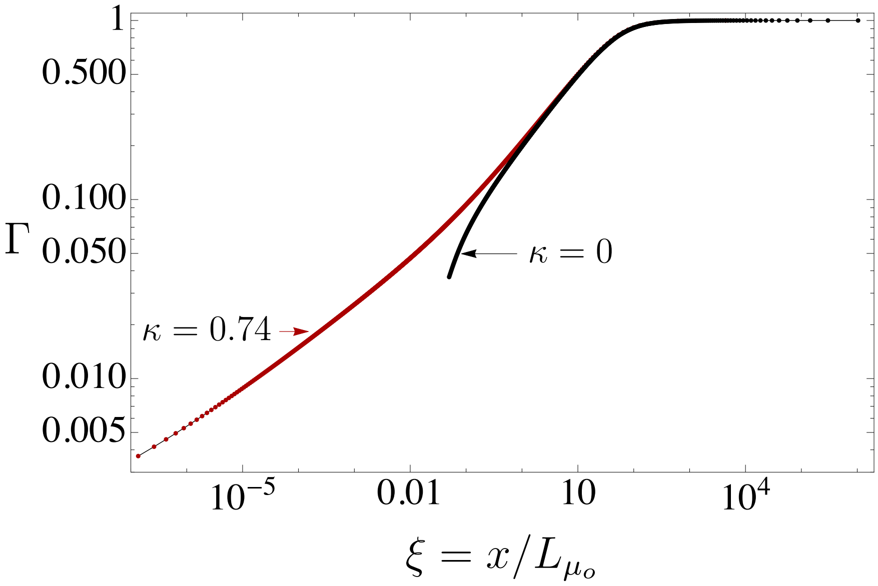

Figure 3.5 – Dimensionless apparent viscosity Γ along the fracture starting from the fluid front $\xi = \Lambda$ for $\kappa = 0$ ($\Lambda = 0.049$) and $\kappa = 0.74$ ($\Lambda = 8.3 \times 10^{-8}$) in log-log scale for $\alpha = 10^2$, $\mu_\infty/\mu_o = 10^{-3}$, and $n = 0.5$.

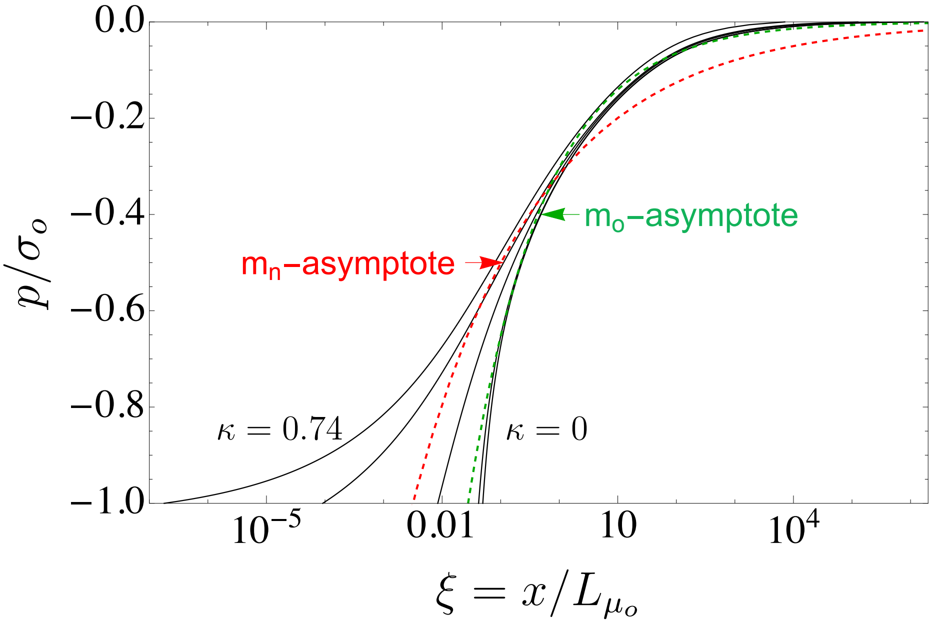

Figure 3.6 – Dimensionless fluid pressure p/σ_o along the fracture for $\kappa = 0, 0.002, 0.008, 0.043, 0.33, 0.74$ in semi-log scale for $\alpha = 10^2$, $\mu_\infty/\mu_o = 10^{-3}$, and $n = 0.5$. The dashed lines correspond to the asymptotic solution of pressure in power-law viscosity regime (m_n-asymptote) and in Newtonian viscosity regime (m_o-asymptote).

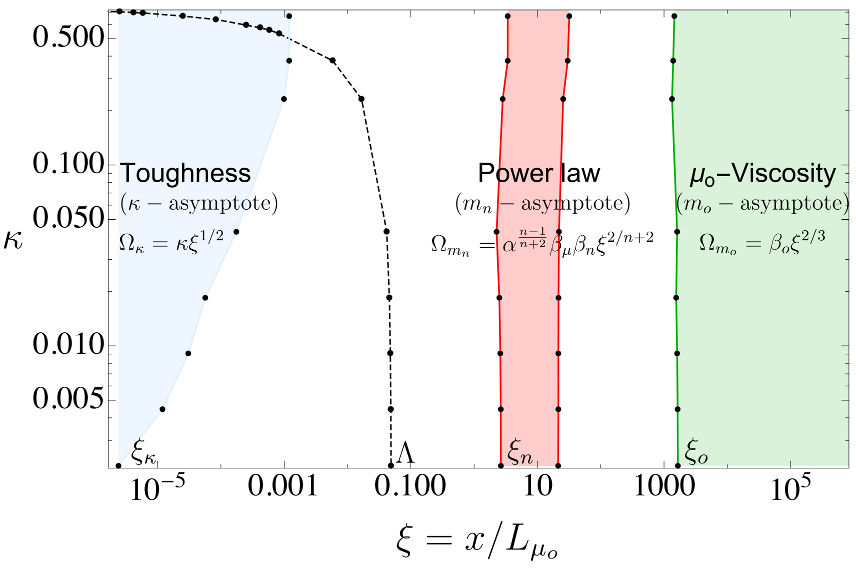

Figure 3.7 – Extent of the regions where the numerical solution can be approximated by the different asymptotes (κ-asymptote, m_n-asymptote, and m_o-asymptote) with accuracy of 10^{-2} as function of dimensionless toughness with $\alpha = 10^2$, $\mu_\infty/\mu_o = 10^{-3}$, $n = 0.5$. The position of the fluid lag is also displayed for comparisons.

For large α, the fluid shear thin faster and as a result the dimensionless lag is getting smaller for a similar value of dimensionless toughness. This can be clearly seen on figure 3.8 where the $\Lambda - \kappa$ evolution is plotted for different values of α for $n = 0.5$ and $\mu_\infty/\mu_o = 10^{-3}$.

More interestingly, the structure of the solution also changes for larger value of α. We present on figure 3.9 the evolution of the dimensionless fracture opening and apparent viscosity for a large dimensionless transition shear stress ratio $\alpha = 10^7$ while the shear thinning index n and extent μ_∞/μ_o are kept the same as in the previous sub-section: $n = 0.5$ and $\mu_\infty/\mu_o = 10^{-3}$. For this case, the dimensionless opening profiles (for different κ) involve an additional viscosity asymptote corresponding to the large shear rate m_∞ viscosity asymptote located in between the toughness and shear thinning asymptotic regions. Even though the toughness region increases with κ, the validity of the m_∞ asymptote roughly starts at the same distance from the fracture tip $\xi \simeq 0.01$ for all values of κ. This can also be clearly seen on the apparent viscosity profiles depicted on figure 3.9b: the apparent viscosity close to the fluid front reaches the large shear rate value at about $\xi \approx 0.1$.

The opening in the shear thinning region actually do not coincide exactly with the m_n power-law asymptote (red dashed line on figure 3.9a). This is the case for all dimensionless toughness. This difference is rooted in the behaviour of the Carreau viscosity at large shear rate. If we zoom in the region of large $\dot{\gamma} > 1000$ on figure 3.1, we observe that the transition from the power-law behaviour to the Newtonian high shear rate behaviour occur over a large range of shear rate for a Carreau rheology. This large transition region can be clearly seen on the apparent viscosity profiles (figure 3.9b), where it departs from the large shear rate value at $\xi \approx 0.1$ and reaches

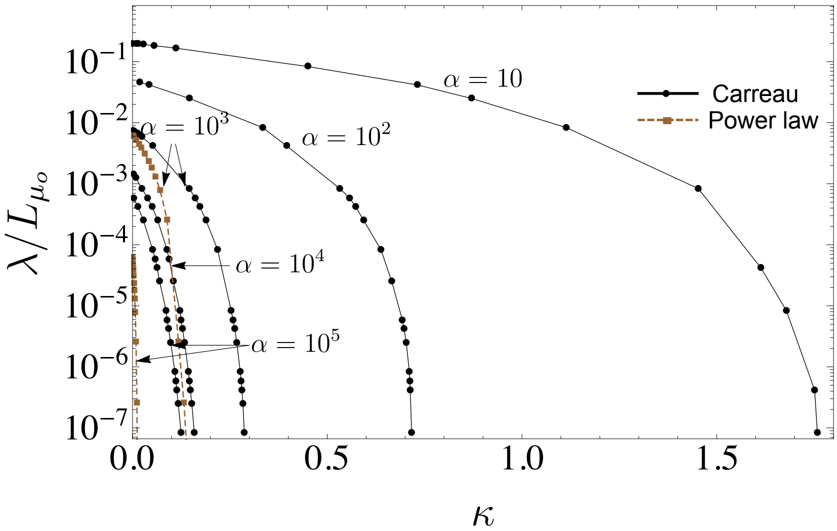

Figure 3.8 – Dimensionless lag length λ/L_{μ_o} versus the dimensionless toughness κ for a Carreau rheology for different value of α ($\mu_\infty/\mu_o = 10^{-3}$, $n = 0.5$). The corresponding results for a power-law rheology are also displayed for $\alpha = 10^5$ and $\alpha = 10^3$ for comparisons.

the power-law branch at about $\xi \approx 100$ (or more). As a result the opening profile beyond the large shear rate viscosity asymptotic region are shifted from the m_n power-law asymptote although they exhibit a similar power-exponent. This difference is negligible for sufficiently small dimensionless shear stress α as observed in the previous section (see e.g. figure 3.4), where the large shear-rate viscosity asymptote was not visible. The difference between the Carreau opening profile and the power-law asymptote in the shear thinning region becomes more significant for large α. It is also worthwhile to point out that for the simulations for $\alpha = 10^7$ reported in figure 3.9a, the extent of our computational domain ($\xi_{max} = 10^4$) was not sufficient to observe the low shear rate asymptotic region.

It is also worth noting that the value of dimensionless toughness (and thus the extent of the lag region) has an effect limited to the near-tip region, such that the transition between the different far-field viscosity asymptotes are not influenced by κ.

3.7.3 Effect of the fluid shear thinning index n

The shear thinning index n dictates how fast the Carreau fluid transition from the low to high shear rate viscosity. For the same value of dimensionless toughness κ, same shear thinning extent μ_∞/μ_o and transition shear stress α, a smaller shear thinning index results in a significantly smaller dimensionless fluid lag as can be seen on figure 3.10. This result is expected as the extent of the fluid lag is governed mostly by the value of the apparent viscosity near the fluid front. The apparent viscosity actually gets toward the large shear rate limit μ_∞/μ_o near the fluid front for small n (steeper shear thinning branch).

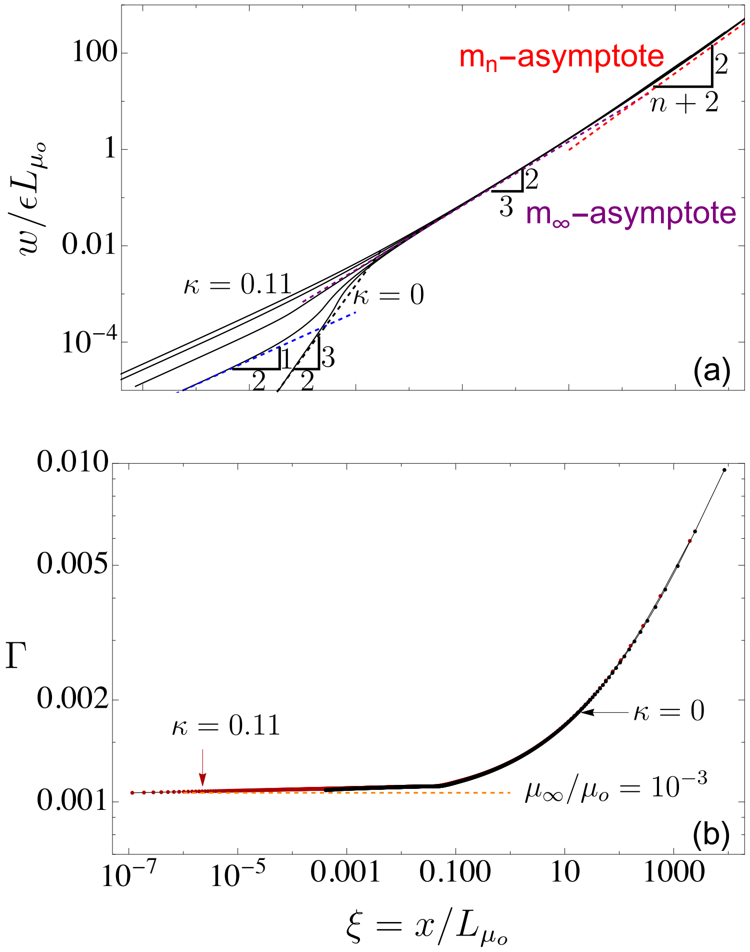

Figure 3.9 – a) Dimensionless fracture opening $w/\epsilon L_{\mu_o}$ along the fracture for $\kappa = 0$, 0.013, 0.045, 0.085, 0.11 (with corresponding lag size $\Lambda = 0.0004$, 0.00025, 5.8×10^{-5}, 2.5×10^{-6}, 8.3×10^{-8}) in log-log scale for $\alpha = 10^7$, $\mu_\infty/\mu_o = 10^{-3}$, and $n = 0.5$ (the dashed lines correspond to the asymptotic solution of opening in the toughness dominated regime (κ-asymptote), high shear rate Newtonian viscosity regime (m_∞-asymptote) and the power-law viscosity regime (m_n-asymptote)). b) Corresponding dimensionless apparent viscosity Γ starting from the fluid front $\xi = \Lambda$ for $\kappa = 0$, 0.11.

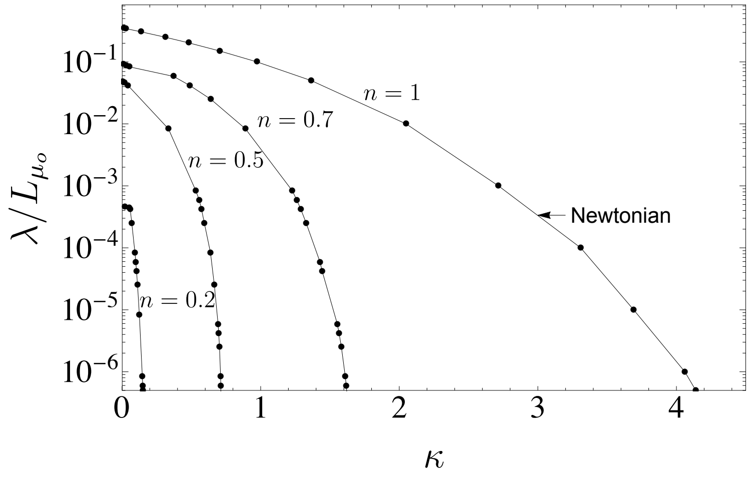

Figure 3.10 – Dimensionless lag length λ/L_{μ_o} versus the dimensionless toughness κ for different values of n, ($\mu_\infty/\mu_o = 10^{-3}$, $\alpha = 10^2$).

3.7.4 Effect of the viscosity ratio μ_∞/μ_o

The overall magnitude of the shear thinning behaviour (between low and high shear rate) is governed by the ratio μ_∞/μ_o. We have so far set this ratio to 10^{-3}, a value corresponding to a relatively large shear thinning magnitude. We now vary this ratio as well as the dimensionless toughness while keeping $\alpha = 10^3$ and $n = 0.5$. The lag size - dimensionless toughness relation for different values of μ_∞/μ_o can be seen on figure 3.11. As expected, the fluid lag is smaller for smaller μ_∞/μ_o (larger shear thinning magnitude). For $\mu_\infty/\mu_o = 1$, we obviously recover the Newtonian case.

3.7.5 Comparison between the Carreau, power-law & Ellis Models

The numerical solver previously discussed can be easily adapted to solve the same problem for a different fluid rheology. Here, we investigate the differences obtained if we use either a power-law or an Ellis model to model the fluid shear thinning behaviour instead of the more complete Carreau rheology. We refer to figure 3.1 for the difference between these models. The only difference in the solution between the different rheologies lies in the lubrication relation (equation (3.6)). As a result, the scalings for the power-law and Ellis models are slightly different than for Carreau. The details of the lubrication equations and the corresponding scalings are described in sections 3.10.2 and 3.10.3 respectively for these two rheologies. The solution for the power-law rheology can actually be re-expressed in the Carreau scaling (see section 3.10.2) using the expression of the power-law consistency parameter as function of the Carreau rheological parameters (see equation (3.1)). The solution for the Ellis model is expressed with the same low shear-rate viscosity scaling than for the Carreau rheology but the dimensionless parameter α_e related to the transition from the low shear-rate plateau to the shear thinning branch is defined differently for the Ellis model (see section 3.10.3, equation

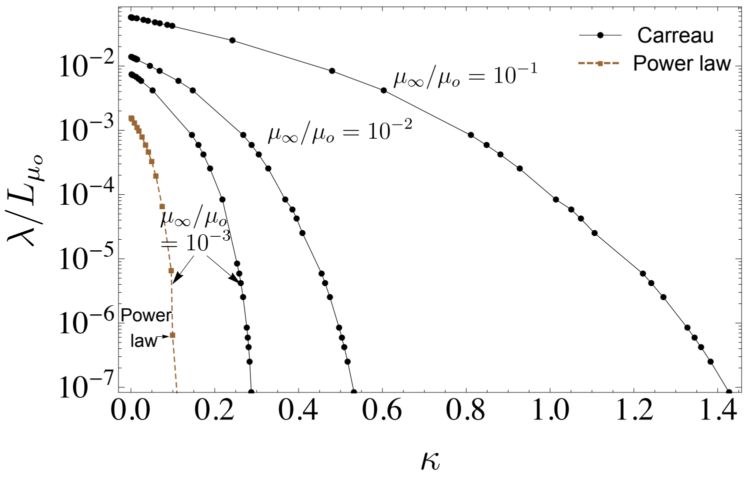

Figure 3.11 – Dimensionless lag length λ/L_{μ_o} versus the dimensionless toughness κ for a Carreau rheology with respect to μ_∞/μ_o ($\alpha = 10^3$, $n = 0.5$). The results for a power-law rheology are also displayed for $\mu_\infty/\mu_o = 10^{-3}$.

(3.33)).

In order to compare the solution obtained with these different rheological models, we set the rheological parameters of the different models to the ones reproducing the rheology of a HPG fluid (see figure 3.1, and table 3.1 for the corresponding rheological parameters of the different models). It is worth re-emphasizing that the large shear rate / low viscosity limit is absent from both the power-law and Ellis models. The power-law rheology also overestimates the viscosity for low shear rate. The deviation of the responses obtained with these two models can be grasped by comparing them with the solution obtained with the Carreau rheology.

We perform simulations for two different values of transition shear stress and dimensionless toughness: $\alpha = 7\times10^3$, $\kappa = 0.01$, and $\alpha = 10^6$, $\kappa = 0.002$ respectively. In order to set the dimensionless shear stress, we set the ratio σ_o^2/E' and thus using the rheological parameters reproducing the HPG fluid, obtain the corresponding transition shear stress for the Ellis model: $\alpha_e = 4975$ and 7.2×10^5 (for $\alpha = 7\times10^3$, and 10^6 respectively). The results of the power-law model are also dependent on both μ_∞/μ_o and α via the relation between the consistency index and the Carreau parameters. The dependence of the power-law results on μ_∞/μ_o is weak however as can be seen from the contribution of μ_∞/μ_o on the correspondence between the power-law - Carreau scaling $(1+\mu_\infty/\mu_o)^{1/n} \simeq 1$ (see equation (3.30) in section 3.10.2).

A similar structure for the fracture opening profile is observed for the Ellis and Carreau on figure 3.12 for the case $\alpha = 7\times10^3$, $\kappa = 0.01$. The toughness region is larger for the Carreau model compared to the other two models as well as the lag size (Carreau $\Lambda = 8.7\times10^{-4}$, Ellis $\Lambda = 3\times10^{-4}$, and power-law $\Lambda = 1.9\times10^{-4}$). As we move away from the tip ($\xi > 10^{-2}$), the Ellis model follows closely the Carreau solution all the way to the far field zero shear rate viscosity asymptote m_o (slope in 2/3). Similarly, the power-law model also follows closely

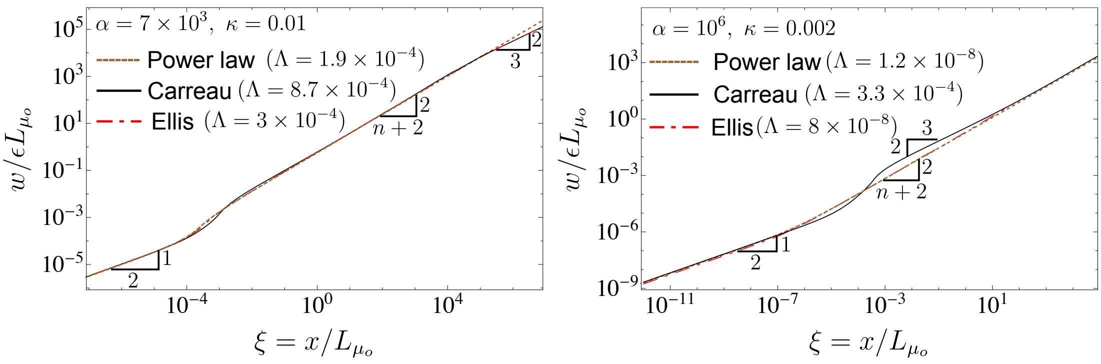

Figure 3.12 – Dimensionless fracture opening $w/\epsilon L_{\mu_o}$ along the fracture in log-log scale for Carreau (with $\mu_\infty/\mu_o = 10^{-3}$), Ellis, power-law rheology: left- $\alpha = 7 \times 10^3$ ($\alpha_e = 4975$, Ellis Model), $n = 0.46$ and $\kappa = 0.01$, right- $\alpha = 10^6$ ($\alpha_e = 7.2 \times 10^5$, Ellis Model), $n = 0.46$ and $\kappa = 0.002$.

the Carreau solution in the intermediate power-law region but starts to deviate in the far-field ($\xi > 10^5$) where the low shear rate plateau (absent from the power-law model) start to dominate. For such a value of dimensionless transition shear stress ($\alpha = 7 \times 10^3$), the tangent apparent viscosity of the Carreau model did not reach the large shear rate Newtonian plateau near the fluid front, and thus the m_∞ asymptote is not visible in the corresponding Carreau opening profiles.

On the contrary, for $\alpha = 10^6$ and $\kappa = 0.002$, the large shear rate asymptote is reached near the fluid front for the Carreau model and the m_∞ asymptote is clearly visible on the opening profile (figure 3.12 right). As a result, both the power-law and Ellis models -which do not capture the large shear rate viscosity - are significantly off from the Carreau rheology for that case. This difference observed in the transition between the near-tip toughness asymptote and the far-field shear thinning regions increases with increasing α. The value of the corresponding dimensionless lag size are respectively Carreau $\Lambda = 3.3 \times 10^{-4}$, Ellis $\Lambda = 8 \times 10^{-8}$, and power-law $\Lambda = 1.2 \times 10^{-8}$. The power-law and Ellis model actually always underestimate the value of the fluid lag for any value of dimensionless shear stress and toughness. This is due to their over-estimation of the shear thinning behavior over the complete range of shear rates.

3.8 Case of a vanishing fluid lag / large dimensionless toughness ($\Lambda \approx 0$ / $\kappa \gg 1$)

3.8.1 Scaling

The limiting case of large dimensionless toughness $\kappa \gg 1$ corresponds to a vanishing lag. As can be observed from equation (3.9), large confining stress σ_o implies large dimensionless toughness. A situation that will necessarily occur at great depth in the sub-surface ($\sigma_o > 1\ MPa$). The limit of zero lag is therefore particularly important in hydraulic fracturing

Characteristic	Carreau/Ellis	Power-law (^{n})
length ℓ	$\ell_{m_ok} = \dfrac{2^{11} K_{Ic}^6}{3^2 \pi^3 V^2 \mu_o^2 E'^4}$	$\ell_{m_nk} = \left(\left(\dfrac{\pi}{32 K_{Ic}^2} \right)^{2+n} V^{2n} E'^{2+2n} M'^2 \right)^{\frac{1}{n-2}}$
net pressure p	$p_{m_ok} = \dfrac{3\pi}{8} \dfrac{\mu_o E'^2 V}{K_{Ic}^2}$	$p_{m_nk} = \left(\left(\dfrac{\pi V}{32 K_{Ic}^2} \right)^{n} M' E'^{1+n} \right)^{\frac{-1}{n-2}}$
width w	$w_{m_ok} = \dfrac{2^7 K_{Ic}^4}{3\pi^2 V \mu_o E'^3}$	$w_{m_nk} = \left(\left(\dfrac{\pi}{32 K_{Ic}^2} \right)^{2} V^n E'^3 M' \right)^{\frac{1}{n-2}}$

Table 3.2 – Characteristic scales for the zero lag case for the three different rheology. The low shear rate viscosity Newtonian scaling is used for both the Ellis and Carreau model.

practice. Moreover, as observed previously, the effect of the fluid lag is localized near the tip region and does not readily influence the transition between the different viscosities - power-law asymptotic regions (see figure 3.7 for example). We will therefore analyze in more depth the influence of the different governing parameters on the extent of these different asymptotic regions on the zero lag case.

The zero lag assumption leads to the disappearance of the pressure boundary condition $p = \sigma_o$ and the net pressure becomes singular at the fracture tip (see Garagash and Detournay (2000); Garagash et al. (2011) for discussion on the Newtonian case). As a result, another scaling -following Garagash et al. (2011)- has to be adopted (see section 3.10.4). We can choose for example to scale the width, net pressure and distance from the tip using the scaling for the transition between the toughness and low shear rate viscosity asymptote. We therefore use a new characteristic opening w_{m_ok}, pressure p_{m_ok} and length ℓ_{m_ok} (see table 3.2) and express the solution as:

$$w = w_{m_ok}\bar{\Omega} \qquad p = p_{m_ok}\bar{\Pi} \qquad x = \ell_{m_ok}\bar{\xi} \tag{3.22}$$

where $\bar{\Omega}$, $\bar{\Pi}$ and $\bar{\xi}$ are the dimensionless width, net pressure and spatial coordinates. The lengthscale ℓ_{m_ok} characterizes the transition from the toughness dominated regime to the m_o viscosity regime. It is defined as the distance x from the tip where the toughness asymptote and the low shear rate viscosity asymptote intersect: $w \sim \ell_k^{1/2} x^{1/2} \sim \ell_{m_o}^{1/3} x^{2/3}$ (see section 3.5 for the expression of the different asymptotes). Similarly w_{m_ok} and p_{m_ok} are the corresponding characteristic pressure and width where these two asymptotes intersect.

In such a zero-lag scaling, the solution of the problem depends now on three remaining dimensionless parameters: the fluid index n, dimensionless transition shear stress and the extent of the shear thinning magnitude μ_∞/μ_o. The dimensionless transition shear stress is now defined slightly differently due to the different definition of the characteristic lengthscale and pressure for this zero lag case. We obtain (see section 3.10.4 for more details):

$$\bar{\alpha} = \left(\frac{3\pi}{8} \right)^2 \frac{\mu_o E'^3 V^2}{\dot{\gamma}_c K_{Ic}^4} \tag{3.23}$$

The value of this dimensionless transition shear stress varies significantly depending on both fluid and rock properties. It may actually span an interval as wide as $\bar{\alpha} \in [10, 10^7]$, taking values for shear thinning fluid (see table 3.1) and typical ranges of rock properties.

The general solution follows the same structure as in the non-zero lag case. In the region near the fracture tip, the fracture toughness is the dominating dissipative process and govern the fracture width. As we move away from the tip, the dissipation in the fluid takes over as the dominant mechanism. Depending on the dimensionless transition shear stress $\bar{\alpha}$, fluid index n and extent of the shear thinning μ_∞/μ_o, three different viscosity asymptotic regions can be observed: high shear rate viscosity asymptote m_∞ for large values of the wall shear stress when the low shear rate Newtonian viscosity plateau $\dot{\gamma}_c$ is small enough (large $\bar{\alpha}$), power-law viscosity asymptote m_n in an intermediate shear thinning region and the low shear rate viscosity asymptote m_o for small value of shear rate / large distance from the tip.

The extent, occurrence and transition between these asymptotic regions can be estimated based on the different limiting asymptotes (see section 3.5), by defining transition lengthscales where two given asymptotes intersect. For example, we can define $\ell_{m_\infty k}$ as the transition lengthscale between the k-asymptote to the m_∞−asymptote as the distance x from the tip where the two asymptotes are comparable: $w \sim \ell_k^{1/2} x^{1/2} \sim \ell_{m_\infty}^{1/3} x^{2/3}$ such that we obtain $x = \ell_{m_\infty k} = \ell_k^3/\ell_{m_\infty}^2$. We can also define a transition lengthscale between the toughness k and power-law m_n asymptotes, the distance x where $w \sim \ell_k^{1/2} x^{1/2} \sim \ell_{m_n}^{n/(2+n)} x^{2/(n+2)}$, i.e. $x = \ell_{m_n k} = \left(\ell_k^{2+n}/\ell_{m_n}^{2n}\right)^{\frac{1}{2-n}}$. Similarly, we can define $\ell_{m_\infty m_n}$ and $\ell_{m_o m_n}$ as the boundaries of the high shear rate-power-law viscosity and low shear rate viscosity-power-law asymptotic regions. The expressions of theses different transition lengthscales can be found in table 3.3 as function of the problem parameters as well as function of the lengthscales ℓ_k, ℓ_{m_∞}, ℓ_{m_n}, and ℓ_{m_o}.

It is important to realize that depending on the dimensionless transition shear stress $\bar{\alpha}$, shear thinning index n and extent μ_∞/μ_o, not all of the different asymptotes may be realized in the solution. For example, the high shear rate viscosity regime can only be seen if the solution transitions first from the toughness k asymptote to the m_∞ and then m_n asymptotes. In other words, if the $m_n k$ transition lengthscale is larger than the $m_\infty k$ transition lengthscale: $\ell_{m_n k} > \ell_{m_\infty k}$. This condition $\ell_{m_n k} > \ell_{m_\infty k}$ can be re-expressed as the boundary of a region in the parametric space $n - \bar{\alpha} - \mu_\infty/\mu_o$. For a given n, this region can be seen on figure 3.13, and expressed in terms of a limiting transition shear stress $\bar{\alpha}_{l_\infty}\left(\mu_\infty/\mu_o, n\right)$ ($\bar{\alpha}_{l_\infty}$ is a decreasing function of μ_∞/μ_o). For $\bar{\alpha} > \bar{\alpha}_{l_\infty}\left(\mu_\infty/\mu_o, n\right)$, the solution exhibits all the possibles asymptotes: k, m_∞, m_n and m_o as we move away from the fracture tip. This limit can be obtained from the equality $\ell_{m_n k} = \ell_{m_\infty k}$ and can actually be expressed analytically as function of n and μ_∞/μ_o :

$$\bar{\alpha}_{l_\infty} = \frac{\sqrt{2^{-2/(n-1)} - 1}}{\left(\frac{6n}{1+2n}\right)^{\frac{n}{1-n}}} \left(\frac{\left(\mu_\infty/\mu_o\right)^{2-n}}{1 + \mu_\infty/\mu_o} \right)^{1/(n-1)} \tag{3.24}$$

$\ell_{m_o k}$	$\dfrac{\ell_k^3}{\ell_{m_o}^2}$	$\dfrac{2^{11} K_{Ic}^6}{3^2 \pi^3 V^2 \mu_o^2 E'^4}$
$\ell_{m_\infty k}$	$\dfrac{\ell_k^3}{\ell_{m_\infty}^2}$	$\dfrac{2^{11} K_{Ic}^6}{3^2 \pi^3 V^2 \mu_\infty^2 E'^4}$
$\ell_{m_n k}$	$\left(\dfrac{\ell_k^{2+n}}{\ell_{m_n}^{2n}}\right)^{\frac{1}{2-n}}$	$\left(\left(\dfrac{32}{\pi}\right)^{\frac{2+n}{2}} \dfrac{K_{Ic}^{2+n}}{M' V^n E'^{1+n}}\right)^{2/(2-n)}$
$\ell_{m_\infty m_n}$	$\left(\dfrac{\ell_{m_\infty}^{2+n}}{\ell_{m_n}^{3n}}\right)^{\frac{1}{2-2n}}$	$V\left(\dfrac{(12\mu_\infty)^{2+n}}{M'^3 E'^{n-1}}\right)^{1/(2-2n)}$
$\ell_{m_o m_n}$	$\left(\dfrac{\ell_{m_o}^{2+n}}{\ell_{m_n}^{3n}}\right)^{\frac{1}{2-2n}}$	$V\left(\dfrac{(12\mu_o)^{2+n}}{M'^3 E'^{n-1}}\right)^{1/(2-2n)}$

Table 3.3 – Transition lengthscales between the different asymptotic regions expressed as function of the asymptotes characteristic scales (equation (3.13)) and directly as function of the problem parameters.

Another case worth considering is when $\ell_{m_n k} > \ell_{m_o m_n}$. This means that the distance at which the solution transition from the power-law to the low shear rate viscosity is smaller than the distance at which the solution transition from the toughness to the power-law region. In other words, because the shear-rate decreases as we move away from the tip, such a situation indicates that no power-law asymptotic region exist. The condition $\ell_{m_n k} = \ell_{m_o m_n}$ therefore defines another boundary of a region in the parametric space where the solution exhibits only two asymptotic regions: the toughness k asymptote near the tip and the low shear-rate viscosity m_o away from the tip. Similarly, for a given n, this boundary can be recasted in term of a limiting value of the dimensionless transition shear-stress $\bar{\alpha}_{l_n}\left(\mu_\infty/\mu_o, n\right)$ expressed as function of n and μ_∞/μ_o ($\bar{\alpha}_{l_n}$ increases with μ_∞/μ_o):

$$\bar{\alpha}_{l_n} = \frac{\sqrt{2^{-2/(n-1)} - 1}}{\left(\frac{6n}{1+2n}\right)^{\frac{n}{1-n}}} \left(\frac{1}{1 + \mu_\infty/\mu_o}\right)^{1/(n-1)} \tag{3.25}$$

The two limits are actually related as

$$\bar{\alpha}_{l\infty} = \bar{\alpha}_{l_n} \times \left(\frac{\mu_\infty}{\mu_o}\right)^{-\frac{2-n}{1-n}}.$$

Figure 3.13 displays these two limits for $n = 0.46$ which therefore define three regions in the parametric space. In region A ($\bar{\alpha} < \bar{\alpha}_{l_n}\left(\mu_\infty/\mu_o\right)$), only two asymptotic regions (k and m_o) are present in the solution. In region B, for $\bar{\alpha}_{l_n}(\mu_\infty/\mu_o) < \bar{\alpha} < \bar{\alpha}_{l_\infty}(\mu_\infty/\mu_o)$, three asymptotic regions k, m_n and m_o are present as we move away from the tip. Finally, $\bar{\alpha} > \bar{\alpha}_{l_\infty}(\mu_\infty/\mu_o)$ defines a third region where all the different asymptotes may be visible: k, m_∞, m_n and m_o in that order from the tip.

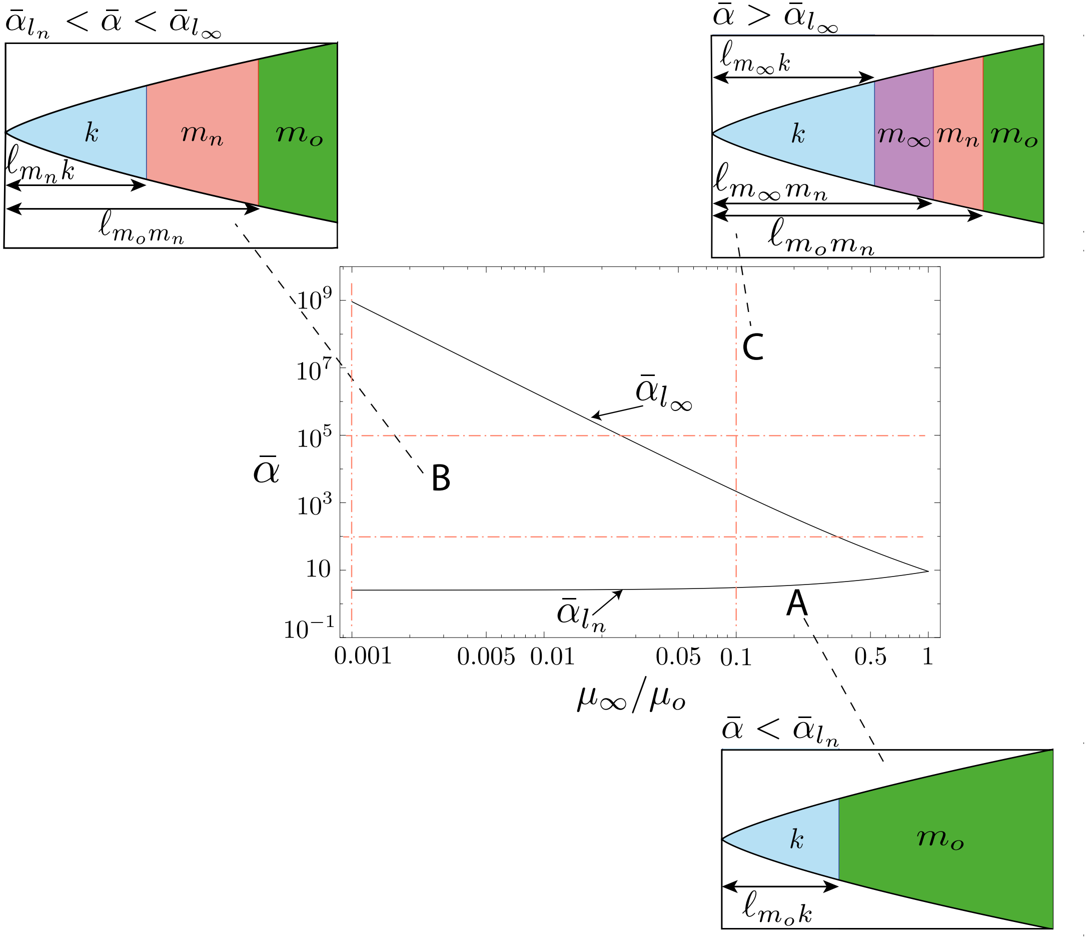

Figure 3.13 – Occurrence of the different viscous asymptotes as function of $\bar{\alpha}$ and μ_∞/μ_o for $n = 0.46$. Three distinct regions separate the parametric space: region (A) defined as $\bar{\alpha} < \bar{\alpha}_{l_n}(\mu_\infty/\mu_o, n)$ where the solution transition from k directly to m_o, region (B) defined as $\bar{\alpha}_{l_n}(\mu_\infty/\mu_o, n) < \bar{\alpha} < \bar{\alpha}_{l_\infty}(\mu_\infty/\mu_o, n)$ where three asymptotes k, m_n and m_o can be observed, and region (C) defined for $\bar{\alpha} > \bar{\alpha}_{l_\infty}(\mu_\infty/\mu_o, n)$ where up to four asymptotes k, m_∞, m_n and m_o may be observed. The dot-dashed orange lines refer to the coordinates of the numerical simulations performed in figure 3.14.

3.8.2 Evolution of the different asymptotic regions

In the previous sub-section, based on scaling considerations, we have defined three distinct regions in the parametric space, where two, three or four asymptotic regions may be observed. Here we compare a large series of numerical results (57 simulations in total) with the limits established previously. We plot as function of the scaled distance from the tip x/ℓ_{m_ok} the limits where the numerical results are within 1% of the different asymptotes as function of $\bar{\alpha}$ (for a given n and μ_∞/μ_o) or μ_∞/μ_o (for a given n and $\bar{\alpha}$). For comparison, we also plot the analytical asymptotic transitions based on the defined lenghtscales (table 3.3).

We perform 4 series of simulations corresponding to 2 vertical and 2 horizontal cross sections of the parametric space $\bar{\alpha} - \mu_\infty/\mu_o$ (see figure 3.13). All reported simulations are for $n = 0.46$ (HPG fluid index). The value of n modifies the shape of the different boundaries but do not change qualitatively the over-all picture. The results of these four series of simulations are summarized in figure 3.14.

Let us first discuss the cases where we vary $\bar{\alpha}$ in the range $\left[10^{-8}, 10^{8}\right]$ for two distinct values of the shear thinning magnitude $\mu_\infty/\mu_o = 10^{-3}$ and $\mu_\infty/\mu_o = 10^{-1}$ (top plots in figure 3.14). The overall extent of the different asymptotic regions as function of tip distance and dimensionless transition shear stress follow the structure presented previously. For small value of $\bar{\alpha}$, only the toughness (near the tip) and low shear rate viscosity m_o asymptotes are visible. Above a given value of $\bar{\alpha}$, the power-law asymptote start to be visible on our numerical results albeit in a very narrow region (for a relative asymptotic error of 1%). Finally, for large $\bar{\alpha}$ for $\mu_\infty/\mu_o = 10^{-1}$, the large shear rate viscosity m_∞ asymptote can be clearly seen on the numerical results. For these two series of simulations for $\mu_\infty/\mu_o = 10^{-3}$ and 10^{-1}, the limiting value $\bar{\alpha}_{l_n}$ under which only the toughness and low shear rate viscosity asymptotes are present is respectively $\bar{\alpha}_{l_n}\left(\mu_\infty/\mu_o = 10^{-1}\right) = 3.03$, and $\bar{\alpha}_{l_n}\left(\mu_\infty/\mu_o = 10^{-3}\right) = 2.55$. Our numerical results report a smaller value for this lower limit $\bar{\alpha}_{l_n}$: $\bar{\alpha}_{l_{n_{num}}}\left(\mu_\infty/\mu_o = 10^{-1}\right) \simeq 10^{-4}$ and $\bar{\alpha}_{l_{n_{num}}}\left(\mu_\infty/\mu_o = 10^{-3}\right) \simeq 10^{-2}$. For the small shear thinning magnitude case ($\mu_\infty/\mu_o = 10^{-1}$), the high shear rate viscosity region is visible in the figure 3.14b for value of $\bar{\alpha}$ greater than $\bar{\alpha}_{l_\infty}\left(\mu_\infty/\mu_o = 10^{-1}\right) = 2.1 \times 10^{4}$, while the numerical value at which we start to observe the m_∞ asymptote is slightly larger $\bar{\alpha}_{l_{\infty_{num}}}\left(\mu_\infty/\mu_o = 10^{-1}\right) \simeq 4.6 \times 10^{4}$. Note that for $\mu_\infty/\mu_o = 10^{-3}$, the high shear rate viscosity region is pushed out of the dimensionless transition shear stress interval investigated here, the analytical expression gives $\bar{\alpha}_{l_\infty}\left(\mu_\infty/\mu_o = 10^{-3}\right) = 9.1 \times 10^{8}$ in that case, and the m_∞ asymptote is not visible on our numerical results.

The extent of the toughness region near the fracture tip is roughly constant for small $\bar{\alpha}$, then increases with $\bar{\alpha}$ until reaching a constant value for sufficiently large $\bar{\alpha}$ (above the limit $\bar{\alpha}_{l_\infty}$) for which the m_∞ asymptote becomes visible. For small enough values of $\bar{\alpha}$ (below $\bar{\alpha}_{l_n}$), the distance at which the numerical results can be approximated by the toughness and low shear rate viscosity asymptote are respectively $x \approx 10^{-7}\ell_{m_ok}$ and $x \approx 1.3\ell_{m_ok}$ which is exactly consistent with the bounds obtained by (Garagash et al., 2011). Similarly for the case of large dimensionless transition shear stress $\bar{\alpha} > \bar{\alpha}_{l_\infty}$, the numerical boundaries demonstrate that the

m_∞ asymptote starts at $x \approx 10^1 \ell_{m_o k}$ from the fracture tip regardless the value of $\bar{\alpha}$.

Similarly we have studied the effect of the viscosity ratio in the range $[10^{-3}, 0.75]$ for two distinct dimensionless transition shear stress $\bar{\alpha} = 10^2$ and 10^5, see figures 3.14c and 3.14d. In both cases, the extent of the toughness region (scaled by $\ell_{m_o k}$) is decreasing with larger value of μ_∞/μ_o. In fact, the evolution of the toughness region tracks the evolution of $\ell_{m_n k}$ and $\ell_{m_\infty k}$ as function of $\bar{\alpha}$ and μ_∞/μ_o for all cases.

For the series of simulation with $\bar{\alpha} = 10^2$, the m_o low shear rate viscosity region has the same domain of validity regardless of the value of μ_∞/μ_o (figure 3.14c). This low shear rate region can not, however, be observed for the series of simulation with $\bar{\alpha} = 10^5$, where it is estimated to appear for distances away from the tip above $10^7 \ell_{m_o k}$. A value which is larger than the extent of our computational domain.

The high shear rate viscosity region m_∞ can be seen for values of μ_∞/μ_o larger than 0.33 ($\bar{\alpha} = 10^2$) and 0.025 ($\bar{\alpha} = 10^5$) respectively from the scaling arguments. These values are in line with the numerical results which gives respectively $(\mu_\infty/\mu_o)_{num} = 0.75$ ($\bar{\alpha} = 10^2$, where this m_∞ region can be seen for the largest value of μ_∞/μ_o only), and $(\mu_\infty/\mu_o)_{num} = 0.07$ ($\bar{\alpha} = 10^5$).

It is also worthwhile to note that for all the simulations reported on figure 3.14, the extent of the power-law region where the numerical results obtained are within 1% of the m_n asymptote is extremely limited, and significantly smaller than the predictions obtained from scaling arguments.

3.8.3 Comparison between the Carreau, power-law & Ellis Models

In this section, we compare these three models in the zero lag case and investigate how close the predictions based on Ellis and power-law models are to the complete Carreau model depending on the occurrence of the different asymptotic regions highlighted in figure 3.13. We use the zero lag scaling (equation 3.22) in all cases. The expressions of the characteristic opening, pressure and length for the power-law model (see table 3.2) are different from the Carreau model (while they are similar for the Ellis model). The scaling and dimensionless problem are detailed in section 3.10.4.

Like previously for the lag case, we fix the rheological parameters to the ones reproducing the rheology of a HPG fluid (see table 3.1 for the different models). We vary the value of the dimensionless transition shear stress $\bar{\alpha}$ (by varying $\frac{E'^3 V^2}{K_{Ic}^4}$ at fix rheological parameters), as well as the shear thinning amplitude ratio μ_∞/μ_o.

We first fix the shear thinning magnitude μ_∞/μ_o at 10^{-3}. Figures 3.15a, b, c and d exhibit the fracture opening for the three models for four different values of $\bar{\alpha}$ (small $\bar{\alpha}$ - figure 3.15a, intermediate $\bar{\alpha}$ - figure 3.15b and c, and large $\bar{\alpha}$ - figure 3.15d). As discussed in section 3.13, there are two limits that define the behaviour of solution for the Carreau model ($\bar{\alpha}_{l_n}, \bar{\alpha}_{l_\infty}$) for a

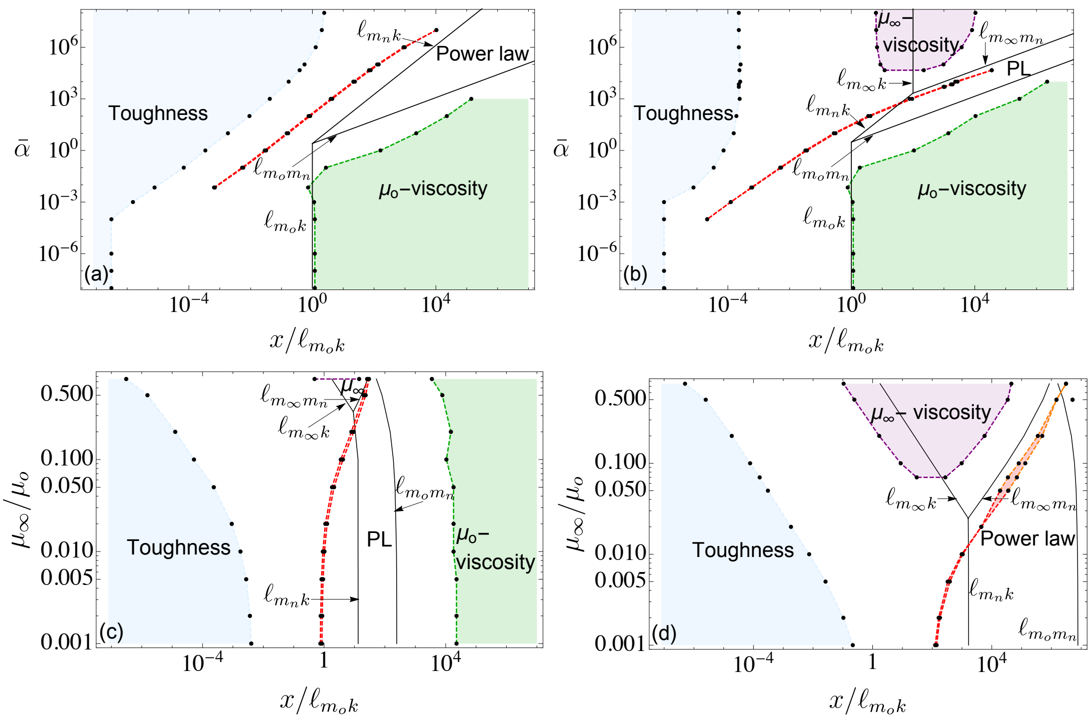

Figure 3.14 – Numerical bounds and transition lengthscales (black solid lines) between the different asymptotic regions:(a) variations of $\bar{\alpha}$ for $n = 0.46$, $\mu_\infty/\mu_o = 10^{-3}$, (b) variations of $\bar{\alpha}$ for $n = 0.46$, $\mu_\infty/\mu_o = 10^{-1}$, (c) variations of μ_∞/μ_o for $n = 0.46$, $\bar{\alpha} = 10^2$, and (d) μ_∞/μ_o for $n = 0.46$, $\bar{\alpha} = 10^5$. The regions where the numerical results fall within 1% of accuracy of an asymptote are also displayed. For the power-law region, limits where the numerical results are within 1% accuracy of the m_n asymptote are displayed in red, and in orange when within 5% of accuracy.

given viscosity ratio and power-law index. These values of the dimensionless transition shear stress can be approximated analytically using the transition lengthscales (see sub-section 3.8.1). For $\mu_\infty/\mu_o = 10^{-3}$, the high shear rate viscosity asymptote may become visible for values of $\bar{\alpha}$ larger than $\bar{\alpha}_{l_\infty} = 9.1 \times 10^8$,whereas the power-law region may appear for $\bar{\alpha}$ larger than $\bar{\alpha}_{l_n} = 2.55$.

For value of $\bar{\alpha}$ smaller than $\bar{\alpha}_{l_n}$ (see figure 3.15a), as expected the Carreau dimensionless opening transition from the toughness k asymptote near the tip to the far-field low shear viscosity asymptote without any visible power-law region. The solution for the Ellis model is matching perfectly the solution of the Carreau rheology for that case (figure 3.15a). As expected, the prediction of the power-law rheology widely differ from Carreau for this small $\bar{\alpha}$ case (due to the large effect of the low shear rate plateau). As the value of $\bar{\alpha}$ exceeds $\bar{\alpha}_{l_n}$, a power-law region appear just beyond the near-tip toughness region. For $\bar{\alpha} = 74$ (see figure 3.15b), the Ellis model still follows closely the complete Carreau rheology - pending a small deviation in the transition between the power-law and far-field region (for $x/\ell_{m_o k} \in [1-100]$). Here again, the power-law model still significantly deviates in the far-field due to the effect of the low shear rate viscosity absent from the power-law model. For larger value of $\bar{\alpha}$ (figure 3.15c), the difference between the Ellis and Carreau rheology slightly increases in the intermediate power-law m_n region where the effect of the transition from the power-law branch to the high shear rate Newtonian plateau in the Carreau rheology starts to influence the overall solution (see section 3.7.2 for details) even tough $\bar{\alpha}$ did not yet reach the bound $\bar{\alpha}_{l_\infty}$. However, the Ellis model still match exactly the Carreau solution in the near-tip toughness region and in the far-field low shear-rate m_o region. The power-law model gets closer to the predictions of the Carreau and the Ellis models except in the far-field low-shear rate m_o region ($x/\ell_{m_o k} > 10^4$) as expected.

All the results depicted in figures 3.15a, b and c are for the case of a large shear thinning amplitude ($\mu_\infty/\mu_o = 10^{-3}$). The effect of its influence can be seen in figure 3.15d for a large value of $\bar{\alpha}$ (46.2×10^3). For such a large value of $\bar{\alpha}$, the power-law region stretches out far away from the tip, actually driving the low-shear rate region outside of our numerical grid. Over those lengthscale, the Ellis and the power-law models are very close to one another. They both differ however from the Carreau rheology outside the near-tip toughness k region. Such a difference increases as the shear thinning amplitude decreases (i.e. for smaller viscosity ratio μ_∞/μ_o). The power-law region significantly decreases in the Carreau solution with increasing viscosity ratio μ_∞/μ_o. The high shear rate viscosity region m_∞ dominates the Carreau response in the intermediate field for the case $\mu_\infty/\mu_o = 10^{-1}$ for $\bar{\alpha} > \bar{\alpha}_{l_\infty}(\mu_\infty/\mu_o = 10^{-1}) = 2.1 \times 10^4$. For both cases $\mu_\infty/\mu_o = 10^{-2}$ and $\mu_\infty/\mu_o = 10^{-3}$, the high shear rate viscosity m_∞ region is still absent from the Carreau solution ($\bar{\alpha}_{l_n}(\mu_\infty/\mu_o = 10^{-2}) = 2.59 < \bar{\alpha} < \bar{\alpha}_{l_\infty}(\mu_\infty/\mu_o = 10^{-2}) = 1.3 \times 10^6$, and $\bar{\alpha} < \bar{\alpha}_{l_\infty}(\mu_\infty/\mu_o = 10^{-3}) = 9.1 \times 10^8$) but the solution is already significantly affected by the rather long transition from the power-law branch to the high shear rate viscosity intrinsic to the Carreau model.

These comparisons are in line with the structure of the solution with respect to the different

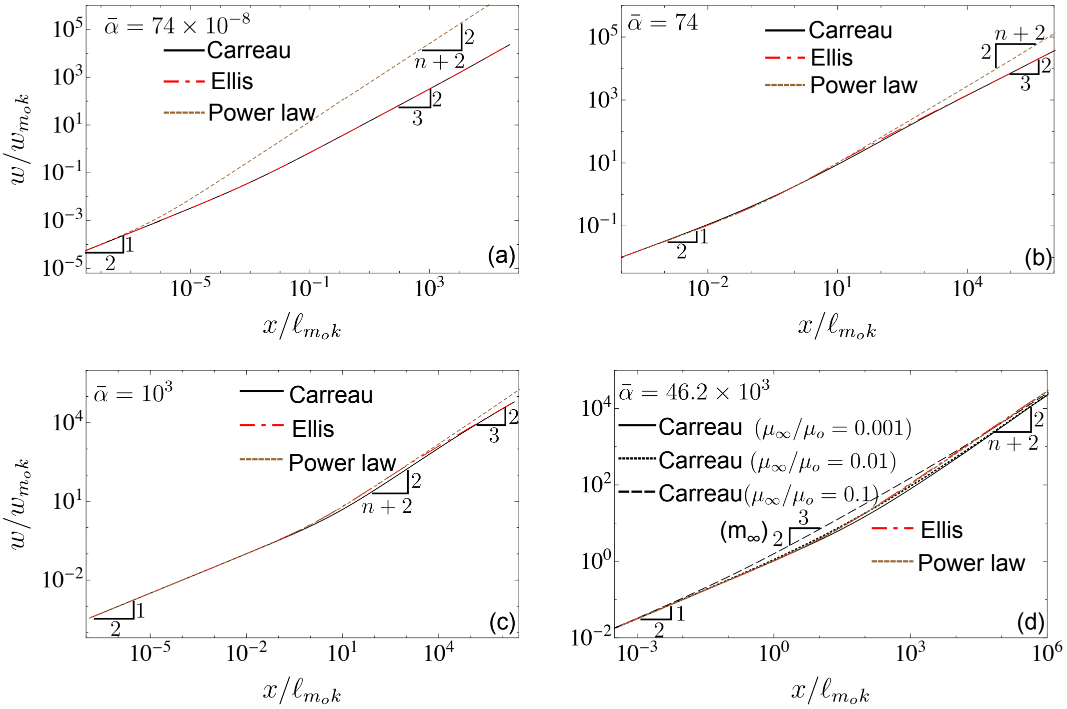

Figure 3.15 – Zero lag case. Dimensionless fracture opening $w/w_{m_o k}$ as function of the dimensionless distance from the tip $x/\ell_{m_o k}$ for the three rheologies (see table 3.2 for the expressions of the characteristic scales $w_{m_o k}$ and $\ell_{m_o k}$). The rheological parameters of the fluid are the one of a HPG. Influence of $\bar{\alpha}$ with $\mu_\infty/\mu_o = 10^{-3}$: (a) $\bar{\alpha} = 74 \times 10^{-8}$ (Ellis $\bar{\alpha}_e = 53.4 \times 10^{-8}$), (b) $\bar{\alpha} = 74$ (Ellis $\bar{\alpha}_e = 53.4$; (c) $\bar{\alpha} = 10^3$ (Ellis $\bar{\alpha}_e = 2088.7$), (d) $\bar{\alpha} = 46.2 \times 10^3$ (Ellis $\bar{\alpha}_e = 33.4 \times 10^3$) with also the solution for different μ_∞/μ_o for the Carreau model. The Ellis model starts to depart from the Carreau in the intermediate region for $\alpha \geq 10^3$ even for a large shear thinning magnitude ($\mu_\infty/\mu_o = 10^{-3}$).

limiting asymptotes depicted in the previous sub-section. We notably see that the scaling estimate of $\bar{\alpha}_{l_n}$ and $\bar{\alpha}_{l_\infty}$ provide the overall trend of the validity of the different models, with the caveat that the transition from the power-law branch to the high shear rate viscosity plateau has a significant effect on the solution even for $\bar{\alpha}$ lower than $\bar{\alpha}_{l_\infty}$. In summary, for value of $\bar{\alpha}$ sufficiently lower than $\bar{\alpha}_{l_\infty}(\mu_\infty/\mu_o, n)$, the Ellis model reproduce relatively well the results obtained with the Carreau rheology. Deviations start to occur for larger values of the dimensionless shear stress $\bar{\alpha}$. The power-law model reproduce poorly the results of the complete Carreau solution in the far-field region in all cases. It may only provide an acceptable approximation up to a distance $x/\ell_{m_o k} \approx 10$ from the tip for intermediate values of $\bar{\alpha}$ in between the limits $\bar{\alpha}_{l_n}(\mu_\infty/\mu_o, n)$ and $\bar{\alpha}_{l_\infty}(\mu_\infty/\mu_o, n)$. This intermediate region between $\bar{\alpha}_{l_n}(\mu_\infty/\mu_o, n)$ and $\bar{\alpha}_{l_\infty}(\mu_\infty/\mu_o, n)$ drastically shrinks for increasing μ_∞/μ_o ratio (i.e. decreasing shear thinning amplitude).

3.9 Conclusions

The use of shear thinning fluid is ubiquitous in hydraulic fracturing applications. By focusing on the near-tip behaviour, we have clarified the impact of the details of the fluid rheological behaviour on the complex coupling between lubrication flow and linear elastic fracture mechanics. Depending on the problem parameters, three scenarios are possible. First (region A in figure 3.13), for small values of dimensionless transition shear stress case: the solution for the Carreau rheology reduces to the Newtonian model with a viscosity given by the low shear rate value. Secondly (region B in figure 3.13) for the case characterised by intermediate values of the dimensionless transition shear stress and large shear thinning amplitude, the solution exhibits three distinct asymptotic regions (and transitions in between) as we move away from the tip: toughness, shear thinning/power-law and a far-field low shear rate viscosity region. Finally for large dimensionless transition shear stress, the solution depends on all the details of the Carreau rheology with up to four different asymptotic regions: toughness, high shear rate viscosity, shear thinning/ power-law and low shear rate viscosity (region C in figure 3.13). The fluid lag always fall within the toughness dominated region near the fracture tip.

For small dimensionless toughness κ, the extent of the fluid lag is drastically impacted by the shear thinning behaviour, with smaller lag for stronger shear thinning fluid. The approximations of the complete rheology by simpler shear thinning models (Ellis, power-law) always under-predict the actual fluid lag size compared to the Carreau model, whereas it is over estimated using a Newtonian model with the low-shear rate viscosity. In order to grasp some order of magnitude, let us compare the dimensional extent of the fluid lag for both a HPG fluid (see table 3.1) and a Newtonian fluid with a viscosity equal to the low shear rate viscosity of the HPG fluid. First, if we take values akin to a laboratory experiment performed in PMMA under a small confinement ($\sigma_o = 0.1$ MPa), and an average value of the propagation velocity realistic for a laboratory experiment ($V = 0.002$ m/s), we obtain a dimensionless toughness $\kappa = 3.24$ (see table 3.4 for the values of the different parameters used). The corresponding estimate of the fluid lag $\lambda = \Lambda L_{\mu_o}$ of 0.0011 cm for the Carreau fluid while for the low shear rate Newtonian fluid we obtain $\lambda = \Lambda L_{\mu_o} \approx 1.63\ cm$, i.e. a extend of the lag three order of magnitude larger for the Newtonian fluid compared to the shear thinning one. Similarly, for a hydraulic fracture propagating under significant confinement ($\sigma_o = 20$ MPa) in a sandstone at an average velocity of 0.5 m/s (see table 3.4 for the corresponding parameters), we obtain a dimensionless toughness $\kappa = 0.527$. The corresponding lag size for a HPG fluid is essentially zero ($\lambda < 10^{-7}$ cm - see figure 3.8 for $\alpha = 10^4$) whereas for a Newtonian fluid (low shear rate viscosity equivalent) the corresponding lag would be of 2.5 cm (see figure 3.10 for $\Lambda(\kappa)$ in that case).

The limiting case of a large dimensionless toughness / vanishing lag is especially relevant in industry practice as it corresponds to the case of a fracture propagating at depth under a sufficient level of confining stress. In that limit, the structure of the solution for a given fluid index and extent of the shear thinning magnitude μ_∞/μ_o can be readily grasped by computing for large κ the dimensionless shear stress $\bar{\alpha}$ defined in equation (3.23). Depending on the value of $\bar{\alpha}$ with respect to the limits $\bar{\alpha}_{l_n}(\mu_\infty/\mu_o, n)$ and $\bar{\alpha}_{l_\infty}(\mu_\infty/\mu_o, n)$, the solution as we move away from the tip consist of two (region A), three (region B) or four (region C) asymptotic regions. An order of magnitude of these different regions can also be readily grasped by computing the different transition lengthscales listed in table 3.3. Furthermore, the computation of these limits $\bar{\alpha}_{l_n}(\mu_\infty/\mu_o, n)$ and $\bar{\alpha}_{l_\infty}(\mu_\infty/\mu_o, n)$ can help in deciding if one of the alternative rheological models (power-law, Ellis and Newtonian) can provide similar results if the complete Carreau model is required. Notably, we have seen that the domain where simpler models (power-law, Ellis) approximate sufficiently well the Carreau solution can also be directly grasped by estimating the relative ordering of $\bar{\alpha}$, $\bar{\alpha}_{l_n}(\mu_\infty/\mu_o, n)$ and $\bar{\alpha}_{l_\infty}(\mu_\infty/\mu_o, n)$. The Ellis model is a good approximation for values of $\bar{\alpha}$ sufficiently lower than $\bar{\alpha}_{l_\infty}(\mu_\infty/\mu_o, n)$. The power-law model has a narrow domain of validity: it is a good approximation of the complete solution only up to a distance $x/\ell_{m_o k} \approx 10$ from the tip and this only for intermediate values of $\bar{\alpha}$, above $\bar{\alpha}_{l_n}(\mu_\infty/\mu_o, n)$ but still sufficiently lower than $\bar{\alpha}_{l_\infty}(\mu_\infty/\mu_o, n)$. As an example of illustration, let us consider a hydraulic fracture driven by a HPG-like fluid (see table 3.1) in a rock with stiffness $E' = 30$ GPa and fracture toughness of $K_{Ic} = 1$ MPa$\sqrt{\text{m}}$ propagating at a velocity $V = 1$ m/s resulting in a dimensionless shear stress $\bar{\alpha} = 50 \times 10^3$. For a HPG fluid with a shear thinning extent $\mu_\infty/\mu_o = 10^{-3}$, this case falls within region B ($\bar{\alpha}_{l_n}\left(\mu_\infty/\mu_o\right) < \bar{\alpha} < \bar{\alpha}_{l_\infty}\left(\mu_\infty/\mu_o\right)$) where the Ellis model (and to a lesser extent the power-law model) can properly reproduce the tip behavior especially because the transition lengthscale $\ell_{m_o m_n}$ is extremely large ($\ell_{m_o m_n} \approx 12.8 \times 10^3$ meters) and thus unlikely to be probed in finite hydraulic fractures in the field. In the case where the shear thinning magnitude is smaller - e.g. for $\mu_\infty/\mu_o = 10^{-1}$, the dimensionless shear stress is larger than $\bar{\alpha}_{l_\infty}$ ($\bar{\alpha} = 50 \times 10^3 > \bar{\alpha}_{l_\infty}(\mu_\infty/\mu_o = 10^{-1}) = 2.1 \times 10^4$) and the solution structure is akin to the one of region C (see figure 3.13): the large shear rate range of the Carreau rheology affect the tip structure (with values for the transition lengthscales $\ell_{m_\infty k} = 0.5$ meters, $\ell_{m_\infty m_n} \approx 40$ meters respectively). This example illustrates how we can easily estimate which asymptotic region may appear at the scale of the finite fracture for a given set of problem parameters from the transition lengthscales defined in table 3.3 and the expression of the critical dimensionless shear stress (equations (3.24) and (3.25)) defining the boundaries between regions A and B, and B and C.

The shear thinning tip solution presented here could eventually be used in numerical scheme for the propagation of finite hydraulic fracture (see Peirce and Detournay (2008); Detournay and Peirce (2014); Peirce (2015) for discussion for a Newtonian fluid). However, in order to be used efficiently in a finite hydraulic fracture simulator, this tip solution needs to be computed extremely fast (as it needs to be inverted), and thus approximated analytically or semi-analytically (see Dontsov and Peirce (2015, 2017) for the Newtonian case). Such an approximation for a Carreau fluid (for which the lubrication relation is not analytical) is far from obvious and would require significant developments.

Besides the importance of shear thinning fluid in hydraulic fracturing industrial practice, it is also interesting to note that the propagation of magmatic dykes toward the earth's surface (see e.g. Spence and Turcotte (1985); Lister (1990)) may also be affected by the shear thinning behaviour of some magmas (Caricchi et al., 2007).

Material	Fluid	K_{Ic}	E'	σ_o	V	α	κ	L_{μ_o}	ϵ
		$MPa.\sqrt{m}$	GPa	MPa	m/s	–	–	m	–
PMMA	HPG	1.3	3.93	0.1	0.002	1.75	3.24	163.09	2.5×10^{-5}
Bebertal sandstone	HPG	1.2	20	20	0.5	1.37×10^4	0.527	0.132	0.001

Table 3.4 – Values of the dimensionless parameters for example hydraulic fracturing fluids and materials for propagating velocity V. PMMA data from Bunger and Detournay (2008) and Bebertal sandstone data from Stoeckhert et al. (2015).

3.10 Supplemental material

3.10.1 Poiseuille flow for a Carreau fluid

The solution for the uni-dimensional pressure-driven flow of a Carreau fluid between parallel plate can be solved semi-analytically (Sochi, 2015). The dimensionless apparent viscosity $\Gamma\left(\frac{\Omega}{2}\left|\frac{\partial\Pi}{\partial\xi}\right|, \alpha, n, \mu_\infty/\mu_o\right)$ is obtained from the dimensionless shear stress at the wall $\tilde{\tau}_w$ as

$$\Gamma\left(\frac{\Omega}{2}\left|\frac{\partial\Pi}{\partial\xi}\right|, \alpha, n, \mu_\infty/\mu_o\right) = \frac{\tilde{\tau}_w^3}{3I(n, \dot{\tilde{\gamma}}_w, \alpha, \mu_\infty/\mu_o)} \tag{3.26}$$

where $I(n, \dot{\tilde{\gamma}}_w, \alpha, \mu_\infty/\mu_o)$ is an analytical function derived by Sochi (2015) which depends on the rheological parameters (n, μ_∞/μ_o, α) and the dimensionless wall shear rate $\dot{\tilde{\gamma}}_w$:

$$\begin{aligned} I(n, \dot{\tilde{\gamma}}_w, \alpha, \mu_\infty/\mu_o) = {} & n'\delta^2\alpha^{-2}\dot{\tilde{\gamma}}_w \left[{}_2F_1\left(\frac{1}{2}, 1-n'; \frac{3}{2}; -\left(\alpha\dot{\tilde{\gamma}}_w\right)^2\right) - {}_2F_1\left(\frac{1}{2}, -n'; \frac{3}{2}; -\left(\alpha\dot{\tilde{\gamma}}_w\right)^2\right)\right] + \\ & n'\delta\alpha^{-2}(\mu_\infty/\mu_o)\dot{\tilde{\gamma}}_w \left[{}_2F_1\left(\frac{1}{2}, 1-\frac{n'}{2}; \frac{3}{2}; -\left(\alpha\dot{\tilde{\gamma}}_w\right)^2\right) - {}_2F_1\left(\frac{1}{2}, -\frac{n'}{2}; \frac{3}{2}; -\left(\alpha\dot{\tilde{\gamma}}_w\right)^2\right)\right] + \frac{(\mu_\infty/\mu_o)^2\dot{\tilde{\gamma}}_w^3}{3} \\ & + \frac{(1+n')\delta^2\dot{\tilde{\gamma}}_w^3 {}_2F_1\left(\frac{3}{2}, -n'; \frac{5}{2}; -\left(\alpha\dot{\tilde{\gamma}}_w\right)^2\right)}{3} + \frac{(2+n')(\mu_\infty/\mu_o)\delta\dot{\tilde{\gamma}}_w^3 {}_2F_1\left(\frac{3}{2}, -\frac{n'}{2}; \frac{5}{2}; -\left(\alpha\dot{\tilde{\gamma}}_w\right)^2\right)}{3} \end{aligned}$$

where $n' = n - 1$, $\delta = 1 - \mu_\infty/\mu_o$, and ${}_2F_1$ is the hypergeometric function with real variables. The dimensionless shear rate at the wall $\dot{\tilde{\gamma}}_w$ is related to the dimensionless wall shear stress $\tilde{\tau}_w$ via the Carreau rheological equation:

$$\tilde{\tau}_w = \frac{\Omega}{2}\left|\frac{\partial\Pi}{\partial\xi}\right| = [\mu_\infty/\mu_o + \delta(1 + (\alpha\dot{\tilde{\gamma}}_w)^2)^{n'/2}]\dot{\tilde{\gamma}}_w, \tag{3.27}$$

In the scaling of section (3.4), the characteristic shear stress and shear rate are given by

$$\tau_* = \epsilon\sigma_o = \alpha\mu_o\dot{\gamma}_c, \qquad \dot{\gamma}_* = \alpha\dot{\gamma}_c$$

where α is defined by equation (3.12).

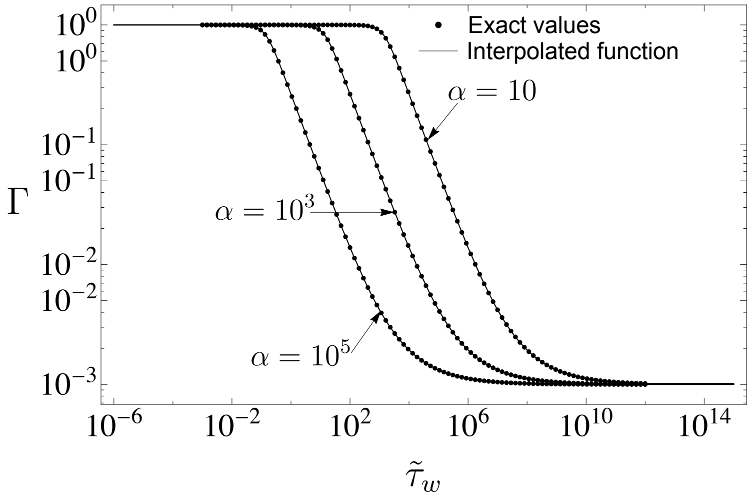

Figure 3.16 – Exact and interpolated values of the dimensionless tangent viscosity in log-log scale with respect to the wall shear stress for different values of α and: $n = 0.46$, $\mu_\infty/\mu_o = 10^{-3}$.

For a given value of dimensionless shear stress at the wall $\tilde{\tau}_w = \dfrac{\Omega}{2}\left|\dfrac{\partial \Pi}{\partial \xi}\right|$, the equation (3.27) can be solved for the corresponding dimensionless wall shear rate $\dot{\tilde{\gamma}}_w$ using quasi-Newton root-finding scheme. We are thus able to get the correspondent apparent viscosity $\Gamma\left(\tilde{\tau}_w, \alpha, n, \mu_\infty/\mu_o\right)$ from equation (3.26). In order to speed up our computation, for a given set of dimensionless rheological parameters (n, μ_∞/μ_o, α), we tabulate the evolution of this dimensionless apparent viscosity Γ as function of the dimensionless wall-shear stress. We then built an interpolation using Mathematica built-in spline routine and use it to solve the semi-infinite hydraulic fracture problem. The tabulated data and the created interpolated function can be seen on figure 3.16 for a given set of dimensionless rheological parameters.

3.10.2 Power-law model

The governing equations for a semi-infinite fracture driven by a power-law fluid propagating at constant velocity V involve the elasticity equation (3.4), the near-tip asymptotic solution (3.3), the boundary condition (3.5) and the flow equation for a power-law fluid. According to lubrication theory, the equation governing the flow of power-law fluid within the fracture is given by Bird et al. (1987)

$$V^n = \frac{w^{n+1}}{M'}\frac{\partial p_f}{\partial x}, \qquad x \in]\lambda, \infty[\tag{3.28}$$

with $M' = \dfrac{2^{n+1}(2n+1)^n}{n^n} M$, and M is defined in equation (3.1).

Following section 3.4, we scale the fracture opening Ω_n, the net pressure Π_n and the moving coordinate ξ_n by the characteristic opening ϵL_n, the far field stress σ_o and the lengthscale L_n

respectively, where

$$L_n = V\left(\frac{M'}{\sigma_o}\right)^{1/n}\left(\frac{E'}{\sigma_o}\right)^{\frac{n+1}{n}}, \qquad \epsilon = \frac{\sigma_o}{E'}$$

The dimensionless equations to be solved are : the elasticity equation (3.7), the propagation condition (3.8), the boundary condition (3.10) and the following dimensionless lubrication equation for the power-law fluid:

$$\Omega_n^{n+1}\frac{\partial \Pi_n}{\partial \xi_n} = 1, \qquad \xi_n \in]\Lambda, \infty[\tag{3.29}$$

The numerical results includes the fracture opening Ω_n, fluid pressure Π_n profiles over the whole fracture as well as the corresponding value of the dimensionless lag Λ_n which depend only on the fluid index n and the dimensionless toughness κ_n:

$$\kappa_n = \sqrt{\frac{32}{\pi}}\frac{1}{V^{1/2}}\left(\frac{\sigma_o^{2-n}}{M'E'^{3n+1}}\right)^{1/2n} K_{Ic}$$

The transition from power-law scaling to the low shear rate viscosity scaling is established via the given length ratio

$$\frac{L_n}{L_{\mu_o}} = \left(\frac{2n+1}{6n}\right)\alpha^{(n-1)/n}\left(\frac{\mu_i/\mu_o + 1}{\left(\sqrt{2^{-2/(n-1)}} - 1\right)^{n-1}}\right)^{1/n} \tag{3.30}$$

such that the dimensionless opening (the dimensionlesss fluid lag and the moving coordinate) in Carreau scaling is calculated as:

$$\Omega = \frac{L_n}{L_{\mu_o}}\Omega_n.$$

The dimensionless toughness in the low shear rate viscosity scaling, can be finally obtained as:

$$\kappa = \sqrt{\frac{L_n}{L_{\mu_o}}}\kappa_n$$

3.10.3 Ellis model

The lubrication flow of an Ellis fluid in a channel has been investigated by Myers (2005) analytically (see also Matsuhisa and Bird (1965)). The flow is subject to no-slip at the top and bottom surfaces. The driving force is the pressure gradient. The fluid pressure is linked to the fracture opening using the following non linear equation:

$$V = -\frac{1}{\mu_o}\frac{\partial p_f}{\partial x}\left[\frac{w^2}{12} + \left(-\frac{1}{\beta}\frac{\partial p_f}{\partial x}\right)^{m-1}\frac{w^{m+1}}{2^{m+1}(m+2)}\right] \tag{3.31}$$

with m is the Ellis index, and β is a characteristic shear stress.

In the low shear rate viscosity scaling, the dimensionless form of this equation is given by

$$-\frac{\partial \Pi}{\partial \xi}\left[\Omega^2+\frac{12}{2^{m+1}(m+2)}\left(-\alpha_e\frac{\partial \Pi}{\partial \xi}\right)^{m-1}\Omega^{m+1}\right]=-1, \tag{3.32}$$

with:

$$\alpha_e=\frac{\sigma_o^2}{\beta E'}; \tag{3.33}$$

where :

$$w=\epsilon L_{\mu_o}\Omega \qquad p=\sigma_o\Pi \qquad \lambda=L_{\mu_o}\Lambda$$

L_{μ_o} and ϵ have the same definitions than the ones introduced in section 3.4 for a Carreau fluid.

3.10.4 Scaling for the zero lag / large κ case

Making use of the elasticity equation (3.4), the lubrication equation on the entire length of the fracture (equations (3.6), (3.28), or (3.31) for $\lambda = 0$), and the propagation condition (equation (3.3)), we find the corresponding expression for the characteristic scales (see table 3.2 for the Carreau/ Ellis model (same expression based on the low shear rate viscosity) and the power-law rheology).

The resulting dimensionless system of equations are: the elasticity equation (equation (3.7)), the fluid flow (equations (3.11) for the Carreau model, (3.29) for power-law, or (3.32) for an Ellis model) and the propagation condition (equation (3.34)). These equations are solved for the new unknowns ($\bar{\Omega}$, $\bar{\Pi}$) using a scheme similar to the non-zero lag case. The only difference

$$\bar{\Omega}=\sqrt{\bar{\xi}} \text{ for } \bar{\xi}\to 0 \tag{3.34}$$

The new dimensionless viscosity for the Carreau rheology $\bar{\Gamma}\left(\frac{\bar{\Omega}}{2}\left|\frac{\partial\bar{\Pi}}{\partial\bar{\xi}}\right|,\ n,\ \mu_\infty/\mu_o,\ \bar{\alpha}\right)$ depends on four parameters: the shear stress $\frac{\bar{\Omega}}{2}\left|\frac{\partial\bar{\Pi}}{\partial\bar{\xi}}\right|$, the fluid index n, the viscosity ratio μ_∞/μ_o, and the dimensionless transition shear stress $\bar{\alpha}$ characterizing the transitional shear stress from Newtonian plateau to the shear thinning behaviour. Due to the change of scales, the dimensionless transition shear stress ratio has now the following expression for the Carreau model:

$$\bar{\alpha}=\left(\frac{3\pi}{8}\right)^2\frac{\mu_o E'^3V^2}{\dot{\gamma}_c K_{Ic}^4} \tag{3.35}$$

In the case of the Ellis model, the dimensionless apparent viscosity depends on a different dimensionless transition shear rate (see equation (3.32)) which we defined for the zero lag case as:

$$\bar{\alpha}_e=\frac{9\pi^2}{2^6}\frac{E'^3\mu_o^2V^2}{\beta K_{Ic}^4}. \tag{3.36}$$

It is worthwhile to note that we can switch from the power-law scaling to the low shear rate viscosity scaling for the three dimensionless parameters ($\bar{\xi}$, $\bar{\Omega}$, and $\bar{\Pi}$) via the following relations:

$$\frac{\ell_{m_n k}}{\ell_{m_o k}} = \left(\left(\frac{2n+1}{6n} \right)^n \frac{\mu_\infty / \mu_o + 1}{\left(\sqrt{2^{-2/(n-1)} - 1} \right)^{n-1}} \right)^{2/(n-2)} \bar{\alpha}^{\frac{2(n-1)}{n-2}}$$

$$\frac{w_{m_n k}}{w_{m_o k}} = \sqrt{\frac{\ell_{m_n k}}{\ell_{m_o k}}}$$

$$\frac{p_{m_n k}}{p_{m_o k}} = \sqrt{\frac{\ell_{m_o k}}{\ell_{m_n k}}}.$$

where the superscript n denotes the characteristic scale for the power-law scaling listed in table 3.2.

4 Planar hydraulic fracture growth in transversely isotropic materials perpendicular to the isotropy plane

This chapter is a modified version of a scientific article currently accepted in Journal of the Mechanics and Physics and Solids (JMPS):

F-E. Moukhtari, B. Lecampion, H. Zia "Planar hydraulic fracture growth in transversely isotropic materials perpendicular to the isotropy plane", 2020.

Contributions:

F-E. Moukhtari has formulated the problem, performed the scaling analysis and implement numerically the constitutive equations of the problem. F-E. Moukhtari and Lecampion developed the analytical solution of the elliptical hydraulic fracture growth in toughness regime. F-E. Moukhtari solved the near-tip hydraulic fracture asymptotes for transverse isotropic (TI) case. H. Zia have developed the open source code PyFrac using ILSA scheme (Implicit level set) for the isotropic case and helped in implementing the governing equations for the TI case. F-E. Moukhtari and B. Lecampion have written the manuscript. B. Lecampion have guided the discussion of the numerical results.

4.1 Abstract

The configuration of a hydraulic fracture (HF) propagating perpendicular to the isotropy plane of a transversely isotropic (TI) material is encountered in most sedimentary basins. We account for both elastic and fracture toughness anisotropy, and investigate fracture growth driven by the injection of a Newtonian fluid at a constant rate from a point source. In addition to the usual dimensionless parameters governing HF growth in isotropy, four dimensionless elastic parameters enter the problem for a TI material: the ratio β of elastic plane-strain modulus in the two orthogonal directions of the material frame, two Thomsen parameters ϵ, δ and the stiffness ratio C_{13}/C_{11}. Moreover, the ratio κ of fracture toughness in the two orthogonal directions as well as the details of the toughness anisotropy also plays a role on the development of the fracture geometry. We quantify HF growth numerically without any a-priori assumptions on the fracture shape. In doing so, we derive the exact expression for the near-tip elastic modulus as a function of propagation direction and extend to TI an implicit level set algorithm coupling a finite discretization with the near-tip solution for a steadily moving HF. A solution for a toughness dominated elliptical HF in a TI material is derived and used to verify our numerical solver. Importantly, the fracture shape is strictly elliptical only for a very peculiar form of toughness anisotropy. The evolution of the HF from the viscosity dominated regime (early time) to the toughness dominated regime (late time) results in an increase of the fracture elongation. The elongation of the fracture in the viscosity dominated regime scales as $0.76\beta^{-1/3}$ and increases as the propagation transition to the toughness dominated regime. We confirm the expressions for the transition time-scales in the two orthogonal directions of the material frame obtained from scaling considerations. The exact form of the toughness anisotropy plays a crucial role on the final fracture elongation in the toughness regime, which scales as β^{-2} for the case of an isotropic toughness, β^{-1} for an isotropic fracture energy and as $(\kappa/\beta)^2$ for the peculiar case of an 'elliptical' fracture anisotropy. Our results also indicate that i) simplified approximations for the near-tip modulus previously derived are only valid for weak anisotropy ($\beta < 1.2$) and that ii) the other elastic parameters have a second order effect on HF growth (at most 10 percent).

4.2 Introduction

Transverse isotropy (TI) is an ubiquitous feature of sedimentary rocks. It is a direct result of the sedimentation process and occurs over a wide range of scales. In particular, shales and mudstones are the results of fine layers deposit of micro-meters to centimeters thickness whose constituents may also be intrinsically anisotropic (Bobko and Ulm, 2008; Sone and Zoback, 2013). Placing ourselves at the continuum level, we model these rocks as transversely isotropic and study in details the growth of a planar three-dimensional fluid-driven fracture perpendicular to the isotropy plane. Such a configuration notably corresponds to the case where the intrinsic rock layering is horizontal and the fracture grows vertically (see figure 4.1). This is notably the case in a large number of sedimentary basins which exhibit a normal or a strike-slip in-situ stress regime where the minimum principal stress direction is horizontal.

Minimizing energy spent, the fracture thus grows in the vertical plane perpendicular to the material isotropy plane (Hubbert and Willis, 1957). In the presence of weak bedding planes (isotropy plane), the fracture may possibly deviates from the vertical direction resulting in T-shape like geometies, or exhibit several jogs/horizontal offset (Bunger, 2017). We do not account for this possibility here and strictly restrict our investigation to cases where the fracture grows in a single plane perpendicular to the material isotropy plane. This corresponds to the limit of either i) very strong isotropy / bedding planes or ii) very large in-situ compressive stress normal to the isotropy / bedding plane (i.e. $\sigma_v \gg \sigma_h$ in the configuration of figure 4.1). In that limit, how a fluid driven fracture originating from a point source develops as function of the material anisotropy and injection parameters (fluid viscosity, injection rate) remains only partly understood. One of the main questions relates to the elongation of the fracture in the horizontal direction when transverse elastic isotropy is accounted for (Zia et al., 2018). Laubie and Ulm (2014) have investigated the problem of a strictly elliptical fracture in the so-called toughness dominated regime where dissipation associated with viscous fluid flow in the fracture is negligible. Using a simplified approach based on Hoenig (1978) solution for an elliptical crack, they have notably obtained a relationship between the aspect ratio of the equilibrium fracture and the ratio of the plane-strain elastic modulus in the 1 and 3 directions. Followed by Bessmertnykh and Dontsov (2018), the fracture elongation was also approximated in the case of a fracture driven by Herschel-Bulkley fluid in both viscosity and toughness regimes. Assuming the same ideal elliptical fracture geometry, scaling laws and approximated growth solutions were recently obtained (Dontsov, 2019).

In this contribution, we investigate the problem numerically in combination with a scaling analysis. We do not impose any a-priori constraint on the fracture shape and do not make any simplifications in our handling of elastic transverse isotropy. This will notably allow to quantify some of the approximations previously put forward (Laubie and Ulm, 2014; Bessmertnykh and Dontsov, 2018). We extend a fully-coupled implicit level set algorithm for hydraulic fracture growth (Peirce and Detournay, 2008) to account for material transverse isotropy both in terms of elasticity and possibly fracture energy. We restrict to the case of low permeability materials and neglect fluid leak-off in the surrounding rock for clarity. Following the classical hydraulic fracture mechanics model, we account for viscous fluid flow in the fracture coupled to mechanical deformation and a linear elastic fracture mechanics criteria for quasi-static growth. One of the peculiarity of hydraulic fractures lie in the competition between the energy dissipation associated with viscous flow and the one associated with the creation of new fracture surfaces. This competition is well understood for an isotropic material and results in very different propagation regimes: either viscosity or toughness dominated (Detournay, 2004, 2016). Moreover, this competition between viscosity and toughness dissipation results in a multi-scale structure of the near-tip region (Garagash et al., 2011) which is extremely difficult to resolve accurately using naive discretization techniques (Lecampion et al., 2013, 2018). Such a near-tip solution for a steadily moving hydraulic fracture can be combined with a finite scale discretization of the fracture, yielding very efficient numerical schemes (Peirce, 2015, 2016).

In the following, we first briefly recall the ingredients of the planar hydraulic fracture (HF) model highlighting the differences brought by transverse isotropy (TI). We then obtain an exact expression for the near-tip elastic operator as a function of propagation direction in a TI material. More precisely, we obtain the near-tip plane-strain elastic modulus entering the so-called Irwin matrix relating co-planar energy release rate and stress intensity factors (Barnett and Asaro, 1972). This enables the extension of the near-tip fluid-driven asymptotic solution to transverse isotropy (TI), and its use in a fully coupled numerical scheme as a result. We also obtain an exact analytical solution for an elliptical hydraulic fracture propagating in the toughness dominated regime. This notably allows to benchmark our simulator for a peculiar case of toughness anisotropy (leading to an elliptical fracture shape). Combining a scaling analysis and numerical simulations, we quantify the growth of a hydraulic fracture in both toughness dominated and viscosity dominated growth in a TI elastic medium under different assumptions on the anisotropy of fracture toughness (isotropic toughness versus isotropic fracture energy vs elliptical toughness anisotropy). We finally explore numerically the transition between the viscosity and toughness dominated regimes and confirm the expressions based on scaling arguments of the transition time-scales in the two different directions.

4.3 Problem formulation

We focus our study on the case of a hydraulic fracture growing in a plane perpendicular to both the direction of the minimum horizontal in-situ stress σ_h and the material isotropy plane (see figure 4.1). We re-use the same notation as in chapter 2: $(\boldsymbol{e_1}, \boldsymbol{e_2}, \boldsymbol{e_3})$ is the material canonical orthonormal basis where $(\boldsymbol{e_1}, \boldsymbol{e_2})$ defines the plane of material isotropy and $\boldsymbol{e_3}$ is the axis of rotational symmetry.

Predictions of HF growth requires to couple linear elastic fracture mechanics with lubrication flow inside the fracture (Detournay, 2016). The solution of such a moving boundary problem consists in the time-evolution of the fracture contour, fracture width and fluid pressure inside the fracture. Numerical modeling of this calls of hydro-mechanical problem is particularly challenging even in the isotropic case - see Lecampion et al. (2018) for a review on recent developments. In the following, we extend the classical hydraulic fracture model to the case of transverse isotropy.

4.3.1 Elastic deformation

In the section 2.2.4, we showed that the Somigliana representation for the elastic traction induced over the planar fracture surface is expressed function of the fundamental solution of the stress at point $\boldsymbol{y}$ due to a unit point force at $\boldsymbol{x}$ in a TI material $\Sigma^k_{ij}(\boldsymbol{y}, \boldsymbol{x})$. In the case of a planar hydraulic fracture (pure mode I fracture) with a normal coinciding with the axis $\boldsymbol{e_2}$ of the material frame ($n_i = \delta_{i2}\boldsymbol{e_2}$ with δ_{ij} is the Kronecker delta) also being a direction of the in-situ principal stress, the quasi-static elastic problem reduces to a single boundary integral

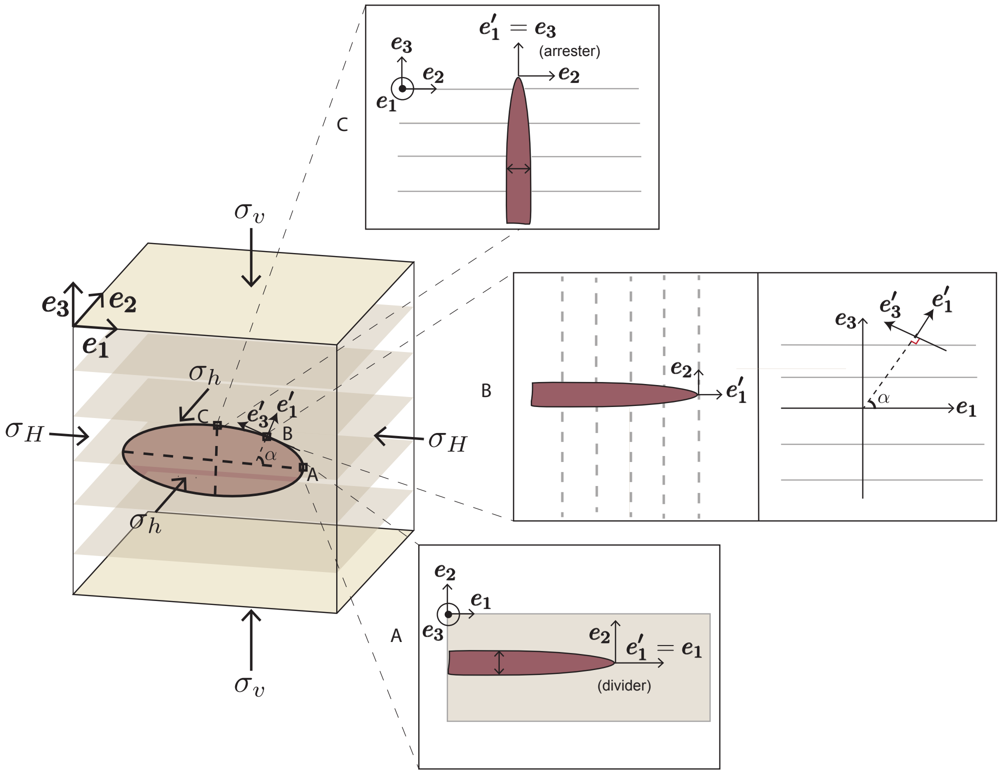
$e_1' = e_3$
(arrester)
e_3
e_2
e_1
C
σ_v
e_3
e_2
e_1
σ_h
σ_H
e_3'
e_1'
B
α
A
σ_H
σ_h
e_2
e_1'
e_3
e_3'
e_1'
α
e_1
σ_v
e_2
e_1
e_3
e_2
$e_1' = e_1$
(divider)

Figure 4.1 – Schematic of a planar three dimensional hydraulic fracture growing perpendicular to the isotropy plane. Different configurations of the near-tip region along the fracture front are also depicted: A) a semi- infinite fracture propagating along the plane of isotropy (divider direction), B) a semi-infinite fracture propagating within the plane $(\boldsymbol{e_1}, \boldsymbol{e_3})$ at angle α from $\boldsymbol{e_1}$ and C) a semi-infinite fracture propagating along the direction perpendicular to the isotropy plane (arrester direction).

equation for the opening mode (sections 2.2.4 and 2.3.2):

$$p(\boldsymbol{y}) = p_f\left(\boldsymbol{y}\right) - \sigma_h = c_{22kl} \int_{\partial\Omega} \Sigma^k_{2j}(\boldsymbol{y}, \boldsymbol{x}) \left(\delta_{2l} \frac{\partial w}{\partial x_j}(\boldsymbol{x}) - \delta_{2j} \frac{\partial w}{\partial x_l}(\boldsymbol{x}) \right) \mathrm{d}x_1 \mathrm{d}x_3 \qquad (4.1)$$

where c_{ijkl} is the stiffness matrix in the frame basis and $p(\boldsymbol{y}) = p_f\left(\boldsymbol{y}\right) - \sigma_h$ is the net pressure controlling the opening of the fracture w. $p_f\left(\boldsymbol{y}\right)$ is the fluid pressure inside the fracture- which is neither uniform nor constant during propagation - and σ_h is the in-situ minimum compressive horizontal stress (see figure 4.1).

4.3.2 Fluid flow inside the fracture

The flow of fluid inside a fracture follows lubrication theory (Batchelor, 1967). For an incompressible fluid and an impermeable surrounding rock, the width averaged mass conservation of the fluid inside the fracture reduces to

$$\frac{\partial w}{\partial t} + \frac{\partial q_i}{\partial x_i} = Q_o \delta(x_1, x_3) \qquad i = 1 \,\&\, 3 \qquad (4.2)$$

where Q_o denotes the constant fluid injection rate located at the origin. The width-averaged balance of momentum of the fluid inside the fracture reduces to Poiseuille's law, which relates the fluid flux $q_i = w v_i$ (where v_i is the 2D fluid velocity in the fracture plane - $i = 1\,\&\,3$ as per figure 4.1) to the fluid pressure gradient:

$$q_i(x_i) = -\frac{w^3}{\mu'} \times \frac{\partial p_f}{\partial x_i} \qquad i = 1 \,\&\, 3 \qquad (4.3)$$

where $\mu' = 12\mu$ is an effective viscosity used here to shorten notation.

4.3.3 Boundary conditions

For a hydraulic fracture propagating in an isotropic material, it can be shown that the fluid and fracture front coalesces when $\frac{\sigma_h K_{I_c}^2}{\mu' V E'_{iso}} \gg 1$ where V is the local front velocity, K_{Ic} the rock fracture toughness and E'_{iso} is the isotropic plane-strain modulus of the rock (Garagash and Detournay, 2000). An in-situ confining stress σ_h of the order of few $O(MPa)$ is sufficient to satisfy such a condition under most practical configurations. As a result, for fracture propagating at depth, any lag between the fracture and fluid front can be neglected. The boundary conditions at the fracture front then reduce to (Detournay and Peirce, 2014)

$$w(\boldsymbol{x}_{\mathscr{C}}, t) = 0, \quad q_i(\boldsymbol{x}_{\mathscr{C}}, t) n_i(\boldsymbol{x}_{\mathscr{C}}, t) = 0, \quad \boldsymbol{x}_{\mathscr{C}} \in \mathscr{C}(t).$$

4.3.4 Fracture Propagation condition

We will investigate the case where in addition to elastic transverse isotropy, the fracture toughness (or alternatively the critical fracture energy G_c) may also be anisotropic. In other words, the fracture toughness of the material may vary depending on the local fracture front propagation direction, i.e. as function of the angle α (figure 4.1). As a result, the propagation condition for a hydraulic fracture propagating under quasi-static equilibrium can be written as

$$K_I(\boldsymbol{x}_{\mathscr{C}}, t) = K_{Ic}(\alpha), \quad \boldsymbol{x}_{\mathscr{C}} \in \mathscr{C}(t),$$

for all point $\boldsymbol{x}_{\mathscr{C}}$ along the fracture front $\mathscr{C}$ with a local propagation direction defined by the angle α.

In order to quantify the degree of anisotropy of fracture toughness, we will use $\kappa = K_{Ic,1}/K_{Ic,3}$ as the ratio between the fracture toughness in the divider ($\boldsymbol{e_1}$) and arrester ($\boldsymbol{e_3}$) directions. The evolution of the material toughness can therefore be schematically expressed as:

$$K_{Ic}(\alpha) = K_{Ic,3} f(\alpha, \kappa, \ldots) \tag{4.4}$$

where the dimensionless function f is obviously material dependent and must be characterized experimentally. In the following, for discussion, we restrict to following three limiting cases.

1. The case of a particular form of toughness anisotropy leading to an elliptical fracture shape under uniform loading (see section 4.11.1). Such a type of anisotropy will notably allow to verify our numerical model.
2. The case of an isotropic fracture toughness: $K_{Ic}(\alpha) = K_{Ic}$ (i.e. $\kappa = 1, f = 1$) such that $G_c(\alpha) = K_{Ic}^2/E'_\alpha$.
3. The case of an isotropic fracture energy: $G_c(\alpha) = G_c$, which gives $K_{Ic}(\alpha) = \sqrt{G_c E'_\alpha}$.

4.4 Near-tip HF asymptotes for a TI material

For a steadily moving hydraulic fracture at velocity V, we showed in section 2.4 that the linear elastic fracture mechanics (lefm) asymptote prevails in the near-field. The lefm asymptote for the fracture width can be written as

$$w = \sqrt{32/\pi}\frac{K_{Ic}(\alpha)}{E'_\alpha}\sqrt{x'_1}, \qquad x'_1 \ll \ell_{mk}^{\infty}. \tag{4.5}$$

where the explicit formula for the near-tip TI elastic modulus E'_α is given in sections 2.3.2 and 2.3.3 and $K_{Ic}(\alpha)$ is the corresponding value of toughness. We should remind that the near-tip elastic modulus E'_α has the following form:

$$\begin{aligned}
E'_\alpha &= < E' > \times \mathscr{F}(\beta = E'_1/E'_3, \epsilon, \delta, C_{13}/C_{11}, \alpha) && (4.6)\\
< E' > &= \left(E'_1 + E'_3\right)/2 && (4.7)
\end{aligned}$$

with Thomsen parameters ϵ and δ are function of the stiffness coefficients in the Voigt notation C_{ij} and β is the ratio between the near-tip elastic modulus along the divider and the arrester directions E'_1 and E'_3 respectively.

$$\begin{aligned}
\epsilon &= \frac{C_{11} - C_{33}}{2C_{33}} && (4.8)\\
\delta &= \frac{(C_{13} + C_{44})^2 - (C_{33} - C_{44})^2}{2C_{33}\,(C_{33} - C_{44})} && (4.9)
\end{aligned}$$

We report the evolution of E'_α and its approximation E'_{app} function of the dimensionless parameters in figure 4.2.

$$\frac{1}{E'_{app}} = \frac{\cos^2(\alpha)}{E'_1} + \frac{\sin^2(\alpha)}{E'_3} \tag{4.10}$$

On the other hand, in the far-field, the solution is dominated by viscous flow. The so-called viscous dominated asymptote for fracture width is given by (Desroches et al., 1994):

$$w = 2^{1/3}3^{5/6}\left(\frac{\mu'}{E'_\alpha}V\right)^{1/3} x_1'^{\,2/3}, \qquad x'_1 \gg \ell^{\infty}_{mk}. \tag{4.11}$$

The transition between the near-tip lefm and the far-field viscosity asymptotes is governed by a lengthscale ℓ^{∞}_{mk} defined as the distance where the width given by two asymptotes are of the same order of magnitude (Garagash et al., 2011):

$$\ell^{\infty}_{mk} = \frac{K_{Ic}}{E_\alpha'^{\,4} V^2 \mu'^2}. \tag{4.12}$$

The solution for the complete transition between the toughness and viscous asymptote can be found in Garagash et al. (2011), and an accurate approximation has been proposed by Dontsov and Peirce (2015).

4.5 Numerical solution

We use the implicit level set algorithm (ILSA) to simulate the growth of a planar 3D hydraulic fracture (Zia et al., 2018; Zia and Lecampion, 2019) in elastic media exhibiting a transverse isotropic behavior. We refer to Peirce and Detournay (2008); Dontsov and Peirce (2017); Peirce (2015) for details of the scheme originally developed for the isotropic case. We discuss here briefly the modifications required to account for transverse isotropy.

The fracture plane is discretized using a Cartesian grid consisting of uniform rectangular

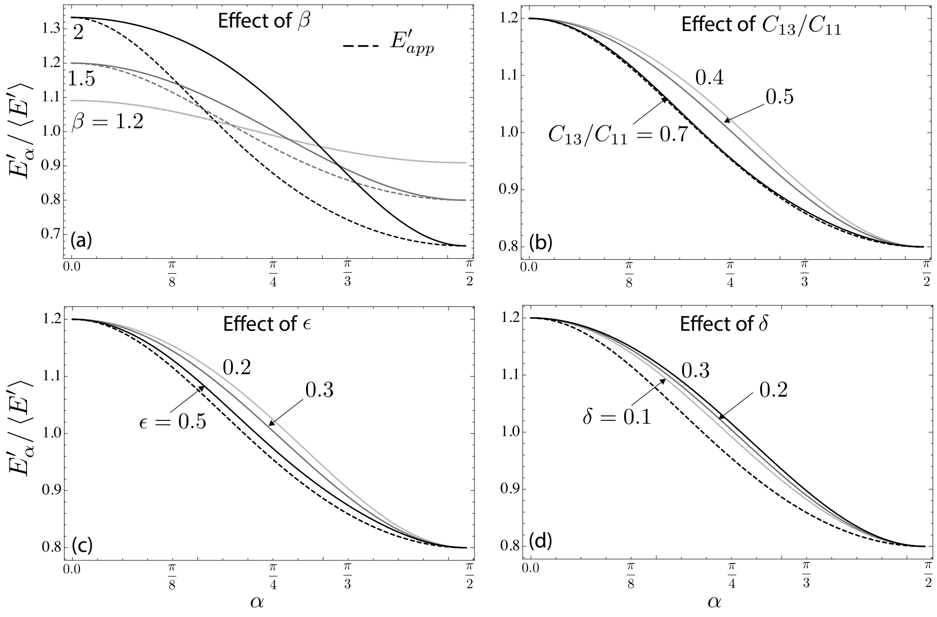

Figure 4.2 – Near-tip elastic modulus as function of α using the exact solution obtained analytically (solid line) and its approximation (Laubie and Ulm, 2014) (dashed line). Reference values: $\beta = 1.5$, $C_{13}/C_{11} = 0.5$, $\epsilon = 0.3$ and $\delta = 0.2$ displayed in dark grey. (a) Effect of $\beta = (1.2, 1.5, 2)$, (b) effect of $C_{13}/C_{11} = (0.4, 0.5, 0.7)$, (c) effect of $\epsilon = (0.2, 0.3, 0.5)$, and (d) effect of $\delta = (0.1, 0.2, 0.3)$.

elements. We discretize the elasticity equation (4.1) using a collocation method based on rectangular displacement discontinuity elements. The solution for a rectangular displacement discontinuity in a TI medium can be found in Pan et al. (2014). The fracture width is thus constant over an element and the fluid pressure is evaluated at the element center. The lubrication flow is discretized spatially with a five-point stencils finite difference scheme and with a backward Euler (implicit) scheme for time integration. The resulting non-linear hydro-mechanical system (elasticity and lubrication) is solved using fixed point iterations for a given position of the fracture front.

A level set function is used to represent the fracture front. The propagation algorithm relies on the coupling of the finite discretization with the near-tip solution of a steadily moving HF (see section 4.4) in the rim of elements near the front. The fracture front is advanced over a time-step through an iterative procedure (until subsequent estimations of the level set falls below a fixed tolerance, set to 10^{-3} here). For a given position of the front, the non-linear hydro-mechanical system is solved. The new trial width in the elements located just before the tip elements (ribbon elements) are used to invert the near-tip solution and obtain the new shortest distance to the fracture front (from the ribbon elements centers). The Eikonal equation is then solved to update the level set function from the tip region outward to the rest of the yet unfractured domain using the fast marching method. The front is then reconstructed in a piece-wise manner and the asymptotic solution enforced in a weak sense in the tip elements (see Peirce (2015) for more details). In the case of a transversely isotropic material, the difference with the isotropic case stems from the fact that the complete near-tip HF solution (spanning the transition from the toughness to the viscosity asymptote) depends on the local propagation direction (via the dependence of E'_α and K_{Ic} on the angle α) beside the local front velocity. This introduces another non-linearity which is solved by iterating on the local propagation direction: by repeatably inverting the tip asymptote and reconstructing new estimate of the front until convergence (Zia et al., 2018). It is worth noting that the local propagation direction (local normal to the front) can be directly obtained from the gradient of the level set function $n_i = \phi_{,i}/\|\phi_{,i}\|$ in the ribbon element. It is then straightforward to estimate its angle α with the $\boldsymbol{e}_1$ axis and the corresponding near-tip elastic modulus (4.6) and toughness (4.4). A tolerance of 10^{-3} has been used to check the convergence of the local propagation direction in all simulations reported here.

4.6 Scaling and structure of the solution

Our aim is to study how the geometry of the HF may deviate from a radial shape due to material isotropy. We thus follow the scaling first introduced by Savitski and Detournay (2002) for the case of a radial hydraulic fracture driven by a Newtonian fluid in an isotropic medium. A characteristic length scale $L(t)$ scales all distances, while the fracture width and pressure are scaled by $W(t)$ and $P(t)$ respectively. We define a normalized fracture contour γ, fracture opening Ω and net pressure Π as:

$$\mathscr{C}(t) = L(t)\gamma\left(\mathscr{P}(t), \beta, \epsilon, \delta, C_{13}/C_{11}, \kappa, f(\alpha,\kappa)\right) \tag{4.13}$$

$$w(x_1, x_3, t) = W(t)\Omega\left(x_1/L(t), x_3/L(t), \mathscr{P}(t), \beta, \epsilon, \delta, C_{13}/C_{11}, \kappa, f(\alpha,\kappa)\right) \tag{4.14}$$

$$p(x_1, x_3, t) = P(t)\Pi\left(x_1/L(t), x_3/L(t), \mathscr{P}(t), \beta, \epsilon, \delta, C_{13}/C_{11}, \kappa, f(\alpha,\kappa)\right) \tag{4.15}$$

where for transverse isotropy in addition to a the evolution parameter $\mathscr{P}(t)$, the solution also depends on the dimensionless elastic parameters previously defined and the ratio of toughness and its evolution function. Following the isotropic case for a radial fracture (Savitski and Detournay, 2002), two different scalings can be obtained either emphasizing the importance of energy dissipation in viscous flow (so-called M/viscosity scaling) or in the creation of new fracture surfaces (K/toughness scaling). The corresponding lengthscales and the associated dimensionless parameter $\mathscr{P}$ governing the solution in both scaling are recalled in table 4.1. We have written them here as function of a characteristic elastic modulus and a characteristic toughness (E_*, K_*). The viscosity dominated propagation regime (M-scaling) is valid at early time of growth. This can be grasped from table 4.1 where one can see that the dimensionless toughness $\mathscr{K}$ increases with time (and is directly related to the dimensionless viscosity in the viscosity scaling $\mathscr{M} = \mathscr{K}^{-18/5}$ which decreases with time). At very early, fracture toughness is irrelevant ($\mathscr{K} \sim 0$) and fracture growth is propagating in the so-called viscosity dominated

	Viscosity (M)	Toughness (K)	Viscosity to toughness (M-K)
$L(t)$	$L_m = \left(\frac{E_* Q_o^3 t^4}{\mu'}\right)^{1/9}$	$L_k = \left(\frac{E_* Q_o t}{K_*}\right)^{2/5}$	$L_{mk} = \frac{\mu' Q_o E_*^3}{K_*^4}$
$W(t)$	$W_m = \left(\frac{Q_o^3 \mu'^2 t}{E_*^2}\right)^{1/9}$	$W_K = \left(\frac{Q_o K_*^4 t}{E_*^4}\right)^{1/5}$	$W_{mk} = \left(\frac{\mu' Q_o E_*}{K_*^2}\right)^{1/2}$
$P(t)$	$P_m = \left(\frac{\mu' E_*^2}{t}\right)^{1/3}$	$P_k = \left(\frac{K_*^6}{Q_o E_* t}\right)^{1/5}$	$P_{mk} = \left(\frac{K_*^{18}}{Q_o^3 E_*^9 \mu'}\right)^{1/6}$
$\mathscr{P}(t)$	$\mathscr{K} = K_* \left(\frac{t^2}{\mu'^5 Q_o^3 E_*^{13}}\right)^{1/18}$	$\mathscr{K} = 1$	$\mathscr{K} = \left(\frac{t}{t_{mk}}\right)^{1/9}$
$\mathscr{P}(t)$	$\mathscr{M} = 1$	$\mathscr{M} = \mu' \left(\frac{Q_o^3 E_*^{13}}{K_*^{18} t^2}\right)^{1/5}$	$\mathscr{M} = \left(\frac{t_{mk}}{t}\right)^{2/5}$

Table 4.1 – Characteristic scales and dimensionless parameters in the viscosity (M), toughness (K) and the transition from viscosity to toughness (M-K). Note that $\mathscr{M} = \mathscr{K}^{-18/5}$.

regime where the solution is self-similar for radial growth (given by the characteristic scales and solution for the dimensionless length, pressure and opening in viscosity scaling all of order 1). At large time, on the contrary, fracture toughness dominates the energy dissipation and viscous flow becomes irrelevant. The fracture propagates in the viscosity dominated regime where the solution is also self-similar. The transition between these two regimes (viscosity to toughness) is captured by the characteristic timescale t_{mk}:

$$t_{mk} = \left(\frac{\mu'^5 {E_*}^{13} Q_o^3}{K_*^{18}}\right)^{1/2}. \tag{4.16}$$

at which $\mathscr{K}(t_{mk}) = \mathscr{M}(t_{mk})$ (or alternatively $L_m(t_{mk}) = L_k(t_{mk})$). A corresponding (M-K) scaling can then be used where the characteristic scales are not independent of time, and the solution only depends on t/t_{mk}. For the case of a transversely isotropic material, several choices can be made for the characteristic modulus and toughness. In view of the configuration investigated here, we take values along the divider direction ($\mathbf{e}_1$) and the arrester direction ($\mathbf{e}_3$). The solution will now be function, in addition to a dimensionless time (e.g. $t/t_{mk,*}$), on the ratio between the dimensionless toughness (or viscosity) between the arrester and the divider directions. This is similar to taking the ratio of the transition time-scales between the arrester and divider directions. Such a ratio is solely function of the ratio of toughness $\kappa = K_{Ic,1}/K_{Ic,3}$ and plane strain elastic modulus $\beta = E'_1/E'_3$:

$$\frac{t_{mk,3}}{t_{mk,1}} = \left(\frac{\mathscr{K}_1}{\mathscr{K}_3}\right)^9 = \beta^{-13/2}\kappa^9 \tag{4.17}$$

We see that a small anisotropy of toughness and elasticity (e.g. $\beta = \kappa^{-1} = 1.2$) induces a strong anisotropy in the transition from viscosity to toughness between the divider and the arrester direction $\left(t_{mk,1}/t_{mk,3} \simeq 17\right)$. The fracture front will likely reaches the toughness propagation regime earlier in the arrester direction for these particular values of β and κ.

The ratio of timescales $t_{mk,3}/t_{mk,1}$ likely captures the main effect of transverse anisotropy on HF growth, but the Thomsen parameters ϵ, δ as well as C_{13}/C_{11} and the details of the toughness evolution function $f(\alpha, \kappa)$ also affect the solution. The fracture shape will also evolve between the early time (viscous dominated) and toughness dominated regime. We quantify these effects numerically in what follows.

Unless otherwise specified, we scale the numerical results with the average value of the plane strain elastic modulus $E_* = \langle E' \rangle = \left(E'_1 + E'_3\right)/2$ and the average toughness $K'_* = \langle K' \rangle = \left(K'_1 + K'_3\right)/2$. We will also refer the half-lengths in the divider ($\boldsymbol{e}_1$) and arrester ($\boldsymbol{e}_3$) directions as a and b respectively, and denote abusively the fracture aspect ratio as b/a although the fracture shape is not necessarily elliptical.

4.7 Viscosity dominated regime

We first focus on propagation in the viscosity dominated regime corresponding to early time (e.g. $t < t_{mk}$ in the tougher direction). In such a regime, the solution is not affected by fracture toughness (see the scaling in table 4.1). The interest therefore lies in the effect of TI elasticity on the potential deviation of the fracture from the radial geometry obtained for isotropic material. We investigate the effect of the dimensionless elastic parameters β, ϵ, δ and C_{13}/C_{11} by varying them around the set of base values already used to illustrate the variation of the near-tip modulus (see figure 4.2).

In all the simulations, the fracture plane is discretized with 100 × 100 rectangular element ($\Delta x_1 = 2\Delta x_3$). Initially the fracture is set as a small circle (compared to the total grid- i.e. with ~ 20 elements) and a fluid pressure slightly above the minimum stress.

The evolution of the dimensionless major and minor semi-axis $a(t)$ and $b(t)$ and the dimensionless width at the injection with time are displayed in figure 4.3 for different values of $\beta = E'_1/E'_3$. The other dimensionless elastic parameters ϵ, δ and C_{13}/C_{11} have almost no effect on the solution (see figures4.3-4.5). The time in these plots is scaled using an timescale t_m corresponding to the time taken to reach a fracture lengthscale of 1m: $L_m(t_m) = 1$. Similarly, the width $w(t)$, the semi-axis $a(t)$ and $b(t)$ are scaled by $W_m(t_m)$ and $L_m(t_m)$ respectively. The results for an isotropic material are also displayed (in dot-dashed line) for reference.

figure 4.3 clearly shows the self similarity of the solution in the viscosity dominated regime. It follows the same power law of time as in the isotropic case: $4/9$ for the radius, and $1/9$ for width. The difference of the fracture semi-axes with the isotropic radial case ($b(t)/a(t) = 1$) is barely visible in such log-log plots, similarly for the width at the injection point - except for $\beta = 2$ (figure 4.3.b)).

As the solution is self-similar in this viscosity dominated regime, we can plot the dimensionless fracture footprint (removing the time-dependence contained in $L_m(t)$) γ_m for different set of parameters in figure 4.4 (we plot a quarter of the fracture due to symmetry), while the

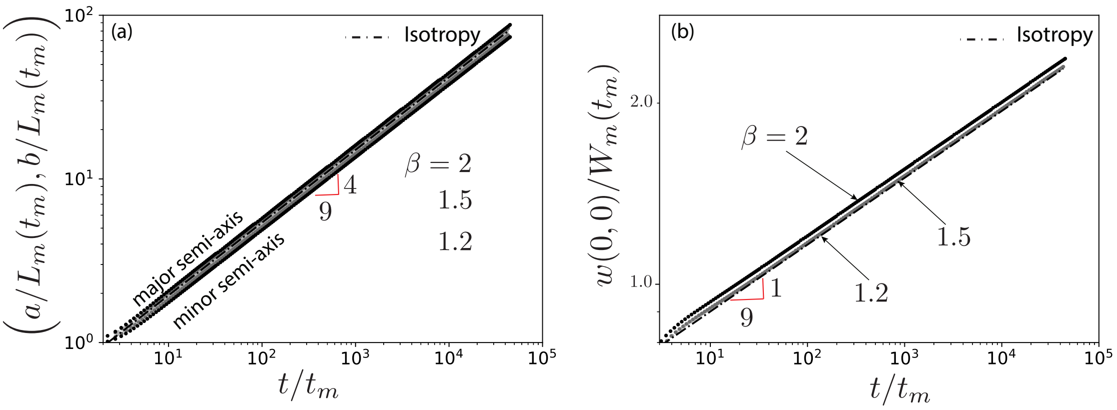

Figure 4.3 – Viscosity dominated propagation: Time evolution of the dimensionless major $a(t)/L_m(t_m)$ and minor $b(t)/L_m(t_m)$ semi axis in (a), and of the dimensionless width at the injection point $w(0,0)/W_m(t_m)$ in (b). The numerical simulations are performed for different values of $\beta = (1.2, 1.5, 2)$ with: $\epsilon = 0.3$, $\delta = 0.2$, and $C_{13}/C_{11} = 0.5$.

corresponding dimensionless profiles of width Ω_m and pressure Π_m along the major axis $\boldsymbol{e_1}$ are exhibited in figures 4.5 and 4.6 respectively.

An elongation of the fracture in the divider direction ($\boldsymbol{e_1}$) for increasing β can be observed from the dimensionless self-similar footprint (figure4.4). The other elastic constants do not appear to influence the solution. A difference of 18% between the fracture height and length is obtained for $\beta = 2$ ($\beta^{-1} = 0.5$). The evolution of the fracture aspect ratio as function of β can be well approximated as $b/a \approx 0.53\beta^{-1/2}$ (see figure 4.4.a-inset). Such a proportionality of b/a with β can be actually be easily recovered analytically from the near-tip solution. Matching the width given by the viscosity asymptote equation (4.11) in both the arrester and divider directions gives $a^{2/3}/E_1'^{1/3}\left(\frac{\mathrm{d}a}{\mathrm{d}t}\right)^{1/3} \propto b^{2/3}/E_3'^{1/3}\left(\frac{\mathrm{d}b}{\mathrm{d}t}\right)^{1/3}$, where $\frac{\mathrm{d}a}{\mathrm{d}t}$ and $\frac{\mathrm{d}b}{\mathrm{d}t}$ are the propagation velocities of the crack tips at the major and the minor axes respectively. Assuming a self-similar growth, the ratio of the these tip velocities should be constant as shown in Bessmertnykh and Dontsov (2018):

$$\frac{\mathrm{d}b}{\mathrm{d}a} = \frac{b}{a} \tag{4.18}$$

As a result, we recover the evolution of the aspect ratio with β: $b/a \propto (E_3'/E_1')^{1/3} = \beta^{-1/3}$. The fracture width and pressure have similar evolution along the minor and major axis ($\boldsymbol{e_3}$ and $\boldsymbol{e_1}$) actually very close to the isotropic solution. Figures 4.5 and 4.6 display the dimensionless width and net pressure profile along the major axis. The fracture width increases slightly with β, while it does not appear to be influenced by ϵ, δ and C_{13}/C_{11}.

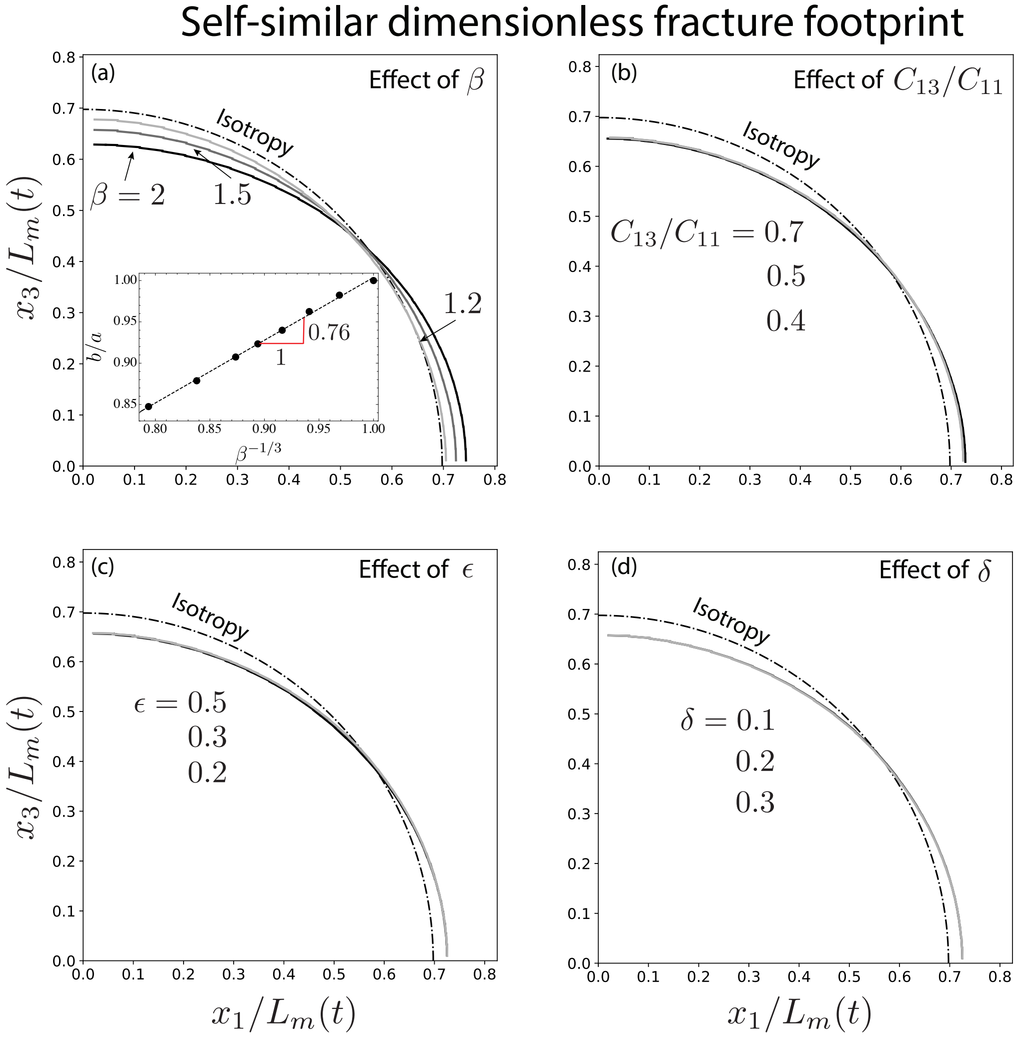

Figure 4.4 – Viscosity dominated propagation: Self similar fracture footprint γ_m for the reference values: $\beta = 1.5$, $C_{13}/C_{11} = 0.5$, $\epsilon = 0.3$, and $\delta = 0.2$. The effect of the dimensionless elastic parameters is also depicted: (a) variations of $\beta = (1.2, 1.5, 2)$, (b) variations of $C_{13}/C_{11} = (0.4, 0.5, 0.7)$, (c) variations of $\epsilon = (0.2, 0.3, 0.5)$, and (d) variations of $\delta = (0.1, 0.2, 0.3)$. The inset figure in (a) show the evolution of the fracture aspect ratio b/a function of β.

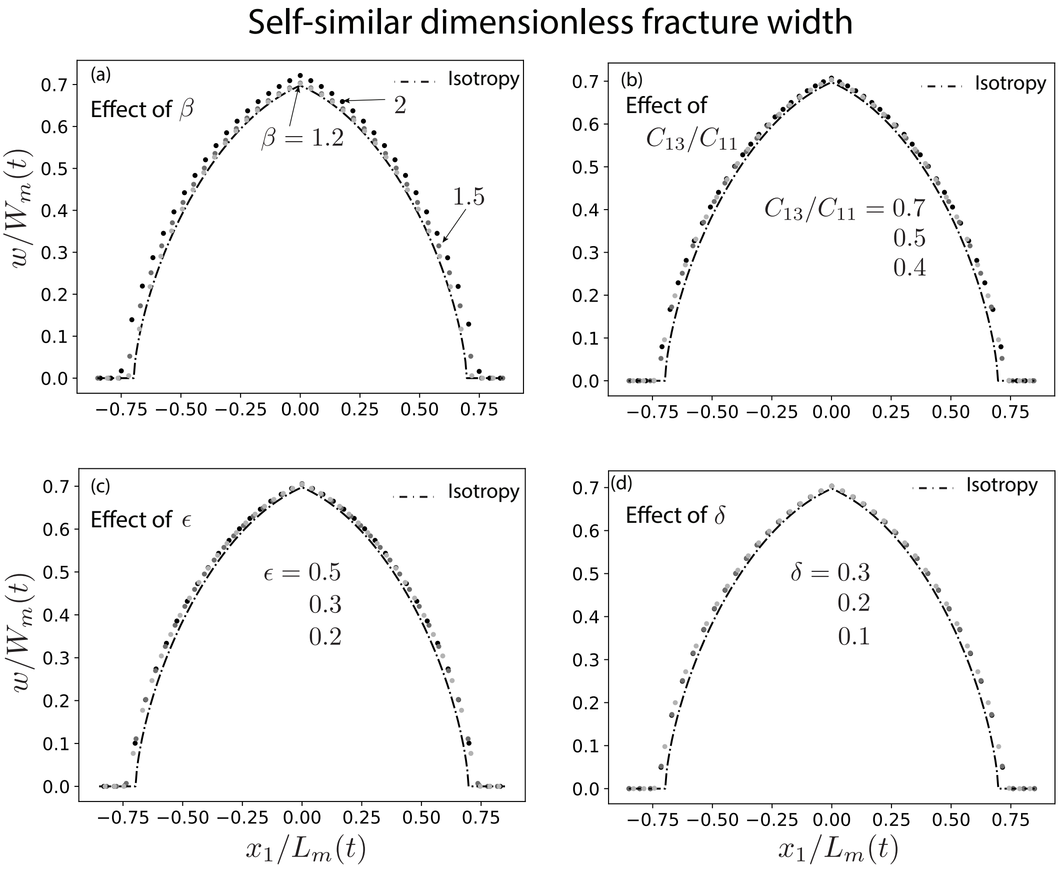

Figure 4.5 – Viscosity dominated regime: Self similar width profiles $\Omega_m = w/W_m(t)$ along the major axis $\boldsymbol{e_1}$ for the reference values: $\beta = 1.5$, $C_{13}/C_{11} = 0.5$, $\epsilon = 0.3$, and $\delta = 0.2$. The effect of the dimensionless elastic parameters is also depicted: (a) variations of $\beta = (1.2, 1.5, 2)$, (b) variations of $C_{13}/C_{11} = (0.4, 0.5, 0.7)$, (c) variations of $\epsilon = (0.2, 0.3, 0.5)$, and (d) variations of $\delta = (0.1, 0.2, 0.3)$.

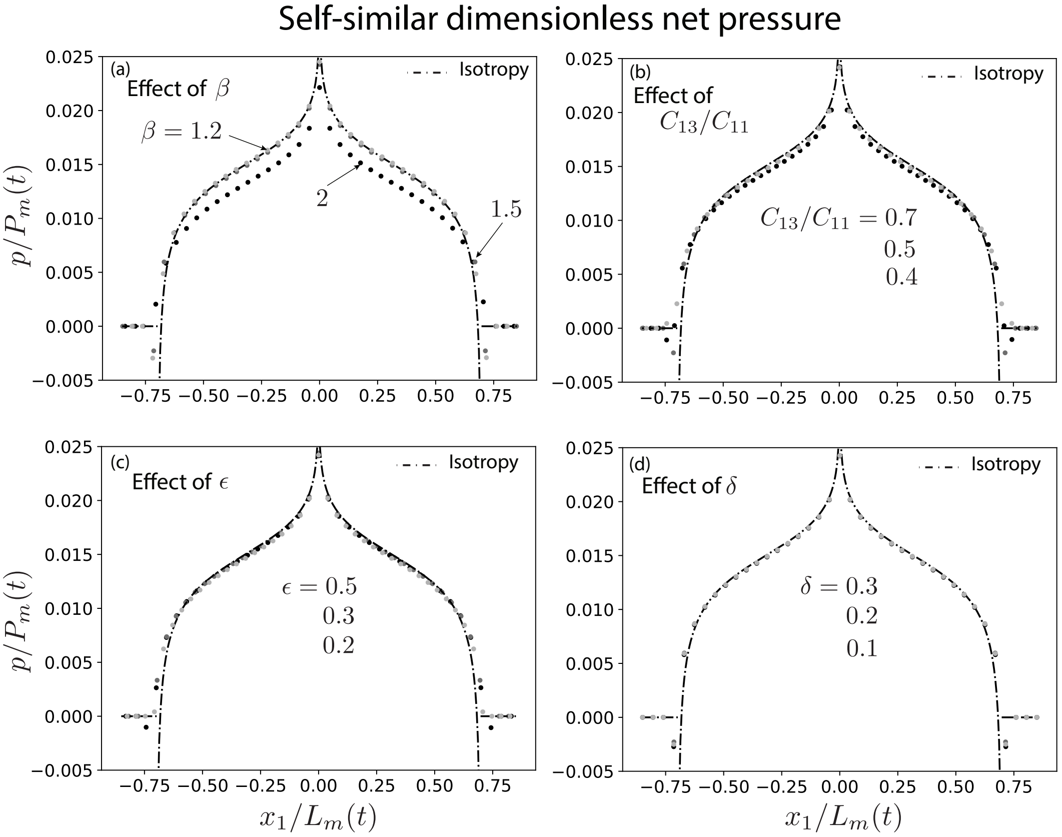

Figure 4.6 – Viscosity dominated regime: Self similar pressure profiles $\Pi_m = p/P_m(t)$ along the major axis $\boldsymbol{e_1}$ for the reference values: $\beta = 1.5$, $C_{13}/C_{11} = 0.5$, $\epsilon = 0.3$, and $\delta = 0.2$. The effect of the dimensionless elastic parameters is also depicted: (a) variations of $\beta = (1.2, 1.5, 2)$, (b) variations of $C_{13}/C_{11} = (0.4, 0.5, 0.7)$, (c) variations of $\epsilon = (0.2, 0.3, 0.5)$, and (d) variations of $\delta = (0.1, 0.2, 0.3)$.

4.8 Toughness dominated regime

We now turn to the toughness dominated propagation regime, valid at large time compared to t_{mk} ($t \gg t_{mk}$). In this regime, viscous flow is negligible and has no effect on the solution: the pressure is uniform (but not constant) inside the fracture. We study here the combined effect of the anisotropy of elasticity and fracture toughness.

4.8.1 Elliptical hydraulic fracture

We first investigate the case of a peculiar form of toughness anisotropy ensuring an exact elliptical shape under uniform loading:

$$K_{Ic} = K_{Ic,3}\left(\frac{E'_\alpha}{E'_3}\right)\left(\sin^2\theta + \left(\frac{b}{a}\right)^2\cos^2\theta\right)^{1/4} \tag{4.19}$$

$$\theta = \arctan\left(\frac{b\tan\alpha}{a}\right) \tag{4.20}$$

Such a toughness evolution directly comes from the solution of the mode I stress intensity factor along the front of an uniformly pressurized elliptical crack in TI medium (section 2.5.2). From such an elastic solution, it is then possible to obtain a solution for the propagation of such an elliptical hydraulic fracture in the toughness dominated regime. The details of such an analytical (and self-similar) HF propagation solution are given in section 4.11.1. It is worth noting that the HF propagates in a self similar manner with the same power law of time as in the isotropic case: $2/5$ for the radius, $1/5$ for width and $-1/5$ for the pressure.

Making use of equation (4.19) at $\alpha = \theta = 0$ (the divider direction) where $K_{Ic} = K_{Ic,1}$ and at $\alpha = \theta = \pi/2$ (the arrester direction) where $K_{Ic} = K_{Ic,3}$, we obtain the following relation for the ellipse aspect ratio:

$$\frac{b}{a} = \left(\frac{K_{Ic,1}}{K_{Ic,3}}\frac{E'_3}{E'_1}\right)^2 = \left(\frac{\kappa}{\beta}\right)^2. \tag{4.21}$$

We use the fracture toughness function (4.19) in our numerical solver for the case $\kappa^{-1} = \beta = 1.2$. The resulting effect of anisotropy of elasticity and toughness are cumulative in that case (see equation (4.21) for $\kappa < 1$ and $\beta > 1$) and the exact aspect ratio is $b(t)/a(t) = 0.47$. We set the other elastic parameters to: $\epsilon = 0.3$, $\delta = 0.2$, and $C_{13}/C_{11} = 0.5$. The fracture is initialized with the analytical (isotropic) solution of a radial fracture propagating in toughness dominated regime. The rectangular domain is divided into 150 cells along $\boldsymbol{e_1}$ and 100 along $\boldsymbol{e_3}$.

The numerical (black dots) and the analytical elliptical (green solid line) HF toughness dominated solutions are both displayed on figure 4.7. We scale the time in figures 4.7.c, d, e and f by t_k, where: $L_k(t_k) = 1$, the pressure by $P_k(t_k)$, the width by $W_k(t_k)$ and semi-axis by $L_k(t_k)(=1)$. The analytical toughness dominated solution for isotropic toughness ($\kappa = 1$) and elasticity ($\beta = 1$) is also reported in figure 4.7 (dash-dotted lines) taking $E_* = \langle E' \rangle$, and $K_* = \langle K' \rangle$ as corresponding isotropic parameters. One clearly see that our numerical solution closely matches the analytical elliptical HF solution for both width profiles, major and minor axis as well as net pressure evolution. The relative error between the numerical results and the analytical solution of the major and minor axis always remain under five percent for about four decades of time - with only small oscillations associated with remeshing. It is worth to recall that the fracture is initialized as a radial following the isotropic solution. Interestingly, the width at the center $w/W_k(t_k)$ and the net pressure $p/P_k(t_k)$ takes slightly more time to converge toward the elliptical HF toughness solution (figures 4.7.e and f) compared to the fracture shape (figures 4.7.c).

This comparison verify our numerical solver, and has proven useful to test its robustness as anisotropy increases. It is also important to re-emphasize than the fracture has exactly an elliptical shape only for the evolution of fracture toughness given by equation 4.19.

4.8.2 Isotropic toughness

We now investigate the case of an isotropic fracture toughness: $K_{Ic}\left(\alpha\right) = K_{Ic}\ (\kappa = 1)$. We vary the different elastic parameters around the same set of reference values as before: $\beta = 1.5$, $\epsilon = 0.3$, $\delta = 0.2$, and $C_{13}/C_{11} = 0.5$.

The numerical results for the self similar footprint γ_k and width profiles $\Omega_k = w/W_k$ along the major and the minor axis $\boldsymbol{e_1}$ and $\boldsymbol{e_3}$ are displayed in figures 4.8 and 4.9 respectively, whereas the pressure at the injection function of time is performed in figure 4.10. We use the toughness scaling defined in table 4.1.

The fracture elongates more in the stiffer direction ($\boldsymbol{e_1}$) as can be seen from figure 4.8a. More importantly, the fracture is not elliptical. The fracture aspect ratio is proportional to β^{-2} as shown in figure 4.8.a-inset. This is also the case for the elliptical fracture ($b/a = \beta^{-2}$ when $K_{Ic,1} = K_{Ic,3}$ in equation (4.21)). However, for isotropic toughness the slope is slightly different: $b/a \approx 0.9\beta^{-2}$. This implies that assuming an elliptical shape for the case of an isotropic toughness will underestimate the fracture aspect ratio by about 10%. Similarly than for the viscosity dominated regime, the relation between the fracture aspect ratio and β can be recovered from the toughness near-tip asymptote (4.5). Similarly to Bessmertnykh and Dontsov (2018), matching the width along the minor and major axis direction from the near-tip asymptote gives $\sqrt{b/a} \propto \dfrac{E'_3}{E'_1}$, in other words $b/a \propto \beta^{-2}$.

We also report in figure 4.8 the numerical results obtained using $E'_{app}(\alpha)$ as the near-tip elastic modulus. As previously discussed, for large value of β, the approximate solution E'_{app} underestimates the elastic near-tip modulus compared to the exact expression E'_{α} (figure 4.2-a). As a result, the computed fracture aspect ratio is also underestimated. As an illustration for $\beta = 2$, the ratio of the minor to major axis obtained using E'_{app} is equal to 0.32, whereas it is of 0.59 when using the exact near-tip elastic modulus E'_{α}. The difference between the

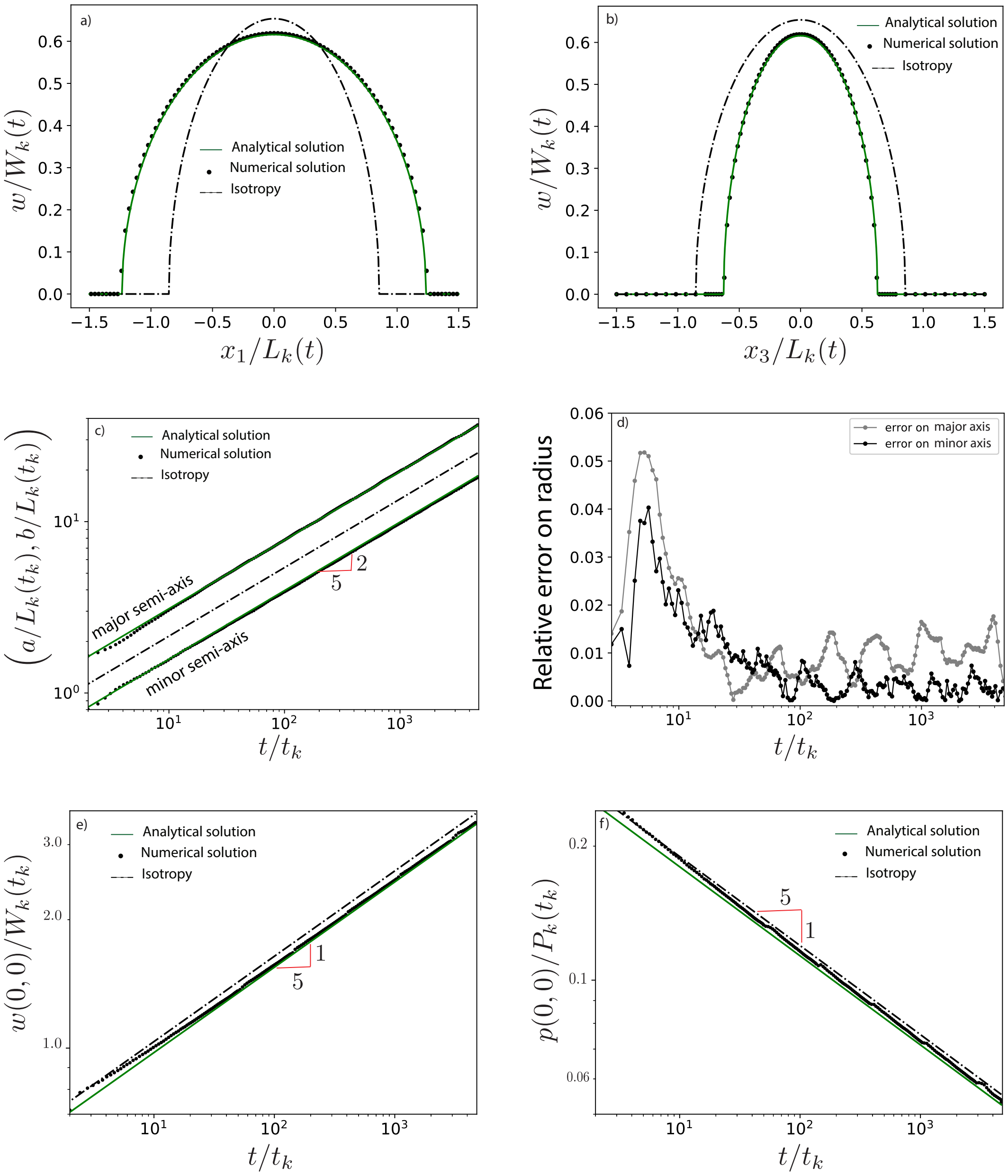

Figure 4.7 – Toughness dominated regime - Elliptical toughness anisotropy: (a,b) dimensionless self-similar width profile Ω_k along $\boldsymbol{e_1}$ and $\boldsymbol{e_3}$ respectively, (c) exhibit the dimensionless length of the major $a(t)/L_k(t_k)$ and minor $b(t)/L_k(t_k)$ semi-axis in semi-log scale as well as the relative error with respect to the analytical solution (section 4.11.1) in (d), and (e,f) exhibit the dimensionless width $w(0,0)/W_k(t_k)$ and pressure $p(0,0)/P_k(t_k)$ respectively at the injection versus the dimensionless time t/t_k for: $\kappa^{-1} = 1.2$, $\beta = 1.2$, $\epsilon = 0.3$, $\delta = 0.2$, and $C_{13}/C_{11} = 0.5$.

fracture footprint obtained using either the exact E'_α and E'_{app} is however not very significant for $\beta \leq 1.5$. In other words, E'_{app} provides a good approximation only for weak anisotropy.

figures 4.8.b and c display the fracture footprint for different C_{13}/C_{11} and ϵ respectively. These two elastic dimensionless parameters have the same effect on the behavior of the fracture footprint, i.e the aspect ratio increases from $b/a \approx 0.48$ for small value of C_{13}/C_{11} ($C_{13}/C_{11} = 0.4$) or ϵ ($\epsilon = 0.2$) to $b/a \approx 0.52$ for larger value of C_{13}/C_{11} ($C_{13}/C_{11} = 0.7$) or ϵ ($\epsilon = 0.5$). This indicates that a faster transition of the near-tip E'_α from E'_1 to E'_3 (see figure 4.2), results in smaller elongation of the fracture footprint (i.e. larger b/a). The effect of the Thomsen parameter δ on the fracture footprint appears relatively small (less than 4% of relative difference) as can be observed from figure 4.8.d.

The corresponding self similar width profiles along the major and the minor axis $\Omega_k = w/W_k$ are shown in figure 4.9. We observe that the fracture width profile appears to be mostly sensitive to β, with little effect of the other dimensionless elastic parameters (C_{13}/C_{11}, and the Thomsen parameters ϵ and δ).

figure 4.10 reports the time-evolution of the dimensionless net pressure $p(t)/P_k(t_k)$ for different values of β, C_{13}/C_{11}, Thomsen parameters ϵ and δ (see figures 4.10a, b, c and d respectively). It evolves with $-1/5$ power law of time, similarly than in the case of isotropic material as anticipated by the scaling analysis. We also directly observe that the dimensionless elastic parameters have no effect on the net pressure. The net pressure corresponds to the solution of the radial isotropic toughness dominated HF.

4.8.3 Isotropic fracture energy

Another possible limiting anisotropic behavior is the case of an isotropic fracture energy $G_c(\alpha) = G_c$. As a result, the fracture toughness $K_{Ic}(\alpha) = \sqrt{G_c E'_\alpha}$ decreases with α in this case, following the variation of the elastic modulus E'_α (see figure 4.2). The toughness ratio, $\kappa = K_{Ic,1}/K_{Ic,3} = \sqrt{\beta}$ is thus greater than 1 such that it somehow compensates the effect of elastic anisotropy (Chandler et al., 2016). Using a similar procedure than before, i.e. matching the width of the toughness dominated near-tip asymptote in the divider and arrester directions ($K_{Ic,1}/E'_1\sqrt{a} \propto K_{Ic,3}/E'_3\sqrt{b}$, we now obtain that b/a should be proportional to β^{-1}, compared to β^{-2} for isotropic toughness (Bessmertnykh and Dontsov, 2018; Laubie and Ulm, 2014). A series of simulation for different values of β recover exactly such an estimate as can be seen from figure 4.11.a. Here again, the time-evolution of fracture shape (figure 4.11.b), width and net pressure follows the same power-law of time than the isotropic case as predicted by the scaling analysis. It is worth noting that the effect of the other elastic parameters (besides β) is, similarly than for the isotropic toughness case, rather small and thus not shown here.

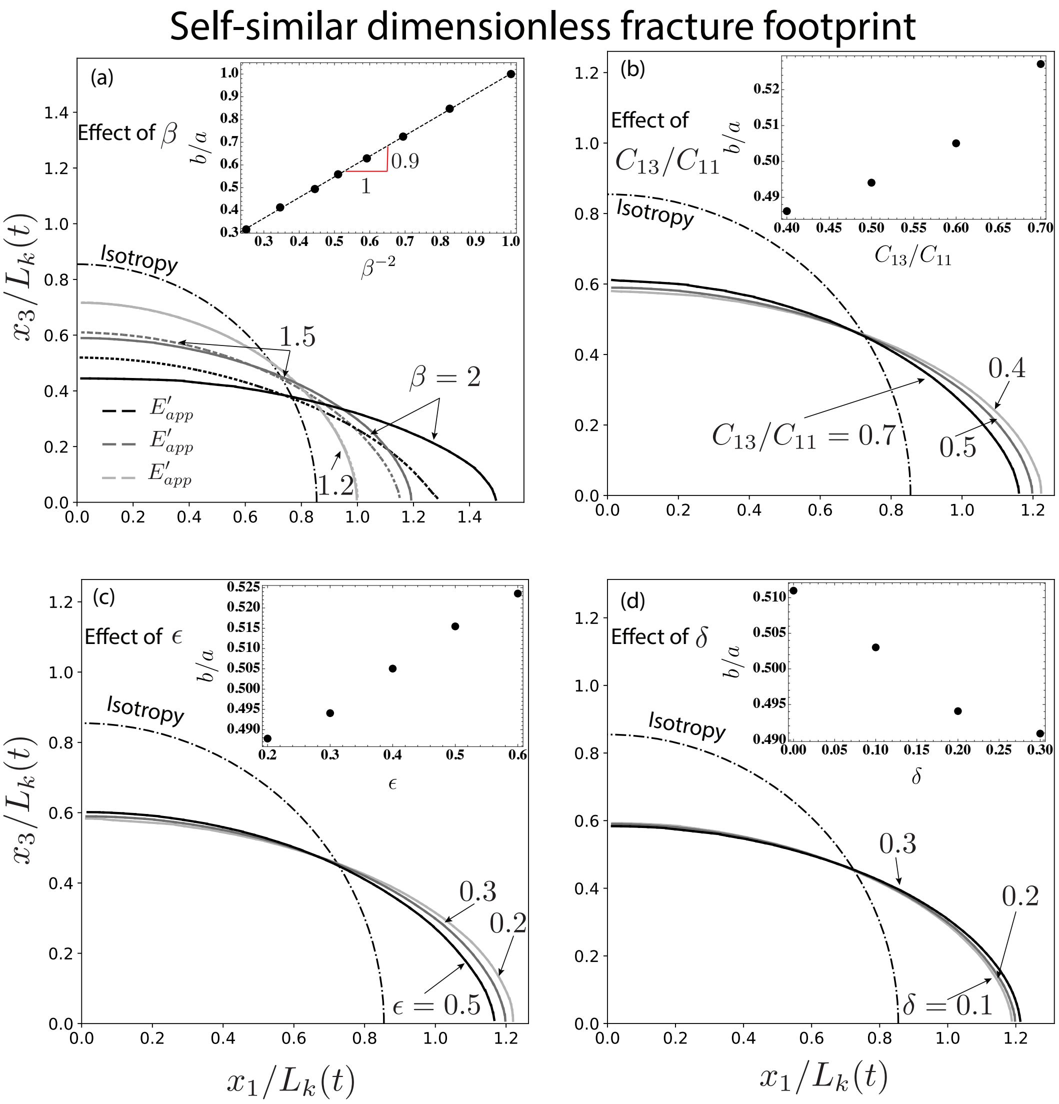

Figure 4.8 – Toughness dominated propagation - Isotropic toughness case: self similar footprint γ_k obtained using the exact expression for E'_α (solid line) and the approximation function E'_{app} (dashed line) as the near-tip elastic modulus. Reference parameters: $\beta = 1.5$, $C_{13}/C_{11} = 0.5$, $\epsilon = 0.3$, and $\delta = 0.2$. (a) variations of $\beta = (1.2, 1.5, 2)$, (b) variations of $C_{13}/C_{11} = (0.4, 0.5, 0.7)$, (c) variations of $\epsilon = (0.2, 0.3, 0.5)$, and (d) variations of $\delta = (0.1, 0.2, 0.3)$. The insets display the corresponding evolution of the fracture aspect ratio b/a.

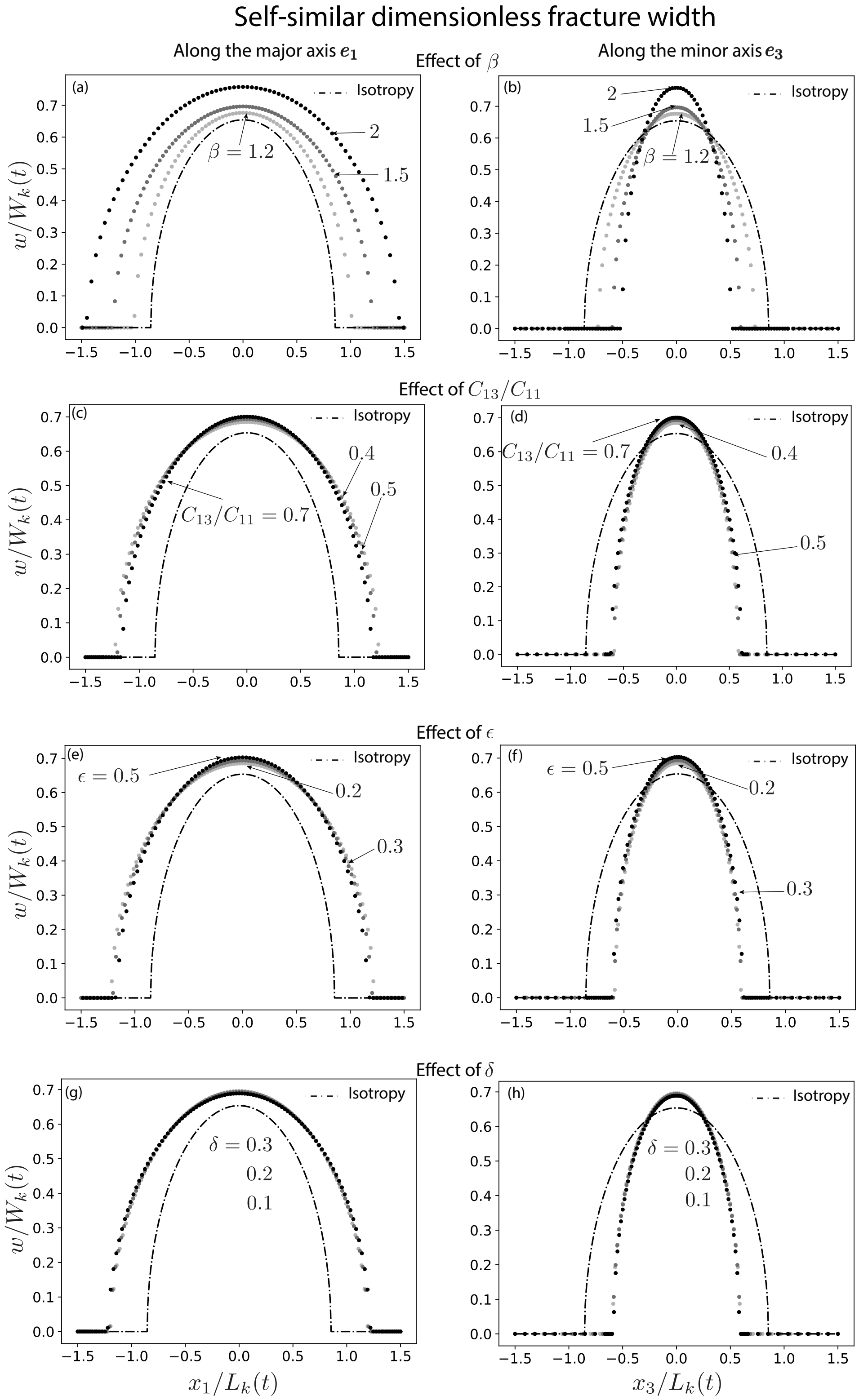

Figure 4.9 – Toughness dominated propagation - Isotropic toughness case: self similar width profiles Ω_k along $\boldsymbol{e_1}$ and $\boldsymbol{e_3}$. Reference parameters: $\beta = 1.5$, $C_{13}/C_{11} = 0.5$, $\epsilon = 0.3$, and $\delta = 0.2$. (a, b) variations of $\beta = (1.2, 1.5, 2)$, (c, d) variations of $C_{13}/C_{11} = (0.4, 0.5, 0.7)$, (e, f) variations of $\epsilon = (0.2, 0.3, 0.5)$, and (g, h) variations of $\delta = (0.1, 0.2, 0.3)$.

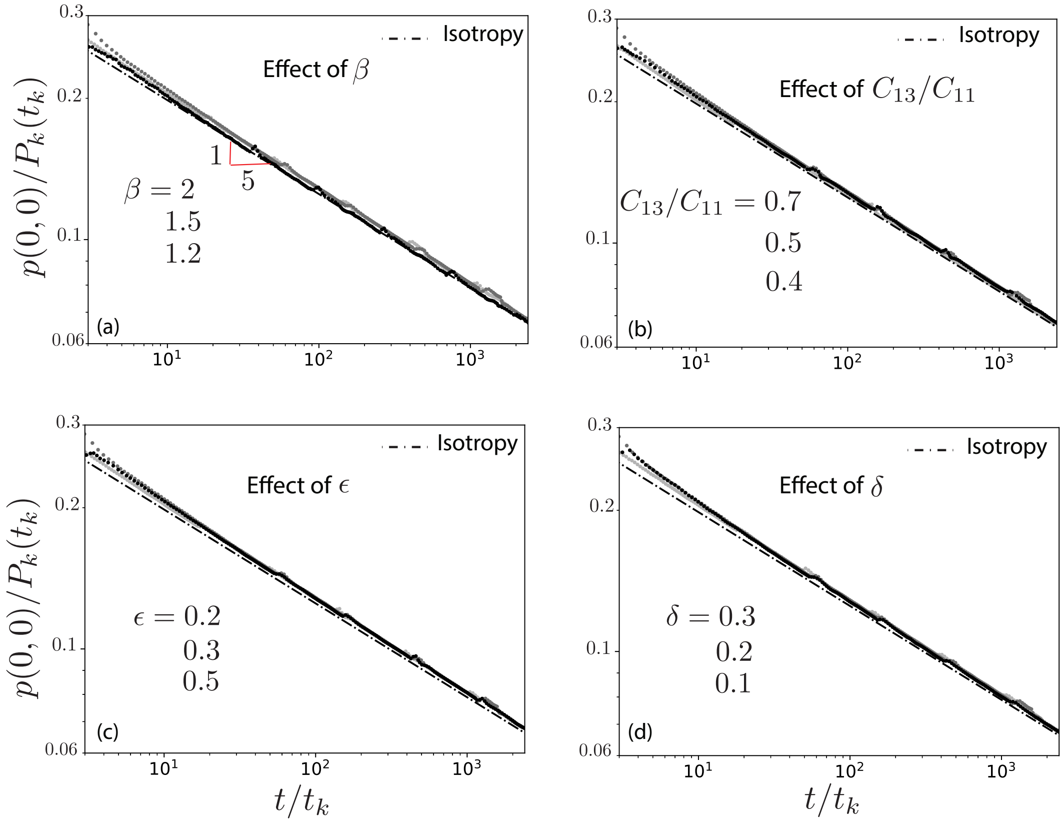

Figure 4.10 – Toughness dominated propagation - Isotropic toughness case: Dimensionless pressure evolution at the injection point $p(0,0)/P_k(t_k)$ with time t/t_k. Reference parameters: $\beta = 1.5$, $C_{13}/C_{11} = 0.5$, $\epsilon = 0.3$, and $\delta = 0.2$. (a) variations of $\beta = (1.2, 1.5, 2)$, (b) variations of $C_{13}/C_{11} = (0.4, 0.5, 0.7)$, (c) variations of $\epsilon = (0.2, 0.3, 0.5)$, and (d) variations of $\delta = (0.1, 0.2, 0.3)$.

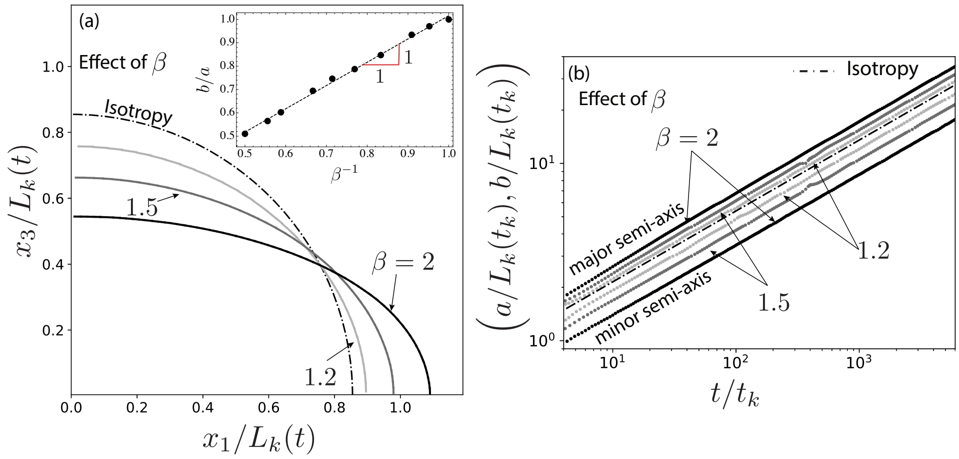

Figure 4.11 – Toughness dominated propagation - Isotropic fracture energy case: (a) Self similar footprint γ_k, and (b) dimensionless major $a(t)/L_k(t_k)$ and minor $b(t)/L_k(t_k)$ semi axis with time t/t_k for different values of $\beta = (1.2, 1.5, 2)$ with $\epsilon = 0.3$, $\delta = 0.2$, and $C_{13}/C_{11} = 0.5$. The inset figure in (a) shows the evolution of the fracture aspect ratio b/a function of β.

4.8.4 Self-similar fracture shape: planar 3D numerical versus approximated elliptical solution

It is interesting to compare our numerical results obtained without any assumptions on the fracture shape and a previous analysis based on the assumption of an elliptical fracture shape (Laubie and Ulm, 2014). In the toughness dominated regime, where the pressure is uniform, one can uses the analytical solution for an elliptical fracture in TI medium (see e.g. section 4.11.1) and either for the assumption of isotropic K_I or G obtain the aspect ratio b/a by minimizing the variations of K_I, respectively G along the front. Using the approximation E'_{app} (4.10) in lieu of the exact E'_α (4.6), Laubie and Ulm (2014); Bessmertnykh and Dontsov (2018) obtained that $b/a \propto \beta^{-1}$ under the assumption of isotropic fracture energy (for weak elastic anisotropy).

Using a similar method (for both E'_{app} or the exact E'_α), we can compare the self-similar fracture aspect ratio in the toughness dominated regime using such an approximated "elliptical" fracture approach with our fully coupled numerical solution. We minimize the variations of either K_I or G along the front using a L_1 norm and twenty sample points in a quadrant of the elliptical fracture front.

The evolution of the aspect ratio as function of β are displayed in figure 4.12 for both the fully coupled numerical results (not assuming an elliptical shape) and the minimization assuming an elliptical shape. The complete numerical results (with the exact E'_α) and elliptical approximation follows the trend $b/a \propto \beta^{-2}$ as expected but with different pre-factors. The discrepancy increases significantly for large anisotropy. For $\beta > 1.25$ (i.e. $\beta^{-1} < 0.8$), the aspect ratio given by the elliptical fracture assumption is overestimated by more than 30%

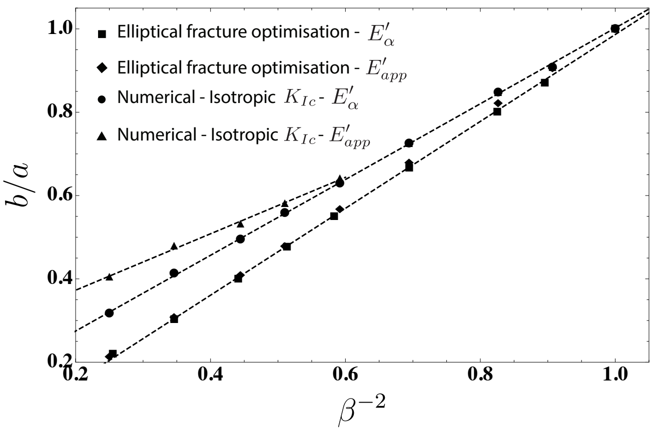

Figure 4.12 – Toughness dominated regime - Isotropic toughness: Comparison of the fracture aspect ratios b/a obtained from the SIF minimization using E'_α (black square) or the approximation E'_{app} (black diamond) for the near-tip elastic modulus and results of the numerical solution using E'_α (black dot) or E'_{app} (black triangles). $\epsilon = 0.3$, $\delta = 0.2$, and $C_{13}/C_{11} = 0.5$ for all cases.

compared to the exact numerical results. For weaker anisotropy ($\beta < 1.25$, i.e. $\beta^{-1} > 0.8$), the two estimations agree well. The numerical results obtained using E'_{app} (black triangles) as the near-tip modulus for the fully HF coupled problem diverge from the ones obtained using E'_α (black dots) for $\beta^{-1} < 0.6$ ($\beta > 1.66$). They underestimate fracture elongation by up to 45%. The variation of the stress intensity factor along the front of an elliptical fracture obviously never exactly disappear (even after minimization) as only a peculiar form of toughness evolution can ensure a exact elliptical shape. Figure 4.13 displays the residual variations obtained after minimization. They are smaller for weak elastic anisotropy, and reaches about 7% in relative term for $\beta = 2$.

The results for the hypothesis of an isotropic fracture energy are summarized in figure 4.14. The difference between the elliptical assumption and the complete numerical solution is smaller than for the case of isotropic toughness. All results follow a trend $b/a \propto \beta^{-1}$. The approximated solutions tends to slightly over-estimate the fracture elongation (especially for stronger elastic anisotropy - $\beta^{-1} < 0.7$). According to figure 4.15, the residuals variations of the stress intensity factor along the elliptical crack are smaller than for the hypothesis of isotropic toughness (at most 4% percent for the largest anisotropy).

4.9 Transition from viscosity to toughness dominated growth

After investigating the hydraulic fracture growth in each of the toughness and viscosity dominated regime, now we focus on the evolution from toughness to viscosity and the time of its occurrence. We compare the numerical results given by the three different toughness functions defined above (elliptical fracture toughness function, isotropic toughness and isotropic fracture energy). The simulations are performed with an initial rectangular do-

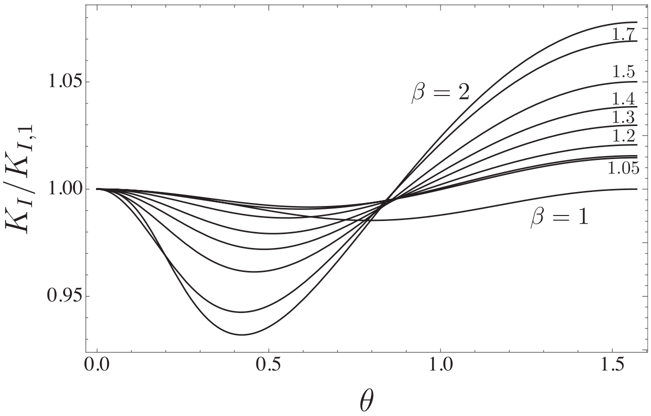

Figure 4.13 – Toughness dominated regime - Isotropic toughness: Residual of the variation of the scaled stress intensity factor $K_I/K_{I,1}$ after minimization as function of $\theta = \arctan\left(\frac{b}{a}\alpha\right)$ with $\epsilon = 0.3$, $\delta = 0.2$, and $C_{13}/C_{11} = 0.5$ for all cases.

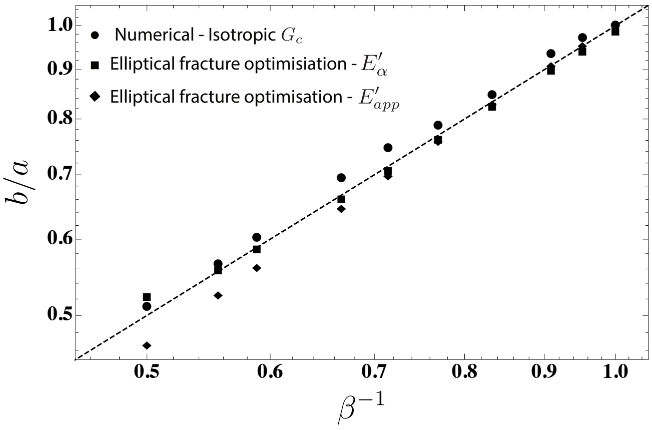

Figure 4.14 – Toughness dominated regime - Isotropic fracture energy: Comparison of the fracture aspect ratios b/a obtained from the numerical solution (black dot), the fracture energy minimization criterion using E'_α (black square) or the approximation E'_{app} (black diamond) for the near-tip elastic modulus as function of β^{-1}. $\epsilon = 0.3$, $\delta = 0.2$, and $C_{13}/C_{11} = 0.5$ for all cases.

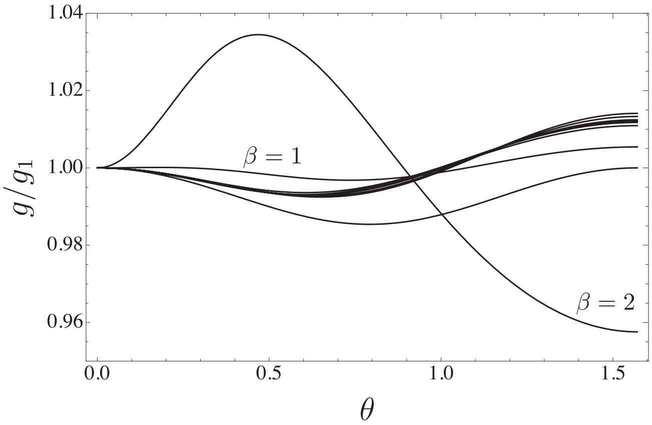

Figure 4.15 – Toughness dominated regime - Isotropic fracture energy: Residual of the variation of the scaled fracture energy G/G_1 after minimization as function of $\theta = \arctan\left(\frac{b}{a}\alpha\right)$ with $\epsilon = 0.3$, $\delta = 0.2$, and $C_{13}/C_{11} = 0.5$ for all cases.

main of 100 cells along $\boldsymbol{e_1}$ and 80 cells along $\boldsymbol{e_3}$. The fracture is initiated with the solution of a radial fracture propagating in viscosity regime. We set the elastic parameters to the values: $(\beta = 1.5, C_{13}/C_{11} = 0.5, \epsilon = 0.3, \delta = 0.2)$. We present the numerical results using the viscosity-to-toughness scaling given in table 4.1 where E_* and K_* are chosen to be inline with the arrester direction $(E_* = E'_1, K_* = K'_1)$. We focus here on the evolution of the semi-major and minor axes function of the dimensionless time $t/t_{mk,1}$ (figures 4.16, 4.17 and 4.18) as the fracture shape, width and pressure profiles are already grasped in the two sections 4.7 and 4.8. We compare our numerical results with the approximated solution M+K (green dot-dashed lines) of Dontsov (2019) obtained by combining the near-tip HF asymptote and the global volume balance assuming an elliptical fracture. This solution depends only on the elasticity ratio β and the toughness ratio κ. It does not account for the proper evolution of the elastic modulus E'_α. It may be applicable in the transitional part when the semi-major axis propagates in the viscosity regime whereas the minor axis has reached the toughness regime (Dontsov, 2019). We should also note that the solution of Dontsov (2019) is valid only for high toughness ratio: $\kappa^{-1} = 10$, however we reported in the figures 4.16, 4.17 and 4.18 for more comparison with the numerical results (despite the significant error that is expected).

We also plot the radial viscosity solution for the isotropic case in blue dot-dashed lines with $\langle E' \rangle$ is the value of the elastic modulus and $\langle K' \rangle$ is the value of the fracture toughness (M-regime in figures 4.16, 4.17 and 4.18). The analytical solution of the elliptical fracture in toughness dominated regime (equations (4.21) and (4.27)) is presented in red dotted-dashed lines. The purple line present the limit where the numerical results for the major (in dashed) and the minor (in dot-dashed) axis are within 7% of the elliptical toughness solution.

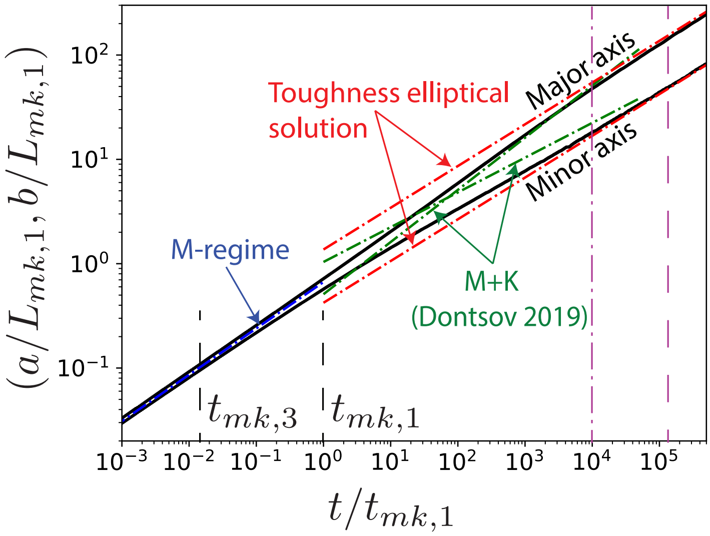

Figure 4.16 – Elliptical toughness - Viscosity to toughness regime: Dimensionless major $a(t)/L_{mk,1}$ and minor $b(t)/L_{mk,1}$ semi axis in log-log scale function of the dimensionless time $t/t_{mk,1}$ for toughness ratio $\kappa^{-1} = 1.2$ with $\beta = 1.5$, $\epsilon = 0.3$, $\delta = 0.2$, and $C_{13}/C_{11} = 0.5$. Comparison with the approximated solution of Dontsov (2019) in green-dashed lines.

4.9.1 Elliptical toughness

Figure 4.16 displays the fracture semi-axis with time for the elliptical toughness anisotropy (4.19) for a toughness ratio $\kappa^{-1} = 1.2$. The ratio of the transition time scales of the arrester and divider direction is (see equation (4.17)) $t_{mk,3}/t_{mk,1} = \beta^{-13/2}\kappa^9 = 0.014$. At early time ($t/t_{mk,1} < 1$), the fracture radius follow closely the isotropic solution of a radial fracture as discussed in section 4.7. In the intermediate regime $10^2 < t/t_{mk,1} < 10^4$, the approximated M+K solution for the major axis $a(t)$ (Dontsov, 2019) is close to the numerical solution but deviates as soon as the fracture radius reaches the elliptical solution for the toughness regime, while for the minor axis, the two solutions (M+K solution and the numerical solution) are obviously different.

The numerical results matches well the exact elliptical HF toughness dominated solution at times larger than $1.3 \times 10^5\, t_{mk,1}$. Notably, The numerical fracture shape evolves in the toughness dominated regime with a constant aspect ratio exactly as predicted by equation (4.21): $b/a = \beta^{-2}\kappa^2 = 3.24$. In terms of dimensionless toughness $\mathcal{K}_1 = (t/t_{mk,1})^{1/9}$ (see table 4.1), the major axis reaches the toughness regime at $\mathcal{K}_1 approx 3.7$ ($t \approx 1.3\, 10^5\, t_{mk,1}$), which is consistent with the estimation obtained for the case of isotropy (Savitski and Detournay, 2002). The minor axis reaches the toughness regime when $\mathcal{K}_3 = \mathcal{K}_1 \times \left(t_{mk,3}/t_{mk,1}\right)^{-1/9} \approx 4.5$ according to figure 4.16 - which corresponds to an earlier time ($t \approx 1.06 \times 10^4\, t_{mk,1} = 75.10^5\, t_{mk,3}$).

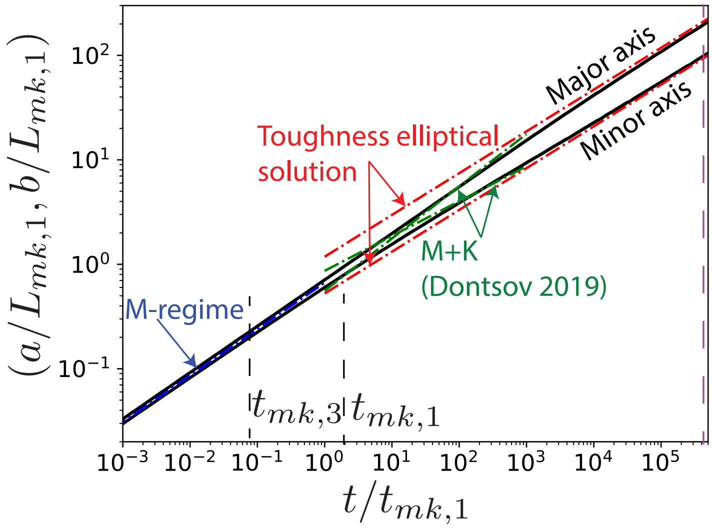

Figure 4.17 – Isotropic toughness ($\kappa = 1$) - viscosity to toughness transition: time evolution of the dimensionless major $a(t)/L_{mk,1}$ and minor $b(t)/L_{mk,1}$ semi axis for $\beta = 1.5$, $\epsilon = 0.3$, $\delta = 0.2$, and $C_{13}/C_{11} = 0.5$. The approximated M+K solution of Dontsov (2019) is displayed in green-dashed lines.

4.9.2 Isotropic toughness

Figure 4.17 presents the numerical solution for the semi-major and minor axes assuming an isotropic toughness function. The analytical solution for the toughness dominated elliptical HF is here plotted for the case $\kappa = 1$. The ratio of timescales is now only function of β: $t_{mk,3}/t_{mk,1} = \beta^{-13/2} = (0.07$ for the chosen $\beta = 1.5)$. The viscosity dominated regime extends further squeezing the transition to a narrow region. The M+K approximated solution captures the order of magnitude of the evolution of the major respectively minor axis in a narrow range of times $70 < t/t_{mk,1} < 3.10^2$ (major), respectively $10^2 < t/t_{mk,1} < 8.10^3$. The slope (power-law) of this approximated solution in both cases clearly do not follow the numerical results.

In this case, our numerical solution indicates that the major and minor axis reach the toughness dominated regime for $\mathcal{K}_1 \approx 4.3$ ($t \approx 5 \times 10^5 / t_{mk,1}$ and $\mathcal{K}_3 \approx 3.7$ ($t \approx 10^4\ t_{mk,1}$) respectively. The relative difference between the numerical solution and the toughness dominated elliptical HF solution is larger in that case. This is directly related to the fact that the fracture does not have strictly an elliptical shape in the toughness dominated regime as discussed in section 4.8.4.

4.9.3 Isotropic fracture energy

The results for the isotropic fracture energy case is given in figure 4.18. The toughness ratio is here a function of the elasticity $\kappa^{-1} = \sqrt{E'_3/E'_1} = \beta^{-1/2}(= 0.8$ for $\beta = 1.5)$ which we use for

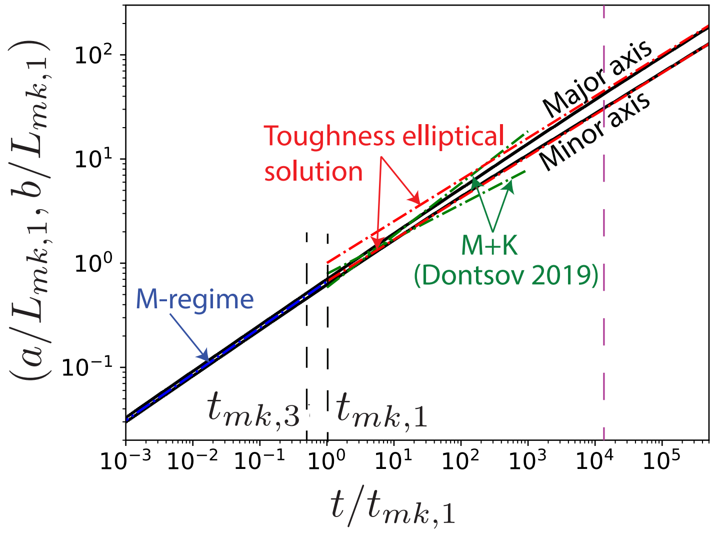

Figure 4.18 – Isotropic fracture energy viscosity to toughness transition: time evolution of the dimensionless major $a(t)/L_{mk,1}$ and minor $b(t)/L_{mk,1}$ semi axis for $\beta = 1.5$, $\epsilon = 0.3$, $\delta = 0.2$, and $C_{13}/C_{11} = 0.5$. The approximated M+K solution of Dontsov (2019) is displayed in green-dashed lines.

the toughness dominated HF elliptical solution. The ratio of the characteristic timescales now reduces to: $t_{mk,3}/t_{mk,1} = \kappa^{9}\beta^{-13/2} = \beta^{-2}(= 0.44)$. The effect of anisotropy of toughness and elasticity are not compounded in this case. As a result, the fracture propagates with a smaller aspect ratio ($b/a = \beta^{-1}$) in the toughness dominated regime. The transition to the toughness regime occurs earlier for such an isotropic fracture energy assumption: at $\mathscr{K}_1 \approx 2.9$ ($t \approx 1.4\times10^{4}\ t_{mk,1}$) for the major axis, and $\mathscr{K}_3 \approx 1.13$ ($t \approx 1.3\times10^{4}\ t_{mk,1}$) for the minor axis. The numerical results at large time follows the elliptical HF toughness dominated solution (with a slight deviation that is barely visible in log-log scale). The fracture shape is not far from being elliptical in that case as discussed in section 4.8.4. The approximated M+K solution (possibly viable in the transition between viscosity and toughness regime) exhibit different power-law of time for the minor and major axis evolution compared to the fully coupled numerical results.

4.10 Conclusions

Propagation of a planar HF perpendicular to the isotropy plane is arguably the most common configuration encountered during the stimulation of unconventional hydrocarbon reservoirs. Using a fully coupled HF solver, we have quantified the impact of transverse isotropy on the growth of a hydraulic fracture, notably the elongation of the fracture in the divider direction and its shortening in the arrester direction.

Using a change of reference frame and the solution for a edge dislocation in an orthotropic medium, we have obtained an exact expression of the elastic modulus controlling the near-tip elastic operator (4.6) as function of the angle between the local fracture propagation direction and the isotropy plane (see figure 4.1). This near-tip elastic modulus enters both in the local near-tip elastic operator and the Irwin matrix relating the energy release rate and the stress intensity factor. This exact expression of the near-tip elastic modulus quantifies the validity of an approximated expression put forward previously (Laubie and Ulm, 2014) which appears to be valid only for weak elastic anisotropy ($\beta \leq 1.2$). As a result, approximated solutions for the growth of a finite HF in a TI material using this approximation in combination with the assumption of an elliptical fracture do compare reasonably well with our fully coupled numerical results only for weak anisotropy ($\beta \leq 1.2$). Assuming the fracture shape to be elliptical overestimates the exact fracture aspect ratio by more than 30% for larger elastic anisotropy ($\beta > 1.5$) and isotropic toughness.

It is important to recall that the fracture has strictly an elliptical shape only for a very peculiar case of toughness anisotropy that can be deduced from the elliptical crack elastic solution (4.11.1). We have derived from the TI elliptical fracture solution, a solution for HF growth in the toughness dominated regime (for such a form of elliptical toughness anisotropy). Our numerical solver perfectly reproduces this toughness dominated solution.

In the viscous dominated regime, toughness does not affect HF growth. Our results show that elastic anisotropy leads to a slight elongation of the fracture in the divider direction in this viscous regime, with aspect ratio scaling as $b/a \approx 0.76\beta^{-1/3}$. The other dimensionless elastic parameters have a relatively small effect.

In the toughness dominated regime, the fracture is more elongated than in the viscosity dominated regime both for the hypothesis of elliptical toughness, isotropic toughness or isotropic fracture energy. The intensity of the elongation strongly depends on the type of toughness anisotropy. As already mentioned, the fracture is elliptical only when toughness evolves according to equation (4.19) where $b/a = (\kappa/\beta)^2$. For an isotropic toughness ($\kappa = 1$), the aspect ratio evolves as $b/a \approx 0.9\beta^{-2}$, consistent with the ratio of the LEFM asymptote between the orthogonal directions ($\boldsymbol{e}_1$ and $\boldsymbol{e}_3$). The other elastic parameters have a second order effect (at most about 10% of variation). The elongation is less pronounced for the case of an isotropic critical fracture energy, where $b/a \approx \beta^{-1}$. Here again the other elastic parameters do not impact fracture growth significantly.

We have explored numerically (for a given set of elastic coefficients), the transition between the viscosity and toughness dominated regimes. Our results confirm the expression of the transition time-scales $t_{mk,1}$ and $t_{mk,3}$ obtained from scaling considerations. The ratio of these time-scales $t_{mk,3}/t_{mk,1} = \beta^{-13/2}\kappa^9$ govern how early fracture elongation start to increase from its initial value in the viscosity dominated regime. The exact time at which the toughness regime is reached depends on the type of toughness evolution. However, to first order it is consistent with the limit obtained for isotropy (Savitski and Detournay, 2002): i.e $\mathscr{K} > 3.5$ for toughness dominated growth. The approximated transitional (M+K) solution (Dontsov, 2019) based on an elliptical fracture and applicable for large toughness ratio ($\kappa^{-1} > 10$) was used for comparison with the numerical results in the case of small toughness ratio $\kappa^{-1} = 1.2$. The two solutions have the same order of magnitude for the fracture dimensions (with different power law of time) in the transition regime between viscosity and toughness dominated growth.

The extension of the implicit level set algorithm to account for transverse isotropy has proven robust for all realistic values of material properties investigated here. It provides a robust solution for planar 3D HF growth in TI. Of course, extreme anisotropy $\beta > 2$ causes numerical difficulties as the fracture curvature becomes extreme in the divider direction ($\boldsymbol{e}_1$) thus requiring finer discretization.

For practical applications, the variation of fracture toughness as function of the local propagation direction (angle α) is clearly of first importance, as already pointed out for the elastic isotropy / toughness anisotropic case (Zia et al., 2018). Our results reinforce the need for better experimental characterization of the mode I fracture toughness of TI material in different directions. Unfortunately, such laboratory measurements are rare and often focus mostly on the plane-strain case of a planar crack propagating at angle with the isotropy plane, and not for different value of α as per the configuration of figure 4.1. Our results indicate a positive effect of anisotropy on vertical containment of hydraulic fractures propagating in finely layered sedimentary formation: a possible explanation for the small vertical extent of HFs in finely layered sedimentary rock even in the absence of in-situ stress contrast. Ultimately, laboratory experiments of HF growth in TI materials with proper measurements of the evolution of the fracture shape are required to further test the theoretical results presented here.

4.11 Supplemental material

4.11.1 Elliptical hydraulic fracture - toughness dominated solution

From the solution of the elliptical fracture under uniform pressure developed in section 2.5.2, the stress intensity factor along the elliptical front is obtained function of elastic constant B_o as:

$$K_I = \frac{B_o}{4}\sqrt{\pi a}E'_\alpha p\left(\sin^2\theta + \left(\frac{b}{a}\right)^2\cos^2\theta\right)^{1/4}. \tag{4.22}$$

$$B_o = 16\left(\frac{b}{a}\right)^{1/2}\frac{1}{\int_0^{2\pi} E'_\alpha(\alpha(\theta)) \times \left((b/a)^2\cos^2\theta + \sin^2\theta\right)^{1/2}\mathrm{d}\theta}. \tag{4.23}$$

with: $\tan\alpha = \dfrac{a}{b}\tan\theta$.

It is rather simple to obtain a growth solution for a hydraulic fracture in the toughness dominated regime. We write $K_{Ic,3}$ as the material toughness in the divider direction $\boldsymbol{e_3}$ and E'_3 the corresponding near-tip elastic modulus. First, to ensure a self similar growth of an elliptical fracture, the toughness must be equal to the stress intensity factor at all points along the fracture front. The toughness variation must therefore has *exactly* the following form:

$$K_{Ic}(\alpha(\theta)) = K_{Ic,3}\frac{E'_\alpha}{E'_3}\left(\sin^2\theta + \left(\frac{b}{a}\right)^2\cos^2\theta\right)^{1/4} \tag{4.24}$$

From the previous equation, we directly obtain the relation between the ellipse aspect ratio (at $\theta = 0, \pi/2$) and the ratios $\beta = E'_1/E'_3$ and $\kappa = K_{Ic,1}/K_{Ic,3}$:

$$\frac{b}{a} = \left(\frac{K_{Ic,1}}{K_{Ic,3}}\frac{E'_3}{E'_1}\right)^2 = \left(\frac{\kappa}{\beta}\right)^2. \tag{4.25}$$

Under quasi-static propagation, $K_I = K_{Ic}$ at all times such that equations (4.22) and (4.24) provide the following expression for the net pressure:

$$p(t) = \frac{4K_{Ic,3}\sqrt{a/b}}{B_o E'_3\sqrt{\pi b(t)}}, \tag{4.26}$$

The evolution of the semi- minor and major axis can then be obtained by enforcing the fact that for an impermeable medium the volume of the fracture must be equal to injected volume: $V_{frac} = Q_o t$. One then obtains:

$$b(t) = \left(\frac{3tQ_o E'_3(b/a)}{8K_{Ic,3}\sqrt{\pi}}\right)^{2/5}, \quad a(t) = \left(\frac{K_{Ic,3}}{K_{Ic,1}}\frac{E'_1}{E'_3}\right)^2 b(t) \tag{4.27}$$

which complete the solution.

5 Laboratory experiments: Materials and Hydraulic Fracture Tests

The experimental program is driven by the desire to explore hydraulic fracture behaviour in different propagation regimes (viscosity vs toughness). We have seen in the previous chapter that the fracture shape is more elongated in the divider direction, but that its exact geometry is not strictly elliptical unless the fracture toughness follows a particular form (chapter 4). In this chapter, we restrict our experimental survey to one material: a slate Del Carmen. This material's elastic properties vary significantly between static and dynamic measurements. Both elastic parameters and fracture toughness are anisotropic and are measured in this chapter. We present preliminary results of two distinct hydraulic fracture tests, in the toughness viscosity dominated regimes. A special consideration is given to the roughness of the fracture surface created during the test.

5.1 Experimental hydraulic fracturing setup

5.1.1 Hydraulic fracturing frame

The experimental setup is restricted to cubic blocks. A true triaxial confinement is applied via six flat-jacks (figure 5.1). The triaxial cell providing this confinement went through a qualification test (see appendix B1). The poly-axial confinement is necessary in order to control the plane of fracture propagation. The fluid is injected using a constant displacement stepping motor pump and therefore tests are considered to be in volume control provided that the system is stiff enough that the fluid compressibility effects dominate only the early stage of the tests. Fractures are initiated from a manufactured flaw and fluid injection proceeds until the fracture interacts strongly with one or more specimen boundaries. The pressure measurements used are transducers which straddle needle-type control valves. The pressure downstream of the valve is corrected for viscous losses in order to give an estimate of the injection pressure at the fracture inlet. The flow control valve serves to dissipate the elastic energy that is stored in the fluid during the pressurization phase.

An active acoustic monitoring system consisting of 64 piezoelectric transducer has been developed in the Geo-Energy Laboratory. Half of the transducers are connected to a function generator and amplifier to be used as excitation sources, while the other 32, acting as receivers, are wired to a high-speed acquisition system to record acoustic data at 50 MHz. The transducers can be placed on all sides of the sample (figure 5.2), with most transducers on the sides parallel to the fracture plane in order to estimate the fracture thickness with transmitted waves. The duration of a full acquisition is approximatively 2.5 seconds, allowing us to track the fracture growth during the fluid injection.

A well is drilled in a cubic block of Del Carmen slate along the minimum horizontal axis as depicted in figure 5.1. The block is notched at mid-distance to enhance the planarity of the fracture. In order to reduce the compressibility effect, a needle valve was placed near the wellbore with a pressure gauge for measuring the upstream and downstream pressure. The maximum confinement is along the vertical direction $\boldsymbol{e_3}$ to clamp the bedding planes as much as possible and promote HF normal to the bedding plane. More details about the procedure of the experiments and the acquisition system are given in appendix B1.

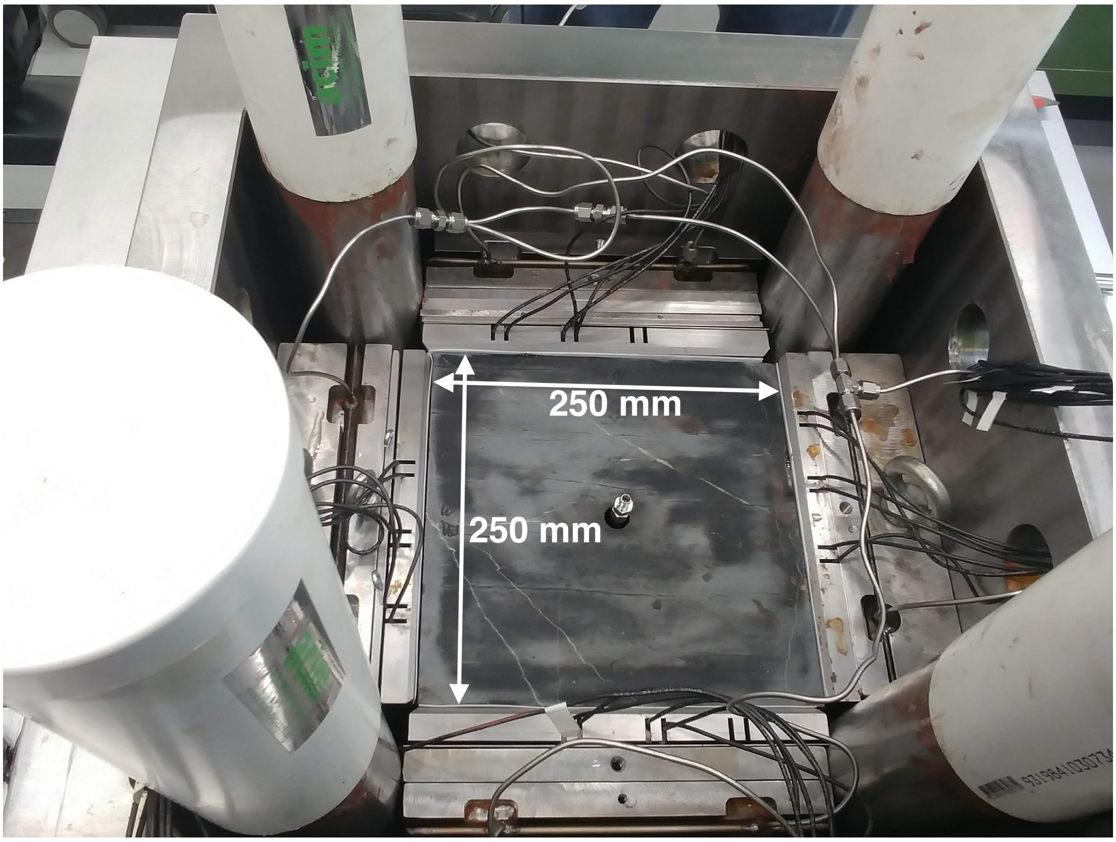

Figure 5.1 – A cubic block of Del Carmen slate in place in the polyaxial cell (without connection of the wellbore).

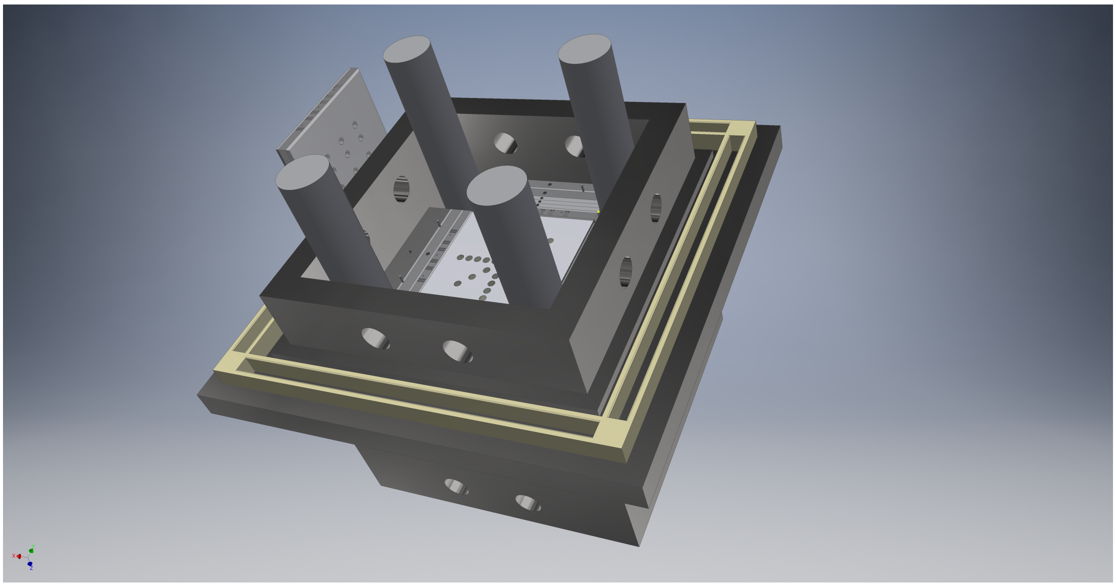

Figure 5.2 – 3D drawing of the reaction frame with top of the cell open. The platens for the acoustic transducers are also displayed in the frame.

5.1.2 Experimental design

Early time-compressibility effect

There are three important phases during a HF test: the pressurization phase (no HF growth), the initiation phase and the propagation phase. The propagation phase is when the fracture is driven by a constant flow rate Q_o, whereas the initiation phase occurs at an early time when the fluid is stored by the compressibility of the system (injection line, wellbore). This effect is mostly governed by the fluid and the injection system and is characterized by the compliance U where (Lecampion et al., 2017; Lhomme, 2005):

$$U = c_f V_{inj}$$

where V_{inj} is the volume of the injection system and c_f is the fluid compressibility c_f (= 10^{-5} MPa^{-1} for glycerol and 2.1×10^{-4} MPa^{-1} for silicone) . After breakdown, the amount of fluid stored in the system will be released such that the flow rate entering the fracture temporarily exceeds the pump rate Q_o. The fluid flux Q_{in} entering the fracture at any given time is derived as the following:

$$Q_{in} = Q_o - U\frac{\partial P}{\partial t}$$

Prior to initiation, Q_{in} is negligible and U is obtained from the slope of the pressurisation phase. Thus, we can estimate the compliance downstream and upstream the valve with the given system of equations:

$$\begin{cases} U_d = & c_f V_{d,inj} \\ U_u = & U - U_d \end{cases}$$

Scaling analysis

In order to properly design the experiments that are relevant with respect to the field conditions, we use dimensional analysis to better determine the most important problem parameters among the injection rate Q_o, the fluid viscosity $\mu' = 12\mu$, the system compliance U, the minimum confining stress σ_h, the near-tip elastic modulus along the divider (or arrester) direction E'_1 (or E'_3 or $\langle E' \rangle = \dfrac{E'_1 + E'_3}{2}$) and the corresponding fracture toughness $K'_1 = \sqrt{\frac{32}{\pi}} K_{Ic,1}$ (or K'_3 or $\langle K' \rangle = \dfrac{K'_1 + K'_3}{2}$).

In each phase (early time/initiation phase and large time/constant injection phase), three limiting regimes govern the HF propagation in impermeable elastic isotropic media (Lecampion et al., 2017) which are also valid for transverse isotropic media (see section 4.4). The fracture begins in a regime where a fluid lag is present (called $\hat{O}$ in figure 5.3 in the early time and O in the large time propagation), transitions to a viscosity regime (called $\hat{M}$ in the early time and M in the large time propagation), and then to a to toughness regime (called $\hat{K}$ in the early time and K in the large time propagation). These transitions depend on the problem parameters and are characterized by the timescales defined in table 5.1.

The field experiments are performed with a large injection rate that enhances the propagation along the viscosity dominated regime (blue trajectory in figure 5.3). In order to reproduce the field experiments at the laboratory scale, we can compensate for the effect of the injection rate ($\sim 10^4 ml/s$ in the field versus $\sim 0.1 ml/s$ in the lab) using a very viscous fluid (see table (5.1)). First, it is interesting to investigate the most probable trajectory regarding the lab facilities which corresponds to the toughness trajectory (red trajectory in figure 5.3). In the following we aim to investigate these two limiting cases by varying the fluid viscosity μ', the flow rate Q_o, and confining stress σ_h.

Six tests were performed in the toughness regime referred as SLATE_K_# and two in the viscosity dominated regime referred as SLATE_M_#. The SLATE_K_# is driven by a solution of glycerine, water and blue dye whose viscosity was measured using a rotating viscosimeter, whereas for SLATE_M_#, we used a silicone oil. Table 5.2 presents the parameters and the initial condition of each test. We qualify a test in table 5.2 as successful when a horizontal hydraulic fracture is visibly observed. Only two tests out of six in the toughness regime were successful, whereas in the viscosity case one out of two was successful. The remaining tests mostly propagated in the bedding plane parallel to the wellbore or even by debonding the epoxy of the wellbore.

The tests parameters of the three successful tests (two in the toughness and one in the viscosity regime) are relisted in table 5.3 whereas the values of the corresponding timescales are given in table 5.4. The system compliance U was computed from the slope of the pressurization phase. From table 5.4, comparing the test duration for both SLATE_K_3 and SLATE_K_4 tests with the large time/constant injection time scale $t_{\hat{k}k}$, the fracture propagation has taken place in the toughness $\hat{K}K$ transition (red trajectory in figure 5.3). For SLATE_M_1 test, it takes place

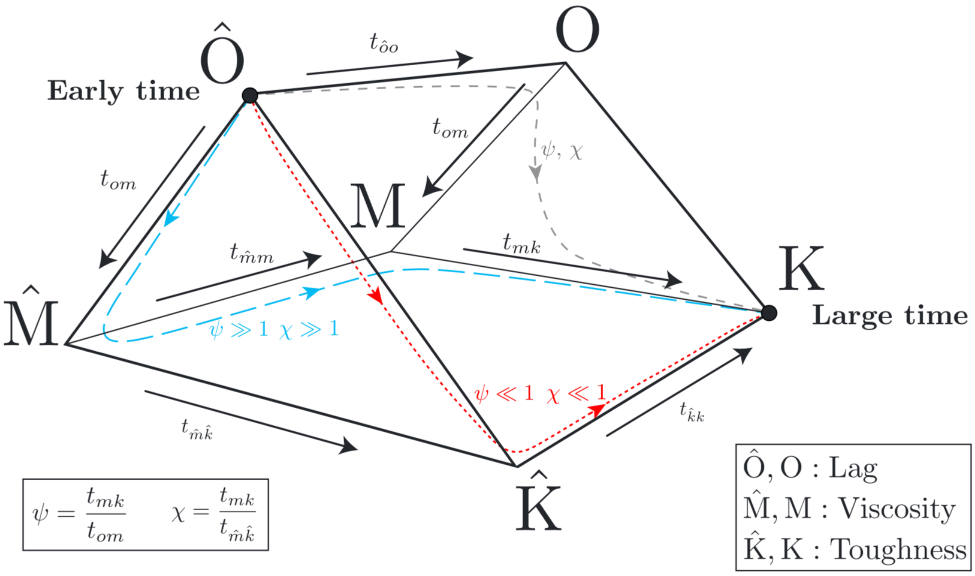
Early time
$\hat{O}$
O
$t_{\hat{o}o}$
t_{om}
t_{om}
ψ, χ
M
$t_{\hat{m}m}$
t_{mk}
K
Large time
$\hat{M}$
$\psi \gg 1 \; \chi \gg 1$
$\psi \ll 1 \; \chi \ll 1$
$t_{\hat{m}\hat{k}}$
$t_{\hat{k}k}$
$\hat{K}$
$\psi = \frac{t_{mk}}{t_{om}}$ $\chi = \frac{t_{mk}}{t_{\hat{m}\hat{k}}}$
$\hat{O}, O$: Lag
$\hat{M}, M$: Viscosity
$\hat{K}, K$: Toughness

Figure 5.3 – Schematic evolution of the initiation and propagation of radial fracture in isotropic impermeable media (taken from Lecampion et al. (2017)).

more in the lag-viscosity transition with $t_{\hat{o}o}$ and t_{om} larger than the test duration. We report in section 5.3 the experimental results of these HF tests.

5.2 Material characterization

5.2.1 Mineralogy

Slate is a fine-grained, foliated metamorphic rock which has issued from a sedimentary type of shale composed of clay or volcanic ash. The foliation is caused by a strong metamorphic compression. The Del Carmen slate is originally from the Cabrera Mountains of North-West Spain. It has a low water absorption, and a bulk density of $\rho = 2.77 \; g/cm^3$.

The mineralogy composition and organic content of Del Carmen slate are determined through powder XRD analysis. The intensity of the diffraction presented as the peak height and as the integrated intensity at peak angle 2θ is given in figure 5.4. We observe a concentration of 35.7% of laminated silicates, in particular chlorite and mica. Depending on the orientation of the bedding, we count for 19 to 145 of layers of mica per millimeter moving from the cross section parallel to the bedding to the cross-section normal to the bedding. Mineral of quartz is also detected in high fractions estimated to be 43.61% of the total volume. Minor constituents identified from the XRD analysis are feldspars (3.15%) and plagioclases (12.84%). Note that neither carbonates nor clay components are found in the powder. Also, at the macroscopic scale, we observe the presence of veins of calcites of centimeter size (figure 5.1).

Time scales	
t_{om}	$\frac{E_1'^2 \mu'}{\sigma_o^3}$
t_{mk}	$\frac{E_1'^{13/2} Q_o^{3/2} \mu'^{5/2}}{K_1'^9}$
$t_{\hat{m}\hat{k}}$	$\frac{E_1'^{5/2} U^{1/2} \mu'}{K_1'^3}$
$t_{\hat{o}o}$	$\frac{E_1'^{1/2} U^{3/4} \mu'^{1/4}}{Q_o^{3/4}}$
$t_{\hat{m}m}$	$t_{\hat{o}o}$
$t_{\hat{k}k}$	$\frac{K_1' U^{5/6}}{E_1'^{1/6} Q_o}$

Table 5.1 – Transition time scales between limiting propagation regimes (Lecampion et al., 2017).

	σ_v (MPa)	σ_H (MPa)	σ_h (MPa)	μ' (Pa.s)	Q_o (ml/s)	status
SLATE_K_1	15	7	0	7.2	10^{-4}	Failure
SLATE_K_2	15	5	0	7.2	10^{-4}	Failure
SLATE_K_3	20	5	0.5	7.2	10^{-2}	Success
SLATE_K_4	20	5	0.5	7.2	2.5×10^{-3}	Success
SLATE_K_5	20	5	0.5	7.2	2.5×10^{-3}	Failure
SLATE_K_6	20	20	1	7.2	10^{-2}	Failure
SLATE_M_1	20	20	1	120	5×10^{-3}	Success
SLATE_M_2	20	20	0.5	120	5×10^{-4}	Failure

Table 5.2 – Sample configuration for laboratory tests in toughness and viscosity dominated regime.

	E_1' (GPa)	K_1' (MPa.m$^{1/2}$)	σ_h (MPa)	μ' (Pa.s)	Q_o (ml/s)	U (ml/GPa)	Pressurization rate Q_o/U (MPa/s)
SLATE_K_3	35.4	7.85	0.5	7.2	10^{-2}	214	0.0467
SLATE_K_4			0.5	7.2	2.5×10^{-3}	170.2	0.0146
SLATE_M_1			1	120	5×10^{-3}	255.8	0.0195

Table 5.3 – Sample configuration and test parameters for the three successful lab experiments. The elastic properties and fracture toughness are taken from the results of static tests (section 5.2.2) and SCB tests (section 5.2.4).

	Propagation time t_p (s)	$t_{\hat{k}k}$ (s)	$t_{\hat{o}o}$ (s)	t_{om} (s)	t_{mk} (s)	$\mathcal{K}_{end} = \left(t_p/t_{mk}\right)^{1/9}$
SLATE_K_3	20	1.8×10^5	-	-	5×10^{-4}	3.24
SLATE_K_4	100	6×10^5	-	-	7×10^{-5}	4.83
SLATE_M_1	100	-	1.8×10^5	10^7	72	1.04

Table 5.4 – Experimental HF propagation time, transition time scales and dimensionless parameters of the three successful lab experiments.

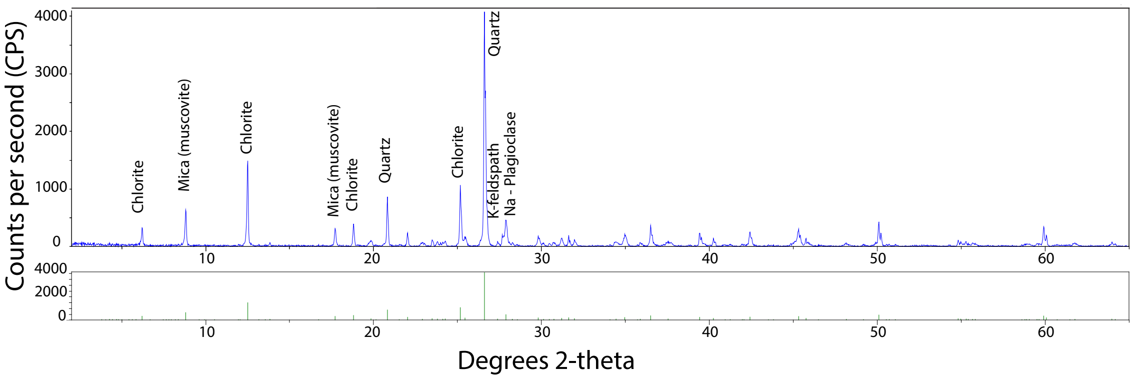

Figure 5.4 – Mineralogical composition of Del Carmen slate in intensity using XRD method. We thank Professor Thierry Adatte for the mineralogical analysis that was done in the institute of Earth Sciences in University of Lausanne.

5.2.2 Static measurements

A transverse isotropic rock has a hexagonal symmetry with five independent elastic constants, which can be determined from either ultrasonic velocity measurements or quasi-static mechanical tests. Three cores were cut in three different orientations with respect to the bedding: parallel, normal and 45° to the symmetry axis (see figure 5.5). We denote θ as the angle between the cylindrical symmetry axis and the horizontal axis $\boldsymbol{e_1}$. We adopt the same notation as before (chapters 2 and 4): $\boldsymbol{e_i}$ refers to the basis in the material frame, whereas $\boldsymbol{e'_i}$ refers to the local (rotated) basis, where: $\boldsymbol{e_3}$ is the normal to the bedding (or so-called "divider"), $\boldsymbol{e_2}$ is the minimum horizontal axis (normal to the fracture plane) and $\boldsymbol{e_1}$ is the horizontal axis ("arrester") (see figure 5.5).

Laboratory experiments were conducted in a servo-controlled displacement apparatus, in which cylindrical samples of 55 mm diameter and 110 mm height were loaded under a uniaxial loading. Besides the pressure sensors, the vertical deformation ϵ_z was measured by a pair of LVDT displacement transducers and the lateral deformation ϵ_r was measured by a circular strain gage extensometer. We are thankful to Laurent Gastaldo and the Laboratory of Experimental Rock Mechanics (LEMR) for their time and their guidance in running these tests.

Figure 5.5 shows the three orientations of the cylindrical cores. The axis of the sample is either along the arrester, the divider or titled at 45° with respect to the bedding planes. The elastic moduli in the divider and the arrester directions (E_1, E_3) and the poisson ratios (ν_{12}, ν_{13}) are determined from the horizontal and the vertical cores (using the elasticity equations in (figure 5.6). The remaining elastic parameter G_{13} is evaluated using the vertical loading-deformation expression for the third sample (see figure 5.6).

Figures 5.7, 5.8 and 5.9 present the vertical compressive stress σ_z function of the vertical deformation ϵ_z for the parallel, normal and tilted (45°) orientations respectively. The samples were loaded until 40 MPa, unloaded to 5 MPa and then reloaded until failure. The rupture

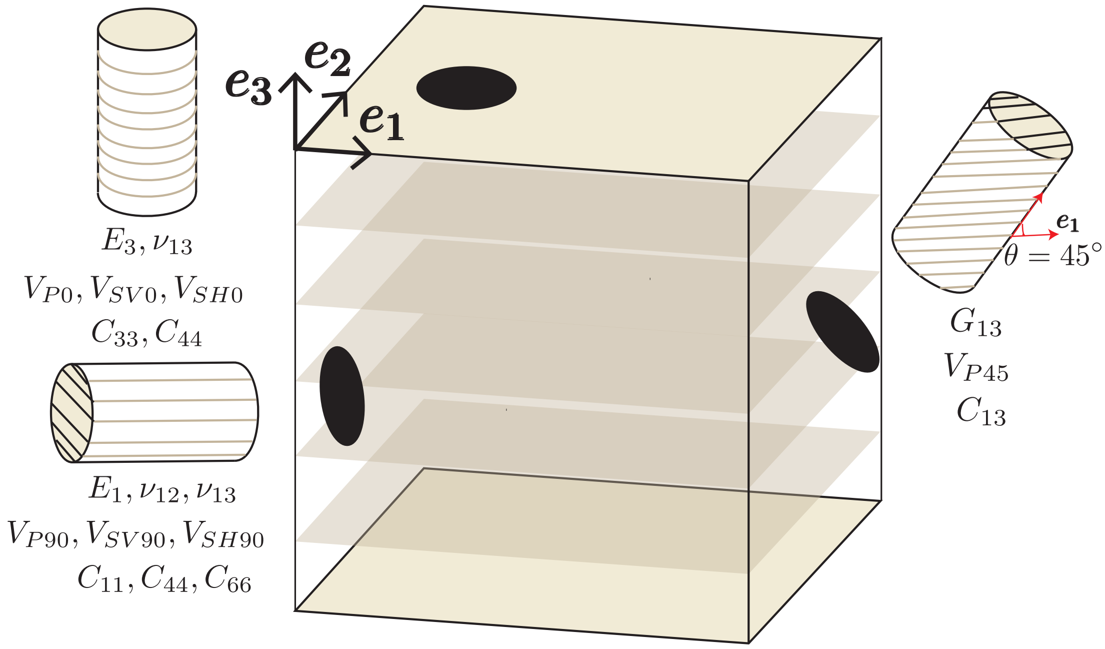
e_3
e_2
e_1
E_3, ν_{13}
V_{P0}, V_{SV0}, V_{SH0}
C_{33}, C_{44}
E_1, ν_{12}, ν_{13}
$V_{P90}, V_{SV90}, V_{SH90}$
C_{11}, C_{44}, C_{66}
e_1
$\theta = 45°$
G_{13}
V_{P45}
C_{13}

Figure 5.5 – Schematic slate block showing the configuration of the three cores and the mechanical properties measured from each orientation.

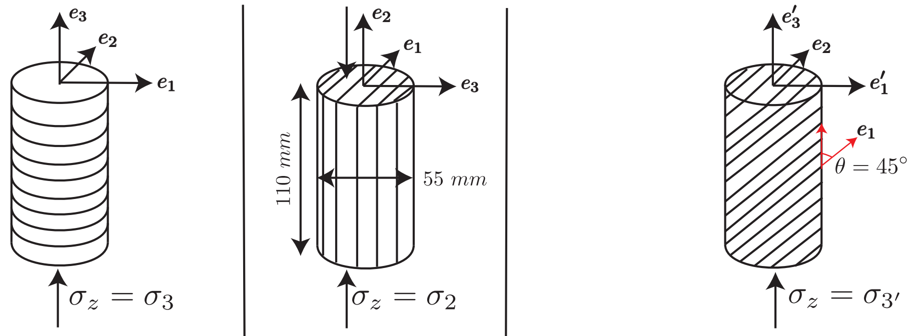
e_3
e_2
e_1
$\sigma_z = \sigma_3$
e_2
e_1
e_3
$110\ mm$
$55\ mm$
$\sigma_z = \sigma_2$
e'_3
e_2
e'_1
e_1
$\theta = 45°$
$\sigma_z = \sigma_{3'}$

$$\epsilon_r = \sqrt{\epsilon_1 + \epsilon_2}$$

$$\frac{\epsilon_3}{\sigma_z} = \frac{1}{E_3}$$

$$\frac{\epsilon_1}{\sigma_z} = \frac{\epsilon_2}{\sigma_z} = -\frac{\nu_{13}}{E_3}$$

$$\epsilon_r = \sqrt{\epsilon_1 + \epsilon_3}$$

$$\frac{\epsilon_2}{\sigma_z} = \frac{1}{E_1}$$

$$\frac{\epsilon_1}{\sigma_z} = -\frac{\nu_{12}}{E_1}$$

$$\frac{\epsilon_3}{\sigma_z} = -\frac{\nu_{13}}{E_3}$$

$$\epsilon_r = \sqrt{\epsilon_{1'} + \epsilon_2}$$

$$\frac{\epsilon_{2'}}{\sigma_z} = -\cos^2\theta\frac{\nu_{12}}{E_1} - \sin^2\theta\frac{\nu_{13}}{E_3}$$

$$\frac{\epsilon_{3'}}{\sigma_z} = \frac{\cos^4\theta}{E_1} + \frac{\sin^4\theta}{E_3} + \frac{\sin^2 2\theta}{4}\left(-\frac{2\nu_{13}}{E_3} + \frac{1}{G_{13}}\right)$$

$$\frac{\epsilon_{1'}}{\sigma_z} = \frac{\sin^2 2\theta}{4}\left(\frac{1}{E_3} + \frac{1}{E_1} - \frac{1}{G_{13}}\right) - \frac{\nu_{13}}{E_3}\left(\sin^4\theta + \cos^4\theta\right)$$

Figure 5.6 – Elastic equations governing the uniaxial compression test for a TI media (Cho et al., 2012).

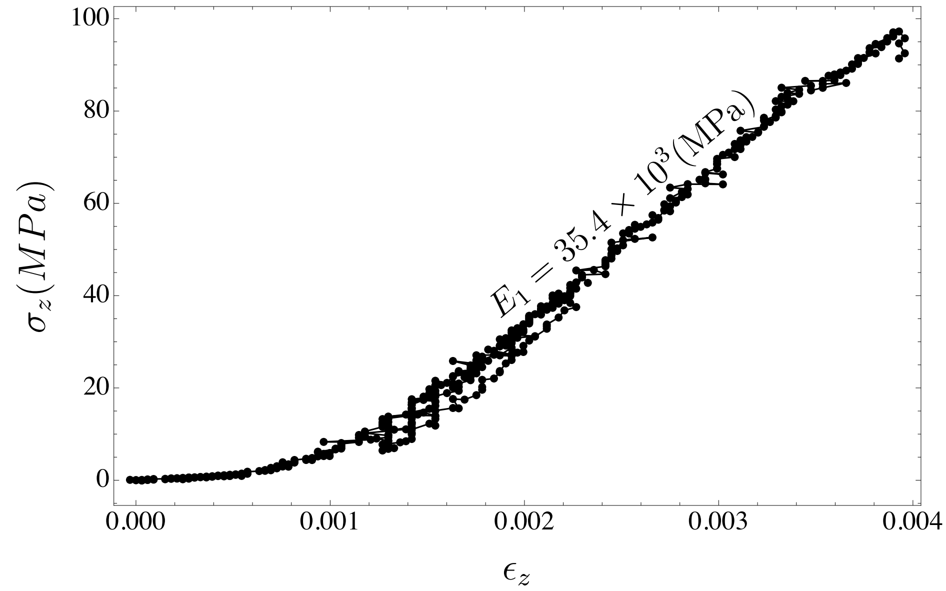

Figure 5.7 – Uniaxial loading function of the vertical strain during a cycle of loading-unloading on a cylindrical core of slate. The axial compression is applied parallel to the bedding.

occurred at a uniaxial compressive strength (UCS) of $\sigma_{z,max}$ = 97.2 MPa along the bedding and of $\sigma_{z,max}$ = 172.6 MPa normal to the bedding. There is almost a ratio of 1.8 of anisotropy of UCS between the two orthogonal directions. The elastic moduli are determined from the second loading curve and are equal to E_1 = 35.4 GPa and E_3 = 26.4 GPa, with E_1/E_3 = 1.34. During loading of the third sample (figure 5.9), the maximum load reached $\sigma_{z,max}$ = 111.3 MPa with the highest elastic modulus of E_{45° = 36.06 GPa. This resulted in a shear coefficient of G_{13} = 21.2 GPa.

The poisson ratios obtained from the $\sigma_z - \epsilon_r$ curves (figure 5.10) are very low in comparison to typical values for rocks ($\sim 0.2 - 0.3$). This is may be due to errors in measurements:

$$\nu_{12} = 0, \quad \nu_{13} = 0.029. \tag{5.1}$$

In terms of the stiffness coefficients, we obtain the following elastic tensor (in GPa) for the Del Carmen slate:

$$\begin{cases} C_{11} = & 35.4 \\ C_{33} = & 26.4 \\ C_{12} = & 0.41 \\ C_{13} = & 1.03 \\ C_{44} = & 21.2 \end{cases} \tag{5.2}$$

The aberrant values of C_{12} and C_{13} are again due to the (almost) zero values of the poisson ratios (see chapter 2 for stiffness-poisson ratios and elastic moduli relation).

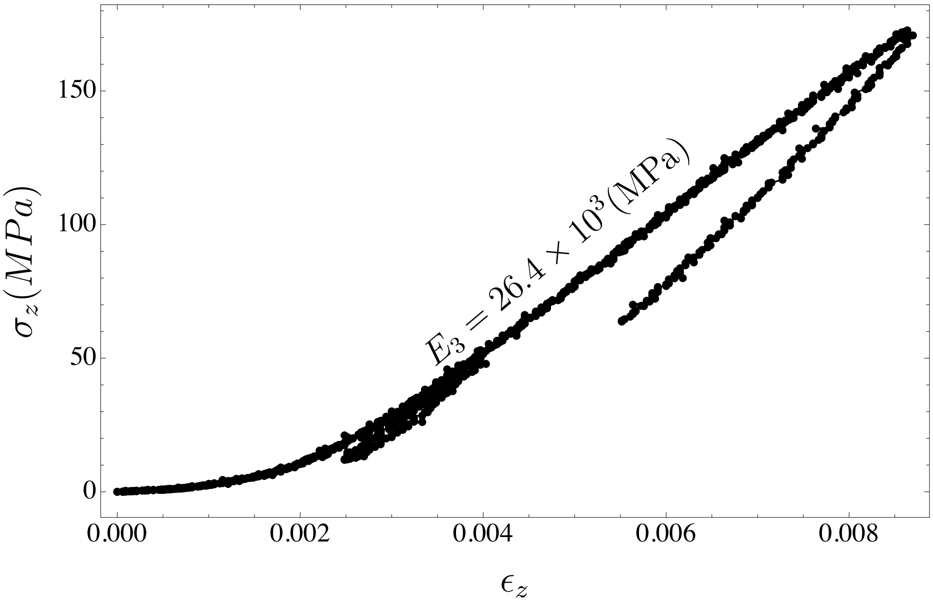

Figure 5.8 – Uniaxial loading function of the vertical strain during a cycle of loading-unloading on a cylindrical core of slate. The axial compression is applied normal to bedding.

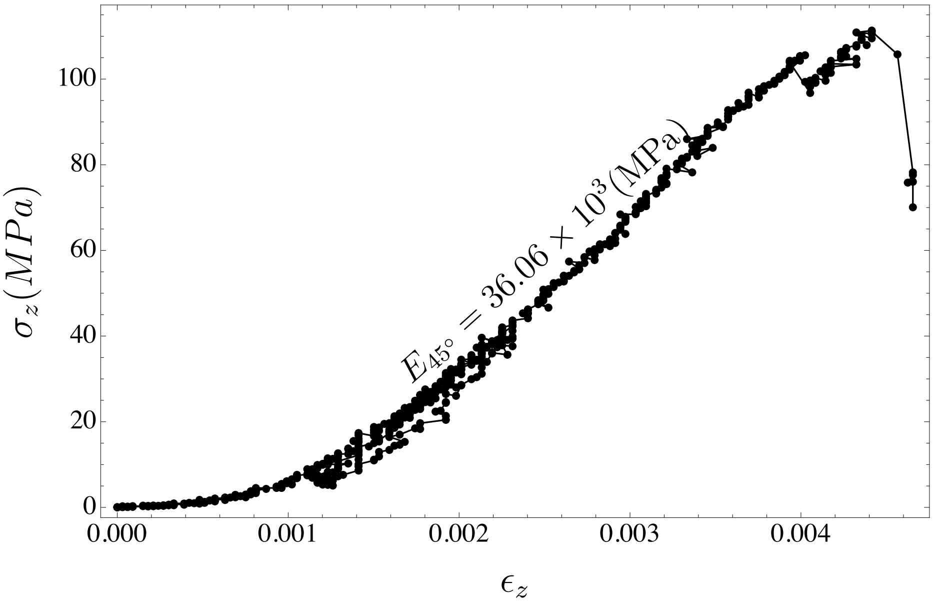

Figure 5.9 – Uniaxial loading function of the vertical strain during a cycle of loading-unloading on cylindrical core of slate. The axial compression is inclined at 45° with respect to the bedding.

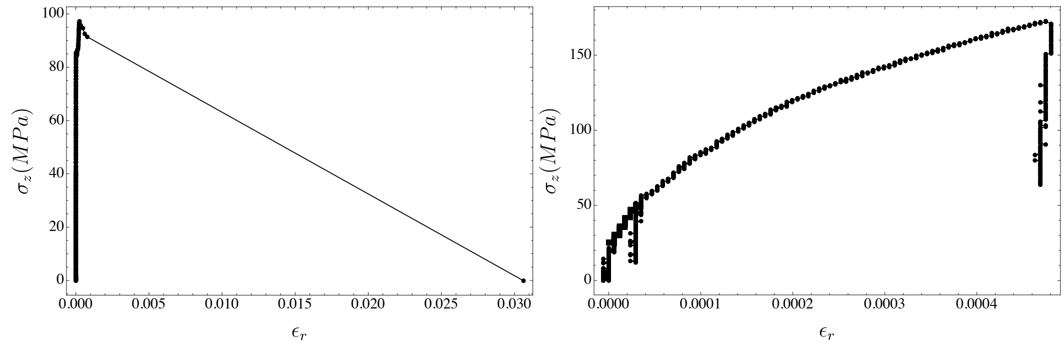

Figure 5.10 – Uniaxial loading function of the radial strain during a cycle of loading-unloading on a cylindrical core of slate. The axial compression is applied parallel to the bedding in the left figure, whereas it is normal to the bedding in the right figure.

5.2.3 Ultrasonic measurements

V_P and V_S

In a vertical TI medium, the P-wave and S-wave velocities change with the wave incidence angle θ (see figure 5.5), measured from the symmetry axis ($\boldsymbol{e_3}$), as in the Christoffel equation (Tsvankin, 2012):

$$\begin{aligned}2\rho V^2(\theta) &= (C_{11}+C_{55})\sin^2\theta + (C_{33}+C_{55})\cos^2\theta \\ &\quad + \sqrt{\left((C_{11}-C_{55})\sin^2\theta - (C_{33}-C_{55})\cos^2\theta\right)^2 + 4\,(C_{13}+C_{55})^2\sin^2\theta\cos^2\theta}\end{aligned} \tag{5.3}$$

Equation 5.3 is the solution of the differential wave equation emerging from Newton's second law of motion (with no body force) for a plane wave propagating in linearly elastic homogenous TI media. In particular, the velocities of the P-wave and the two polarized S (SV and SH) waves propagating along the axis of symmetry $\boldsymbol{e_3}$ ($\theta = 0°$) are given by (Blum et al., 2013):

$$V_{P0} = \sqrt{\frac{C_{33}}{\rho}}, \quad V_{SV0} = \sqrt{\frac{C_{44}}{\rho}}, \quad V_{SH0} = \sqrt{\frac{C_{44}}{\rho}}. \tag{5.4}$$

Similarly, for the vector of velocity along the direction parallel to the bedding (divider):

$$V_{P90} = \sqrt{\frac{C_{11}}{\rho}}, \quad V_{SV90} = \sqrt{\frac{C_{44}}{\rho}}, \quad V_{SH90} = \sqrt{\frac{C_{66}}{\rho}}. \tag{5.5}$$

We use acoustic sensors to measure velocities averaged over four sources-receivers pairs. Figures 5.12 and 5.13 show an example of velocity data at a given pressure from the anisotropic dataset conducted on a cubic sample of 250*250*250 mm^3 of Del Carmen slate. We apply the confining stresses in several steps (figure 5.11). The confining stress varied from 0 to 15 MPa in the vertical and horizontal directions and from 0 to 0.5 MPa for the minimum horizontal

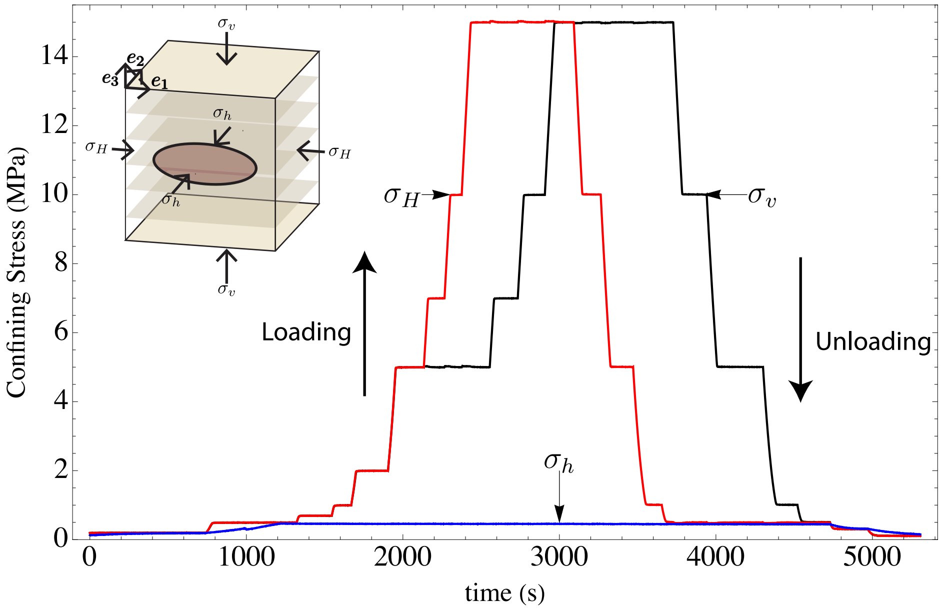

Figure 5.11 – Confining stress (in MPa) function of time (in s) for a cycle of loading-unloading of the cubic block.

stress (see figure 5.11-inset for stress configuration). The horizontal and vertical stress are increase to simultaneously until reaching a pressure of $\sigma_H = \sigma_v = 5$ MPa. Then, the horizontal stress is first increased to the target pressure of 15 MPa, to be followed by σ_v. This same procedure was adopted for the unloading. Thus, the dynamic properties were measured for both loading/unloading pressure steps at various stress levels.

We observe from the tops of figures 5.12 and 5.13 that σ_H has a small effect on the P-waves and that those P-waves are mostly governed by the vertical stress (figures 5.12-bottom and 5.13-bottom). For a given stress, the velocity along the unloading path is greater than the one measured during loading as expected. Under ambient conditions, the bedding planes are microscopically open, the signal for the P-waves crossing the bedding is not even detected up to a threshold stress of $\sigma_{v,m} = 3.5$ MPa for the loading path and to $\sigma_{v,m} = 2.5$ MPa for the unloading path (bottom figure of 5.12). For $\sigma_v > \sigma_{v,m}$, the P-velocity along the slow direction is uniform with 2% of relative error. Additionally, the P-waves parallel to the bedding are measured without minimum confinement with less than 1% of relative error when increasing σ_v (figure 5.13-bottom).

C_{ij} constants from ultrasonic wave velocities

Four of the elastic constants are given by the velocity measurements along the principal material axis $\boldsymbol{e_1}$ and $\boldsymbol{e_3}$ as can be seen from equations (5.4) and (5.5). To determine the fifth elastic parameter C_{13}, we make use of the P-wave velocity in the direction of angle $\theta \neq \{0, 90°\}$

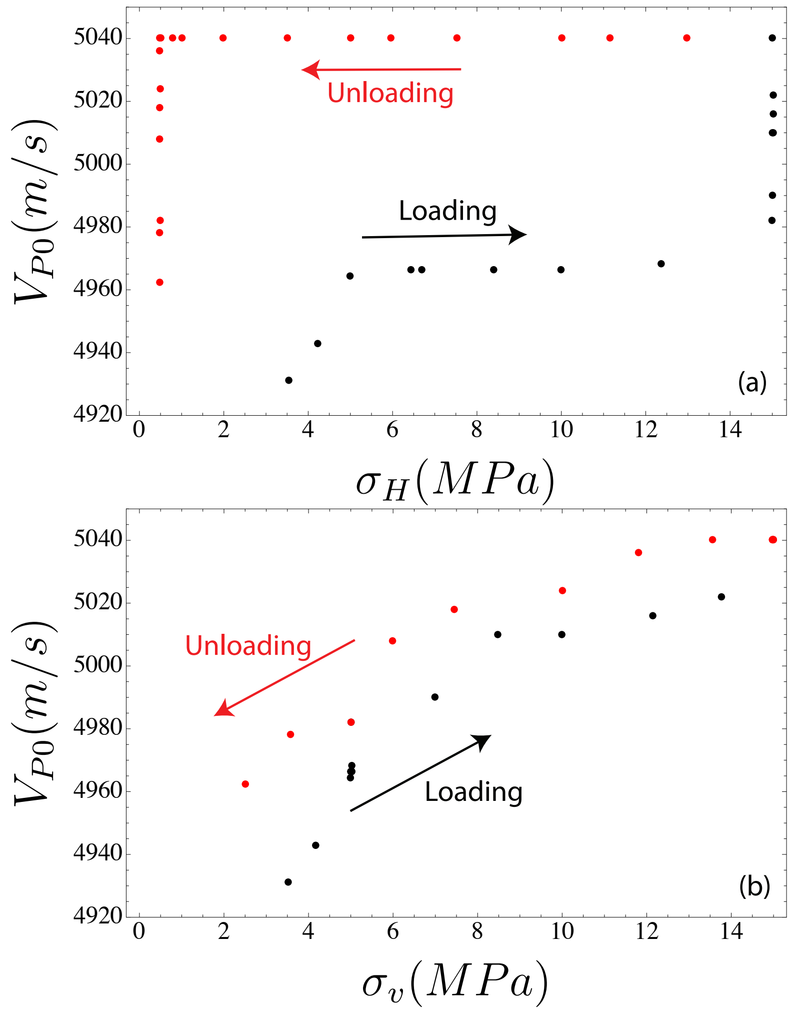

Figure 5.12 – Velocities of the P-waves propagating in the arrester direction of the horizontal (top-figure) and vertical (bottom-figure) confining stress for the loading-unloading cycle defined in figure 5.11.

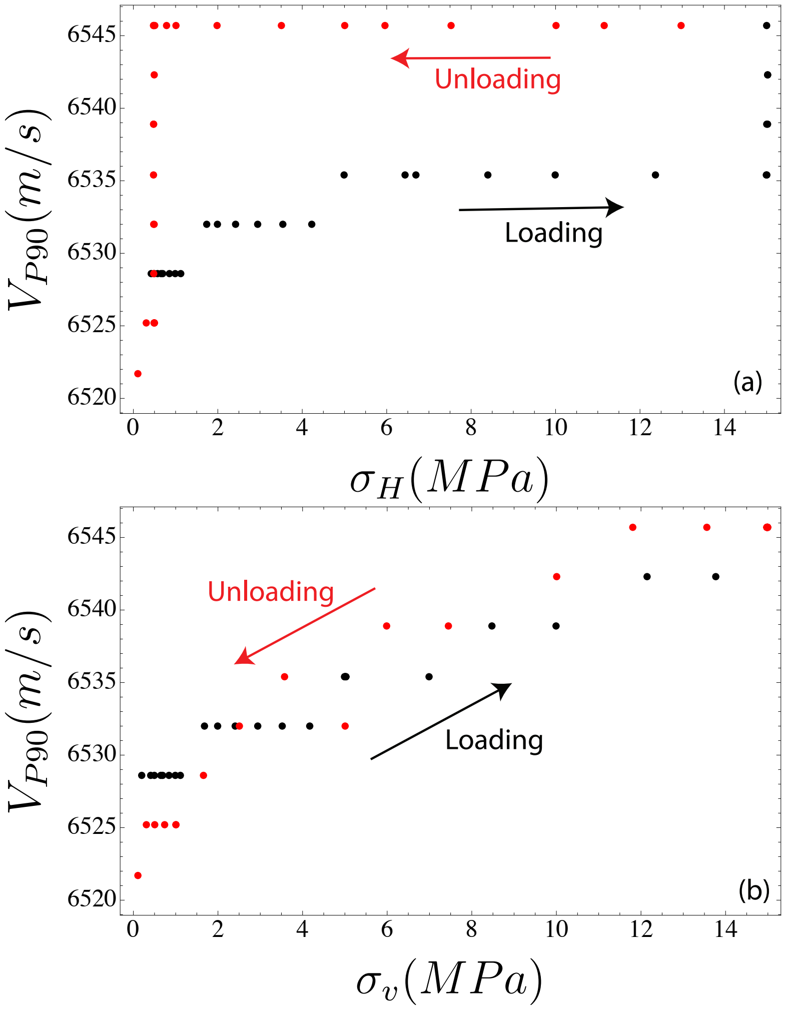

Figure 5.13 – Velocities of the P-waves propagating in the divider direction of the horizontal (top-figure) and vertical (bottom-figure) confining stress for the loading-unloading cycle defined in figure 5.11.

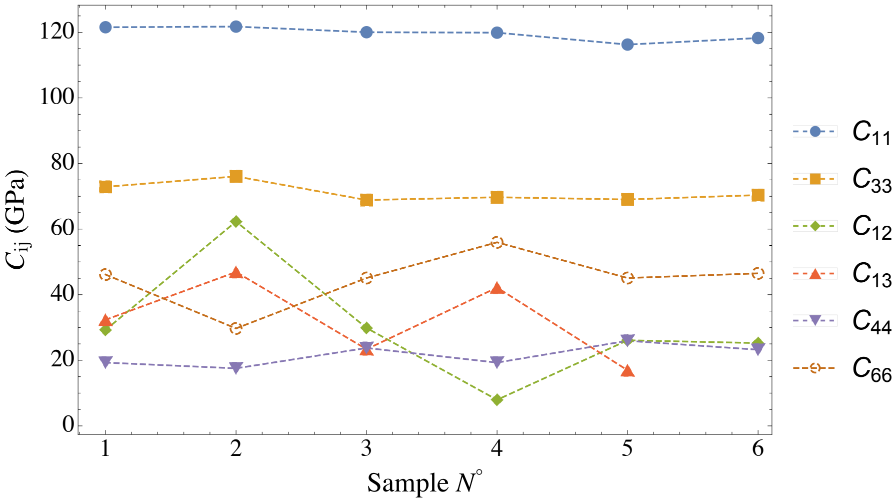

Figure 5.14 – The dynamic stiffness coefficients C_{ij} in GPa for six slate Del Carmen samples.

(ideally 45°) with respect to the symmetry axis $\boldsymbol{e_3}$. For most of our experimental measurements, we had: $\theta = \{20, 68°\}$. We used acoustic transducers of diameter less than the ratio of travel distance $H/20$ which promotes measurement of group velocities instead of phase velocities (Dellinger and Vernik, 1994). Tsvankin (2012) shows that the P-wave group velocity $U_P(\theta)$ is given as a function of the phase velocity $V_P(\theta)$ (equation (5.3)):

$$U_P(\theta) = V_P(\theta)\sqrt{1+\left(\frac{1}{V_P(\theta)}\frac{\mathrm{d}V_P}{\mathrm{d}\theta}\right)^2} \tag{5.6}$$

In the cases of fast and slow velocity directions: $\theta = 0°$ and $90°$, we have $V_P = U_P$. Thus, the set of stiffness coefficients can be defined completely using at least $V_{P0}, V_{P90}, V_{SV0}, V_{SH90}, V_{P45}$ and is derived in figure 5.14 for six test samples. The values of C_{11}, C_{33}, and C_{44} are consistent over the six measurements, as we can see from figure 5.14, with less than ±2 GPa of difference (see table 5.5 for the average values). The error bar for the S-wave measurements is relatively larger than for the P-wave measurements, which enlarges the confidence interval for the C_{66} measurements (±8.4 GPa). For C_{44}, we use a combination of V_{SV0}, V_{SH0}, and V_{SV90} to reduce the relative error. one explanation for the discrepancy in the C_{13} measurements for the six samples (table 5.5) is the numerical solution of the nonlinear equation (5.6), in addition to the error in measuring the angle θ. To determine C_{12}, we use the expression $C_{12} = C_{11} - 2C_{66}$, so that the error of measurement is systematic.

In order to characterize the anisotropy of the slate, we plot the stiffness ratios C_{11}/C_{33}, C_{66}/C_{44} and C_{13}/C_{12} in figure 5.15. For isotropic media, these ratios are equal to unity. The direct compression coefficient is 68% higher along the divider than in the arrester direction $C_{11}/C_{33} \approx 1.68$, whereas it is roughly isotropic for the indirect compression, $C_{13}/C_{12} \approx 1$ (except for the fourth sample). The rock is 70% stiffer to direct shear in the isotropic plane than in the symmetric plane, $C_{66}/C_{44} \geq 1.7$ (figure 5.15).

C_{ij}	C_{11}	C_{33}	C_{12}	C_{13}	C_{44}	C_{66}
GPa	119.62 ± 2	71.15 ± 2.8	30.12 ± 17.7	32.36 ± 12.5	21.51 ± 3.2	44.75 ± 8.4

Table 5.5 – C_{ij} coefficients from six ultrasonic measurements: mean value and standard deviation in GPa.

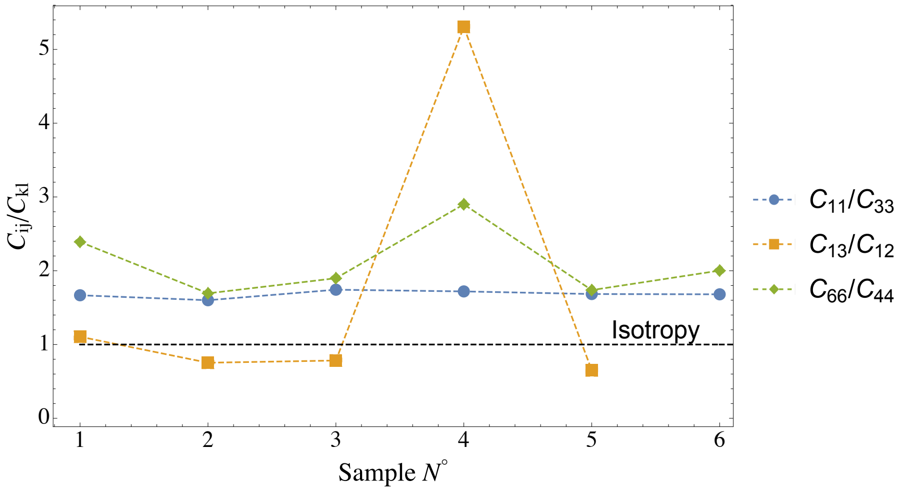

Figure 5.15 – Stiffness ratios C_{11}/C_{33}, C_{13}/C_{12} and C_{66}/C_{44} for six Del Carmen slate ultrasonic measurements.

Discussion

As we can observe from the static and ultrasonic measurements, the dynamic C_{ij} are greater than the the static equivalents (table 5.5 and equation (5.2)). The magnitudes of strain involved in the passage of ultrasonic waves are on the order of 10^{-7} (Mavko et al., 2009). Such a small deformation causes a stress perturbation of 1 kPa magnitude, whereas the stiffness coefficients are of order of $\sim 20-100$ GPa (table 5.5). Only deformation due to elastic deformation of minerals is measured using ultrasonic tests and not that which is due to deformation of the pore structure. Alternately, static deformation captures (besides the pore pressure deformation and the elastic deformation of minerals) some additional energy dissipation due to friction and micro-cracks.

Another source of difference in measurement worth mentioning is the heterogeneity of the sample. The calcite veins, for example, may weaken the material. Besides, the two tests were performed on different scales: the static test was carried out on cylindrical cores of 110 mm, whereas the ultrasonic one was carried out on cubic blocks of 250 mm.

Many fitting laws have been proposed to correlate between static and ultrasonic properties depending on the type of rock and which elastic constants one can fit (engineering elastic moduli, Thomsen' s parameters, or stiffness constants) (Sone, 2012; Lu, 2016; Prioul et al., 2018). Unfortunately, our static measurements are not reliable due to the errors in the measurement of the poisson ratios (5.1) which prevent any further analysis.

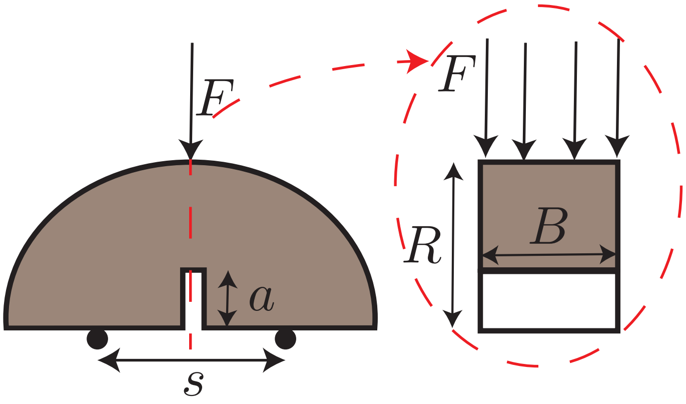

Figure 5.16 – A notched semi-circular specimen in bending (SCB specimen): front view (left-figure) and side view (right-figure).

5.2.4 Fracture toughness tests

The fracture toughness is the critical value of the stress intensity factor (SIF), defined in the framework of Linear Elastic Fracture Mechanics (lefm), at which the crack starts to propagate. The mode I loading characterized by the fracture toughness referred to as K_{Ic} is the most dominant loading in many applications.

To obtain consistent and precise values of K_{Ic}, the International Society for Rock mechanics (ISRM) recommends four tests namely: Chevron-notched short rod in splitting (SR), Chevron-notched round bar in bending (CB), Cracked Chevron-Notched Brazilian Disk in diametrical compression (CCNBD) and Notched semi-circular specimen in bending (SCB). The guidelines providing the requirements for sample preparation is given in Ulusay (2014) as well the explicit formulas for the fracture toughness via finite element analysis.

A semi-circular bending test (see figure 5.16) is performed using a standard servo-control axial compressive frame under a constant vertical displacement rate 0.2 mm/min. A series of SCB tests were carried out for different orientations of the bedding plane with respect to the axial load, in order to elaborate the complete evolution of the anisotropic K_{Ic} function of the angle α (the angle between the propagation direction and the divider direction $\boldsymbol{e}_1$). The advantages of using SCB are that the machining of the sample is simple and that its geometry is relatively small (Kuruppu et al., 2014).

Experimental setup and specimen preparation

Circular disks of thickness $B = 20 \pm 1$ mm are sawed using a high-precision diamond tool and cut into two symmetrical semi-circular cores of radius $R = 37 \pm 1$ mm. Each semi-circular sample is notched at the center of the diameter through 10 ± 0.5 mm of length ($a = 10 \pm 0.5$ mm

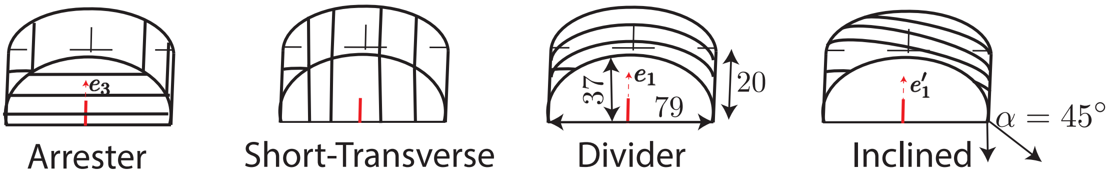

Figure 5.17 – Principal crack orientations with respect to the bedding planes, left to right: Arrester, short-transverse, divider and 45° inclined configurations. The angle α characterizes the fracture propagation direction with respect to the divider.

in figure 5.16) with a diamond saw of 1 mm of thickness. Four configurations of the bedding are considered as can be seen in figure 5.17: bedding planes normal to the notch (Arrester direction: $\alpha = 90°$), bedding planes parallel to the notch (short-transverse), bedding planes parallel to the transversal plane (divider: $\alpha = 0°$), and bedding planes inclined with respect to the transversal plane of $\alpha = 45°$. A minimum of three to four semi-circular specimens were prepared for each configuration to obtain accurate repeatable results. We note that 30% of the samples were not properly manufactured or broken during notching or cutting.

The specimen is placed on the two cylindrical rollers positioned symmetrically with respect to the plane of the notch and distant from each roller by $s = 42$ mm (see figure 5.16). The axial loading is applied by a cylindrical roller at the top of the sample. The vertical load should occur symmetrically between the two bottom rollers. The frame is equipped with an acquisition system for the axial load, time and the axial displacement through LVDT sensor.

Load-displacement curves

We plot in figures 5.18, 5.19, 5.20, and 5.21 an example of the vertical load function of the vertical displacement for the four configurations presented in figure 5.17. A non linear behavior is observed during loading especially over the range of small displacements. The rock is much stiffer compared to typical rocks (Kuruppu et al., 2014). The maximal critical load F_{max} of 11.92 kN is shown in figure 5.18 for a fracture propagating in the arrester direction, while the minimal peak load is in the short-transverse direction, $F_{max} = 2.38$ kN (figure 5.19). Local peaks are also detected (see figure 5.18) due to the propagation of secondary fractures (figures 5.20-inset and 5.21-inset) or to roughness of the fracture plane (see figure 5.18-inset). The fracture propagates along the vertical plane only when the propagation is occurring along the bedding planes (see figure 5.19-inset). Besides the orientation of the bedding planes with respect to the initial notch, the presence of calcite veins (figure 5.19-inset) has a secondary effect on the fracture propagation. For the case of crack propagation in the divider or in the tilted direction of $\alpha = 45°$ (figures 5.20-inset and 5.21-inset), a splitting of the bedding planes is produced simultaneously with the propagation of the main fracture in the all test samples (three samples for the configuration of the parallel notch to the divider direction and four samples for the configuration of the notch inclined at 45° to the bedding). This is expected since the fracture tends to propagate along the weaker plane, reducing the fracture energy.

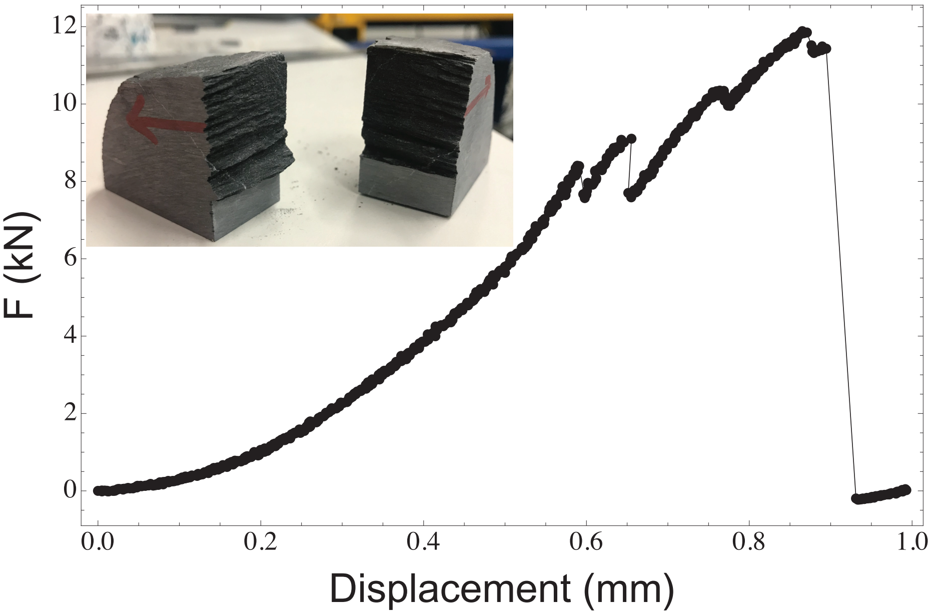

Figure 5.18 – Example of load in kN versus vertical displacement in mm for the arrester configuration (figure 5.17). The critical load is $F_{max} = 11.92$ kN.

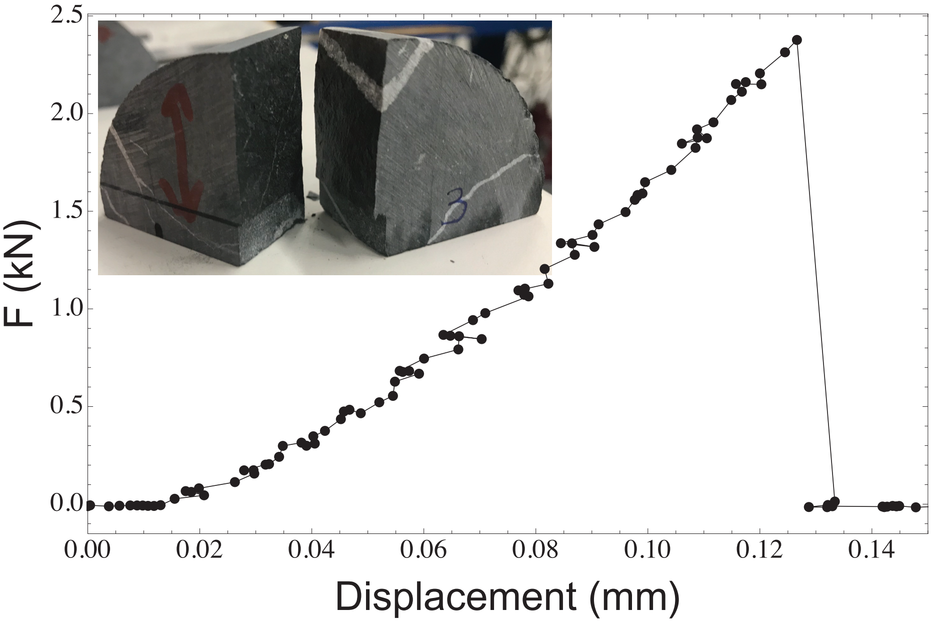

Figure 5.19 – Example of load in kN versus vertical displacement in mm for the short-transverse configuration (figure 5.17). The critical load is $F_{max} = 2.38$ kN.

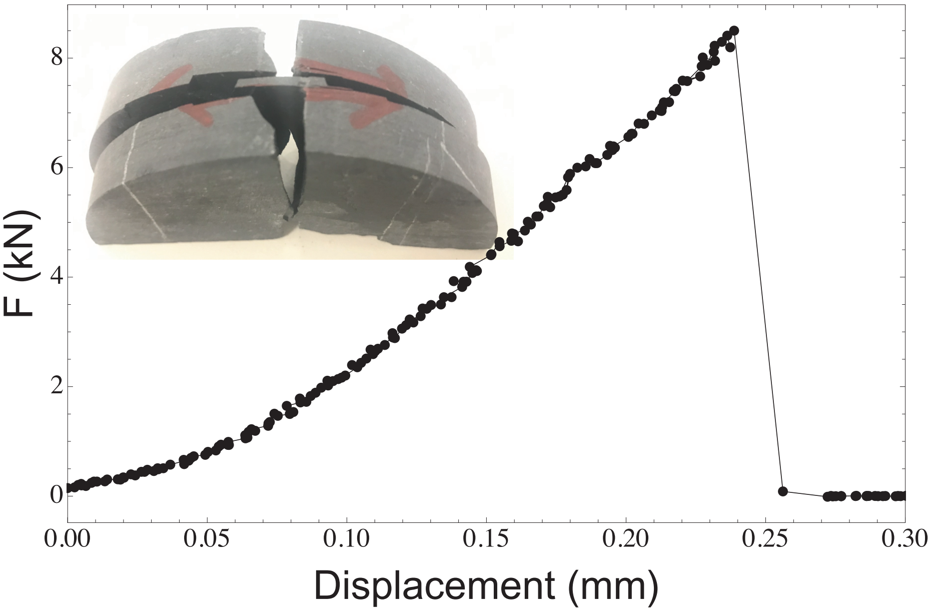

Figure 5.20 – Example of load in kN versus vertical displacement in mm for the divider configuration (figure 5.17). The critical load is $F_{max} = 8.5$ kN.

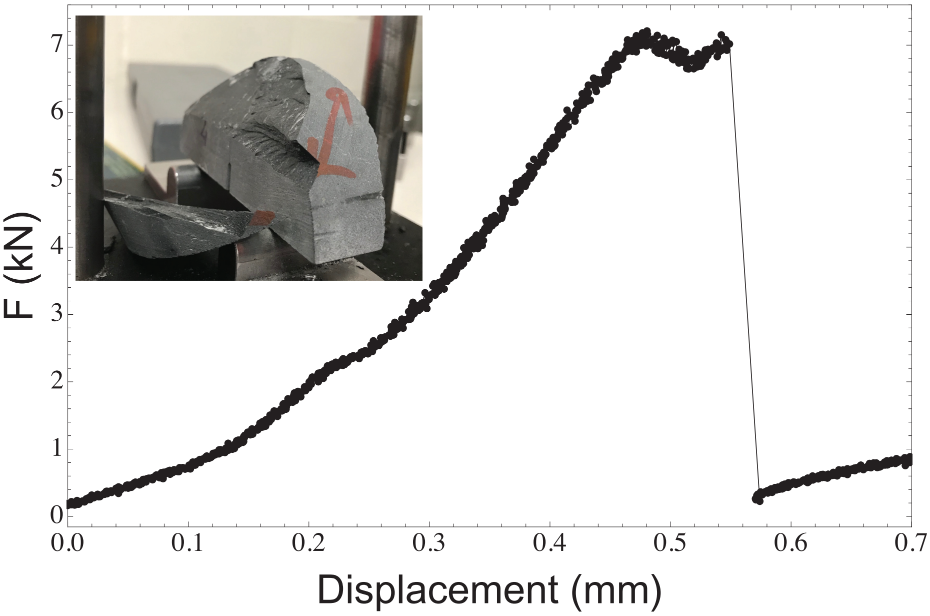

Figure 5.21 – Example of load in kN versus vertical displacement in mm for the 45° inclined configuration (figure 5.17). The critical load is $F_{max} = 7.04$ kN.

	Arrester ($\alpha = 90°$)	Short-transverse	Divider ($\alpha = 0°$)	Inclined ($\alpha = 45°$)
K_{Ic} (MPa.m$^{0.5}$)	3.97	0.83	2.46	3.15

Table 5.6 – Mean value of K_{Ic} for the four configurations: arrester, short-transverse, divider and 45° inclined.

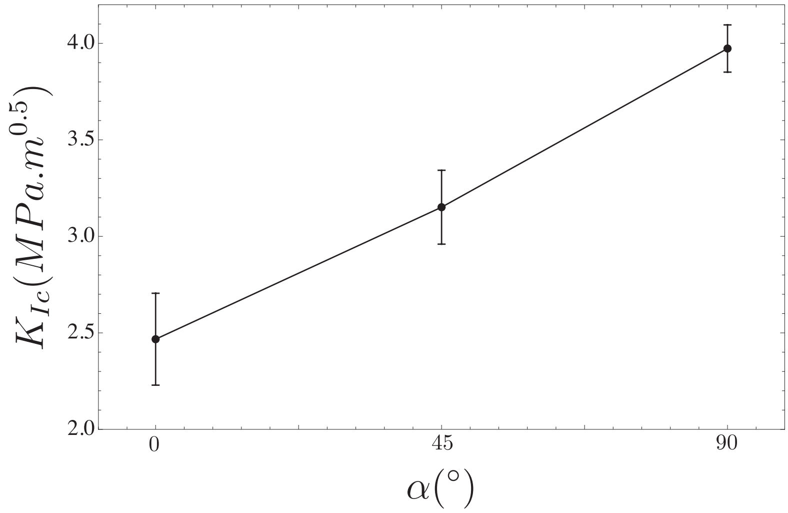

Figure 5.22 – Mean value and standard deviation of K_{Ic} as function of α.

Fracture toughness K_{Ic}

Mode I fracture toughness is determined using the peak load F_{max}, such that (Kuruppu et al., 2014):

$$K_{Ic} = Y' \frac{F_{max}\sqrt{\pi a}}{2RB},$$

$$Y' = -1.297 + 9.516\frac{s}{2R} - \frac{a}{R}\left(0.47 + 16.457\frac{s}{2R}\right) + \left(\frac{a}{R}\right)^2\left(1.071 + 34.401\frac{s}{2R}\right),$$

where Y' is a dimensionless factor depending on the test dimensions and derived using the finite element method under plane-strain conditions. This formula is given for the isotropic media. However it has been shown that the influence of anisotropy on Y' is negligible, in particular for the fracture toughness along the divider and the short transverse (less than 2%) (Nejati et al., 2019).

Table 5.6 shows the mean value of the fracture toughness in the arrester, short-transverse, divider and the tilted direction with respect to the bedding. The fracture toughness is lower along the short-transverse and higher along the arrester $\boldsymbol{e_3}$. The ratio of the fracture toughnesses between the arrester and divider direction is: $\kappa^{-1} = \left(K_{Ic,I}/K_{Ic,3}\right)^{-1} = 1.6$. The evolution of the fracture toughness function of α is illustrated in figure 5.22, where the fracture toughness is an increasing function of α. The accuracy of the results is calculated via the standard deviation with respect to the mean value and is below ±0.23 MPa.m$^{0.5}$.

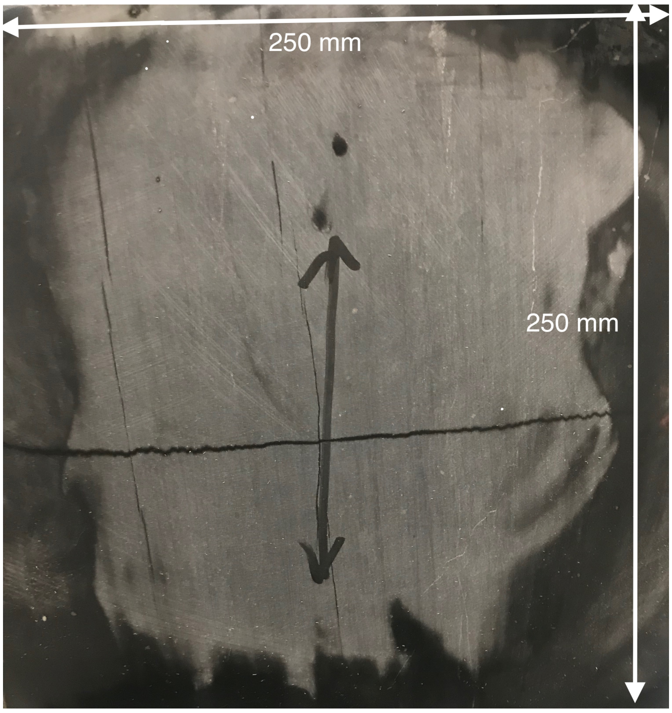

Figure 5.23 – SLATE_K_3 test: A planar hydraulic fracture crossing all sides of the block. The black arrow indicates the orientation of the bedding plane.

5.3 Hydraulic fracturing tests: Preliminary results

5.3.1 Toughness tests

SLATE_K_3 test

A hydraulic fracture test was performed with the configuration given in table 5.2. The test was relatively fast: 25 min of injection with 20s of propagation (table 5.4). To better characterize the propagation regime of this test, we calculate a dimensionless toughness $\mathcal{K}_{end} = \left(t_p / t_{mk}\right)^{1/9} = 3.24$ (table 5.4) which indicates that above $\mathcal{K}_{end} = 3.5$, we reach the toughness dominated regime (Savitski and Detournay, 2002).

The hydraulic fracture propagates planarly as we can observe from figure 5.23. Figure 5.24a represents the pressure at the well as a function of time given by pressure gauges upstream and downstream of the needle valve, whereas figure 5.24b represents the flux entering the fracture as a function of time. At 10 MPa, we adjusted the needle valve in order to decrease the compressibility effect (figure 5.24a). It is hard to differentiate between the initiation pressure and the breakdown pressure, which is estimated to be $P_{d,m} = 34.6$ MPa. We observe from figure 5.24b that there is a sudden jump in the flow rate entering the fracture which exceeds eight times the pump rate Q_o. Unfortunately, we could not proceed further in our analysis due to the bad quality of the acoustic data.

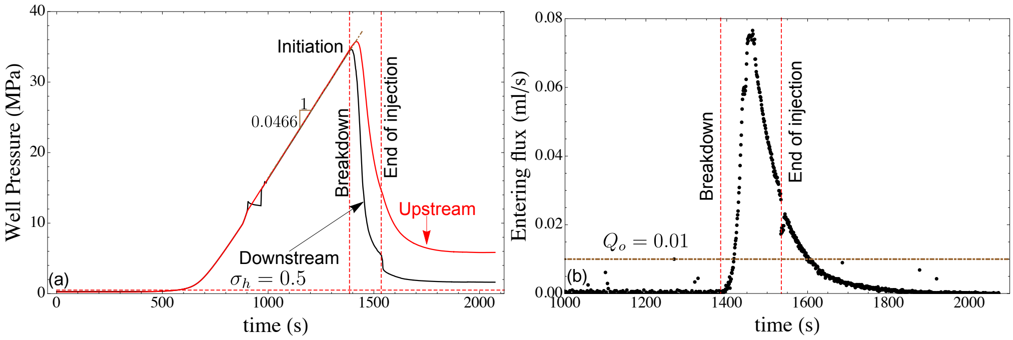

Figure 5.24 – SLATE_K_3 test: Experimental data for the pressure at the well upstream and downstream of the valve in (a), and the flux entering the fracture in (b).

SLATE_K_4 test

The test lasted for 2 hours with 100 seconds of propagation corresponding to a dimensionless toughness $\mathscr{K}_{end} = 4.83$ (table 5.4). The fracture propagated asymmetrically with respect to the well. It was located in the upper-left quarter of the block (the red quadrant in figure 5.25-left). Despite the high ratio between the normal confinement to the bedding plane and the minimum stress $\sigma_v/\sigma_h = 100$, the fracture deviated from the $(\boldsymbol{e_1}, \boldsymbol{e_3})$ plane and opened the bedding planes. After cutting the block in half at mid-height and then at mid-distance along the vertical direction, we extracted the fractured quarter section (the red quadrant in figure 5.25-left) and sliced it in the direction of the minimum stress into a piece of length 5 cm. A sketch of the sliced part of dimensions 10*5*10 cm is presented in figure 5.25-right. We observe that the fracture exhibited a complex patterns. It initiated at the notch and split into two fractures. One fracture followed a bedding plane across the whole block at one centimeter from the well, whereas the main horizontal fracture propagated further and stopped at a bedding plane just before the end of the block. We note that not all the bedding planes are opened (in fact, around 10% are opened). The fracture has not emerged from the right side of the well.

Figure 5.26a displays the pressure at the well with a zoom into the propagation in figure 5.26b. The non linear behavior at the beginning of the pressurization is due to leaks at the tubing connections. As soon as the leaks were fixed, the pressure increases linearly with a pressurization rate of 0.0146 MPa/s. The initiation occurred a few minutes before the breakdown as we can see from figure 5.26a. The breakdown pressure was measured as $P_{d,m} = 31.5$ MPa downstream. During the short propagation time (100s), the pressure decays as a power law function of time, characterizing the toughness dominated regime (1/5) as shown in figure 5.26b.

In figure 5.27a, there is a very significant entery flux overshoot into the fracture (ratio of four between the nominal injection rate and the maximum flux) followed by a stable fracture propagation of a constant rate close to the end of injection. With respect to the propagation duration (100s), we can conclude that the fracture propagation did not reach the steady-state large time regime.

A sudden decrease in the volume of the flat jacks (see appendix B1 for details of the frame) is observed at the moment of initiation as we can see in figure 5.27b. This is expected since the fracture propagated in all three directions (see figure 5.25-right). However, along the plane normal to the minimum stress $\boldsymbol{e_2}$, the flat jacks are more compressed (twice the volume of the flat-jacks normal to the horizontal and vertical directions) compensating for increase of volume of the block in the main horizontal fracture.

Figure 5.28 shows snapshots of the fracture width at eight source-receiver pairs located in the central line in the $\boldsymbol{e_3}$ direction (red-dashed line in figure 5.25-left). The opening profile is a function of the distance from the wellbore at different time of propagation. Only one source-transducer pair notably captured a visible change in signal with an estimated opening of a small magnitude of 80 μm. We observe again that the opening is not evolving symmetrically. Details on the opening analysis is in appendix B1.

Figure 5.29 exhibits the relative change of the acoustic data with respect to the direct diffracted wave before propagation (see appendix B1 for details). The combination of source-receivers considered for the diffraction is presented in purple dots in figure 5.25-left. The vertical axis denotes the recorded time in microseconds whereas the horizontal axis is the experiment time. We focus on the acoustic data corresponding to the period of time of the breakdown and the propagation of HF (see the corresponding downstream pressure plot in black solid line). We observe a change in the arrival time of the diffracted events related to a change in the fracture-tip location. The first arrival of the diffracted signals is delayed by a few seconds from the breakdown time. These events become stationary in time as soon as the fracture tip intersects with the end of the block. The magnitude of the diffracted events is low and it is thus difficult to construct a proper fracture front.

Fracture surface roughness characterization

It is interesting to analyze the postmoterm geometry of the fracture surfaces, in particular in the case of rough surfaces, can be seen from figure 5.30 in the top and bottom faces of the fracture. One common approach is scaling invariance analysis via the concept of self-affine symmetry. A surface is called self-affine when it is statically invariant under the transformation $r \to \lambda r$ and $h \to \lambda^{\xi} h$, where r characterizes the spatial location in the fracture surface, h is the surface height and ξ is the self-affine exponent (Ponson et al., 2006). A number of methods have been developed for measuring the self-affine exponent (Schmittbuhl et al., 1995). We adopt the variable bandwidth method for one dimensional profiles. Two relevant directions are considered: parallel to bedding ($\boldsymbol{e_1}$) and normal to bedding ($\boldsymbol{e_3}$). We divide the profile of length L into windows of width $\delta = \delta_{r_0}$ indexed by the first point r_0. The standard deviation of the height $\sigma = \langle h(\delta) \rangle_{r_0}$ and the difference in height between the maximum and minimum

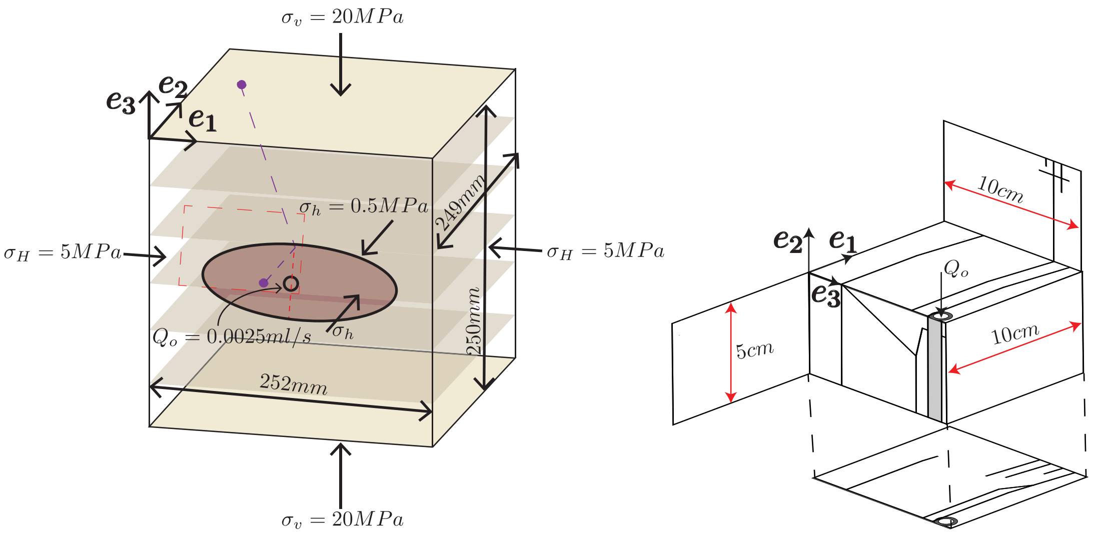
$\sigma_v = 20MPa$
e_3
e_2
e_1
$\sigma_h = 0.5MPa$
249mm
$\sigma_H = 5MPa$
$\sigma_H = 5MPa$
$Q_o = 0.0025ml/s$
σ_h
250mm
252mm
$\sigma_v = 20MPa$
10cm
e_2
e_1
e_3
Q_o
5cm
10cm

Figure 5.25 – SLATE_K_4 test: Left- Loading configuration of SLATE_K_4 test with the exact block size. Right- Schematic of the fracture patterns (black lines) for the upper-left quarter of the block (red dashed quadrant in left figure).

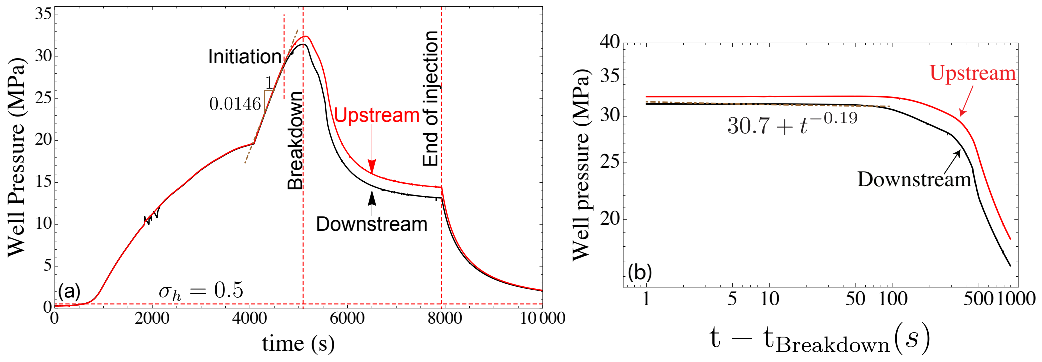

Figure 5.26 – SLATE_K_4 test: Experimental data for the pressure at the well upstream and downstream of the valve in (a), with a zoom at the propagation in log-log scale in (b).

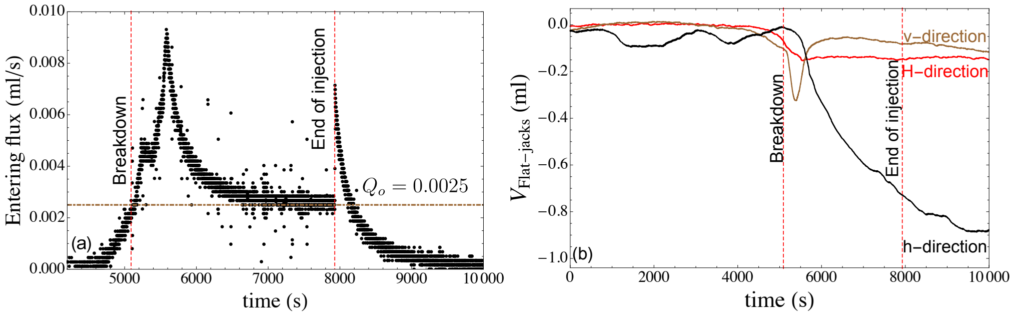

Figure 5.27 – SLATE_K_4 test: (a) Experimental data for the flux entering the fracture with time and (b) Experimental data for the flat-jack volumes with time.

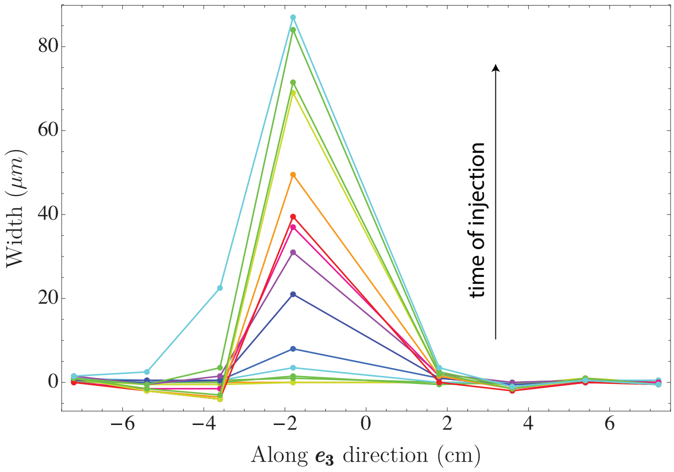

Figure 5.28 – SLATE_K_4 test: Snapshots of the width profiles along the vertical axis $\boldsymbol{e_3}$ of the main horizontal fracture obtained from ultrasonic measurements.

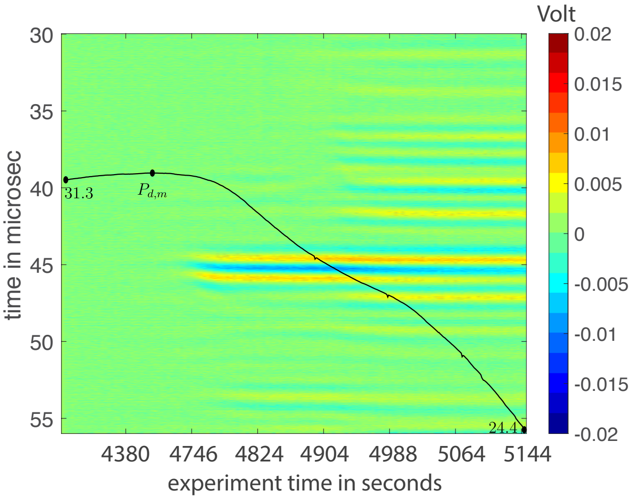

Figure 5.29 – SLATE_K_4 test: Record time function of the experiment time for compressional-diffraction data for a set of source-receiver presented in purple-dashed line in figure 5.25-left. The corresponding interval of the downstream pressure (in MPa) is plotted in the black solid line.

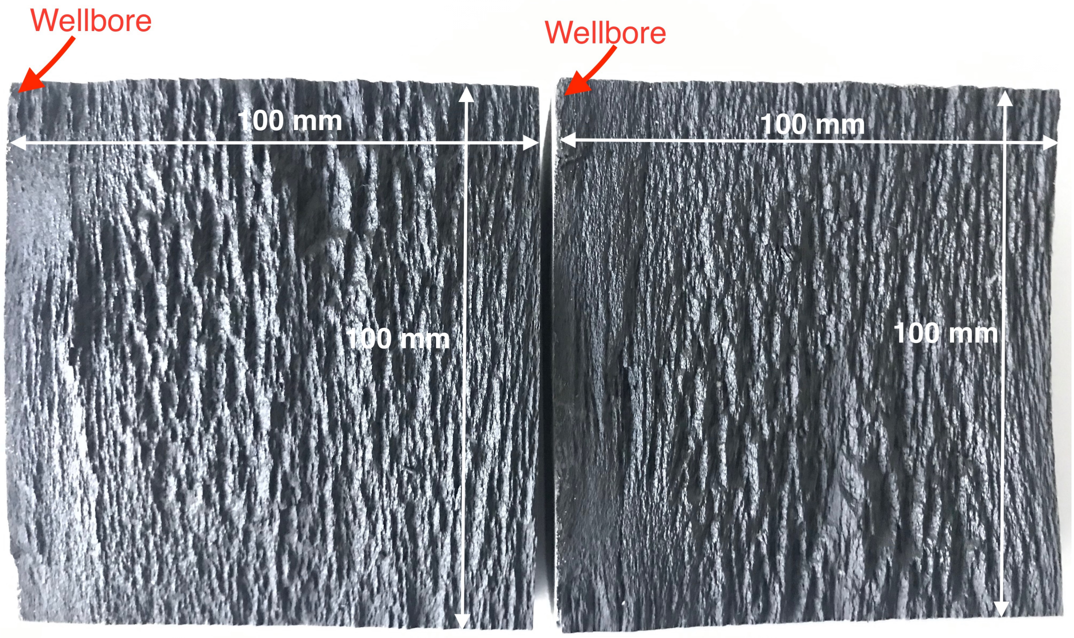

Figure 5.30 – SLATE_K_3: Image corresponding to the upper (left-figure) and lower (right-figure) quarter part of the surface of the fracture resulting from the toughness dominated regime test. The red arrows refer to the wellbore location.

$\Delta h_{r_0} = \Delta h$ should follow a power law in δ:

$$\sigma \propto \delta^{\xi}, \quad \Delta h \propto \delta^{\xi}$$

with: $0 \leq \xi \leq 1$ (Pelliccione and Lu, 2008).

SLATE_K_3 test

We focus on the SLATE_K_3 test for the toughness dominated regime case where the fracture was more planar. We used the optical profilometer Keyence VR-3200 provided by the FLEX Laboratory-EPFL, and are very thankful to professor Pedro M. Reis for his help. We scanned the fracture surface using 0.1 μm vertical and 47 μm horizontal resolution. The repeatability of the measurement was verified by multiple scans as being 0.5 μm. The maps contain 1230×1942 points while the fields of view are 58×91 millimeters. Figure 5.31 shows an example of a 3D map that displays troughs and bumps of quarter of the fracture surface. The fracture plane is tilted as we observe from figure 5.31 ($-2 \leq h \leq 10$ mm). In figure 5.32a we plot a surface profile parallel to the bedding at a given distance $x_3 = cst$ (after the correction of the tilt) located far from the initiation. The amplitude of the largest bumps is of the order of 0.8 millimeters, a typical amplitude for rocks (Ponson et al., 2007).

Figure 5.32b represents in log-log scale the variation of Δh and σ as function of δ averaged

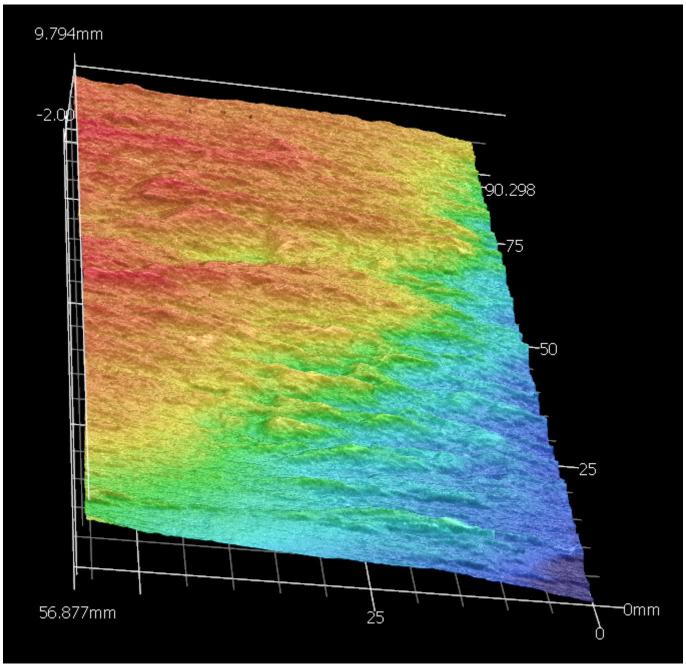

Figure 5.31 – SLATE_K_3: Topographic image corresponding to the upper quarter part of the surface of the fracture. The 3D scan corresponds to the sample in figure 5.30.

over different profiles at given distances x_3. Three distinct behaviors are observed: for small (< 1 mm) and intermediate (< 10 mm) horizontal distance, Δh (or σ) varies as a power of δ with the distinct exponents 1 and 0.9 respectively, whereas for large spatial distance (> 20 mm) the behavior remains roughly constant. For small δ, where: $\Delta h \propto \delta$ ($\xi = 1$) the surface is said to exhibit a self-similar scaling (Pelliccione and Lu, 2008). In other words, the scaling factors in the horizontal and vertical directions are equal. Over the large scale, the surface is flat and is characterized by a correlation length L_c indicating the beginning of the plateau ($L_c \sim 6$ mm) (Schmittbuhl et al., 1995).

Different behavior is depicted in the surface profile in the direction normal in the bedding. The surface is much rougher with a greater amplitude of 1.5 millimeter of maximum magnitude (figure 5.32c). The peaks in the height plot describe the distribution of the bedding planes. The log-log plot of height-height correlation (figure 5.32d) shows a stationary behavior over intervals of distance. We can conclude from figure 5.32d that the distribution of bedding is locally independent of the elevation with a global increase in large scales.

5.3.2 Viscosity test: SLATE_M_1

We now consider fractures which propagate in the the viscosity regime (with a possible significant lag). We report the results of the SLATE_M_1 test for which we applied a deviatoric stress into the cubic block of $\sigma_v = \sigma_H = 20\sigma_h = 20$ MPa as depicted in figure 5.33. We plot in figure 5.34a the pressure at the wellbore downstream and upstream of the valve with a zoom

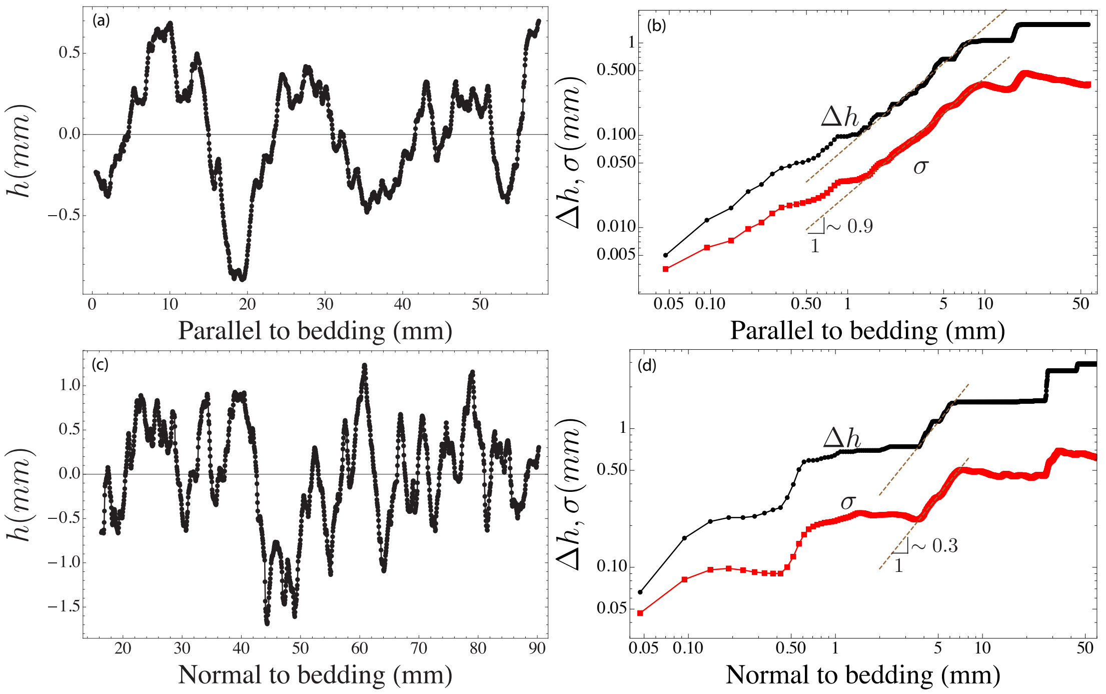

Figure 5.32 – SLATE_K_3: (a,c): Height profile along $\boldsymbol{e_1}$ and along $\boldsymbol{e_3}$ respectively. (b,d): Δh and σ representation in log-log scale averaged over profiles at different x_3 as function of $\delta = \Delta x_1$ in (b) and at different x_1 as function of $\delta = \Delta x_3$ in (d).

into the breakdown and propagation period in figure 5.34b. The entery flux Q_{in}, the width profiles along the vertical direction $\boldsymbol{e_3}$ at different points in time and the diffraction signals are presented in figure 5.35, 5.36 and 5.37 respectively.

The sample is pressurized linearly up to the breakdown pressure of $P_{d,m} = 46.7$ (see figure 5.34a) which is 30% higher than the breakdown pressure in the toughness regime (figure 5.26). A steeper decay in the pressure during propagation is observed in this case. In figure 5.34b, we zoom in to the propagation time, where the pressure at the well follows a power law in time (starting from the breakdown time) of exponent -1/3, the same as for the M scaling (Lecampion et al., 2017).

Similarly to the toughness tests, the instantaneous flux entering the fracture at the breakdown is much higher than the nominal flow rate (see figure 5.35). The propagation of the HF thus occurred in the transient/early time regime. The hydraulic fracture propagated symmetrically in this case with respect to the $\boldsymbol{e_3}$ direction as we can see from the width profiles in figure 5.36. The width magnitude is of the order of 20 μm at 100 seconds of propagation.

The diffracted signal is illustrated in figure 5.37 for the only transducer pair that provided relevant data (see figure 5.33 for the location of the sensors). The magnitude of the signal is much stronger in this case (see figure 5.37).

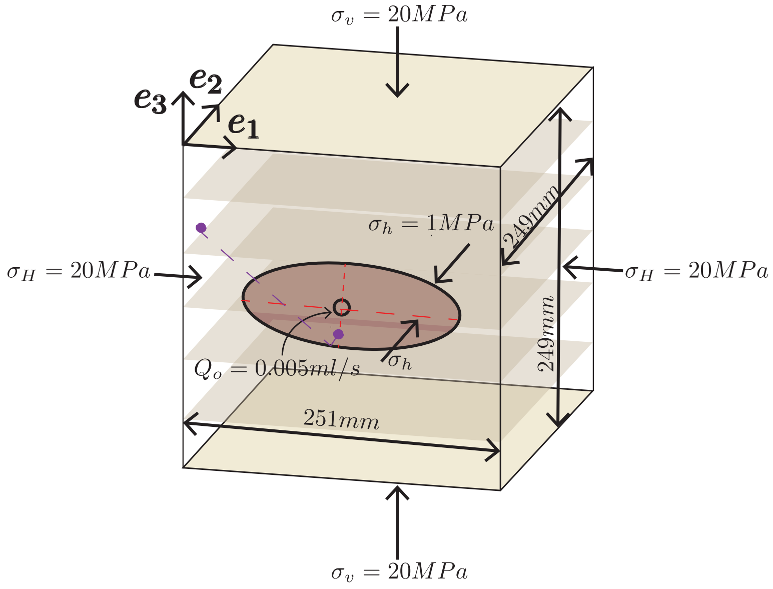
$\sigma_v = 20MPa$
e_3
e_2
e_1
$\sigma_h = 1MPa$
$249mm$
$\sigma_H = 20MPa$
$\sigma_H = 20MPa$
$Q_o = 0.005ml/s$
σ_h
$251mm$
$249mm$
$\sigma_v = 20MPa$

Figure 5.33 – SLATE_M_1 test: Loading configuration of SLATE_M_1 test with the exact block size. The purple dots represent the positions of the acoustic sensors for the diffracted signal.

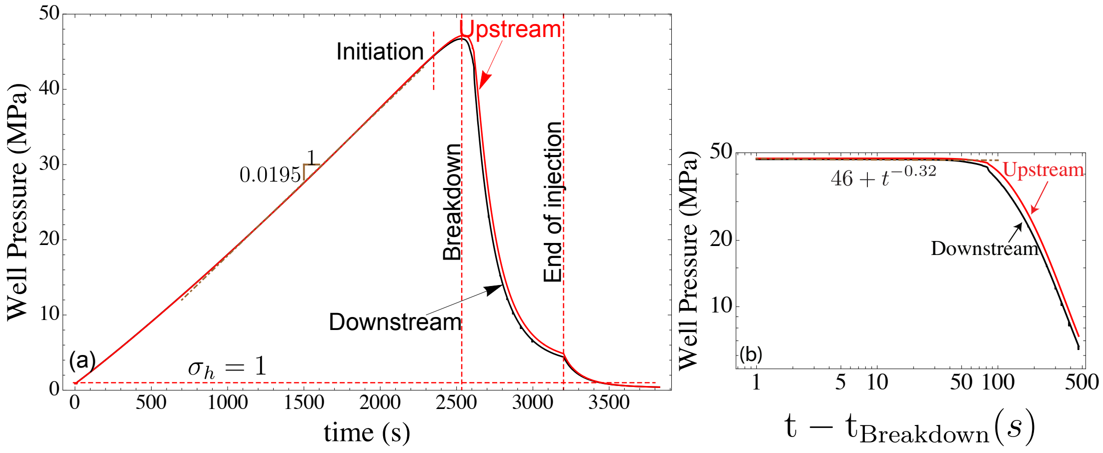

Figure 5.34 – SLATE_M_1 test: Experimental data for the pressure at the well upstream and downstream of the valve in (a), with a zoom at the propagation in log-log scale in (b).

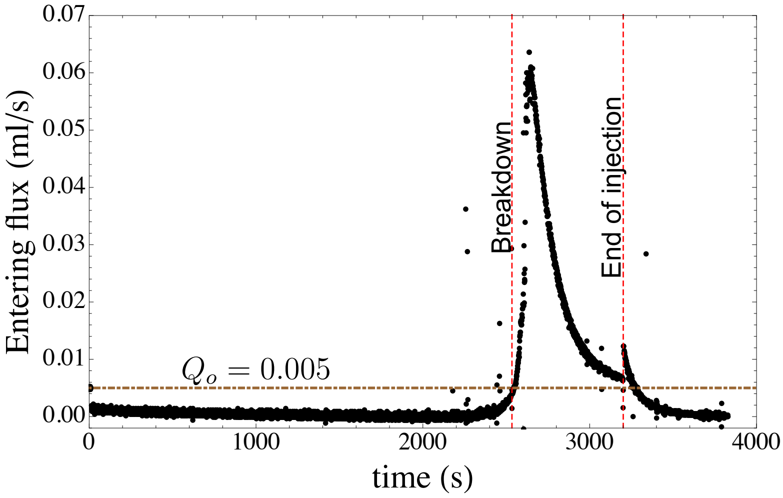

Figure 5.35 – SLATE_M_1 test: Experimental data for flux into the fracture as a function of time.

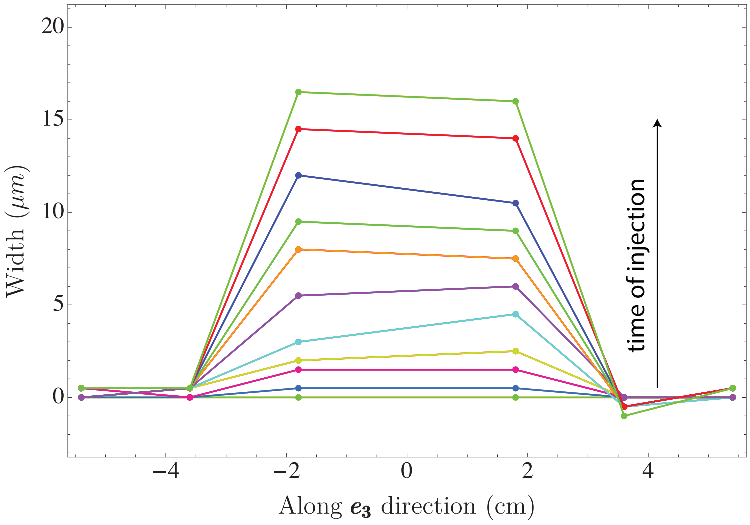

Figure 5.36 – SLATE_M_1 test: Snapshots of the width profiles along the vertical axis $\boldsymbol{e_3}$ of the main horizontal fracture obtained from ultrasonic measurements.

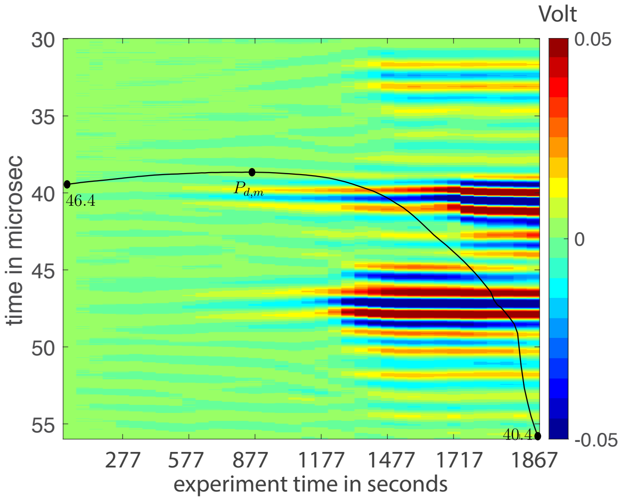

Figure 5.37 – SLATE_M_1 test: Record time function of the experiment time for compressional-diffraction data for a set of source-receiver presented in purple-dashed line in figure 5.33. The corresponding interval of the downstream pressure (in MPa) is plotted in the black solid line.

Fracture surface roughness characterization

Here again we scanned a quarter of the fracture surface of 90 × 75 mm dimension (1915 × 1579 sampling points) created during the HF experiment. We analyze, as before, the 1D profiles along the two normal directions: $\boldsymbol{e_1}$ and $\boldsymbol{e_3}$, both located sufficiently far from the initiation point (figures 5.38a and 5.38c). Parallel to the bedding (figure 5.38a), three domains of variation are visible and correspond to: two power laws of exponents 1 and 0.7 as δ increases, and cutoff at large δ. In the intermediate range of δ, the roughness is smaller than in the toughness case: $\xi = 0.7$ vs $\xi = 0.9$ for toughness case (figure 5.32b). The correlation length for this case is relatively larger, $L_c = 10$ mm.

Figure 5.38c shows the elevation h in millimeters along the normal to the bedding ($\boldsymbol{e_3}$), whereas figure 5.38d shows the standard deviation σ and the average relative elevation Δh for the different height profiles at given x_1. The height profile is rougher along this axis. A power law correlation of exponent 1.1 is observed over the small interval of distance $1 < \delta < 5$ cm of exponent 1.1. However, the overall behavior corresponds to stationary cutoffs by stepping, similarly to figure 5.32d.

5.4 Conclusions

The semi-circular bending test performed on Del Carmen slate results in a high anisotropy of toughness between the divider and the arrester directions: $\kappa^{-1} = \left(K_{Ic,I}/K_{Ic,3}\right)^{-1} = 1.6$. The discrepancy between the dynamic and the static measurements of the stiffness constants may be due to open beddings and to micro-cracks inside the sample. From the uniaxial static tests, we can compute the ratio β from the near tip elastic modulus in the divider and the

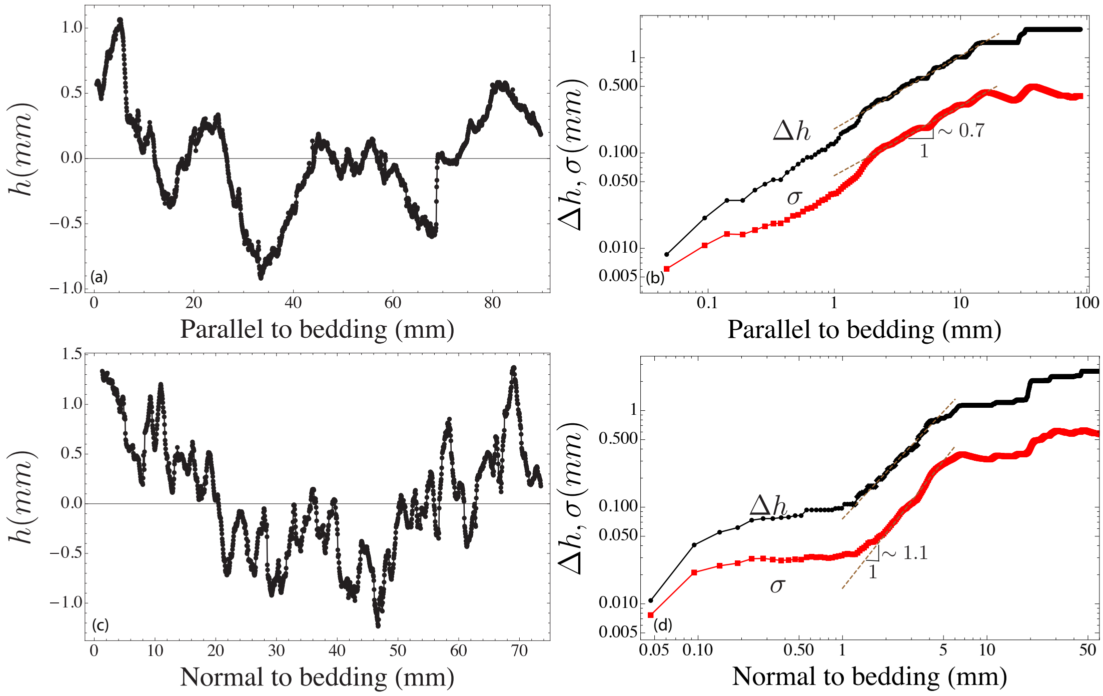

Figure 5.38 – SLATE_M_1: (a,c): Height profile along $\boldsymbol{e_1}$ and along $\boldsymbol{e_3}$ respectively. (b,d): Δh and σ representation in log-log scale averaged over profiles at different x_3 as a function of $\delta = \Delta x_1$ in (b) and at different x_1 as a function of $\delta = \Delta x_3$ in (d).

arrester directions: $\beta = E'_1/E'_3 = 1.03$ (chapter 2). Assuming an elliptically shaped fracture in a toughness dominated regime, we can estimate a-priori the fracture ratio as $b/a = \beta^{-2}\kappa^2 = 0.36$ (chapter 4). We were not able to measure the development of the fracture shape. More tests are required to investigate the elongation of the fracture in the divider direction.

In the toughness dominated regime, the hydraulic fracture in most cases propagates through the bedding planes even for a ratio of 20 between the minimum horizontal stress and the maximum vertical stress. The fracture width is very small, causing strong attenuation of the diffracted waves. As for the roughness, the asperities of the fracture surface are of the order of millimeters and follow a self-affine behaviour of exponent 0.9 parallel to bedding and 0 normal to bedding.

In the viscosity regime, the penetration of more viscous fluid into the initial defect is more difficult, resulting in a larger breakdown pressure. The resulting hydraulic fracture is symmetric with respect to the wellbore with more visible diffracted waves than in the toughness case. Similarly to the toughness regime, the fracture surface roughness is stationary in the direction of the arrester and is self-affine in the divider.

6 Conclusions

6.1 Main contributions

In the framework of this thesis we have aimed to understand how a fluid driven fracture propagates in transverse isotropic media and understand the impact of both elastic anisotropy and fracture energy/toughness anisotropy on the shape of the fracture.

A numerical solver has been developed for a planar hydraulic fracture embedded in impermeable transversely isotropic elastic media. The hydraulic fracture is assumed to propagate normal to the isotropy plane and to the minimum horizontal in-situ stress. The fluid is injected from a point source. The presence of fluid lag at the fracture tip is neglected, by assuming a sufficiently deep fracture. We also investigated the small scale region near the fracture front. The elastic integral representation for a pure tensile configuration is similar to that in the isotropic case depending on the use of an anisotropic plane-strain elastic modulus E'_α, a function of the local propagation direction. The aspect ratio of the finite hydraulic fracture is to the first order a function of: i) the ratio β of the near tip elastic modulus along the major axis (divider) with respect to the minor axis (arrester), and ii) the ratio κ of the fracture toughnesses in these two directions. The fracture elongation in the toughness dominated regime exhibiting strong anisotropy is underestimated by about 70% when using the isotropic radial solution and overestimated by about 30% when using the TI elliptical solution. The shape of the fracture is strongly dependent on the toughness anisotropy. The hypotheses of isotropic toughness and isotropic fracture energy result in elongation scaling with β^2 and β respectively. In the viscosity dominated regime, the effect of anisotropy is less pronounced (elongation scales as $\beta^{1/3}$). The deviation of the numerical solution from the radial geometry is visible only for strong anisotropy. The transition from the viscosity to the toughness dominated regime is quantified by two timescales: one related to the arrester direction (faster transition) and the other to the divider direction (slower transition).

In the course of this work, we have also compared with the existing elastic fundamental solutions in TI media and discrepancies have been noticed in a number of them. An exact solution for the uniformly pressurized elliptical static fracture normal to the isotropic plane is re-derived analytically and benchmarked against a finite element solution. This has then been used to derive the self-similar toughness dominated hydraulic fracture growth solution. We must keep in mind that to generate an elliptical hydraulic fracture, the fracture toughness must depend on the local propagation in a very special form that is highly unlikely for any real rock.

Hydraulic fracturing block tests have been performed using Del Carmen slate under true triaxial confinement. Acoustic monitoring was used to estimate the fluid thickness/fracture width in time lapse during the experiment. Three experiments: two in the toughness dominated regime and one in the viscosity dominated regime were successful. A minimum ratio of 20 between the minimum horizontal in-situ stress and the maximum – normal to bedding – stress is required in order to promote a planar fracture growing normal to bedding. The roughness of the resulting fracture surfaces has been measured. The roughness is self affine along the divider direction (parallel to the bedding) and stationary in the arrester direction (perpendicular to the bedding). A bump in height is observed when the hydraulic fracture crosses the bedding planes. The self-affine roughness exponent is lower in the viscosity dominated fracture.

The effect of shear-thinning fluid on the region near the tip of a steady state hydraulic fracture growth is another problem tackled in this thesis. This fracture was driven by a Carreau fluid in impermeable linearly elastic material. Up to four asymptotic regions may arise as we move away from the tip. Besides the linear elastic fracture mechanics asymptote in the region adjacent to the tip, the additional three viscosity asymptotic solutions follow the evolution of the Carreau rheology: two Newtonian plateaus for low and large shear rate and a power law region for the intermediate values of shear rate. A mapping of the extent of the asymptotic regions has been obtained analytically as a function of the dimensionless parameters. Depending on the dimensionless transition shear stress, we have quantified if one of the alternative rheological models (Ellis, power law and Newtonian) can reproduce the results of the Carreau rheology in the zero fluid lag case. In the zero confining stress limit, the size of the fluid lag is orders of magnitude smaller for the same dimensionless toughness if the fluid is shear-thinning compared to Newtonian.

6.2 Recommendations for future work

- In this thesis, we have focused on the growth of perpendicular fractures perpendicular to bedding. Our experiments have confirmed that even for large in-situ stress normal to the bedding, a deviation into the bedding planes and offsetting occurs. Even for macroscopic planar fracture, the fracture roughness is highly anisotropic. More experimental and theoretical work is required to further decipher the combined effects of in-situ stress, rock properties and injection parameters on deviation into the bedding planes.

- The numerical solver should be extended to include the effect of system compliance and the presence of a finite notch to initiate the fracture. Both are important at early time. This is essential for a good comparison with experiments. In the present work we assume a constant injection rate from a point source. In addition, the solution should also account for the fluid leak-off in permeable media. An approximation solution for the linear diffusion equation perpendicular to the fracture face known as the Carter's leak-off model in the case of tight rocks could be relatively easy to implement.

- Experiments with different level of anisotropy (elasticity and fracture toughness) and different fluid viscosity are needed to further compare with theoretical modelling.
- Lack of clear acoustic diffraction data have prevented us to reconstruct the fracture front. The short injection duration, the small opening magnitudes and the low data quality could be the reasons for the poor diffraction results. Passive microseismic measurements are another possible technique for monitoring fracture growth. Combining both active and passive measurements has potential for improving fracture.
- The strong fracture roughness observed experimentally questions the validity of the Poiseuille law used in the modeling of HF growth. It also questions the use of the flat fluid-filled layer model to analyse the acoustic transmission data. More work is needed to quantify the effect of roughness and include it in the theoretical model.
- An accurate characterisation of the elastic properties, fracture toughness and permeability is essential for comparison between theory and experiments.
- In order to account for shear-thinning rheology in the simulation of planar 3D hydraulic fractures, the semi-infinite solution developed here would need to be approximated/tabulated for numerical efficiency.

Appendices Part

A1 Relation between the different set of elastic constants in TI

The relationships between the different set of constants are given in the material basis $(\boldsymbol{e_1}, \boldsymbol{e_2}, \boldsymbol{e_3})$.

A1.1 Compliance tensor S_{ij}

We rewrite the elastic stress-strain relation function of the tensor S_{ij} as:

$$\begin{pmatrix} \epsilon_{11} \\ \epsilon_{22} \\ \epsilon_{33} \\ 2\epsilon_{23} \\ 2\epsilon_{13} \\ 2\epsilon_{12} \end{pmatrix} = \begin{pmatrix} S_{11} & S_{12} & S_{13} & 0 & 0 & 0 \\ S_{12} & S_{11} & S_{13} & 0 & 0 & 0 \\ S_{13} & S_{13} & S_{33} & 0 & 0 & 0 \\ 0 & 0 & 0 & S_{44} & 0 & 0 \\ 0 & 0 & 0 & 0 & S_{44} & 0 \\ 0 & 0 & 0 & 0 & 0 & 2(S_{11}-S_{12}) \end{pmatrix} \begin{pmatrix} \sigma_{11} \\ \sigma_{22} \\ \sigma_{33} \\ \sigma_{23} \\ \sigma_{13} \\ \sigma_{12} \end{pmatrix} \tag{A1.1}$$

where:

$$\begin{aligned} S_{11} &= \frac{C_{11}C_{33} - C_{13}^2}{(C_{11}-C_{12})\left(C_{33}(C_{11}+C_{12}) - 2C_{13}^2\right)} \\ S_{33} &= \frac{C_{11}+C_{12}}{C_{33}(C_{11}+C_{12}) - 2C_{13}^2} \\ S_{12} &= \frac{C_{13}^2 - C_{12}C_{33}}{(C_{11}-C_{12})\left(C_{33}(C_{11}+C_{12}) - 2C_{13}^2\right)} \\ S_{13} &= \frac{-C_{13}}{C_{33}(C_{11}+C_{12}) - 2C_{13}^2} \\ S_{44} &= \frac{1}{C_{44}} \end{aligned} \tag{A1.2}$$

The compliance tensor is also expressed function of the Young's moduli and Poisson's ratios as:

$$
\begin{aligned}
S_{11} &= \frac{1}{E_1} \\
S_{33} &= \frac{1}{E_3} \\
S_{12} &= -\frac{\nu_{12}}{E_1} \\
S_{13} &= \frac{-\nu_{13}}{E_3} \\
S_{44} &= \frac{1}{G_{23}}
\end{aligned}
\tag{A1.3}
$$

A1.2 Elastic constants E_i, ν_{ij} and G_{13}

We rewrite the elastic stress-strain relation function of the transversal and vertical elastic moduli $\{E_1, E_3\}$ as:

$$
\begin{pmatrix} \epsilon_{11} \\ \epsilon_{22} \\ \epsilon_{33} \\ 2\epsilon_{23} \\ 2\epsilon_{13} \\ 2\epsilon_{12} \end{pmatrix}
=
\begin{pmatrix}
1/E_1 & -\nu_{12}/E_1 & -\nu_{13}/E_3 & 0 & 0 & 0 \\
-\nu_{12}/E_1 & 1/E_1 & -\nu_{12}/E_1 & 0 & 0 & 0 \\
-\nu_{13}/E_3 & -\nu_{12}/E_1 & 1/E_3 & 0 & 0 & 0 \\
0 & 0 & 0 & 1/G_{13} & 0 & 0 \\
0 & 0 & 0 & 0 & 1/G_{13} & 0 \\
0 & 0 & 0 & 0 & 0 & 2\left(1/E_1 + \nu_{12}/E_1\right)
\end{pmatrix}
\begin{pmatrix} \sigma_{11} \\ \sigma_{22} \\ \sigma_{33} \\ \sigma_{23} \\ \sigma_{13} \\ \sigma_{12} \end{pmatrix}
\tag{A1.4}
$$

and function of the compliance parameters we have:

$$
\begin{aligned}
E_1 &= \frac{1}{S_{11}} \\
E_3 &= \frac{1}{S_{33}} \\
\nu_{12} &= -\frac{S_{12}}{S_{11}} \\
\nu_{13} &= \frac{-S_{13}}{S_{33}} \\
G_{13} &= \frac{1}{S_{44}}
\end{aligned}
\tag{A1.5}
$$

The elastic parameters can be also determined from the stiffness tensor as:

$$\begin{aligned}
E_1 =& \frac{(C_{11}-C_{12})\left(C_{33}(C_{11}+C_{12})-2C_{13}^2\right)}{C_{11}C_{33}-C_{13}^2}\\
E_3 =& \frac{C_{33}(C_{11}+C_{12})-2C_{13}^2}{C_{11}+C_{12}}\\
\nu_{12} =& \frac{C_{13}^2-C_{12}C_{33}}{C_{13}^2-C_{11}C_{33}}\\
\nu_{13} =& \frac{C_{13}}{C_{11}+C_{12}}\\
G_{13} =& C_{44}
\end{aligned} \tag{A1.6}$$

We report in table A1.1 the elastic constants $\{E_{1,3}, G_{13}\}$ in GPa and the poisson's ratios for the same set of TI rocks.

A1.3 Stiffness tensor C_{ij}

Inverting the system of equations (A1.3) and (A1.7), one can reformulate the stiffness tensor function of tensor S_{ij} and the set of elastic constants $\{E_1, E_3, \nu_{12}, \nu_{13}, G_{13}\}$ respectively.

$$\begin{aligned}
C_{11} =& \frac{S_{11}S_{33}-S_{13}^2}{(S_{11}-S_{12})\left(S_{33}(S_{11}+S_{12})-2S_{13}^2\right)}\\
C_{33} =& \frac{S_{11}+S_{12}}{S_{33}(S_{11}+S_{12})-2S_{13}^2}\\
C_{12} =& \frac{S_{13}^2-S_{12}S_{33}}{(S_{11}-S_{12})\left(S_{33}(S_{11}+S_{12})-2S_{13}^2\right)}\\
C_{13} =& \frac{-S_{13}}{S_{33}(S_{11}+S_{12})-2S_{13}^2}\\
C_{44} =& \frac{1}{S_{44}}
\end{aligned} \tag{A1.7}$$

$$\begin{aligned}
C_{11} =& \frac{E_1\left(E_1\nu_{13}^2 - E_3\right)}{(1+\nu_{12})\left(2E_1\nu_{13}^2 - E_3(1-\nu_{12})\right)}\\
C_{33} =& \frac{E_3^2(1-\nu_{12})}{E_3(1-\nu_{12}) - 2E_1\nu_{13}^2}\\
C_{12} =& \frac{E_1\left(E_3\nu_{12} + E_1\nu_{13}^2\right)}{(1+\nu_{12})\left(-2E_1\nu_{13}^2 + E_3(1-\nu_{12})\right)}\\
C_{13} =& \frac{E_1E_3\nu_{13}}{E_3(1-\nu_{12}) - 2E_1\nu_{13}^2}\\
C_{44} =& G_{13}
\end{aligned} \tag{A1.8}$$

For a generally anisotropic elastic solid characterized by the Voigt stiffness tensor C_{ij}, or its inverse the compliance tensor S_{ij}, the requirement imposed by thermodynamics that the elastic energy must be positive, can be expressed as follows (Theocaris and Philippidis, 1992):

$$\psi = \frac{1}{2}\boldsymbol{\sigma}.\boldsymbol{\epsilon} = \frac{1}{2}\boldsymbol{\sigma}.S.\boldsymbol{\sigma} > 0 \tag{A1.9}$$

Since the relation (A1.9) must be valid for any $\boldsymbol{\sigma}$ or $\boldsymbol{\epsilon}$, the elastic tensor must be positive definite. In terms of the elastic Young's moduli and Poisson's ratios, the following system of inequalities must hold for a TI material:

$$|\nu_{12}| < 1 \tag{A1.10}$$

$$|\nu_{13}| < \left(\frac{E_1}{E_3}\right)^{1/2} \tag{A1.11}$$

$$2\nu_{13}^2\nu_{12}\frac{E_3}{E_1} < 1 - \nu_{12}^2 - 2\nu_{13}^2\frac{E_3}{E_1} \tag{A1.12}$$

$$E_1, E_3, G_{13} > 0 \tag{A1.13}$$

We can derive from the inequalities (A1.10)-(A1.13), the following constraints on the stiffness coefficients:

$$-C_{44} < C_{13} < \sqrt{C_{33}C_{11}}$$

and:

$$C_{11} > 0, \quad C_{33} > 0, \quad C_{44} > 0, \quad C_{66} = \frac{1}{2}(C_{11} - C_{12}) > 0.$$

Material	E_1 (GPa)	E_3 (GPa)	G_{13} (GPa)	$\nu_{12}(-)$	$\nu_{13}(-)$
Isotropy-Stripa granite (Alm et al., 1985)	65	65	26.9	0.21	0.21
Olkiluoto mica gneiss (Hakala et al., 2007)	79	56	24	0.17	0.21
Gas-saturated Shaly Coal (Wang, 2002)	18.86	10.81	3.71	0.37	0.041
Woodford53 shale (Laubie, 2013)	23.5	13.42	5.6	0.14	0.23
Opalinius Clay (Thöny, 2014)	3.8	1.3	0.9	0.25	0.35
Yeocheon schist (Cho et al., 2012)	72.1	21.2	13.7	0.25	0.16
Calcareous mudstone (Chertov, 2012)	44.66	12.82	6.49	0.14	0.28
Callovo-Oxfordian (David et al., 2007)	16.53	11.46	5.22	0.34	0.17
Jurassic shale (Hornby, 1998)	28.29	17.18	6.9	0.19	0.3
Slate Del Carmen (this study)	35.4	26.4	21.2	0	0.029

Table A1.1 – Example of elastic moduli $\{E_1, E_3, G_{13}\}$ and Poisson ratios ν_{ij} for TI rocks.

B1 A polyaxial frame for hydraulic stimulation experiments with acoustic monitoring

This chapter is a modified version of a scientific article currently under preparation:

T. Blum, B. Lecampion, F-E Moukhtari, "A polyaxial frame for hydraulic stimulation experiments with acoustic monitoring ".

Contributions:

B. Lecampion and T. Blum have developed the triaxial frame and the protocol of the HF tests. T. Blum run the qualification tests of the frame and developed the acoustic acquisition system. F-E. Moukhtari has analysed the stress distribution inside the block under confining using finite element Abaqus software.

B1.1 Abstract

Laboratory investigation of hydraulic fracture propagation allow to bridge the gap between field data and numerical models, by providing a close representation of propagation conditions in the field while accounting for extensive monitoring of the fractured material before, during and after propagation of the fracture. In particular, scaled-down hydraulic fracturing experiments can be used to investigate fracture-tip asymptote and fracture propagation regimes. The goal of this chapter is to present the true-triaxial frame used for performing hydraulic fracturing growth experiment with acoustic active monitoring.

B1.2 Polyaxial frame & injection system

B1.2.1 Description of the frame

High-pressure cell

The main component of the hydraulic fracturing experimental setup is a polyaxial pressure cell, with inner dimensions of 450 x 450 x 500 mm (L x W x H). It is made of four sides of AS 3678 Grade 350 steel plate (Standards Australia, 2011), 50 mm thick, welded using Gas-Metal Arc Welding (GMAW) and machined afterwards to ensure parallelism of the inside faces. Three reinforcing “ribs” also made out of 50 mm thick steel plates surround the four sides for added stiffness. A total of 16 bores, 40 mm in diameter, located at the top and bottom of each lateral sides, allow passage for sensor and actuator cables as well as high pressure lines (see figure B1.1). Water tightness can be obtained by placing cable feed-through with rubber cores inside the side bores, as well as cylindrical steel pieces with fittings for the high pressure lines.

The top and bottom of the pressure cell are 120 mm thick steel covers that are held together with four 80 mm diameter steel rods (see figures B1.1 and B1.2). The steel rods are threaded at each end, and the steel nuts tightly close the covers against the top and bottom edges of the square cell. Finally, a watertight rubber seal is placed between the covers and the cell edges in order to apply pore pressure inside the cell.

Attached to one side of the pressure cell is a table with rails fitted to the sides. A motorized gantry crane slides along theses rails in order to lift or drop both the vertical stack containing the bottom spacer plates, flat-jack, platen and sample block, as well as drop or lift the steel lid, before or after an experiment is done (figure B1.3).

Sample pressure loading

Inside the high-pressure cell, we use a system of flat-jacks and spacers to apply compressional stresses to cubic samples with dimensions 250 x 250 x 250 mm. The sample is placed at the center of the cell, with a stack of 250 x 250 mm plates on each of the six sides (see figure B1.2), to position the sample and transfer stresses. From the inside wall to the center of the cell, each

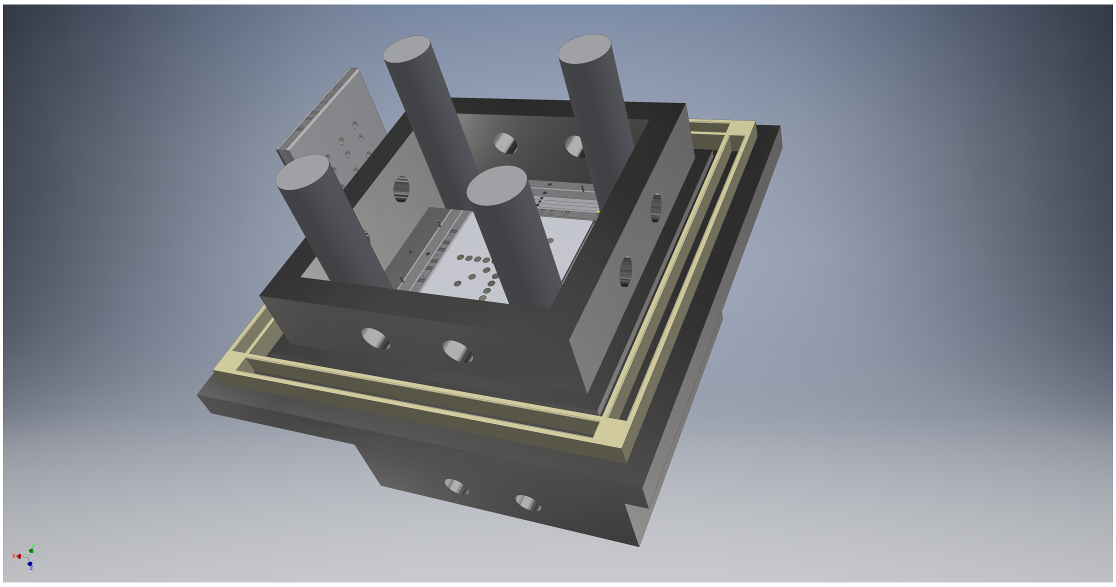

Figure B1.1 – 3D drawing of the reaction frame with top of the cell open. The four steel rods used to tighten the top and bottom covers are clearly apparent, threads are not shown here.

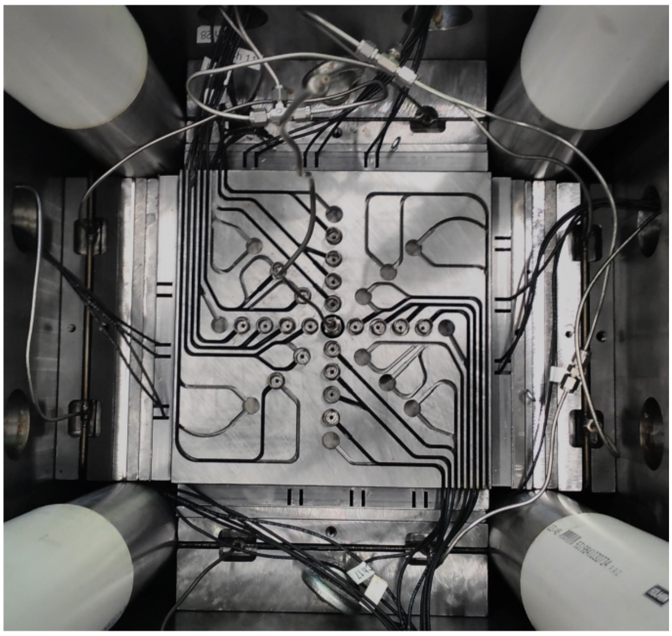

Figure B1.2 – Top view of the reaction frame, loaded with sample, platen and flat-jacks on the side, and top platen.

stack consist several steel spacer plates, followed by a flat jack, another steel space plate, and finally an aluminum platen with a specially designed layout to place piezoelectric transducers (see section B1.3.3 for more details).

Our flat-jacks are made from 1 mm thick, 250 x 250 mm square steel plates welded together at

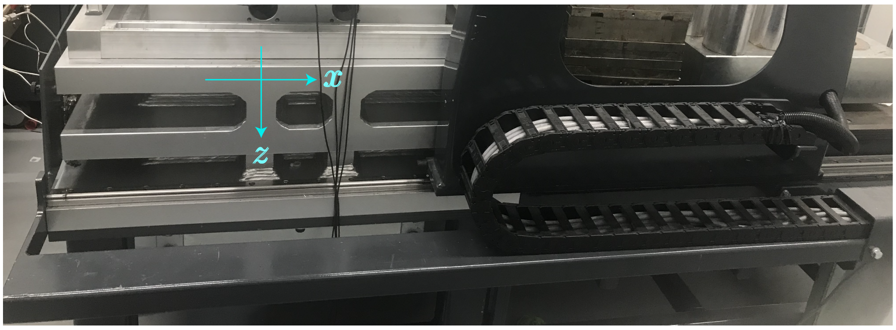

Figure B1.3 – Polyaxial frame from the side view with the configuration of the frame axis.

the edges, with two high-pressure line fittings welded on one side. By filling them through one fitting with water, and connecting an open valve to the other fitting, we are able to fill them with water and purge the air. We then connect them by pairs to GDS pressure controllers, as shown in figure B1.4. With three pressure controllers we are therefore able to independently apply stresses up to 20 MPa along the three axes defined by the geometry of the cell. We describe the qualification test we performed to test the high-pressure cell combined with flat-jacks in the next subsection.

B1.2.2 Stiffness qualification tests

The objective of the tests is to validate the specifications of the triaxial cell before its first use. For this we pressurize the cell along the three axes consecutively, and finally we apply a pore pressure inside the watertight closed cell. Load is provided using an ISCO Model 260D pump connected to flat-jacks applying pressure against the cell walls. We use the pump pressure transducer for pressure readings. The cell strain is measured with a pair of RDP Linear Variable Differential Transformers (LVDTs) mounted along the axis being loaded (figure B1.5).

Inside the cell we place a 250 x 250 x 250 mm block of 6061 T651 aluminum alloy, substituting for the rock samples that will be used in future experiments. As described in the subsection above, steel spacer plates are used to fill the space on the sides of the sample, and sandwich the flat jacks positioned on each side, so that there is contact between all the elements inside the cell and the walls of the cell (see figure B1.7). Here we only use spacer plates and not platen against the sample faces. For each axis, we test the frame by applying up to 25 MPa with the flat-jack pair in steps of 5 MPa, then maintaining 25 MPa for at least one hour, before releasing the confining pressure in multiple stages. We then measure the cell strain by positioning two LVDTs against the outside of the cell. For each axis, we very carefully attach the LVDTs to the supporting frame (blue legs in figure B1.5 and B1.6) so that the load cell can move freely with respect to the sensors. The LVDT signals are digitized at 10 Hz by an acquisition module and recorded on a laptop, as well as the voltage output of the pressure gauge mounted on the pump. These signals are synchronized and thus provide the cell strain as a function of the load.

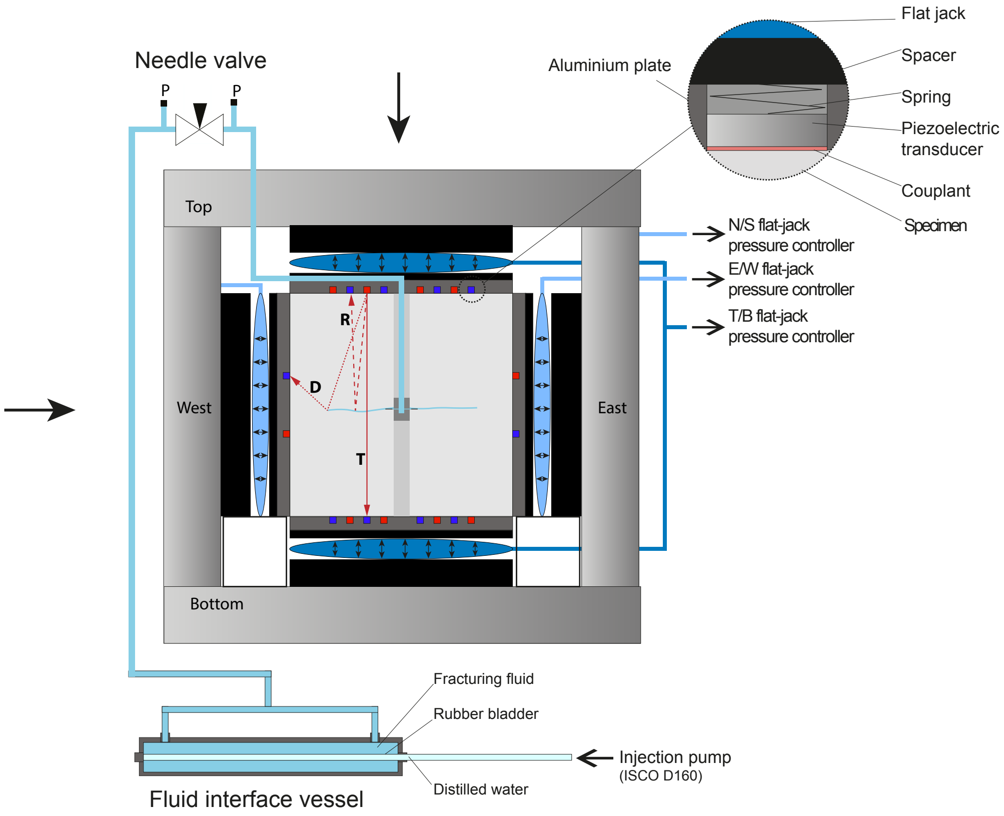
Needle valve
P
P
Aluminium plate
Flat jack
Spacer
Spring
Piezoelectric transducer
Couplant
Specimen
Top
N/S flat-jack pressure controller
E/W flat-jack pressure controller
T/B flat-jack pressure controller
R
D
West
East
T
Bottom
Fracturing fluid
Rubber bladder
Injection pump (ISCO D160)
Distilled water
Fluid interface vessel

Figure B1.4 – Schematic of the reaction frame.

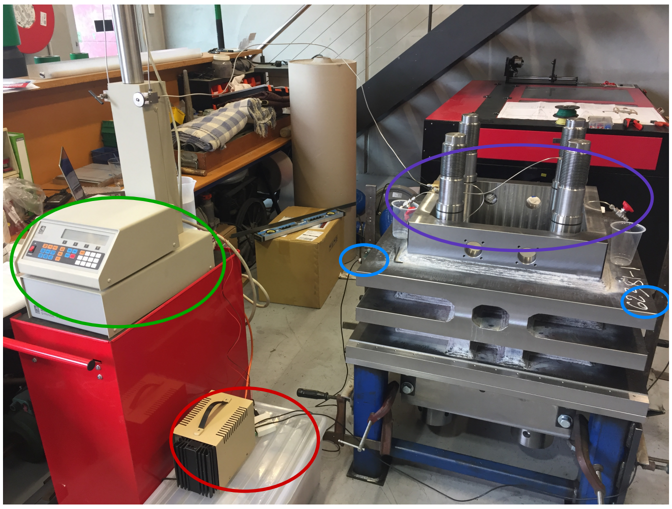

Figure B1.5 – Photo of the setup with main features highlighted. Green: ISCO pump, Blue: LVDTs, Red: LVDT power supply and acquisition board, Purple: high-pressure lines and valves connecting the flat jacks.

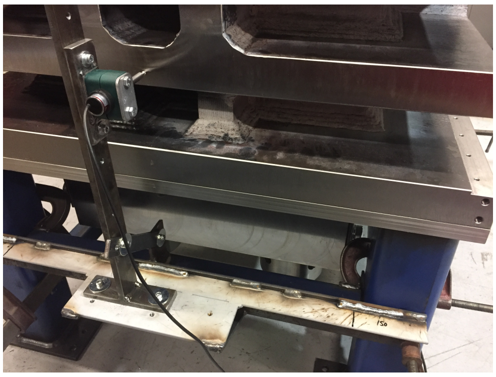

Figure B1.6 – Close up of LVDT positioned in the center of the middle rib, along the $\boldsymbol{x}-$axis, with mounting bracket.

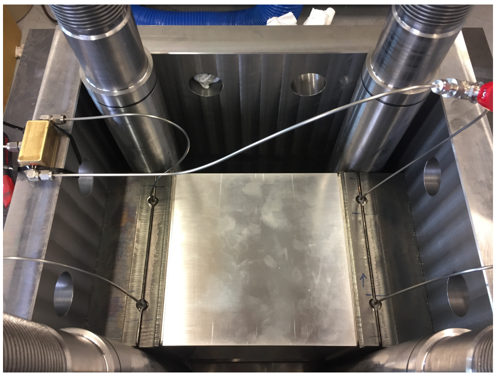

Figure B1.7 – Top view of the cell with aluminum block, steel spacer plates and flat-jacks sandwiched between steel plates on each side of the aluminum block.

Rib position	bottom	middle	top
Max pressure (MPa)	24.15	24.15	24.09
Max displ. (μm)	265	319	308

Table B1.1 – Maximum pressure and maximum displacement for stiffness test along $\boldsymbol{x}-$axis.

Results

For the remaining of this document we set the axis of the rails and gantry apparatus at the $\boldsymbol{x}-$axis, the normal horizontal axis as the $\boldsymbol{y}-$axis and the vertical axis as the $\boldsymbol{z}-$axis (figure B1.3).

$\boldsymbol{x}-$axis: For both horizontal axes, we pressurize and measure the cell deformation on each of the three reinforcement “ribs”. The total cell deformation is given by adding the displacements measured by the two LVDTs opposite each other. The table B1.1 shows the maximum displacement measured at the maximum pressure for each rib.

Figure B1.8 shows the evolution of the pressure and displacement during the cell load. We see that the increases (resp. decreases) in displacement track closely with the increases (resp. decreases) in pressure. There is a small hysteresis that seems to disappear after a few minutes when the load drops, but otherwise the cell response is very linear.

$\boldsymbol{y}-$axis: The measurements along the $\boldsymbol{y}-$axis are very similar to the previous ones. Unfortunately, a crash of the logging during the acquisition of the bottom rib response means that there is no data for this measurement. The other two measurements are summarized in table B1.2 with the evolution of displacement function of pressure in time is displayed in figure B1.9. Similarly to $\boldsymbol{x}-$axis, the maximum displacement is about 304 μm in average.

$\boldsymbol{z}-$axis: Along the $\boldsymbol{z}-$axis, we only do one displacement measurement at the center of the top and bottom plates closing the cell, since they are of constant thickness, we expect the strongest

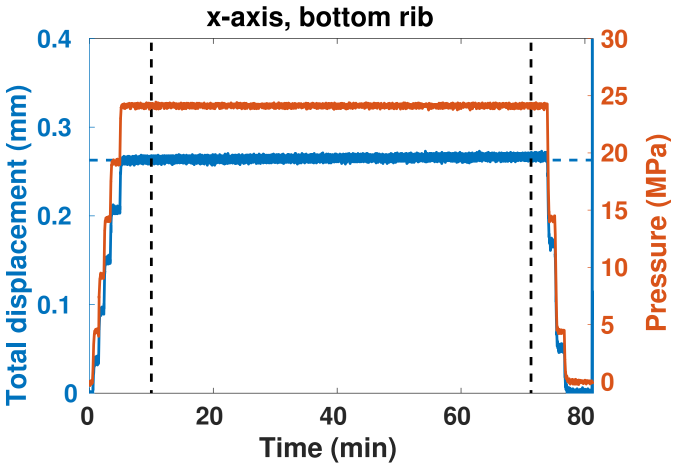

Figure B1.8 – Results for the bottom rib along the $\boldsymbol{x}-$axis. The total displacement is plotted in blue and the flat-jack pressure in red. The measured displacement follows increases and decreases in pressure.

Rib position	middle	top
Max pressure (MPa)	23.86	24.13
Max displ. (μm)	309	298

Table B1.2 – Maximum pressure and maximum displacement for stiffness test along $\boldsymbol{y}-$axis.

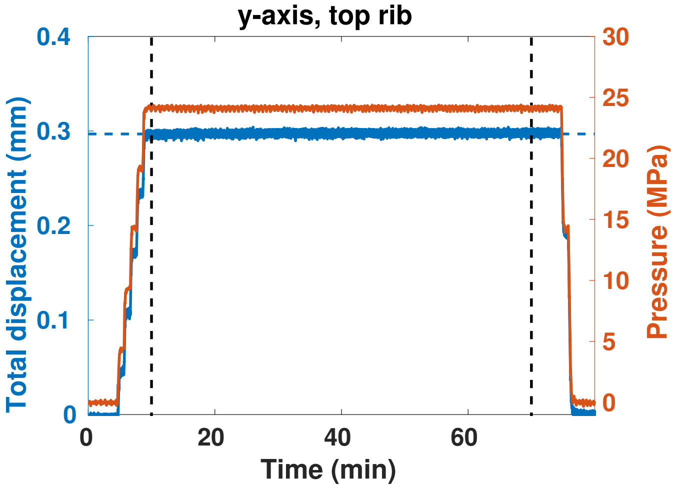

Figure B1.9 – Results for the top rib along the $\boldsymbol{y}-$axis. The total displacement is plotted in blue and the flat-jack pressure in red. The measured displacement follows increases and decreases in pressure.

deformation at the center. As before, the LVDTs are fixed to the supporting frame, as shown in figure B1.10. The results, in figure B1.11, show a maximum displacement of ~ 450 μm at 24 MPa.

Pore pressure: Finally, we fill the cell with water in order to verify the water tightness for a

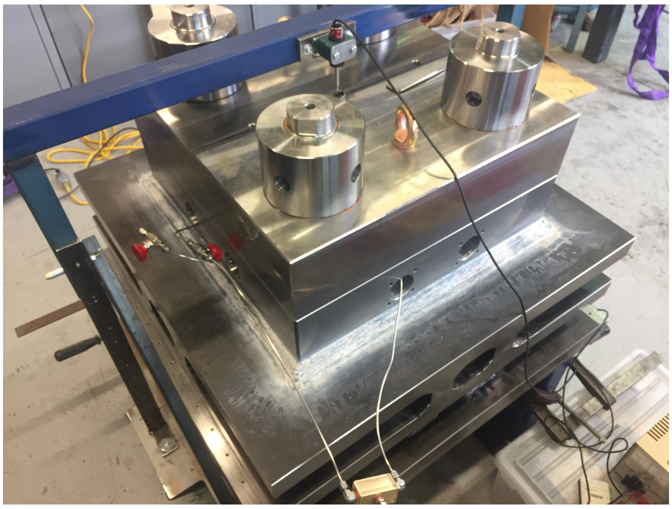

Figure B1.10 – Photo of the LVDT setup for loading along the $z-$axis.

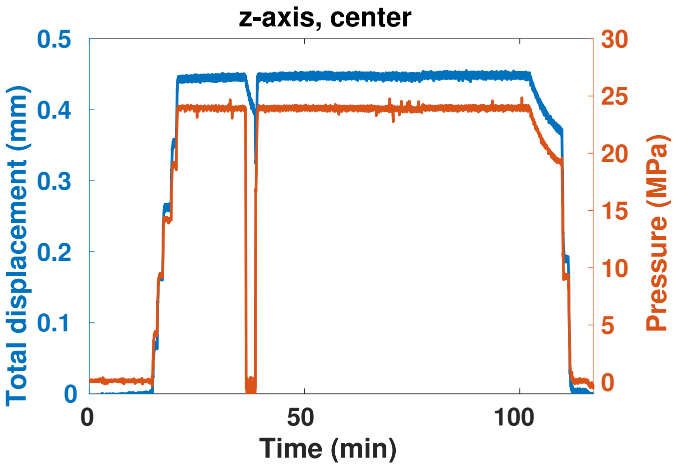

Figure B1.11 – Results for the $z-$axis at the center of the top and bottom plates. The total displacement is plotted in blue and the flat-jack pressure in red. Due to a leaky flat-jack, we had to refill the pump which caused a drop in pressure at $T = 36$ min. During that time, the pump sensor records the refill (room) pressure, and not the flat-jack (confining) pressure. At the end ($T = 110$ min, we let the pressure decrease from the leak only, and again we see that the displacement matches the pressure drop.

pore pressure of 4 MPa. For this test, the aluminum block is left inside with the bottom space plates and flat-jack, leaving a bigger volume of water than would otherwise be in a triaxial use. The holes for the cable pass-through are in this case plugged with solid pieces of steel with two rubber o-rings each to ensure water tightness, except for one piece that has a fitting for the high-pressure line. After the lid is closed and tightened, the pressure is increased with the ISCO pump. Some volume of air is trapped inside, therefore a lot of water must be pumped inside before the pressure rises noticeably. We had to refill the pump several times, the last refill is visible on the graph in figure B1.12. Once the maximum pore pressure of 4.8 MPa is reached, the flow required to maintain the pressure is less than 0.02 mL/min, showing that the leaking is minimal. The deformation of the cell in the center of the top and bottom plate comes to a total of ~ 350 μm.

This series of validation tests show that the triaxial cell is performing as expected with a small deformation when a load or pore pressure is applied. In general, the strain in roughly proportional to the load, stays almost constant at constant load, and returns to zero when the cell is unloaded.

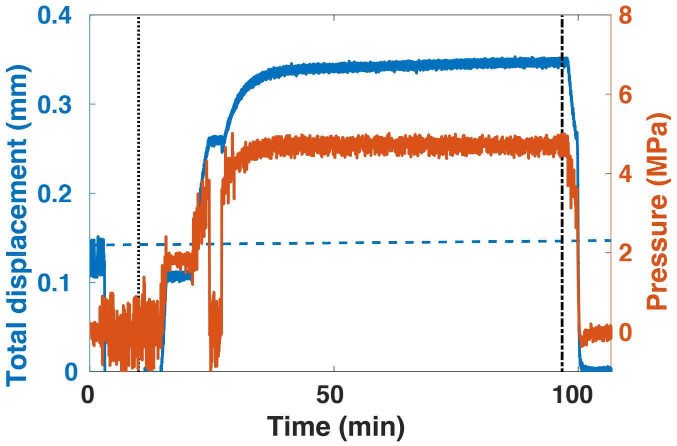

Figure B1.12 – Results for the pore pressure test. Ramping up the pressure requires a lot of fluid volume, thus we have to refill the pump at $T = 25$ min. As for the previous measurement, during that time the measured pressure is not the pore pressure.

B1.2.3 Numerical model of the applied stresses

We used the finite element Abaqus software to analyze the stress distribution inside the block sample of slate Del Carmen. We consider only the quarter of the assembly of the rock and platens (see figure B1.13). The platens are made from 7075 aluminium alloy with the given properties: $E' = 75$ GPa , $\nu' = 0.33$. The contact is maintained using Teflon sheet which we model as hard contact with tangential behaviour of friction coefficient: $\mu = 0.15$.

We set a symmetry condition for both sides defined by the normal $\boldsymbol{x}$ and $\boldsymbol{y}$. The vertical displacements at two symmetrical nodes at the middle of the lateral platens are set to zero. Two state of stresses are considered in this study: hydrostatic stress where $\sigma_x = \sigma_y = \sigma_z = 20$ MPa and deviatoric stress where $\sigma_x = \sigma_y = 4\sigma_z = 20$ MPa.

Results

We focus in particular on the horizontal plane where the hydraulic fracture should evolve. Figures B1.14 and B1.15 display the normal stress σ_{33} and the shear stress σ_{13} at the mid-

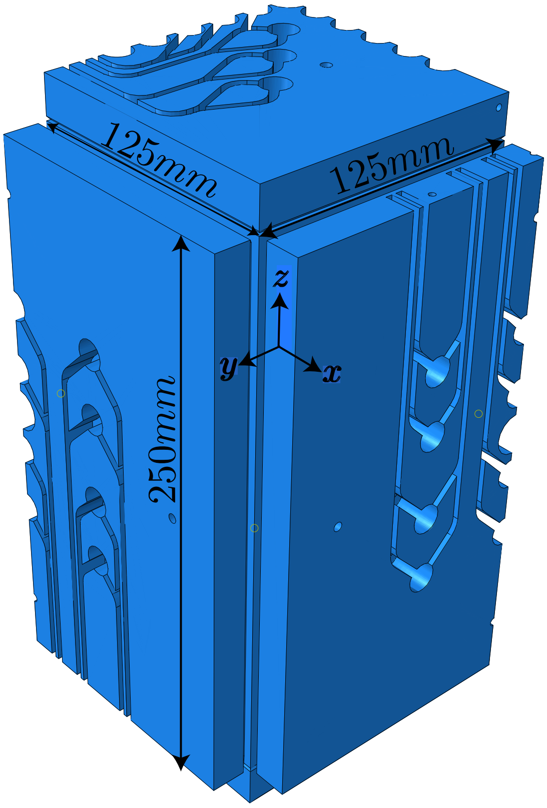

Figure B1.13 – The assembly of the quarter of cubic block with the aluminium platens. The axis $\boldsymbol{z}$ is along the vertical top-bottom direction.

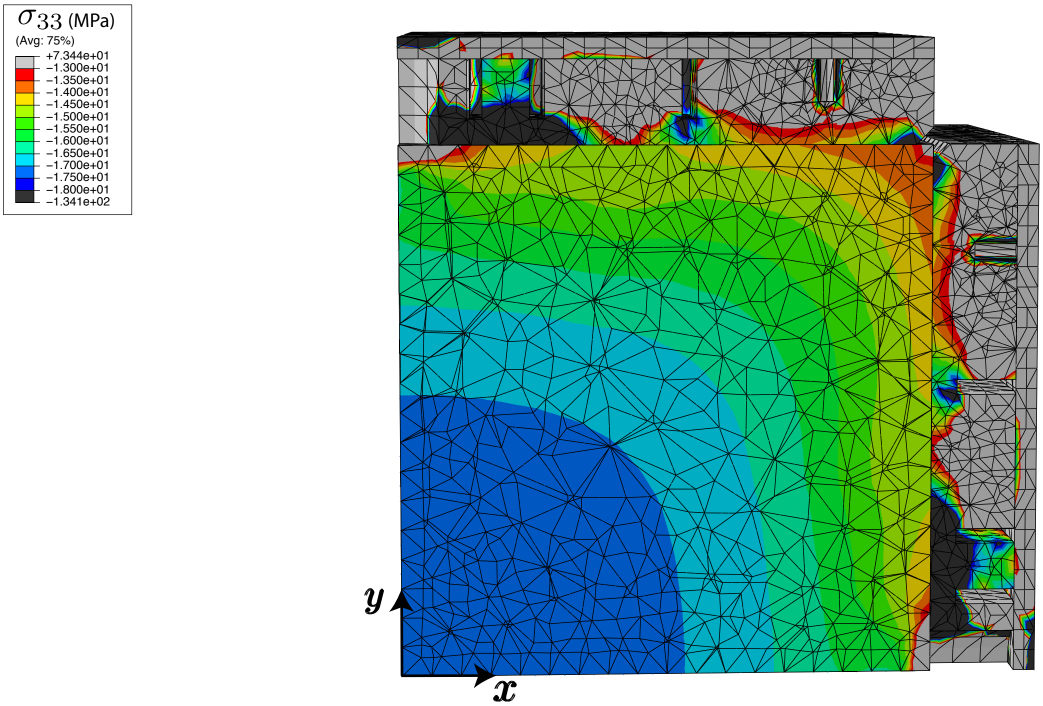

Figure B1.14 – Hydrostatic loading: σ_{33} in MPa for the eighth of the block (at the mid-height of the frame-figure B1.13). Each color represents a surface of iso-stress in linear scale of 0.5 MPa gradient. Here negative values of stress refer to compression tensor.

height of the block for the isotropic loading case ($\sigma_i = 20$ MPa). The normal stress is gradually increasing from the edge to the center of the sample. It varies between 17.5 and 17 MPa in a radius of 60 mm from the center which is less than 15% of relative error with respect to the in-situ stress. Note that the stress tensor is homogeneous and the effect of the holes in the platens starts to dissipate at a distance of 15 mm from them. We observe from figure B1.15 that the shear stress is less than 0.2 MPa for the entire fracture plane. Also, it is worth mentioning that the total displacement of the frame is less than 0.1 mm.

Figure B1.16 presents stress σ_{33} normal to the surface plane for the deviatoric loading case ($\sigma_x = \sigma_y = 4\sigma_z = 20$ MPa). Similarly to first case (figure B1.15), the stress increases linearly from the corners to the center of the block. The stress interval is within $[4, 4.5]$ MPa for $1/3$ of the block (starting from the center), which is less than 20% of the minimum stress. The same results as for the isotropic loading case are observed for the shear stress σ_{13} and the displacement.

B1.2.4 Sample preparation and injection system

We carefully prepare all rock samples used for injection experiments. We first ensure that the sample dimensions are 250 x 250 x 250 mm, with adjacent faces perpendicular to each other. If

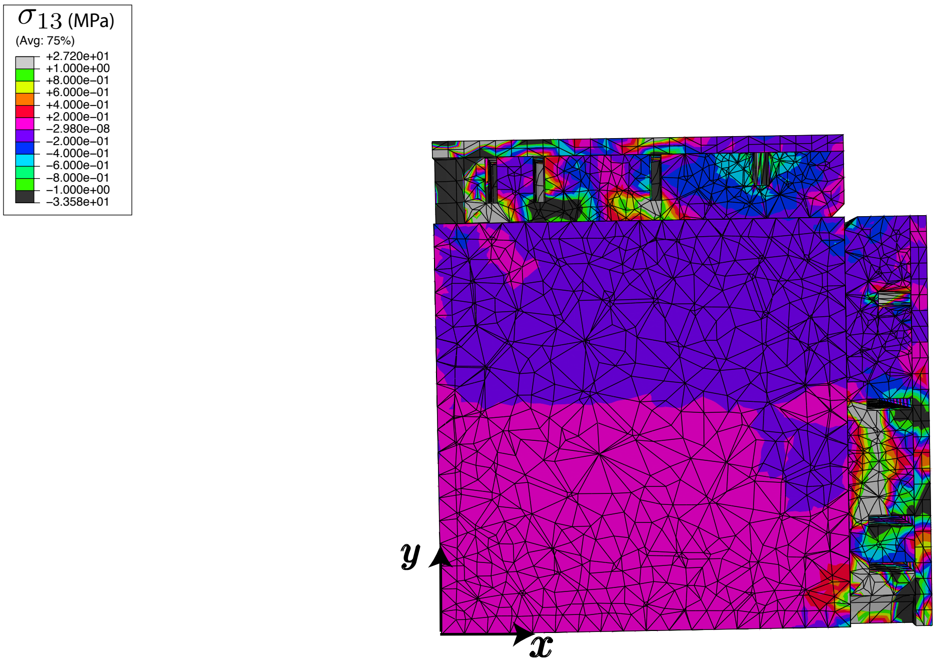

Figure B1.15 – Hydrostatic loading: σ_{13} in MPa for the eighth of the block (at the mid-height of the frame-figure B1.13). The linear scale varies from -1 MPa to 1 MPa. Here negative values of stress refer to compression tensor.

necessary, we can saw or rectify sample faces to achieve the proper dimensions. It is possible to use samples with up to a few extra millimiters in length along any direction. We cannot however use smaller samples, as adjacent side platen, while chamfered on the edges, risk touching each other after stresses are applied and therefore do not allow margin for smaller dimensions.

We then drill the sample with a 16 mm coring tool in order to get a through borehole. We use a customized diamond-coated, disk shaped bit mounted to a surface router in order to create a notch in the middle of the borehole (see figure B1.4). At the notch depth, we place a completion tool consisting in two metal cylinders screwed together, with rubber O-rings at the top and bottom, side holes in the middle allowing the injection fluid to exit horizontally and pressurize the notch. A piece of steel tubing welded to the completion tool plays the role of the well and is the final section of the injection line; a connection at the wellhead on the top face of the sample links it to the rest of the line.

The injection system consist in an ISCO syringe pump rated for 51.7 MPa. The pump is filled with water and connected to a high-pressure interface vessel. This vessel is a steel cylinder filled with the fluid used for the injection. A rubber bladder is placed at the center of the cylinder, inside along its longitudinal axis. The bladder is filled with water and connected to the injection pump. When the water pressure increases, it is transmitted to the injection fluid, and this fluid is then pushed into the injection line connected to the outside wall of

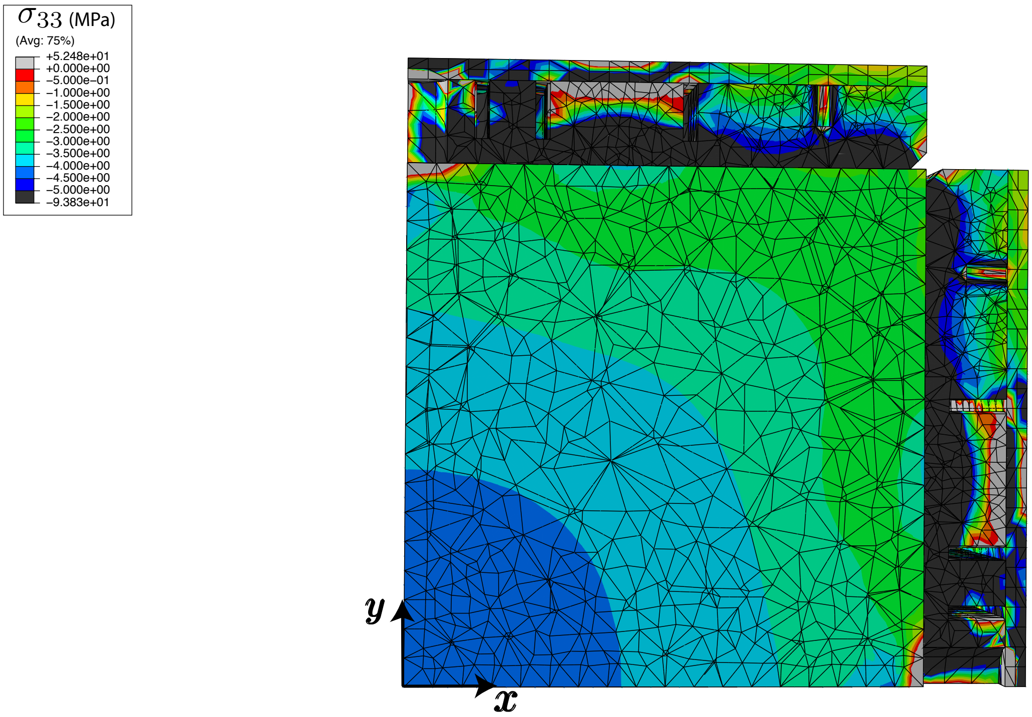

Figure B1.16 – Deviatoric loading: σ_{33} in MPa for the eighth of the block (at the mid-height of the frame-figure B1.13). Each color represents a surface of iso-stress in linear scale of 0.5 MPa gradient. Here negative values of stress refer to compression tensor.

the cylinder. We then place a needle valve along the injection line in order to limit fluid flow during the fracture initiation. Finally, we place two pressure gauges, respectively just upstream and downstream of the needle valve, right before the injection line is finally connected to the wellhead (see figure B1.4).

B1.3 Measurement system

In order to control and record as many experimental parameters as possible, we use a PC-based controller, connected to all sensors and actuators in the experimental setup. This section describes the measurement system step-by-step.

B1.3.1 General experimental control system

The general experimental control system is build out of the following components:

- Main National Instruments (NI) PXI chassis with a PC-based controller unit,
- Single channel, 14 bit, 100 MS/s function generator used to create the elastic excitation signal,
- Multiplexer board with 32 channels, capable of up to 140 cycles/s, used to sequentially excite all acoustic sources,
- High-frequency 32 channel acquisition board digitizing over 12 bits at 50 Mega Samples per second (MS/s) for active acoustic monitoring,
- High-frequency 16 channel acquisition board digitizing over 14 bits at 50 MS/s for passive acoustic monitoring,
- Low-frequency, 16 channel acquisition board digitizing over 16 bits at 250 kS/s for injection flow, pressure, and volume monitoring.

We also use a 55 dB high-voltage amplifier from Electronics & Innovation (E&I) in order to amplify the excitation signal from the volt range out of the function generator into hundreds of volts to excite piezoelectric transducers.

Moreover, the controller unit is connected to the ISCO injection pump, as well as the GDS pressure controller through USB connections, in order to handle all communications with control and measurement devices included in the experimental system. Therefore, it allows us to set all relevant experimental parameters digitally and record them, follow the evolution of recorded data in real-time, and finally to store all these recorded data and parameters in a filesystem for further processing and analysis.

This is achieved through a LabVIEW program that interfaces with all components listed above, as well as with the GDS and ISCO equipment.

B1.3.2 Pressure and volume control and recording

The main virtual instrument (VI) interfaces with both GDS and ISCO equipments through USB connections are used in the following ways:

- For the GDS pressure controllers, we set the target pressure for each controller, which is then applied to an axis of the sample with the flat-jack pairs. We record the pressure and volume of each controller every second, and use this information to estimate deformation of the sample, as well leakage for flat jack pairs.
- On the ISCO pump we can choose between requesting constant flow or constant pressure targets. Typically we perform injection experiments in a constant flow configuration, while recording the volume, pressure and flow rate every second.

Both type of equipments provide pressure readings from pressure gauges at the outlet of the cylinder.

We also use two pressure gauges in order to monitor the pressure on the injection line just upstream and downstream of the needle valve (figure B1.4). These gauges are factory calibrated and have a range of 0 to 60 MPa, covering the maximum possible injection pressure with the ISCO pump. We connect the analog output of the gauges to the low-frequency acquisition board, and sample the corresponding signals at 1 kHz, before averaging over 1000 values, leading to saved data at 1 Hz.

B1.3.3 Active elastic wave monitoring

The active elastic wave monitoring system consists in 64 piezoelectric transducers arranged in 32 sources and 32 receivers. The transducers are custom-made units from Olympus NDT, with disk-shaped active elements, 9.5 mm in diameter and with a frequency response centred on 800 kHz. We use a mix of 54 compression transducers and 10 shear transducers in order to use both P- and S-waves for the fracture growth monitoring.

In practice, we generate an excitation signal with the single-channel function generator board included in the NI control system. This low-voltage signal is then amplified by the 55 dB high-voltage amplifier, in order to get a final amplitude of approximately 350 V_{pp}. The high-voltage signal is then routed through the multiplexer in order to excite sequentially all source transducers. The function generator sends excitation signals at 2 kHz repetition rate, and simultaneously generates a trigger pulse that starts the recording over all 32 receiver transducers on the 50 MHz, 32-channel acquisition board. For each channel 8000 points are recorded, resulting in 160 μs of recording time.

For each individual source transducer, we stack the recorded signals of 50 consecutive excitations in order to improve the signal-to-noise ration (SNR) of the active elastic wave recordings.

A complete sequence of excitation and recording over all sources and receivers including stacking typically takes on the order of 2.5 s.

In order to optimise monitoring of changes in the fractured sample, we can change the acquisition period between consecutive excitation sequences. Typically we start with a long period (on the order of a few minutes) when first pressurizing the injection line. Once the fluid pressure reaches a predetermined level, defined from the experimental conditions, we reduce the acquisition period down to 4 s in order to capture fast changes in the sample properties after the fracture initiates. Once the fracture grows, the propagation of the fracture front slows down and we increase the period between acquisition sequences again.

B1.3.4 Data recording and storage

The recorded data are stored in a folder containing all the information related to an experiment, with each individual file named after the start time of the experiment, and starting with a header section describing all the experimental parameters and configuration for the specific experiment. This header contains its length in the first byte, and is easily readable in a JSON-style format.

For each experiment, one file contains the low rate pressure and volume recordings as a function of experimental time. Another file contains the active elastic wave data stored in binary format. For each acquisition sequence, we combine the stacked recorded signals of one specific source for all receivers end-to-end, and then append the signals from the next source, and so forth. We then append the signals from the following sequence to the same file. Therefore, the size of the file grows predictably after each acquisition sequence, by 32 (sources) × 32 (receivers) × 8000 (number of data points) × 8 (12-bit data rescaled to double precision) = 62.5 MB per sequence.

B1.4 Signal processing and analysis sequence

B1.4.1 Transmitted waves: fluid thickness estimation

The fluid thickness is given by the change in transmission coefficient between a reference signal before the start of the injection, and the signal of interest at time t. The normal transmission coefficient through a planar fluid layer of thickness h is given by (Groenenboom and Fokkema, 1998):

$$T(\omega, h) = \frac{(1 - r_{ff}^2)\exp(i\alpha)}{1 - r_{ff}^2 \exp(2i\alpha)} \tag{B1.1}$$

where ω is the signal frequency; $r_{ff} = \frac{z_r+1}{z_r-1}$, $z_r = \frac{\rho_f c_f}{\rho_s c_s}$; ρ_s, ρ_f are the densities of the solid and fracturing fluid, respectively; and c_s, c_f the P-wave velocities of the solid and fracturing fluid, respectively. In practice we use the inversion procedure described in Kovalyshen et al. (2014)

in order to estimate the fluid thickness for a given transmitted ray at a given time.

To calculate the fracture width (see example in figure B1.17), we minimise the following objective function in the frequency domain:

$$f(h) = \sum_{\nu} \left| \hat{u}_f(\nu) - T(\nu, h)\,\hat{u}_r(\nu) \right|^2 \tag{B1.2}$$

where $\hat{u}_r(\nu)$ and $\hat{u}_f(\nu)$ are the Fourier transforms of the reference signal (without the fracture) $u_r(t)$ and the signal that passed through the fracture $u_f(t)$ respectively.

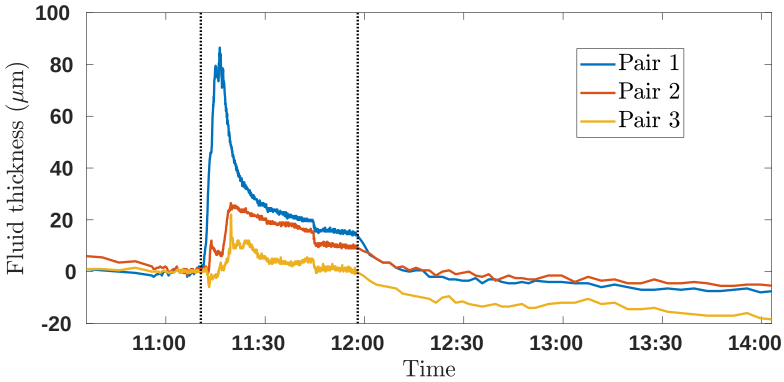

Figure B1.17 – Estimation of the fracture opening using the technique described in Groenenboom and Fokkema (1998).

B1.4.2 Diffracted waves

Thin, planar fractures diffract incident elastic waves (Blum et al., 2011). Diffraction of the incident wave by the fracture tip is sketched in figure B1.18. The difference between the signals received after the fracture started to propagate and the direct signal is translated in delay in arrival time. The diffraction travel-time depends on the position of the tip with respect to the source and receiver locations.

In practise we remove the incident wave obtained before the fracture What remains is scattered energy related to the fracture growth (see example in section 5.3.1). Besides, the change of the arrival time of the diffracted events is related to a change in the fracture-tip location.

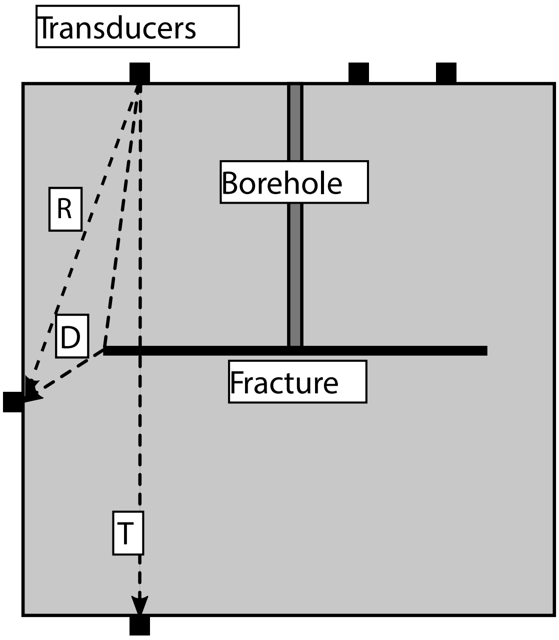
Transducers
Borehole
R
D
Fracture
T

Figure B1.18 – Schematic of elastic propagation modes inside a cubic sample with transducers on the sides. D: wave diffracted at the fracture tip, T: transmitted wave, R: direct wave.

Bibliography

Abe, H., Keer, L., and Mura, T. (1976). Growth rate of a penny-shaped crack in hydraulic fracturing of rocks. *Journal of Geophysical Research*, 81(35):6292–6298.

Adachi, J. and Detournay, E. (2002). Self-similar solution of a plane-strain fracture driven by a power-law fluid. *International Journal for Numerical and Analytical Methods in Geomechanics*, 26(6):579–604.

Adachi, J., Detournay, E., and Savitski, A. (2001). Simulation of hydraulic fracturing using an explicit moving mesh algorithm. In *DC Rocks 2001, The 38th US Symposium on Rock Mechanics (USRMS)*. American Rock Mechanics Association.

Adachi, J. I., Detournay, E., and Peirce, A. P. (2010). Analysis of the classical pseudo-3d model for hydraulic fracture with equilibrium height growth across stress barriers. *International Journal of Rock Mechanics and Mining Sciences*, 47:625–639.

Adams, J. and Rowe, C. (2013). Differentiating applications of hydraulic fracturing. In *ISRM International Conference for Effective and Sustainable Hydraulic Fracturing*. International Society for Rock Mechanics and Rock Engineering.

Alm, O., Jaktlund, L.-L., and Shaoquan, K. (1985). The influence of microcrack density on the elastic and fracture mechanical properties of stripa granite. *Physics of the Earth and Planetary Interiors*, 40(3):161–179.

Barbati, A., Desroches, J., Robisson, A., and McKinley, G. (2016). Complex fluids and hydraulic fracturing. *Annual review of chemical and biomolecular engineering*, 7:415–453.

Barenblatt, G. (1962). The mathematical theory of equilibrium cracks in brittle fracture. In *Advances in applied mechanics*, volume 7, pages 55–129. Elsevier.

Barnett, D. and Asaro, R. (1972). The fracture mechanics of slit-like cracks in anisotropic elastic media. *Journal of the Mechanics and Physics of Solids*, 20(6):353–366.

Barnett, D. and Swasger, L. (1971). The elastic energy of a straight dislocation in an infinite anisotropic elastic medium. *Physica Status Solidi (b)*, 48(1):419–428.

Batchelor, G. (1967). *An introduction to fluid dynamics*. Cambridge university press, Cambridge, UK.

Berryman, J. (1979). Long-wave elastic anisotropy in transversely isotropic media. *Geophysics*, 44(5):896–917.

Bertani, R. (2016). Geothermal power generation in the world 2010–2014 update report. *Geothermics*, 60:31–43.

Bessmertnykh, A. and Dontsov, E. (2018). Aspect ratio of hydraulic fracture in homogeneous transversely isotropic material. In *52nd US Rock Mechanics/Geomechanics Symposium*. American Rock Mechanics Association.

Bird, R., Armstrong, R., and Hassager, O. (1987). *Dynamics of polymeric liquids. Vol. 1: Fluid mechanics*. John Wiley and Sons Inc., New York, NY.

Blum, T., Adam, L., and Van Wijk, K. (2013). Noncontacting benchtop measurements of the elastic properties of shales. *Geophysics*, 78(3):C25–C31.

Blum, T., Snieder, R., Van Wijk, K., and Willis, M. (2011). Theory and laboratory experiments of elastic wave scattering by dry planar fractures. *Journal of Geophysical Research: Solid Earth*, 116(B8).

Bobko, C. and Ulm, F. (2008). The nano-mechanical morphology of shale. *Mechanics of Materials*, 40(4-5):318–337.

Bonnet, M. (1999). *Boundary integral equation methods for solids and fluids*, volume 34. Springer, Wiley-Blackwell edition.

Brodkey, R. S. (1969). *The phenomena of fluid motions*. Dover.

Bunger, A. (2005). *Near-surface hydraulic fracture*. PhD thesis, University of Minnesota.

Bunger, A. and Detournay, E. (2008). Experimental validation of the tip asymptotics for a fluid-driven crack. *Journal of the Mechanics and Physics of Solids*, 56(11):3101–3115.

Bunger, A., Jeffrey, R. G., Detournay, E., et al. (2005). Application of scaling laws to laboratory-scale hydraulic fractures. In *Alaska Rocks 2005, The 40th US Symposium on Rock Mechanics (USRMS)*. American Rock Mechanics Association.

Bunger, A.and Lecampion, B. (2017). Four critical issues for successful hydraulic fracturing applications. Technical report, CRC Press.

Caricchi, L., Burlini, L., Ulmer, P., Gerya, T., Vassalli, M., and Papale, P. (2007). Non-Newtonian rheology of crystal-bearing magmas and implications for magma ascent dynamics. *Earth and Planetary Science Letters*, 264(3):402–419.

Carreau, P. (1972). Rheological equations from molecular network theories. *Transactions of the Society of Rheology*, 16(1):99–127.

Chandler, M., Meredith, P., Brantut, N., and Crawford, B. (2016). Fracture toughness anisotropy in shale. *Journal of Geophysical Research: Solid Earth*, 121(3):1706–1729.

Chertov, M. (2012). Closed-form solution for vertical fracture width in anisotropic elastic formations. *International Journal of Rock Mechanics and Mining Sciences*, 53:70–75.

Cho, J., Kim, H., Jeon, S., and Min, K. (2012). Deformation and strength anisotropy of asan gneiss, boryeong shale, and yeoncheon schist. *International Journal of Rock Mechanics and Mining Sciences*, 50:158–169.

Cross, M. (1965). Rheology of non-Newtonian fluids: a new flow equation for pseudoplastic systems. *Journal of colloid science*, 20(5):417–437.

Crouch, S. and Starfield, A. (1983). *Boundary element methods in solid mechanics*. Allen & Unwin, London.

Cruse, T. A. (1996). BIE fracture mechanics analysis: 25 years of developments. *Computational Mechanics*, 18(1):1–11.

Daneshy, A. (1978). Hydraulic fracture propagation in layered formations. *Society of Petroleum Engineers Journal*, 18(01):33–41.

David, C., Robion, P., and Menéndez, B. (2007). Anisotropy of elastic, magnetic and microstructural properties of the callovo-oxfordian argillite. *Physics and Chemistry of the Earth, Parts A/B/C*, 32(1):145–153.

Dellinger, J. and Vernik, L. (1994). Do traveltimes in pulse-transmission experiments yield anisotropic group or phase velocities? *Geophysics*, 59(11):1774–1779.

Desroches, J., Detournay, E., Lenoach, B., Papanastasiou, P., Pearson, J., Thiercelin, M., and Cheng, A. (1994). The crack tip region in hydraulic fracturing. *Proceedings of the Royal Society of London A: Mathematical, Physical and Engineering Sciences*, 447(1929):39–48.

Detournay, E. (2004). Propagation regimes of fluid-driven fractures in impermeable rocks. *International Journal of Geomechanics*, 4(1):35–45.

Detournay, E. (2016). Mechanics of hydraulic fractures. *Annual Review of Fluid Mechanics*, 48:311–339.

Detournay, E., Cheng, A., and McLennan, J. (1990). A poroelastic pkn hydraulic fracture model based on an explicit moving mesh algorithm. *Journal of energy resources technology*, 112(4):224–230.

Detournay, E. and Garagash, D. (2003). The near-tip region of a fluid-driven fracture propagating in a permeable elastic solid. *Journal of Fluid Mechanics*, 494:1–32.

Detournay, E. and Peirce, A. (2014). On the moving boundary conditions for a hydraulic fracture. *Int. J. Eng. Sci.*, 84:147–155.

Dontsov, E. (2019). Scaling laws for hydraulic fractures driven by a power-law fluid in homogeneous anisotropic rocks. *International Journal for Numerical and Analytical Methods in Geomechanics*, 43(2):519–529.

Dontsov, E. and Peirce, A. (2015). A non-singular integral equation formulation to analyse multiscale behaviour in semi-infinite hydraulic fractures. *Journal of Fluid Mechanics*, 781:R1.

Dontsov, E. and Peirce, A. (2017). A multiscale implicit level set algorithm (ILSA) to model hydraulic fracture propagation incorporating combined viscous, toughness, and leak-off asymptotics. *Computer Methods in Applied Mechanics and Engineering*, 313:53–84.

Economides, M. and Nolte, K. (2000). *Reservoir stimulation*, volume 18. Wiley New York.

Eshelby, J., Read, W., and Shockley, W. (1953). Anisotropic elasticity with applications to dislocation theory. *Acta metallurgica*, 1(3):251–259.

Fabrikant, V. (1989). *Applications of potential theory in mechanics: a selection of new results*, volume 51. Dordrecht; Boston: Kluwer Academic Publishers.

Fabrikant, V. (2004). A new form of the green function for a transversely isotropic body. *Acta mechanica*, 167(1-2):101–111.

Fabrikant, V. (2011). Non-traditional crack problem for transversely-isotropic body. *European Journal of Mechanics-A/Solids*, 30(6):902–912.

Foreman, A. (1955). Dislocation energies in anisotropic crystals. *Acta metallurgica*, 3(4):322–330.

Garagash, D. (2009). Scaling of physical processes in fluid-driven fracture: perspective from the tip. *IUTAM symposium on scaling in solid mechanics, Springer*, pages 91–100.

Garagash, D. and Detournay, E. (1998). Similarity solution of a semi-infinite fluid-driven fracture in a linear elastic solid. *Comptes Rendus de l'Académie des Sciences-Series IIB-Mechanics-Physics-Chemistry-Astronomy*, 326(5):285–292.

Garagash, D. and Detournay, E. (2000). The tip region of a fluid-driven fracture in an elastic medium. *Journal of applied mechanics*, 67(1):183–192.

Garagash, D., Detournay, E., and Adachi, J. (2011). Multiscale tip asymptotics in hydraulic fracture with leak-off. *Journal of Fluid Mechanics*, 669:260–297.

Geertsma, J. and De Klerk, F. (1969). A rapid method of predicting width and extent of hydraulically induced fractures. *Journal of Petroleum Technology*, 21(12):1–571.

Green, G. (1828). *An essay on the application of mathematical analysis to the theories of electricity and magnetism.* Wezäta-Melins Aktiebolag.

Groenenboom, J. and Fokkema, J. (1998). Monitoring the width of hydraulic fractures with acoustic waves. *Geophysics*, 63(1):139–148.

Guillot, D. and Dunand, A. (1985). Rheological characterization of fracturing fluids by using laser anemometry. *Society of Petroleum Engineers Journal*, 25(01):39–45.

Haimson, B. and Cornet, F. (2003). Isrm suggested methods for rock stress estimation-part 3: Hydraulic fracturing (hf) and/or hydraulic testing of pre-existing fractures (htpf). *International Journal of Rock Mechanics and Mining Sciences*, 40.

Hakala, M., Kuula, H., and Hudson, J. (2007). Estimating the transversely isotropic elastic intact rock properties for in situ stress measurement data reduction: a case study of the olkiluoto mica gneiss, finland. *International Journal of Rock Mechanics and Mining Sciences*, 44(1):14–46.

Hills, D., Kelly, P., Dai, D., and Korsunsky, A. (2013). *Solution of crack problems: the distributed dislocation technique*, volume 44. Springer Science & Business Media.

Hirth, J. P. and Lothe, J. (1982). *Theory of dislocations*. John Wiley and Sons, Inc.

Hoenig, A. (1978). The behavior of a flat elliptical crack in an anisotropic elastic body. *International Journal of Solids and Structures*, 14(11):925–934.

Hornby, B. (1998). Experimental laboratory determination of the dynamic elastic properties of wet, drained shales. *Journal of Geophysical Research: Solid Earth*, 103(B12):29945–29964.

Hubbert, M. K. and Willis, D. (1957). Mechanics of hydraulic fracturing. *Trans. Am. Inst. Min. Eng.*, 210:153–158.

Hwu, C. and Ting, T. (1989). Two-dimensional problems of the anisotropic elastic solid with an elliptic inclusion. *The Quarterly Journal of Mechanics and Applied Mathematics*, 42(4):553–572.

Ioakimidis, N. and Theocaris, P. (1980). The practical evaluation of stress intensity factors at semi-infinite crack tips. *Engineering Fracture Mechanics*, 13(1):31–42.

Irwin, G. (1962). Crack-extension force for a part-through crack in a plate. *Journal of Applied Mechanics*, 29(4):651–654.

Kanaun, S. (2007). An elliptical crack in an anisotropic elasic medium subjected to a constant external field. *International Journal of Fracture*, 148(1):95–102.

Kefi, S., Lee, J., Pope, T., Sullivan, P., Nelson, E., Hernandez, A., Olsen, T., Parlar, M., Powers, B., and Roy, A. (2004). Expanding applications for viscoelastic surfactants. *Oilfield Rev*, 16(4):10–23.

Khristianovic, S. and Zheltov, Y. (1955). Formation of vertical fractures by means of highly viscous fluids. In *Proc. 4th world petroleum congress, Rome*, volume 2, pages 579–586.

Kovalyshen, Y., Bunger, A., Kear, J., and Kasperczyk, D. (2014). Comparison between ultrasonic and photometric methods for hydraulic fracture laboratory monitoring. *International Journal of Rock Mechanics and Mining Sciences*, 100(70):368–374.

Kuruppu, M., Obara, Y., Ayatollahi, M., Chong, K., and Funatsu, T. (2014). Isrm-suggested method for determining the mode i static fracture toughness using semi-circular bend specimen. *Rock Mechanics and Rock Engineering*, 47(1):267–274.

Lancellotta, R., Flora, A., and Viggiani, C. (2017). *Geotechnics and Heritage: Historic Towers*. CRC Press.

Laubie, H. (2013). Linear elastic fracture mechanics in anisotropic solids: Application to fluid-driven crack propagation. Master's thesis, Massachusetts Institute of Technology.

Laubie, H. and Ulm, F. (2014). Irwin's conjecture: Crack shape adaptability in transversely isotropic solids. *Journal of the Mechanics and Physics of Solids*, 68:1–13.

Lavrov, A. (2015). Flow of truncated power-law fluid between parallel walls for hydraulic fracturing applications. *Journal of Non-Newtonian Fluid Mechanics*, 223:141–146.

Lecampion, B., Bunger, A. P., and Zhang, X. (2018). Numerical methods for hydraulic fracture propagation: A review of recent trends. *Journal of Natural Gas Science and Engineering*, 49:66–83.

Lecampion, B. and Desroches, J. (2015). Simultaneous initiation and growth of multiple radial hydraulic fractures from a horizontal wellbore. *Journal of the Mechanics and Physics of Solids*, 82:235–258.

Lecampion, B., Desroches, J., Jeffrey, R., and Bunger, A. (2017). Experiments versus theory for the initiation and propagation of radial hydraulic fractures in low-permeability materials. *Journal of Geophysical Research: Solid Earth*, 122(2):1239–1263.

Lecampion, B., Peirce, A., Detournay, E., Zhang, X., Chen, Z., Bunger, A., Detournay, C., Napier, J., Abbas, S., Garagash, D., and Cundall, P. (2013). The impact of the near-tip logic on the accuracy and convergence rate of hydraulic fracture simulators compared to reference solutions. In *ISRM International Conference for Effective and Sustainable Hydraulic Fracturing*. International Society for Rock Mechanics and Rock Engineering.

Lhomme, T. (2005). *Initiation of hydraulic fractures in natural sandstones*. PhD thesis, Delft University of Technology.

Lin, W. and Keer, L. (1989). Three-dimensional analysis of cracks in layered transversely isotropic media. *Proceedings of the Royal Society of London A: Mathematical, Physical and Engineering Sciences*, 424(1867):307–322.

Lister, J. (1990). Buoyancy-driven fluid fracture: the effects of material toughness and of low-viscosity precursors. *Journal of Fluid Mechanics*, 210:263–280.

Loloi, M. (2000). Boundary integral equation solution of three-dimensional elastostatic problems in transversely isotropic solids using closed-form displacement fundamental solutions. *International Journal for Numerical Methods in Engineering*, 48(6):823–842.

Lu, K. (2016). *Gas Shale Anisotropy and Mechanical Property: Laboratory Measurements and Mathematical Modeling*. PhD thesis, University of Houston.

Madyarova, M. and Detournay, E. (2003). Fluid-driven penny-shaped fracture in permeable rock. Master's thesis, University of Minnesota.

Malén, K. and Lothe, J. (1970). Explicit expressions for dislocation derivatives. *Physica Status Solidi (b)*, 39(1):287–296.

Massonnet, C. (1965). Numerical use of integral procedures. *Stress analysis. Wiley, New York*, pages 198–235.

Matsuhisa, S. and Bird, R. (1965). Analytical and Numerical Solutions for Laminar Flow of the Non-Newtonian Ellis Fluid. *AIChE Journal*, 11(4):588–595.

Mavko, G., Mukerji, T., and Dvorkin, J. (2009). *The rock physics handbook: Tools for seismic analysis of porous media*. Cambridge university press.

Medlin, W. and Masse, L. (1984). Laboratory experiments in fracture propagation. *Society of Petroleum Engineers Journal*, 24(03):256–268.

Mogilevskaya, S. (2014). Lost in translation: crack problems in different languages. *International Journal of Solids and Structures*, 51(25-26):4492–4503.

Montgomery, C. and Smith, M. (2010). Hydraulic fracturing: history of an enduring technology. *Journal of Petroleum Technology*, 62(12):26–40.

Moukhtari, F.-E. and Lecampion, B. (2018). A semi-infinite hydraulic fracture driven by a shear-thinning fluid. *Journal of Fluid Mechanics*, 838:573–605.

Myers, T. (2005). Application of non-Newtonian models to thin film flow. *Physical Review E*, 72(6):066302.

Nejati, M., Aminzadeh, A., Saar, M., and Driesner, T. (2019). Modified semi-circular bend test to determine the fracture toughness of anisotropic rocks. *Engineering Fracture Mechanics*, 213:153–171.

Pan, E., Yuan, J., Chen, W., and Griffith, W. (2014). Elastic deformation due to polygonal dislocations in a transversely isotropic half-space. *Bulletin of the Seismological Society of America*, 104(6):2698–2716.

Pan, Y. and Chou, T. (1976). Point force solution for an infinite transversely isotropic solid. *Journal of Applied Mechanics*, 43(4):608–612.

Peirce, A. (2015). Modeling multi-scale processes in hydraulic fracture propagation using the implicit level set algorithm. *Computer Methods in Applied Mechanics and Engineering*, 283:881–908.

Peirce, A. (2016). Implicit level set algorithms for modelling hydraulic fracture propagation. *Philosophical Transactions of the Royal Society A: Mathematical, Physical and Engineering Sciences*, 374(2078).

Peirce, A. P. and Detournay, E. (2008). An implicit level set method for modeling hydraulically driven fractures. *Computer Methods in Applied Mechanics and Engineering*, 197(33-40):2858–2885.

Pelliccione, M. and Lu, T. (2008). Evolution of thin film morphology. In *Springer Series in Materials Science*, volume 108. Springer.

Perkins, T. K. and Kern, L. R. (1961). Widths of hydraulic fractures. *Journal of Petroleum Technology*, 222:937–949.

Pipe, C., Majmudar, T., and McKinley, G. (2008). High shear rate viscometry. *Rheologica Acta*, 47(5-6):621–642.

Ponson, L., Auradou, H., Pessel, M., Lazarus, V., and Hulin, J. (2007). Failure mechanisms and surface roughness statistics of fractured fontainebleau sandstone. *Physical Review E*, 76(3):036108.

Ponson, L., Auradou, H., Vié, P., and Hulin, J. (2006). Low self-affine exponents of fractured glass ceramics surfaces. *Physical review letters*, 97(12):125501.

Pouya, A. (2007). Green's function solution and displacement potentials for transformed transversely isotropic materials. *European Journal of Mechanics-A/Solids*, 26(3):491–502.

Prioul, R., Nolen-Hoeksema, R., Loan, M., Herron, M., Akkurt, R., Frydman, M., Reynolds, L., Sanchez, M., Graf, G., Karg, H., and Caniggia, J. (2018). Using cuttings to extract geomechanical properties along lateral wells in unconventional reservoirs. *Geophysics*, 83(3):MR167–MR185.

Rice, J. (1968). Mathematical analysis in the mechanics of fracture. *Fracture: an advanced treatise*, 2:191–311.

Rivalta, E., Taisne, B., Bunger, A., and Katz, R. (2015). A review of mechanical models of dike propagation: Schools of thought, results and future directions. *Tectonophysics*, 638:1–42.

Rutter, E., Mecklenburgh, J., and Taylor, K. (2017). Geomechanical and petrophysical properties of mudrocks: introduction. *Geological Society, London, Special Publications*, 454(1):1–13.

Savic, M. (1995). *Ultrasonic scattering from a hydraulic fracture: Theory, computation and experiment*. PhD thesis, Delft University of Technology.

Savitski, A. and Detournay, E. (2002). Propagation of a penny-shaped fluid-driven fracture in an impermeable rock: asymptotic solutions. *International Journal of Solids and Structures*, 39(26):6311–6337.

Schmittbuhl, J., Vilotte, J., and Roux, S. (1995). Reliability of self-affine measurements. *Physical Review E*, 51(1):131.

Sih, G., Paris, P., and Irwin, G. (1965). On cracks in rectilinearly anisotropic bodies. *International Journal of Fracture Mechanics*, 1(3):189–203.

Simonson, E. R., Abou-Sayed, A. S., and Clifton, R. J. (1978). Containment of massive hydraulic fractures. *SPE Journal*, 18(1):27–32.

Sochi, T. (2014). Using the Euler-Lagrange variational principle to obtain flow relations for generalized Newtonian fluids. *Rheologica Acta*, 53(1):15–22.

Sochi, T. (2015). Analytical solutions for the flow of Carreau and Cross fluids in circular pipes and thin slits. *Rheologica Acta*, 54(8):745–756.

Sone, H. (2012). *Mechanical properties of shale gas reservoir rocks, and its relation to the in-situ stress variation observed in shale gas reservoirs.* PhD thesis, Stanford university.

Sone, H. and Zoback, M. (2013). Mechanical properties of shale-gas reservoir rocks—part 1: Static and dynamic elastic properties and anisotropy. *Geophysics*, 78(5):D381–D392.

Sousa, J., Carter, B., and Ingraffea, A. (1993). Numerical simulation of 3D hydraulic fracture using Newtonian and power-law fluids. *International journal of rock mechanics and mining sciences & geomechanics abstracts*, 30(7):1265–1271.

Spence, D. and Sharp, P. (1985). Self-similar solutions for elastohydrodynamic cavity flow. *Proceedings of the Royal Society of London. A. Mathematical and Physical Sciences*, 400(1819):289–313.

Spence, D. and Turcotte, D. (1985). Magma-driven propagation of cracks. *Journal of Geophysical Research: Solid Earth*, 90(B1):575–580.

Standards Australia, A. . (2011). Structural steel–hot-rolled plates, floor plates and slabs.

Stoeckhert, F., Molenda, M., Brenne, S., and Alber, M. (2015). Fracture propagation in sandstone and slate-Laboratory experiments, acoustic emissions and fracture mechanics. *Journal of Rock Mechanics and Geotechnical Engineering*, 7(3):237–249.

Stroh, A. (1958). Dislocations and cracks in anisotropic elasticity. *Philosophical magazine*, 3(30):625–646.

Távara, L., Mantič, V., Ortiz, J., and París, F. (2012). Unique real-variable expressions of the integral kernels in the Somigliana stress identity covering all transversely isotropic elastic materials for 3D BEM. *Computer Methods in Applied Mechanics and Engineering*, 225(128–141).

Távara, L., Ortiz, J., Mantič, V., and París, F. (2008). Unique real-variable expressions of displacement and traction fundamental solutions covering all transversely isotropic elastic materials for 3D BEM. *International journal for numerical methods in engineering*, 74(5):776–798.

Theocaris, P. and Philippidis, T. (1992). True bounds on poisson's ratios for transversely isotropic solids. *The Journal of Strain Analysis for Engineering Design*, 27(1):43–44.

Thomsen, L. (1986). Weak elastic anisotropy. *Geophysics*, 51(10):1954–1966.

Thöny, R. (2014). *Geomechanical analysis of excavation-induced rock mass behavior of faulted Opalinus Clay at the Mont Terri Underground Rock Laboratory (Switzerland)*. PhD thesis, Diss., Eidgenössische Technische Hochschule ETH Zürich, Nr. 21415.

Ting, T. (1996). *Anisotropic elasticity: theory and applications*. Oxford University Press on Demand.

Tsai, V. and Rice, J. R. (2010). A model for turbulent hydraulic fracture and application to crack propagation at glacier beds. *J. Geoph. Res. - Earth Surface*, 115(F3):F03007.

Tsvankin, I. (2012). *Seismic signatures and analysis of reflection data in anisotropic media*. Society of Exploration Geophysicists.

Ulusay, R. (2014). *The ISRM Suggested Methods for Rock Characterization, Testing and Monitoring: 2007–2014*. Springer.

Viesca, R. and Garagash, D. (2015). Ubiquitous weakening of faults due to thermal pressurization. *Nature Geoscience*, 8(11):875–879.

Wan, R. (2011). *Advanced well completion engineering*. Gulf professional publishing.

Wang, Z. (2002). Seismic anisotropy in sedimentary rocks, part 2: Laboratory data. *Geophysics*, 67(5):1423–1440.

Williams, M. (1961). The bending stress distribution at the base of a stationary crack. *Journal of applied mechanic*, 28(1):78–82.

Willis, J. (1968). The stress field around an elliptical crack in an anisotropic elastic medium. *International Journal of Engineering Science*, 6(5):253–263.

Wrobel, M., Mishuris, G., and Piccolroaz, A. (2017). Energy release rate in hydraulic fracture: Can we neglect an impact of the hydraulically induced shear stress? *International Journal of Engineering Science*, 111:28–51.

Wu, R., Bunger, A., Jeffrey, R., and Siebrits, E. (2008). A comparison of numerical and experimental results of hydraulic fracture growth into a zone of lower confining stress. In *The 42nd US rock mechanics symposium (USRMS)*. American Rock Mechanics Association.

Yuan, J., Pan, E., and Chen, W. (2013). Line-integral representations for the elastic displacements, stresses and interaction energy of arbitrary dislocation loops in transversely isotropic bimaterials. *International Journal of Solids and Structures*, 50(20-21):3472–3489.

Zia, H. and Lecampion, B. (2019). Explicit versus implicit front advancing schemes for the simulation of hydraulic fracture growth. *Int. J. Numer. Anal. Meth. Geomech.*, 43(6):1300–1315.

Zia, H., Lecampion, B., and Zhang, W. (2018). Impact of the anisotropy of fracture toughness on the propagation of planar 3D hydraulic fracture. *International Journal of Fracture*, 211(1-2):103–123.

Fatima-Ezzahra Moukhtari
Rue de Bassenges 2, 1024 Ecublens, Suisse
+41787350779
fatimaezzahra.moukhtari@gmail.com
Date of birth: 23 July 1992
Nationality: Moroccan
Driven license B

Diplomas

2015-2020	**Ecole Polytechnique Fédérale de Lausanne, Lausanne, Switzerland** PhD candidate in mechanics (January 2020) Geo-Energy Laboratory– Gaznat chair on Geo-Energy (GEL) Subject: « Propagation of fluid driven fractures in transversely isotropic material» Swiss National Science Foundation grant (SNF)
2014-2015	**Ecole des Ponts ParisTech, Paris, France.** Master M2 in mechanics of soils, rocks, and structure in their environment (MSROE)
2012-2014	**Ecole Hassania des Travaux Publics, Casablanca, Morocco.** Civil Engineering degree
2010-2012	**Centre Ibn Abdoun, Khouribga, Morocco.** Two-years intensive program preparing for the national competitive entrance exam to engineering schools, Mathematics-Physics (MP)
2009-2010	**Lycée Ibn Yassine, Khouribga, Morocco.** Secondary school diploma in Mathematics

Work experiences

2015-2019	**Teaching assistant, EPFL, Lausanne, Switzerland.** Courses: Geotechnical design, Reservoir Geo-mechanics engineering Projects: Limit analysis for geotechnical engineering.
March- July 2015	**Master thesis, Navier Laboratory, école Ponts ParisTech, France.** Subject: Fracture mechanics: experimentation and numerical modelling.
June-August 2014	**Internship, Conseil Ingénierie et Développement, Rabat, Morocco.** Subject: Design and stability study of cope wall of a seaport.
July 2013	**Internship, Tezibat Sarl, Mohammedia, Morocco.** Subject: Construction of a residence.
2016-2017	**Teaching experience, Lausanne, Suisse.** Subject: Private teaching assistant in maths and physics.

Languages

Arabic	Mother tongue
French	Bilingual
English	Fluent

Skills

Programming	C++, Python, Matlab, Mathematica, Optum CE, Abaqus, FreeFem++ Pack office, Autocad, Adobe illustrator
Technical	Numerical modelling, Finite element, Integral equations, Optimisation methods Experimental design, Data analysis, Teaching skills

Interests

- Travelling
- Volunteering work (Child care project in Tanzania – IVHQ association)
- Reading
- Cooking

Scientific publications

- Moukhtari, Fatima-Ezzahra, and Brice Lecampion. "A semi-infinite hydraulic fracture driven by a shear-thinning fluid." Journal of Fluid Mechanics 838 (2018): 573-605.
- Moukhtari Fatima-Ezzahra, and Brice Lecampion, and Haseeb Zia "Propagation of a planar hydraulic fracture in transversely isotropic material". Journal of the Mechanics and Physics of Solids, Elsevier (JMPS), 2020.
- Moukhtari Fatima-Ezzahra, and Brice Lecampion, and Haseeb Zia "Propagation of a planar hydraulic fracture perpendicular to the isotropy plane of a transversely isotropic material". 53th US Rock Mechanics/Geomechanics Symposium. American Rock Mechanics Association, 2019.

Conferences

- Oral presentation in “53rd US Rock Mechanics / Geomechanics Symposium”. New York, USA, 23-26 June 2019: http://www.armasymposium.org
- Oral presentation in “Winter School on Geomechanics for Energy and the Environment”. Villars-sur-Ollon, Switzerland, 23-25 Jan. 2018: https://gete-school.epfl.ch
- Oral presentation in “Hydraulic Fracturing: Modelling, Simulation, and Experiment”. Banff International Research Station, Canada, 3-8 June 2018. The link for the presentation: https://www.birs.ca/events/2018/5-day-workshops/18w5085/videos/watch/201806051531-Moukhtari.html
- Oral presentation in “6th International Conference on Coupled THMC Processes in Geosystems”. Paris, France, 5-7 July 2017: https://geoproc2017.sciencesconf.org/data/pages/book_of_abstracts.pdf
- Poster presentation in “14th Swiss Geoscience meeting”. Geneva, Switzerland, 18-19 Nov. 2016: https://geoscience-meeting.ch/sgm2016/wp-content/uploads/SGM_2016_Abstract_Volume_s.pdf
- Poster presentation in “SCCR-SoE annual conference”. Sion, Switzerland, 12-13 Sep. 2016: http://www.sccer-soe.ch/en/news/events/annual-conference-2016/

References

- Brice Lecampion, thesis director
  Professor, EPFL, Switzerland
  brice.lecampion@epfl.ch
  Tel: +41 21 693 27 07
  http://gel.epfl.ch

- Jean Sulem, Master thesis supervisor
  Professor, École des Ponts ParisTech, France
  Head of Navier-CERMES Lab, France
  jean.sulem@enpc.fr
  Tel : (+33) 1 64 15 35 45